DEVELOPMENT OF TITANIUM ALLOYS FOR HYDROGEN STORAGE

Jimoh Mohammed Abdul
Student number: 672848

A thesis submitted to the Faculty of Engineering and Built Environment, University of the Witwatersrand, Johannesburg, in fulfilment of the requirements for the degree of Doctor of Philosophy in Engineering

Johannesburg, 2016

DECLARATION

"I hereby declare that the thesis submitted for the degree of Doctor of Philosophy, Ph.D.: Metallurgical and Material Science, at the University of the Witwatersrand is my own work and has not previously been submitted before for any other degree or examination to any other University. I further declare that all sources cited are indicated and acknowledged by means of a comprehensive list of references".

Name: J.M. Abdul (672848) Signature_____

4th Day of December 2015
(Day) (Month) (Year)

DEDICATION

To the Almighty God for his mercy and protection over me; and for making the Ph.D. a reality despite **all odds**

To my late parents for their care.

To my beloved wife and children for their understanding and support.

ABSTRACT

The thesis investigated the effect of partial substitution of Cr or Ti with 2-6 at.% Fe, or 0.05-0.10 at.% Rh/Pd on the structure, hardness, corrosion behaviour and hydrogen storage characteristics of an arc-melted $Ti_{35}V_{40}Cr_{25}$ at.% alloy. The effects of an annealing and a quenching heat treatment on the properties were also investigated.

Melting of the eight alloys was done in a water-cooled, copper-hearth arc melting furnace under an argon atmosphere. Each of the eight ingots was cut into three: one as the as-cast sample and the other two separately quartz-sealed and loaded in two batches in a heat treatment oven and heated to 1000 °C for 1 hour. The first set of quartz tubes were immediately removed and broken in cold water to quench the alloy, hence locking the microstructure. The second batch was loaded into the furnace, heated to 1000 °C for 1 hour and then slowly furnace-cooled. The alloys (as-cast and heat treated) were characterised for phase identification using optical microscopy, X-ray diffraction (XRD), and scanning electron microscopy (SEM) with Electron Diffraction X-ray Spectroscopy (EDS) using an Oxford system. Thermo-Calc software was used to model the phases using the Solid Solution 4 and Titanium 3 Databases. The hardness values (under a 2 kg load) of all samples were recorded. Potentiodynamic corrosion tests were performed in 6M KOH at 25 °C, and Tafel curves were recorded from -1.4V to -0.2V with a scanning rate of 1mV/sec. A Sievert's apparatus was used for pressure composition temperature (PCT) measurements at 30, 60 and 90 °C.

All the alloys contained a primary bcc (V) phase. The secondary phases were a combination of αTi, $Ti(Cr,V)_2$ Laves phases (C14, C15 or C36) and a minor ωTi phase. The cell volume of the primary (V) phase decreased with addition of Fe and 0.05 Rh but increased with 0.1 Rh and Pd.

The hardness of the base alloy increased with additions of Fe and 0.10 at.% Pd, but decreased with additions of Rh and 0.05 at.% Pd. Additions of Rh, Pd and 2 at.% Fe decreased the corrosion rate, while additions of 5 and 6 at.% Fe increased the corrosion rate. The reversible hydrogen storage capacity (RHSC) of the base alloy, otherwise known as useful capacity, was enhanced with addition of Pd and Rh, but decreased with Fe addition.

Both annealing and quenching increased the hardness of the 0.05 at.% Rh and all the Fe containing alloys. Heat treatment decreased the hardness of the base alloy, both Pd alloys and

the 0.10 at.% Rh samples. Quenching decreased the hardness of the 0.10 at.% Rh and both Pd-containing alloys.

The corrosion rate of the 0, 5 and 6 at.% Fe, 0.05 at.% Rh and the Pd-containing alloys decreased after annealing.at.% FeThe rate increased after annealing the 2 at.% Fe and 0.10 at,% Rh samples. The as-cast sample containing 2 at.% Fe had the lowest corrosion rate (0.0004 mm/y) and the quenched 6 at.% Fe was the least corrosion resistant sample with a corrosion rate of 0.037 mm/y.

The quenched 5% Fe alloy had the highest hardness (460 MPa), while the annealed 0.10 at.% Rh sample had the lowest (388 MPa).

The quenched 0.05 at.% Pd sample had the highest RHSC (2.28 wt%) while the lowest RHSC of 0.44 wt% was observed in the as-cast 2 at.% Fe sample.

Annealing improved the RHSC of all samples except the base $Ti_{35}V_{40}Cr_{25}$ and 6 at.% Fe alloys, while quenching was detrimental to RHSC of all the samples but the 2 at.% Fe, 0.05 at.% Pd and 0.10 at.% Rh alloys.

Increasing the addition of palladium from 0.05 to 0.10 at.% Pd showed no significant improvement on RHSC of the base alloy, thus addition of 0.05 at.% Pd would be sufficient. The RHSC of the annealed 0.05 Rh alloy (2.25 wt% H) was close to the value of the 0.10 at.% Pd, so rhodium could be considered as an alternative to the quenched 0.05 at.% Pd. The RHSC was 1.56, 0.44, 0.75 and 0.68 wt% for 0, 2, 5 and 6 at.% Fe as-cast alloys respectively. Although the 2 at.% Fe alloy had the lowest RHSC, it could find its application as electrode in 6M KOH solution electrolyte because of its low corrosion rate.

ACKNOWLEDGMENTS

First and foremost, my profound gratitude to God Almighty, He was, He is and He shall be sufficient for me all days of my life.

I wish to express my gratitude and deep appreciation to my supervisor, Dr Lesley H. Chown for nurturing me till the end of this research work. I will remain grateful to you, for your effective supervision, mentorship, dedication, understanding and moral support. When all hope seemed lost, you wiped off my tears, and rescued my sinking boat. Thank you and cheers!

I also wish to thank Prof. Lesley Cornish, the Director of the Centre of Excellence in Strong Materials, for her painstaking contribution to the success of this work. My profound appreciation also goes to Tetfund/Federal Polytechnic Offa, and to the DST-NRF Thuthuka fund, African Materials Science and Engineering Network (AMSEN), and the DST-NRF Centre of Excellence in Strong Materials for financial assistance.

I would like to thank Melanie Smit and Kedibone Thulani at Mintek for putting in extra hours to train me on electrochemical testing and microscopy respectively. I am indebted to Dr Kwo Young and Jean Nie on their support during PCT testing. I would also like to thank Mr Bryner Nelwalani for his assistance during the SEM analysis, Shadrack and Shaheeda for help with sample preparation and Professor Dave Billing for training and access to the XRD instrument at the School of Chemistry, University of the Witwatersrand.

My profound gratitude goes to all the postgraduate students of RW 418, for their love, understanding and companionship. Special thanks to Silas Hango, Muzi, Jethro, Genga, and Shaheeda for your good companionship and support.

Finally, my profound gratitude and appreciation goes to my beloved wife, Fatimoh Bolanle ABDUL, for understanding, support, endurance and above all, taking good care of my children throughout the period of study. I promise to continue to love you more. To my children, Hadiza Morenikeji, Aliyu Olayinka, Rofiat Ayodeji, Robiat Opeyemi and Habeeb Olohuntoyin, thank you for your endurance and cooperation with Mummy, while I was away. I LOVE YOU ALL!!!.

TABLE OF CONTENTS

CHAPTER 1: INTRODUCTION 1

1.1 BACKGROUND 1

1.2 WHY CHOOSE A LAVES PHASE-RELATED BCC SOLID SOLUTION ALLOY? 4

1.3 RESEARCH AIM AND OBJECTIVES 5

1.4 SIGNIFICANCE OF THE STUDY - INDUSTRIAL APPLICATIONS 5

1.5 THESIS STRUCTURE 6

CHAPTER 2: LITERATURE REVIEW 7

2.1 OVERVIEW 7

2.2 OVERVIEW OF ALLOYS 7

2.3 HYDROGEN STORAGE PROPERTIES OF MATERIALS 7

2.3.1 Storage capacity 8

2.3.2 Long-term cycling stability 10

2.3.3 Gaseous impurity resistance 10

2.3.4 Ease of activation 11

2.3.5 Thermodynamic properties 11

2.3.6 Kinetic properties 11

2.3.7 Effect of substituting elements on hydrogen storage properties 14

2.4.1. Effect of production methods on hydrogen storage alloys 25

2.4 PHASE DIAGRAMS IN THE TI-V-CR SYSTEM 31

2.4.1. Binary systems 31

2.4.2. $TiCr_2$ - V pseudobinary system 33

2.5 ELECTROCHEMICAL CORROSION MEASUREMENT 36

CHAPTER 3: EXPERIMENTAL PROCEDURE 39

3.1. OVERVIEW 39

3.2. CHOICE OF ALLOY COMPOSITION 39

3.3. MATERIALS PROCESSING AND PROCEDURE 40

3.4. ALLOY PRODUCTION 41

3.5. HEAT TREATMENT OF SAMPLES 42

3.6. METALLOGRAPHIC PREPARATION 42

3.6.1 MOUNTING 42

3.6.2 GRINDING AND POLISHING 42

3.7. CHARACTERISATION OF THE ALLOYS 43

3.7.1 OPTICAL MICROSCOPY 43
3.7.2 XRD 43
3.7.3 SEM 43
3.8. HARDNESS TEST 43
3.9. CORROSION TESTS 43
3.10. PRESSURE COMPOSITION TEMPERATURE PCT MEASUREMENTS 44
3.11. THERMO-CALC MODELLING 45
CHAPTER 4: RESULTS 46
OVERVIEW 46
4.1. COMPARISON OF THE ACTUAL AND NOMINAL COMPOSITIONS OF ALL ALLOYS 46
4.2. MICROSTRUCTURES OF ALLOYS A1 TO A8 46
4.2.1. MICROSTRUCTURES AND PHASE ANALYSIS OF ALLOY A1 (Ti_{25}:V_{40}:Cr_{35}) 46
4.2.2. MICROSTRUCTURES AND PHASE ANALYSIS OF ALLOY A2 (Ti24:V40:Cr34:Fe2) 50
4.2.3. MICROSTRUCTURES AND PHASE ANALYSIS OF ALLOY A3 (Ti_{25}:V_{37}:Cr_{33}:Fe). 54
4.2.4. MICROSTRUCTURES, AND PHASE ANALYSIS OF ALLOY A4 57
4.2.5. MICROSTRUCTURES AND PHASE ANALYSIS OF ALLOY A5 ($Ti_{24.975}$:V_{40}:$Cr_{34.975}$:$Rh_{0.05}$) 60
4.2.6. MICROSTRUCTURES AND PHASE ANALYSIS OF ALLOY A6 ($Ti_{24.95}$:V_{40}:$Cr_{34.95}$:$Rh_{0.1}$) 64
4.2.7. MICROSTRUCTURES AND PHASE ANALYSIS OF ALLOY A7 ($Ti_{24.98}$:V_{40}:$Cr_{34.97}$:$Pd_{0.05}$) 68
4.2.8. MICROSTRUCTURES AND PHASE ANALYSIS OF ALLOY A8 (Ti_{25}:V_{40}:$Cr_{34.9}$:$Pd_{0.1}$) 71
4.3. HARDNESS OF ALLOYS A1 TO A8 75
4.4. CORROSION BEHAVIOUR OF AS-CAST AND HEAT TREATED ALLOYS IN KOH SOLUTION 78
4.4.1. POTENTIODYNAMIC BEHAVIOUR IN 6M KOH SOLUTION 78
4.4.2. CORROSION RATES OF THE ALLOYS IN 6M KOH SOLUTION 80
4.5. HYDROGEN STORAGE CHARACTERISTICS OF THE Ti_{25}:V_{40}:Cr_{35} ALLOYS 84
4.5.1. ABSORPTION/DESORPTION BEHAVIOUR 84
4.5.2. REVERSIBLE HYDROGEN STORAGE CAPACITY 88
4.6. THERMO-CALC CALCULATIONS 93
4.6.1 CALCULATION OF PHASES IN A1 93
4.6.2 CALCULATION OF PHASES IN A2 95
4.6.3 CALCULATION OF PHASES IN A3 96
4.6.4 CALCULATION OF PHASES IN A4 98
4.6.5 CALCULATION OF PHASES IN A5 99
4.6.6 CALCULATION OF PHASES IN A6 100

4.6.7 CALCULATION OF PHASES IN A7 102

4.6.8 CALCULATION OF PHASES IN A8 103

CHAPTER 5: EFFECT OF FE SUBSTITUTION AND HEAT TREATMENT ON PROPERTIES OF AS-CAST $TI_{25}V_{40}CR_{35}$ 108

OVERVIEW 108

5.1. EFFECT OF IRON AND HEAT TREATMENT ON THE MICROSTRUCTURE AND PHASES 108

5.1.1 EFFECT OF IRON ADDITION ON MICROSTRUCTURE AND PHASES 108

5.1.2. EFFECT OF HEAT TREATMENT ON MICROSTRUCTURE AND PHASES 112

SHORT SUMMARY 115

5.2 EFFECT OF IRON ADDITION AND HEAT TREATMENT ON HARDNESS 115

5.2.1. EFFECT OF IRON ADDITION ON HARDNESS OF AS-CAST $TI_{25}V_{40}CR_{35}$ ALLOY 115

5.2.2. EFFECT OF HEAT TREATMENT ON HARDNESS 116

5.3. EFFECT OF IRON ADDITION AND HEAT TREATMENT ON CORROSION RATE 117

5.3.1 EFFECT OF IRON ADDITION ON CORROSION RATE 117

5.3.2 EFFECT OF HEAT TREATMENT ON CORROSION RATE 118

5.4. EFFECT OF IRON ADDITION AND HEAT TREATMENT ON HYDROGEN STORAGE 120

5.4.1. EFFECT OF IRON ADDITION ON HYDROGEN STORAGE PROPERTIES OF A1 120

5.4.2. EFFECT OF ISOTHERM TEMPERATURE ON ABSORPTION CAPACITY. 124

5.4.3. EFFECT OF HEAT TREATMENT ON HYDROGEN STORAGE PROPERTIES 125

SUMMARY OF THE CHAPTER 129

CHAPTER 6: EFFECT OF RHODIUM SUBSTITUTION AND HEAT TREATMENT ON PROPERTIES OF $TI_{25}V_{40}CR_{35}$ 130

OVERVIEW 130

6.1. EFFECT OF RHODIUM ADDITION AND THE HEAT TREATMENT ON THE MICROSTRUCTURE AND PHASES 130

6.1.1. EFFECT OF RHODIUM ADDITION ON THE MICROSTRUCTURE AND PHASES 130

6.1.2 EFFECT OF HEAT TREATMENT ON THE MICROSTRUCTURE AND PHASES 132

SUMMARY 134

6.2. EFFECT OF RHODIUM ADDITION AND HEAT TREATMENT ON HARDNESS 135

6.2.1. EFFECT OF RHODIUM ADDITION ON HARDNESS 135

6.2.2. EFFECT OF HEAT TREATMENT ON HARDNESS 135

SUMMARY 136

6.3. EFFECT OF RHODIUM ADDITION AND HEAT TREATMENT ON CORROSION PROPERTIES 136

6.3.1. EFFECT OF RHODIUM ADDITION ON CORROSION 136

6.3.2. EFFECT OF HEAT TREATMENT ON CORROSION RATE 138

SUMMARY 139

6.4. EFFECT OF RHODIUM ADDITION AND HEAT TREATMENT ON HYDROGEN STORAGE 139

6.4.1. EFFECT OF RHODIUM ADDITION ON HYDROGEN STORAGE PROPERTIES 139

6.4.2. EFFECT OF MEASUREMENT TEMPERATURE ON MAXIMUM HYDROGEN CAPACITY 145

6.4.3. EFFECT OF HEAT TREATMENT ON HYDROGEN STORAGE PROPERTIES 147

SUMMARY 151

SUMMARY OF THE CHAPTER 151

CHAPTER 7: EFFECT OF PALLADIUM SUBSTITUTION AND HEAT TREATMENT ON PROPERTIES OF $TI_{25}V_{40}CR_{35}$ 153

7.1. EFFECT OF PALLADIUM ADDITION AND HEAT TREATMENT ON MICROSTRUCTURE AND PHASES OF $TI_{25}V_{40}CR_{35}$ 153

7.1.1. EFFECT OF PALLADIUM ADDITION ON THE MICROSTRUCTURE AND PHASES 153

7.1.2. EFFECT OF HEAT TREATMENT ON THE MICROSTRUCTURE AND PHASES 156

SUMMARY 158

7.2. EFFECT OF PALLADIUM ADDITION AND HEAT TREATMENT ON HARDNESS 158

7.2.1. EFFECT OF PALLADIUM ADDITION ON HARDNESS 158

7.2.1. EFFECT OF HEAT TREATMENT ON HARDNESS 159

SUMMARY 160

7.3. EFFECT OF PALLADIUM ADDITION AND HEAT TREATMENT ON CORROSION 160

7.3.1. EFFECT OF PALLADIUM ADDITION ON CORROSION 160

7.3.1. EFFECT OF HEAT TREATMENT ON CORROSION 163

SUMMARY 164

7.4. EFFECT OF PALLADIUM AND HEAT TREATMENT ON HYDROGEN STORAGE 164

7.4.1. EFFECT OF PALLADIUM ADDITION ON HYDROGEN STORAGE 164

7.4.2. EFFECT OF TESTING TEMPERATURE ON HYDROGEN STORAGE 168

7.4.3. EFFECT OF HEAT TREATMENT ON HYDROGEN STORAGE PROPERTIES 170

SUMMARY 172

SUMMARY OF THE CHAPTER 172

CHAPTER 8: SUMMARY 174

OVERVIEW 174

8.1. EFFECT OF SUBSTITUTING FE OR A PGM ON THE BASE ALLOY 174

8.1. EFFECT OF HEAT TREATMENT ON THE ALLOYS 175

CHAPTER 9: CONCLUSIONS 180

CHAPTER 10: RECOMMENDATIONS 182

LIST OF FIGURES

Figure 1.1 Schematic diagram showing storage of gaseous hydrogen in HP tank[3].....2
Figure 1.2 Schematic diagram showing storage of cryogenic hydrogen in HP tank[3].....2
Figure 1.3. Schematic diagram showing the storage of hydrogen in solids. [3] 3
Figure 2.1 Hydrogen absorption and desorption PCIs for $LaNi_5$.[42].....8
Figure 2.2 Ti-V phase diagram.[39] 32
Figure 2.3 Ti-Cr phase diagram.[39] 32
Figure 2.4 V-Cr phase diagram.[39].....33
Figure 2.5 Pseudobinary $TiCr_2$ section through the Cr-Ti-V phase diagram.[37,38] 34
Figure 2.6. Isothermal sections through Ti-V-Cr system at 1000°C[39].....35
Figure 2.7. Classic Tafel curve. [44].....37
Figure 3.1. Photographs of water-cooled copper-crucible furnace (Mintek, South Africa). ...41
Figure 3.2. Computer controlled Sievert's apparatus. 44
Figure 4.1. Microstructures of alloy A1 (Ti_{25}:V_{40}:Cr_{35}). 47
Figure 4.2. XRD patterns of as-cast and heat treated alloy A1.....50
Figure 4.3. Microstructure of alloy A2. 51
Figure 4.4. XRD patterns of as-cast and heat treated alloy A2.....52
Figure 4.5. Microstructures of as-cast and heat treated alloy A3. 56
Figure 4.6. XRD patterns of as-cast and heat treated alloy A3.....57
Figure 4.7. Microstructures of as-cast and heat treated alloy A4. 58
Figure 4.8. XRD patterns of as-cast and heat treated alloy A4.....60
Figure 4.9. Microstructures of alloy A5.....61
Figure 4.10. XRD patterns of as-cast and heat treated alloy A5.....64
Figure 4.11. XRD patterns of alloy A6. 66
Figure 4.12. Microstructures of alloy A6.....67
Figure 4.13. Microstructure of alloy A7. 70
Figure 4.14. XRD patterns in alloy A7. 71
Figure 4.15. Microstructures of alloy A8.....73
Figure 4.16. XRD patterns of alloy A8. 74
Figure 4.17 Hardness (HV_2) of as-cast and heat treated $Ti_{25-0.5x}V_{40}Cr_{35-0.5x}Fe_x$ (x = 0, 2, 5, 6 at.%) alloy. 76
Figure 4.18 Hardness (HV_2) of as-cast and heat treated $Ti_{25-0.5x}V_{40}Cr_{35-0.5x}Rh_x$ (x = 0.05, 0.10 at.%) alloy. 77

Figure 4.19. Hardness (HV_2) of as-cast and heat treated $Ti_{25-0.5x}V_{40}Cr_{35-0.5x}Pd_x$ (x = 0.05, 0.10 at.%) alloy. 77
Figure 4.20. Potentiodynamic curves of as-cast and heat treated $Ti_{25-0.5x}V_{40}Cr_{35-0.5x}Fe_x$ (x = 0, 2, 5, 6 at.%) alloy. 78
Figure 4.21. Potentiodynamic curves of as-cast and heat treated $Ti_{25-0.5x}V_{40}Cr_{35-0.5x}Rh_x$ (x = 0.05, 0.10 at.%) alloys. 79
Figure 4.22. Potentiodynamic curves of as-cast and heat treated $Ti_{25-0.5x}V_{40}Cr_{35-0.5x}Pd_x$ (x = 0.05, 0.10 at.%) alloys. 79
Figure 4.23. Corrosion rates of as-cast and heat treated $Ti_{25-0.5x}V_{40}Cr_{35-0.5x}Fe$ (x = 0, 2, 5, 6) at.% alloy. 80
Figure 4.24. Corrosion rates of as-cast and heat treated $Ti_{25-0.5x}V_{40}Cr_{35-0.5x}Rh_x$ (x = 0.05, 0.10 at.%) alloy. 81
Figure 4.25. Corrosion rates of as-cast and heat treated $Ti_{25-0.5x}V_{40}Cr_{35-0.5x}Pd_x$ (x = 0.05, 0.10 at.%) alloy. 81
Figure 4.26. Selected desorption curves of as-cast and heat treated $Ti_{25-x}V_{40}Cr_{35-x}Fe_x$ (x = 0, 2, 5, 6 at.%) alloy. 85
Figure 4.27. The desorption curves of as-cast and heat treated $Ti_{25-0.5x}V_{40}Cr_{35-0.5x}Rh_x$ (x = 0.05, 0.1 at.%) alloy at 303K. 86
Figure 4.28. The desorption curves of as-cast and heat treated $Ti_{25-0.5x}V_{40}Cr_{35-0.5x}Rh_x$ (x = 0.05, 0.1 at.%) alloy at 303K. 86
Figure 4.29. RHSC of the as-cast, annealed and quenched $Ti_{25-0.5x}V_{40}Cr_{35-0.5x}Fe_x$ (x = 0, 2, 5, 6 at.%) alloy. 89
Figure 4.30. RHSC of the as-cast, annealed and quenched $Ti_{25-0.5x}V_{40}Cr_{35-0.5x}Rh_x$ (x = 0.05, 0.10 at.%) alloy. 91
Figure 4. 31. RHSC of the as-cast, annealed and quenched $Ti_{25-x}V_{40}Cr_{35-x}Pd_x$ (x = 0.05, 0.10 at.%) alloy. 91
Figure 4.32. SSOL4 Thermo-Calc calculation of phases in A1. 94
Figure 4.33. TTTI3 Thermo-Calc calculation of phases in A1. 94
Figure 4.34. SSOL4 Thermo-Calc calculation of phases in A2 95
Figure 4.35. TTTI3 Thermo-Calc calculation of phases in A2. 96
Figure 4.36. SSOL4 Thermo-Calc calculation of phases in A3. 97
Figure 4.37. TTTI3 Thermo-Calc calculation of phases in A3. 97
Figure 4.38. SSOL4 Thermo-Calc calculation of phases in A4. 98
Figure 4.39. TTTI3 Thermo-Calc calculation of phases in A4. 99

Figure 4.40. SSOL4 Thermo-Calc calculation of phases in A5. 100
Figure 4.41. TTTI3 Thermo-Calc calculation of phases in A5.....100
Figure 4.42. SSOL4 Thermo-Calc calculation of phases in A6. 101
Figure 4.43. TTTI3 Thermo-Calc calculation of phases in A6.....101
Figure 4.44. SSOL4 Thermo-Calc calculation of phases in A7. 102
Figure 4.45. TTTI3 Thermo-Calc calculation of phases in A7.....103
Figure 4.46. SSOL4 Thermo-Calc calculation of phases in A8. 104
Figure 4.47. TTTI3 Thermo-Calc calculation of phases in A8.....104
Figure 5.1. XRD patterns of as-cast $Ti_{25-0.5x}V_{40}Cr_{35-0.5x}Fe_x$ (x = 0, 2, 5, 6) alloys.....110
Figure 5.2. Variation of lattice parameter with Fe content. 110
Figure 5.3. Influence of Fe addition and heat treatment on cell volume. 113
Figure 5.4. Effect of heat treatment on hardness values of $Ti_{25-0.5x}V_{40}Cr_{35-0.5x}Fe_x$ (x = 0, 2, 5, 6 at.%) alloys. 116
Figure 5.5. Effect of heat treatment on corrosion rate of $Ti_{25-0.5x}V_{40}Cr_{35-0.5x}Fe_x$ (x = 0, 2, 5, 6). 119
Figure 5.6. Absorption/desorption isotherms of $Ti_{25-0.5x}V_{40}Cr_{35-0.5x}$ Fe_x (x = 0, 2, 5, 6 at.%) alloys. 121
Figure 5.7. Effect of Fe on H desorption in $Ti_{25-0.5x}V_{40}Cr_{35-0.5x}Fe_x$ (x = 0, 2, 5, 6 at.%) alloys. 122
Figure 5.8. Influence of (a) BCC cell volume and (b) Laves cell volume on useful capacity. 123
Figure 5.9. Effect of isotherm temperature on maximum H capacity of the Fe alloys.....124
Figure 5.10. Effect of %Fe in heat treated sample on RHSC of $Ti_{25-0.5x}V_{40}Cr_{35-0.5x}$ Fe_x (x = 0,2,4,6). 125
Figure 6.1. XRD patterns of as-cast $Ti_{25-0.5x}V_{40}Cr_{35-0.5x}Rh_x$ (x = 0, 0.05, 0.10) at.% alloy....131
Figure 6.2. XRD patterns of as cast and heat treated $Ti_{25-0.5x}V_{40}Cr_{35-0.5x}Rh_x$ (x = 0, 0.05, 0.10 at.%) alloy. 133
Figure 6.3. Effect of Rh substitution and heat treatment on cell volume of BCC and Laves phases. 134
Figure 6.4. Effect of rhodium additions and heat treatment on hardness. 136
Figure 6.5. Potentiodynamic curves of as-cast $Ti_{25-0.5x}V_{40}Cr_{35-0.5x}Rh_x$ (x = 0, 0.05, 0.10 at.%) alloys. 137
Figure 6.6. Effect of Rh composition and heat treatment on corrosion rate of $Ti_{25}V_{40}Cr_{35}$. .138

Figure 6.7. Effect of Laves proportion in $Ti_{25-0.5x}V_{40}Cr_{35-0.5x}Rh_x$ (x = 0, 0.05, 0.10 at.%) alloys on corrosion rate. 139
Figure 6.8. Absorption/desorption PCT curves of as-cast $Ti_{25-0.5x}V_{40}Cr_{35-0.5x}Rh_x$ (x = 0, 0.05, 0.10) alloys.....140
Figure 6.9. Influence of Rh composition on useful capacity of as-cast $Ti_{25}V_{40}Cr_{35}$. 141
Figure 6.10. Desorption curves of as-cast $Ti_{25-0.5x}V_{40}Cr_{35-0.5x}Rh_x$ (x = 0, 0.05, 0.10) at 303 K. 141
Figure 6.11. Effect of heat treatment on RHSC of $Ti_{25-0.5x}V_{40}Cr_{35-0.5x}Rh_x$ (x=0, 0.05, 0.10 at.%) alloy. 143
Figure 6.12. Effect of testing temperature and addition of Rh on maximum H capacity of: a) as-cast; b) annealed; c) quenched $Ti_{25-0.5x}V_{40}Cr_{35-0.5x}Rh_x$ (x = 0, 0.05, 0.10) alloys. 146
Figure 6.13. Van`t Hoff plot of effect of heat treatment on $Ti_{24.975}V_{40}Cr_{34.975}Rh_{0.05}$.....149
Figure 6.14. Van`t Hoff plot of effect of heat treatment on $Ti_{24.95}V_{40}Cr_{34.95}Rh_{0.10}$. 150
Figure 7.1. XRD patterns of as-cast $Ti_{25-0.5x}V_{40}Cr_{35-0.5x}Pd_x$ (x = 0, 0.05, 0.10 at.%) alloys...155
Figure 7.2. XRD patterns of as-cast, annealed and quenched $Ti_{25-0.5x}V_{40}Cr_{35-0.5x}Pd_x$ (x = 0, 0.05, 0.10 at %) alloys 157
Figure 7.3. Effect of Pd and heat treatment on cell volume of phases. 158
Figure 7.4. Effect of heat treatment on hardness of $Ti_{25-0.5x}V_{40}Cr_{35-0.5x}Pd_x$ (x = 0, 0.05, 0.10 at.%) alloys. 160
Figure 7.5. Potentiodynamic curves for $Ti_{25-0.5x}V_{40}Cr_{35-0.5x}Pd_x$ (x = 0, 0.05, 0.10 at.%) alloys in 6M KOH solution. 161
Figure 7.6. Effect of heat treatment on corrosion rate of $Ti_{25-0.5x}V_{40}Cr_{35-0.5x}Pd_x$ (x = 0, 0.05, 0.10 at.%) alloy in 6M KOH solution.....162
Figure 7.7. Influence of a) BCC proportion and b) secondary phase proportion on corrosion rate of $Ti_{25-0.5x}V_{40}Cr_{35-0.5x}Pd_x$ (x = 0.05, 0.10 at.%) alloys. 163
Figure 7.8. Ab/desorption curves of as-cast a) 0.05 at.% Pd alloy and b) 0.10 at.% Pd alloy. 165
Figure 7.9. Effect of Pd on desorption curve of as-cast $Ti_{25}V_{40}Cr_{35}$ at 303 K.....165
Figure 7.10. Effect of BCC volume on RHSC of $Ti_{25-0.5x}V_{40}Cr_{35-0.5x}Pd_x$ (x = 0.05, 0.10 at.%) alloys. 166
Figure 7.11. Van`t Hoff plot of $Ti_{25-0.5x}V_{40}Cr_{35-0.5x}Pd_x$ (x = 0, 0.05, 0.10 at.%) alloy.....167
Figure 7.12. Effect of isotherm temperature and Pd on maximum H capacity. 169
Figure 7.13. Effect of heat treatment on RHSC of $Ti_{25-0.5x}V_{40}Cr_{35-0.5x}Pd_x$ (x = 0, 0.05, 0.10 at.%) alloys. 170

Figure 7.14. Van’t Hoff plots showing the effect of heat treatment on Pd alloys. 171
Figure 8.1. Effect of additives and heat treatment on hardness of all alloys. 175
Figure 8.2. Effect of additives and heat treatment on corrosion rate of all the alloys. 178
Figure 8.3. Effect of additives and heat treatment on RHSC of all alloys.....179

LIST OF TABLES

Table 2.1 Effect of alloying additions on hydrogenation properties. 26
Table 2.2 Cr-Ti-V crystal structure and lattice parameter data.[38] 34
Table 2.3. Possible cell volume of Laves and other phases. 35
Table 2.4 Value of constants used in corrosion rate calculations[44]. 38
Table 3.1 Mass of elements for arc-melting of 10g samples. 41
Table 4.1. Targeted and analysed compositions of the alloys. 46
Table 4.2. EDX compositions and XRD crystallographic parameters of phases in alloy A1 (Ti_{25}:V_{40}:Cr_{35}). 49
Table 4.3. EDX compositions and crystallographic parameters of phases in alloy A2 (Ti_{24}:V_{40}:Cr_{34}:Fe_2). 53
Table 4.4. EDX compositions and crystallographic parameters of phases in alloy A3. 55
Table 4.5. EDX compositions and crystallographic parameters of phases in alloy A4. 59
Table 4.6. EDX compositions and crystallographic parameters of phases in alloy A5. 63
Table 4.7. EDX compositions and crystallographic parameters of phases in alloy A6. 65
Table 4.8. EDX compositions and crystallographic parameters of phases in alloy A7. 69
Table 4.9. EDX compositions and crystallographic parameters of phases in alloy A8. 72
Table 4.10. Summary of absorption/desorption data for alloys A1 to A8. 87
Table 4.11. Thermodynamic properties of alloys A1 to A8. 92
Table 4.12. Figure numbers of the Thermo-Calc property diagrams showing calculation of the phases in alloys A1 to A8. 93
Table 4.13. Summary of ThermoCalc calculations, listing the amount and composition of phase at 1000°C and 200°C in alloys A1 to A8. 105
Table 5.1. EDX analyses and crystallographic parameters of as-cast $Ti_{35-0.5x}V_{40}Cr_{25-0.5x}Fe_x$ (x = 0, 2, 5, 6 at.%). 109
Table 5.2. Hydrogen storage properties of $Ti_{25-0.5x}V_{40}Cr_{35-0.5x}Fe_x$ (x = 0, 2, 5, 6 at.%). 123
Table 5.3. Effect of heat treatment on H capacity and plateau pressure of $Ti_{25-0.5x}V_{40}Cr_{35-0.5x}Fe_x$ (x = 0, 2, 4, 6) at 303K. 127
Table 6.1: EDS of as-cast $Ti_{25-0.5x}V_{40}Cr_{35-0.5x}Rh_x$ (x = 0, 0.05, 0.10) 131
Table 6.2. Thermodynamic properties of as-cast nominal $Ti_{25-0.5x}V_{40}Cr_{35-0.5x}Rh_x$ (x = 0, 0.05, 0.10 at.%) alloys. 142
Table 6.3. Calculation of desorption enthalpy and entropy for $Ti_{24.975}V_{40}Cr_{34.975}Rh_{0.05}$ 149

Table 6.4. Calculation of desorption enthalpy and entropy of as-cast and heat treated $Ti_{24.95}V_{40}Cr_{34.95}Rh_{0.10}$ 150
Table 7.1. EDS of as-cast $Ti_{25-0.5x}V_{40}Cr_{35-0.5x}Pd_x$ (x = 0, 0.05, 0.10).....154
Table 7.2. Thermodynamic properties of as-cast $Ti_{25-0.5x}V_{40}Cr_{35-0.5x}Pd_x$ (x = 0, 0.05, 0.10 at.%) alloy.....168
Table 7.3. Thermodynamics properties of as-cast and heat treated Pd containing alloys. 172
Table 8.1. Summary of all results. 177

CHAPTER 1: Introduction

1.1 BACKGROUND

Currently, most automobiles, trains and planes are fuelled almost exclusively by petroleum products such as gasoline and diesel and most power plants use oil, natural gas and coal as fuel. Without fossil fuels, there would have been no industrialisation. As important as fossil fuel is, it creates four major problems:

i. **Air pollution** - Combustion products of the internal combustion engine are carbon monoxide (a poisonous gas), nitrogen oxides (the main source of urban smog) and unburned hydrocarbons (the main source of urban ozone).[1]

ii. **Environmental pollution** - The process of transporting and storing oil has a detrimental impact on the environment whenever something goes awry; an oil spill, pipeline explosion or well fire can create an environmental disaster.[2]

iii. **Global warming** - The carbon dioxide released from every vehicle's exhaust is a greenhouse gas which is slowly raising the temperature of the planet, with the consequent dramatic climate changes that could affect everyone on the planet.[3] For example, if the ice caps melt, sea levels will rise significantly, flooding and destroying all coastal cities.

iv. **Dependence** - When Middle East oil producers decide to raise the price of oil, the rest of the world has little choice but to pay the higher price.

In the future, hydrogen will probably play an important economic role as a raw material and as a source of energy, hence becoming a viable alternative to fossil fuel.[2] Hydrogen has been used for a variety of purposes: the hydrogen decrepitating (HD) process has been applied to successfully produce $SmCo_5$, $Sm_2(Co, Fe, Cu, Zr)_{17}$ and $Nd_2Fe_{14}B$-type magnets.[3] Other wide areas of applications of hydrogen include petroleum and chemical companies, food industries, aviation industry, manufacturing industries, and in a limited capacity, as clean fuel and power.[4] The waste product of electrical power generated from hydrogen is water, which is environmentally friendly, unlike radioactive waste from redundant nuclear power plants.

Hydrogen energy has to be stored before use, because, like petrol or diesel fuel, it is a use-as-you-go energy source.[5] However, one major aspect of using hydrogen will be the challenges of safe storage facilities.[6] For use in fuel cell cars, hydrogen storage will be required on-board in vehicles, at hydrogen production sites, hydrogen-refuelling stations, and stationary power sites.[7] This has led substantial research in reversible hydrides for hydrogen storage, especially for mobile use.[8]

Hydrogen storage in metal hydrides has been described as a measure of interaction between metal and hydrogen. [9-12] Hydrogen storage alloys (HSAs) are intermetallic compounds capable of absorbing hydrogen by forming hydride phases of suitable stability.[13] So HSAs are alloys which have potential use as hydrogen, or energy storage compounds[14]. They also include metallic materials that have a unique ability to reversibly absorb and release significant amounts of hydrogen electrochemically or from the gas phase.[15, 16] Developing safe, reliable, compact, and cost-effective hydrogen storage technologies are one of the most technically challenging barriers to its widespread use as a form of energy.[15] Hydrogen can be stored in three forms[3]:

- Gaseous hydrogen (Figure 1.1)
- Cryogenic hydrogen (Figure 1.2)
- Advanced materials (Figure 1.3)

Safety challenges are high in the first and second methods as the storage are usually in high-pressure tanks (up to 700 bars). Between 2007 and 2012, a total of 204 hydrogen accidents occurred as a result of usage and storage, where ~102 were linked to failure in piping fittings and valves.[17] Compressed gas and liquid hydrogen tanks are much larger and heavier than what is ultimately desired for most practical applications.[5] Physical storage of cryogenic hydrogen involves cooling to -253°C, at pressures of -350 bar in insulated tanks [6], which adds to storage costs[3].

Figure 1.1 Schematic diagram showing storage of gaseous hydrogen in HP tank[3].

Figure 1.2 Schematic diagram showing storage of cryogenic hydrogen in HP tank[3].

In view of the above hydrogen storage challenges, researchers are evaluating light-weight, safe, composite materials that can reduce the weight and volume of compressed gas storage systems, mostly through alloying of metallic elements[18].

Storage of hydrogen in advanced materials has been found to be safe and cost effective[18]. Hydrogen can be stored on the surfaces of solids by adsorption or within solids by absorption as shown in Figure 1.3. In adsorption (Figure 1.3a), hydrogen attaches to the surface of a material either as hydrogen molecules (H_2) or hydrogen atoms (H). In absorption (Figure 1.3b), hydrogen molecules dissociate into hydrogen atoms that are incorporated into the solid lattice framework. This method may make it possible to store larger quantities of hydrogen in smaller volumes at low pressure and at temperatures close to room temperature. Finally, hydrogen can be strongly bound within molecular structures, as chemical compounds containing hydrogen atoms (Figure 1.3 c and d).

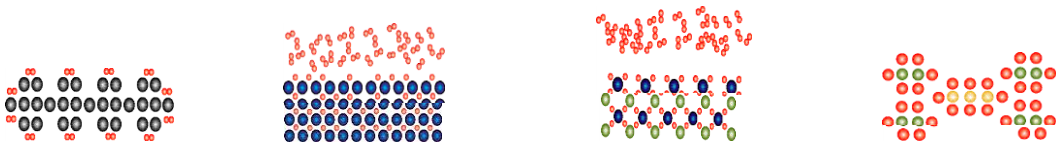

a) Surface adsorption b) Intermetallic hydride c) Complex hydride d) Chemical hydride

Figure 1.3. Schematic diagram showing the storage of hydrogen in solids. [3]

Currently, the only safe alternative to fossil fuel is having an on-board metallic alloy that can store a significant amount of hydrogen fuel to power a car. The only by-product is oxygen and a trickle of water, neither of which will cause any harm to human health or the environment.

Intermetallic hydrogen storage alloys are categorised into four major groups; namely A_2B, AB_2, AB_5, and AB[21].

1. A combination of an alkali earth metal A and a transition metal B forms A_2B alloys, e.g. Mg_2Ti.
2. The AB_2 alloys, also known as Laves phase alloys, that are suitable for hydrogen storage, contain titanium, zirconium or hafnium at the A-site and a transition metal at B-site (e.g. Mn, Ni, Cr or V).

3. The AB_5 alloys combine a hydride-forming metal A, usually a rare earth metal (La, Ce, Nd, Pr, Y or a mixture known as Mischmetal), with a non-hydride forming element such as nickel.
4. Combination of two transition metals forms AB alloys e.g. FeTi.

Solid solution alloys are formed by dissolving a hydrogen-absorbing metal element in another[21]. These alloys are based on elements such as V, Ti, Pd and Zr. Zr- and Ti- based solid solutions are usually too stable and palladium is too expensive. Solid solution alloys based on vanadium have good absorption properties.

Solid solution alloys, commonly based on a V and Ti bcc solid solution, that contain a small amount of Laves phase (preferably C14), are called *Laves phase-related bcc solid solution* alloys e.g. based on Ti-V-Cr[22].

1.2 WHY CHOOSE A LAVES PHASE-RELATED BCC SOLID SOLUTION ALLOY?

Ti-V based Laves phase-related bcc solid solution hydrogen storage alloys have been intensely studied for use as negative electrodes in nickel–metal hydride (Ni-MH) batteries[23]. The V-based bcc phase is the major hydrogen-absorbing phase, while the C14 Laves phase not only absorbs hydrogen, but also acts as a catalyst in electrochemical hydrogenation/ dehydrogenation of the bcc phase. The

Ti-Cr-V based alloys have a high effective hydrogen storage capacity of over 2 wt%, with a theoretical storage capacity of 3.8 wt%[24].

For this research work, the Ti-V-Cr based alloys have been chosen, as South Africa has extensive reserves of titanium, chromium and vanadium.

This work will add to the pool of knowledge on storage capacity of metallic hydride alloys, thereby facilitating the industrial applications, for example in fuel cell cars and commercial use as electrodes in metallic hydride batteries.

1.3 RESEARCH AIM AND OBJECTIVES

The aim of this research work was to develop and assess titanium alloys based on the Ti-Cr-V system for hydrogen storage.
The specific objectives were to:

a) Produce, process and characterise as-cast alloys for hydrogen storage.
b) Investigate the effect of substituting Fe or PGMs (Pd and Rh) at Cr/Ti sites on structure, corrosion properties, hardness and hydrogen storage characteristics of the alloys.
c) Determine the effects of various heat treatments on the structure, corrosion properties, hardness and hydrogen storage characteristics
d) Identify the most promising Ti-Cr-V-Fe-PGM composition for future work in producing, processing and characterising powder metallurgy alloys for hydrogen storage.

1.4 SIGNIFICANCE OF THE STUDY - INDUSTRIAL APPLICATIONS

Study of hydrogen storage is significant because hydrogen is the ideal candidate as an energy carrier for domestic, mobile and stationary applications, while averting adverse effects on the environment, and reducing dependence on imported oil [16].

Development of a solid metallic hydrogen storage alloy as proposed in this work becomes very significant, as the use of liquid hydrogen requires the addition of a refrigeration unit to maintain a cryogenic state, thus adding weight and energy costs, and a resultant 40% loss in energy [21]. Designs involving the use of methane as a hydrogen source require the addition of a steam reformer to extract the hydrogen from the carbon which adds weight, additional space requirements and the need for a device to isolate CO_2 [22]. High-pressure storage of hydrogen gas is limited by the weight of the storage canisters and the potential for developing leaks[2]. In addition, storage of hydrogen in liquid or gaseous forms poses important safety risks for on-board transport applications [23].

About 20% of the world's 4,221,000 tons of titanium is mined in the form of TiO_2 in South Africa [24]. Therefore, this work was aimed at promoting the use of an abundant, locally

available mineral, which is a key objective in the Beneficiation Strategy tabled in Parliament by the Department of Mineral Resources (DMR) in 2010 [24].

Modifier elements such as platinum group metals (PGMs) coated on hydrogen storage alloys enhance both the absorption and desorption of hydrogen, even under rapid charging and discharging times [25]. As South Africa produces ~74% of the global PGM supply [155], the proposed inclusion of PGMs to the hydride alloys will enhance the relevance of this country in the area of hydrogen storage technology in addition to enhancing the GDP.

In an attempt to investigate the hazard in inhaling exhaust smoke from diesel engines, Silverman[26], chief of environmental epidemiology for the National Cancer Institute, reported that in her 50 years study of 12 000 miners, the non-smoking miners who were heavily exposed to diesel fumes underground had seven times the normal lung cancer risk of smokers. So the use of hydrogen in the form of hydride-containing batteries as a fuel in mines would greatly reduce the health- and fire- hazards posed by the use of diesel.

Hydrogen storage alloys are sometimes used as anodes in NiMH batteries, hence the need to investigate the corrosion behaviour of the alloy in a similar medium.

1.5 THESIS STRUCTURE

Chapter 2 reviews relevant literature in five sections. The first is a brief overview of the alloys. This is followed by phases and phase diagrams in the ternary Ti-V-Cr and pseudo-binary $TiCr_2$ – V system. The third section discusses the important practical properties of hydrogen storage alloys, the fourth section reviews relevant published work on Ti-V-Cr based hydrogen storage alloys, while the last section provides a brief overview of electrochemical corrosion measurement.

The experimental methodology, equipment and materials are described in Chapter 3. Chapter 4 presents results of laboratory work, in Chapter 5 the effect of substituting Fe on properties of the base alloy ($Ti_{25}V_{40}Cr_{35}$) is discussed, while in Chapters 6 and 7 the effects of Rh and Pd on properties of the base alloy are discussed respectively. The effect of heat treatment on the properties of the alloys is discussed in each chapter. A summary of the results is given in Chapter 8, the conclusions are presented in Chapter 9 and recommendations for future work are given in Chapter 10.

CHAPTER 2: Literature review

2.1 OVERVIEW

A brief overview of alloys is given, followed by information on the binary (Ti-V, V-Cr, Ti-Cr) and pseudo-binary ($TiCr_2$ - V) phase diagrams of the Ti-V-Cr system. The important practical properties of hydrogen storage alloys are discussed. Relevant published work on Ti-V-Cr based hydrogen storage alloys is reviewed, specifically: properties of HSAs, the effects of substituting one or more elements and the influence of production methods and heat treatment on the hydrogen storage properties. In the last section, measurement of electrochemical/corrosion properties is reviewed.

2.2 OVERVIEW OF ALLOYS

A metallic alloy is a mixture or metallic solid solutions composed of two or more elements[27]. Complete solid solution alloys give a single solid phase microstructure, while partial solutions give two or more phases that may or may not be homogeneous in distribution, depending on thermal (heat treatment) history. Alloys usually have different properties from those of the component elements. In this work, the major elements Ti, Cr and V are considered.

2.3 HYDROGEN STORAGE PROPERTIES OF MATERIALS

In order to assess the suitability of material for widespread use as a hydrogen store, the physical and chemical properties include those related to safety and design of hydrogen storage systems. Other practical considerations are the cost of the material and its raw constituents, and their natural abundance. However, the properties of prime technological importance are those relating to hydrogen sorption, which include the following[33] :

a. Storage capacity (reversible, gravimetric and volumetric)
b. Long-term cycling stability
c. Gaseous impurity resistance
d. Ease of activation
e. Thermodynamic properties (enthalpy of adsorption and enthalpy of hydride formation and decomposition)
f. Kinetic properties (hydrogen adsorption and absorption)

2.3.1 Storage capacity

Reversible storage capacity

The reversible storage capacity of a material is the quantity of hydrogen absorbed and desorbed between the lower and upper operating pressures of a hydrogen store[20]. The United States DOE 2020 targets[45] suggest that the minimum and maximum delivery pressure from storage system should be 5 and 12 bar (abs) (0.5 and 1.2 MPa). Any change in this pressure range is likely to change the reversible capacity of a given material to a certain extent.[44] The reversible storage capacity for an interstitial hydride will be determined by the width of the plateau in the Pressure-Composition-Isotherm (PCI) as shown in Figure 2.1. The test was performed at 60°C (333 K), with a charging pressure of 2 MPa and delivery pressure of 0.3 MPa.[42]

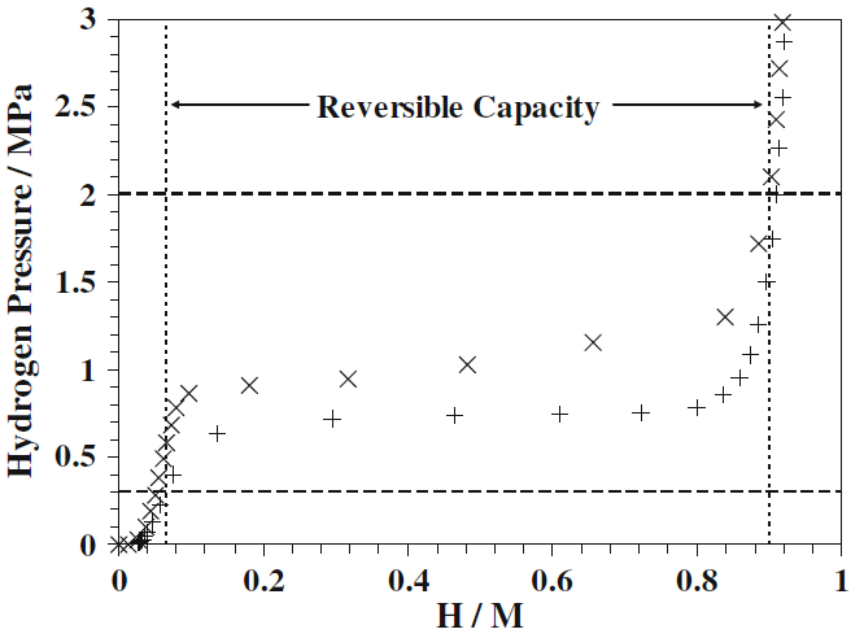

Figure 2.1 Hydrogen absorption and desorption PCIs for $LaNi_5$.[42]

For any given hydride, including binary compounds, the absorption plateau pressure will increase with increasing temperature, and will generally follow the van't Hoff relationship:[53]

$$In\ P = \frac{\Delta H}{RT} - \frac{\Delta S}{R} \quad \ldots\ldots 2.1$$

where P is the operating pressure, ΔH is the enthalpy of hydride formation or decomposition, ΔS is the entropy of formation or decomposition, R is the universal gas constant and T is the operating temperature in K.

The natural logarithm (*ln*) of plateau pressures in PCT curves for 3 or more isotherm temperatures are used to obtain the van't Hoff plot. Let the slope of the line be *m* and the intercept be *c*, it then follows that:

$$\Delta H = Rm$$

and $$\Delta S = Rc$$

However, in situations where one of the three PCT curves does not have plateau, the van`t Hoff equation can be solved simultaneously. Suppose the respective plateau pressures P_1 and P_2 were obtained from two PCT curves measured at isotherms temperatures T_1 and T_2. It then follows that from Equation 2.1:

$$Ln\ P_1 = \frac{\Delta H}{RT_1} - \frac{\Delta S}{R} \ldots\ldots\ldots\ldots\ldots\ldots\ldots\ldots\ldots\ldots\ldots\ldots\ldots\ldots\ldots\ldots\ldots\ldots (2.1a)$$

$$Ln\ P_2 = \frac{\Delta H}{RT_2} - \frac{\Delta S}{R} \ldots\ldots\ldots\ldots\ldots\ldots\ldots\ldots\ldots\ldots\ldots\ldots\ldots\ldots\ldots\ldots\ldots\ldots (2.1b)$$

Equation 2.1a – Equation 2.1b gives:

$$\Delta H = \frac{Ln\ P_1 - Ln\ P_2}{\frac{1}{RT_1} - \frac{1}{RT_2}} \ldots\ldots\ldots\ldots\ldots\ldots\ldots\ldots\ldots\ldots\ldots\ldots\ldots\ldots\ldots\ldots\ldots\ldots (2.2)$$

Make ΔS the subject of Equation 2.1a to get:

$$\Delta S = \left[\frac{1}{RT_1}\Delta H - Ln\ P_1\right] R \ldots\ldots\ldots\ldots\ldots\ldots\ldots\ldots\ldots\ldots\ldots\ldots\ldots\ldots\ldots\ldots\ldots (2.3)$$

In situations where two plateaus were observed, *i.e.* the van't Hoff graph could not be plotted, Equations 2.2 and 2.3 were used to determine the values of ΔH and ΔS respectively.

Gravimetric storage capacity

The gravimetric storage capacity is the amount of hydrogen stored per unit mass of material. This can be expressed as a weight percentage (wt%) kg H_2 per kg material, or mol/kg [19]. In the case of a metal hydride, it is a clearly defined quantity and is typically calculated from the ratio of the mass of hydrogen stored within the metal or compound to the mass of the host material including the absorbed hydrogen[20]. The capacity in wt%, $C_{\text{wt}}\%$, is given by[141]:

$$C_{\text{wt}}\% = \left(\frac{(H/M)M_H}{M_{host}+(H/M)M_H} \times 100\%\right) \ldots\ldots\ldots\ldots\ldots\ldots\ldots\ldots\ldots\ldots\ldots\ldots\ldots\ldots 2.2$$

where *H/M* is the hydrogen-to-metal or material host atom ratio, M_H is the molar mass of hydrogen, and M_{host} is the molar mass of the host material or metal.

The 2010 target set by US DOE in collaboration with the automotive industry[177] was 6 wt%, which was later reduced to 4.5 wt%. The 2020 target is currently set at 5.5 wt% and a net system storage cost of less than $10 kWh or $333/kg H_{stored}^{-1}. The target for 2020 is 1.8 kWh/kg (0.055 kg H_2/kg system)[45].

Volumetric storage capacity

The volumetric storage capacity defines the amount of hydrogen stored per unit volume of the material[19]. In the case of hydrides, this quantity is the amount of hydrogen stored per unit volume of the bulk metal. The units for this include $kg.m^{-3}$ and $mol.m^{-3}$. It can also be expressed as an energy storage density, the 2020 requirements is a volumetric energy density of at least 1.3 $kWh.L^{-1}$ (0.04 $kg.L^{-1}$).[46]

2.3.2 Long-term cycling stability

The long-term cycling stability of a material is defined as its ability to retain its reversible storage capacity during repeated hydrogen charge and discharge cycles. The 2020 US DOE storage targets specify an ability to undergo 1500 hydrogenation/dehydrogenation cycles[177]**.** Metal hydrides invariably undergo physical and chemical degradation during prolonged hydrogen cycling[47]. This is true even for the compounds that are the most resistant to degradation[67]. If the metal hydride can be made stable and free of impurities, the cycling stability would be greatly enhanced[48, 49].

2.3.3 Gaseous impurity resistance

Gaseous impurities could also cause adverse effects on the hydrogenation properties of an alloy. There are very few documented studies on the effect of gaseous impurities on hydrogen stores.[50] However, it was found that the hydrogen capacity of the super-activated carbon AX-31M was reduced by the presence of nitrogen at a level of 500 ppm.[51] The reduction reached 30% at pressures above ~5.0MPa and a working temperature of 150K. Gaseous impurities that could be found in hydrogen storage alloys, such as $Ti_{0.98}Zr_{0.02}Cr_{0.05}V_{0.43}Fe_{0.09}Mn_{1.5}$, are N_2, CH_4, CO, CO_2, O_2 and H_2O.[48]

2.3.4 Ease of activation

In a microporous adsorbent, the hydrogen absorption/desorption processes are delayed because of environmental adsorbates in the internal pore structure and external surfaces of solid[52]; which can be contaminants and remnants of solvents in alloys produced using wet chemistry[33]. Generally, the contaminants and remnants are removed by exposing the sample to vacuum at elevated temperatures[53]. Samples can also be flushed through with an inert gas to remove pre-adsorbed species[53]. The removal process is monitored by weight change during degassing (gravimetric system) or decrease in the pressure (volumetric system).[23]

2.3.5 Thermodynamic properties

The operating temperature and pressure ranges of hydrogen stores are governed by their thermodynamic properties[52]. Although they are considered in conjunction with the reversible storage capacity and the kinetic hydrogen sorption properties of a material, these values are a fundamental measure of the hydrogen storage properties of a particular host.[20]

2.3.6 Kinetic properties

The kinetic hydrogen sorption properties of a hydrogen store determines the rate at which it can be charged and discharged. A good hydrogen store should take up and release hydrogen in a practical time frame. Goodell *et al*.[6] proposed a practical way of measuring the rate using parameters $T_{1/2}$ (the time in minutes to reach half completion) and $R_{1/2}$ (the reaction rate at this time).

Enthalpy of adsorption

Strength of the interaction between a molecule and the adsorbent surface or pore structure is provided by its enthalpy of adsorption[53]. The enthalpy of adsorption can be defined in a number of ways, such as: the transformed molar surface excess enthalpy, transformed differential surface excess enthalpy, transformed differential enthalpy, transformed integral molar enthalpy, differential surface excess enthalpy and the differential enthalpy of adsorption. The last of these, also called *isosteric enthalpy of adsorption*,[54] is the most acceptable and it is typically determined experimentally from the following expression [135]:

$$\Delta H_{iso} = -\frac{RT_1T_2}{T_2 - T_1} In\left(\frac{P_2}{P_1}\right) \ldots\ldots\ldots\ldots\ldots\ldots\ldots\ldots\ldots\ldots\ldots\ldots\ldots\ldots\ldots\ldots 2.3$$

where T_1 and T_2 are two closely spaced measurement temperatures, P_1 and P_2 are the pressures at which a given quantity of hydrogen is adsorbed, and R is the universal gas constant. 10 K is a typical temperature difference, so that T_2-T_1=10K, and, due to the convenience of using liquid nitrogen and liquid argon, T_1 = 77 K and T_2 = 87 K are often chosen[55].

Enthalpy of hydride formation and decomposition

The enthalpy of hydride formation or decomposition is commonly calculated from Pressure-Composition-Isotherms using a graph of the natural log of the plateau pressure versus inverse temperature, which is commonly known as a van't Hoff plot. [53] Following Equation 2.1, the slope of the line gives the enthalpy term and the intercept gives the entropy.

Surwarno *et al.* [56] prepared ~5g argon arc melted buttons of $Ti_{0.8}V_{0.2}$ and $Ti_{0.9}V_{0.1}$ (at.%) alloys. The alloys were cut into smaller pieces for hydrogenation in their as-cast form. It was observed that the microstructure of the alloys had large grains with diameters exceeding 500μm. The grain size of $Ti_{0.8}V_{0.2}$ which has a βTi structure was found to be smaller than that of $Ti_{0.9}V_{0.1}$ with a mixture of αTi and βTi phases (αTi hcp dominating). It was also found that both alloys absorbed hydrogen within 1 minute, but the quantity absorbed depended on the hydrogenation temperature (3.95% H mass fraction at room temperature and 3.0-3.7% at 450°C).

In another study by Yang *et al.* [63], titanium and nickel powder were mixed in a mass ratio 1:1, then sintered at 850°C for four hours using solid phase sintering under an argon atmosphere. XRD showed that the sintered alloy had the Ti_2Ni phase coexisting with TiN, Ni, $TiNi_3$ phases. The alloy had a maximum discharge capacity of 205mAh/g at a discharge current of 60 mA/g, and this value decreased as the number of cycles increased.

Investigations on the hydrogen storage behaviour of flat sheet of near-α titanium alloy (Ti600), α+β titanium alloy (TC21) and β titanium alloy (Ti40) was carried out by Xiaoli *et al.*[64]. The specimens were polished mechanically to remove the surface oxide and surface finished by cleaning the surface ultrasonically with acetone before the hydrogen absorption/desorption test. The results show that the initial temperatures of hydrogen

absorption/desorption for Ti600 were 573°C and 578.5°C, 580°C and 628.1°C for TC21 alloy and 515°C and 540°C for Ti40 alloy. The hydrogen absorption/desorption behaviour of Ti600 was similar to that of TC21 and the hydrogen absorption/desorption properties of Ti40 was the best.

In the work of Santos and Huot [65], $TiCr_{1.2}(FeV)_x$ (x= 0.4, 0.5, 0.6 at.%) bcc solid solution alloys were considered attractive candidates for hydrogen storage due to their relatively large hydrogen absorbing capacities near room temperature. The microstructures of these alloys were found to consist of dendrites and the co-existence of bcc solid solution and C14 Laves phase in all compositions. The hydrogen storage capacity increased with decreasing content of (FeV). The best results were obtained for the $TiCr_{1.2}(FeV)_{0.4}$ alloy, which achieved 2.79 mass% of hydrogen storage capacity and 1.36 mass% of reversible hydrogen storage capacity.

Young *et. al*[87] studied effect of annealing (between 800 and 1100°C) on hydrogen storage properties of $Ti_{15.6}Zr_{2.1}V_{40.0}Cr_{11.2}Mn_{6.9}Co_{1.4}Ni_{22.5}Al_{0.3}$. They found bcc, TiNi, and C14 phases in the as-cast sample. Annealing at 800 and 900°C increased the main hydrogen storage BCC phase abundance and decreased the C14 and TiNi catalytic phases and Zr and TiO_2 debris. Annealing at 1000°C promoted the formation of Ti_2Ni phase. A б-VNi phase appeared after annealing at 1100°C. Annealing at 900°C for 12-h optimized the storage capacity, high-rate performance, and activation due to a favourable balance in abundance between the hydrogen storage phase (bcc) and the catalytic phases (C14 and TiNi).

Electrochemical loading of hydrogen in single and binary mixtures of the intermetallic compounds, TiNi, TiFe, $Zr_{30}Ni_{70}$ and $Zr_{70}Ni_{30}$ (at.%) have been carried out after mechanical milling [66]. It was observed that hydrogen storage of the 50/50 (by weight) TiNi/ZrNi binary mixtures was enhanced after high energy milling (at 450 rpm for 12 h). Good electrochemical loading (98 mAh/g) was exhibited at 25°C for a binary mixture of the high energy milled $TiFe/Zr_{30}Ni_{70}$ alloys in ratios 50/50 and 30/70. However, this capacity decreased by ~12% on increasing the temperature to 55°C. An increase of ~65% hydrogen capacity was observed for the 70/30 $TiFe/Zr_{30}Ni_{70}$ binary mixtures over the same temperature range (25-55°C).

Two alloys with compositions: $Ti_{33.5}Cr_{34.7}V$ (Alloy A) and $Ti_{9.5}Cr_{14.7}Mn_2V$ (Alloy B) (wt%) were produced and the hydrogen storage properties were compared by Wang *et al.*.[181] Increasing the Ti/Cr ratio in the $Ti_{9.5}Cr_{14.7}Mn_2V$ alloy and excluding Mn improved the hydrogen storage capacity. In addition, Alloy A absorbed 3.6 wt% hydrogen in the first cycle, while Alloy B absorbed 2.4 wt% H_2 at 25°C and only desorbed at 400°C. It was concluded that Alloy B was inferior to A in terms of hydrogen uptake and release.

A study was conducted on hydrogen absorption properties of Ti–0.2Pd alloy immersed in 2.0% and 0.2% acidulated phosphate fluoride (APF) solutions using thermal desorption analysis (TDA)[66] revealed that during the early stage of the immersion in the 2.0% APF solution, the mass of absorbed hydrogen was lower than 500ppm. This value was found to be lower than that of commercially pure titanium. In the 0.2% APF solution, the alloy absorbed 100–200 mass ppm and one-half or two-thirds of that of commercial pure titanium. In neutral 2.0% NaF solution, hydrogen absorption was negligible.

2.3.7 Effect of substituting elements on hydrogen storage properties

There are several studies on the evaluation of hydrogen storage capacity of different alloys, the effect of substituting elements and the influence of heat treatment on hydrogenation characteristics.

Effect of V and Cr on Ti-based alloys

The influence of vanadium V on the H storage of $(TiCr)_{95}V_5$, $(TiCr)_{90}V_{10}$ and $(TiCr)_{65}V_{35}$ (at.%) alloys with Ti/Cr = 5/8 was studied.[67] It was observed that increasing V content increased the hydrogen uptake. Among the alloys studied, $(TiCr)_{65}V_{35}$ had the highest H_2 storage capacity and desorption ratio of 2.86 wt% and 61 wt% respectively.

Shirasaki *et. al.*[80] found that the hysteresis factor of pure V was almost unchanged, but that of heat treated Ti-Cr-*x*V (*x* = 5, 15, 30, 60) decreased with increase in cycle number. The plateau pressure of Ti-Cr-V alloys in absorbing process dropped significantly with increased cycle number, but there was no change in the PCT curve for pure vanadium.

Substituting some Fe atoms in FeTi by metals such as Cr and V eased activation of the alloy and the hydriding pressure was also lowered.[81, 82]

Alloying of vanadium up to 40% in $(Ti_{0.8}Cr)_{1-x}V_x$ with the particular ratio of Ti/Cr = 0.8 resulted in insignificant changes of the hydrogenation properties[132]. For each sample, similar and significant hydrogen uptake (1.4 wt%) was observed due to the capacities of lower hydrides (β1, β2) and the hydrogen solid solution (α) with higher stability.

Ghosh *et al.*[57] found that the V-4Ti-4Cr alloy solidified to a bcc solid solution phase and the V-39Ti-54Cr alloy formed a V-substituted cubic $TiCr_2$ Laves phase. V-50Ti and V-40Ti-20Cr alloys upon solidification formed a bcc solid solution phase that showed a tendency of phase separation into V-rich and V-poor regions. The phases in V-40Ti-20Cr alloy were either rich or poor in V and Ti, while Cr was almost homogeneously distributed between the phases.

$Ti_{0.17}Zr_{0.08}V_{0.34}Pd_{0.01}Cr_{0.1}Ni_{0.3}$ electrode alloy was investigated by XRD, SEM–EDS, ICP, EIS and charge–discharge measurement[73]. It was found that the alloy is composed of a V-based solid solution main phase with bcc structure and C14 Laves phase with hexagonal structure. The alloy electrode has a higher discharge capacity within a wider temperature region from 303 K to 343 K. The charge transfer resistance decreases with increasing temperature

TiCrV and $Ti_{0.8}Cr_{1.2}V$ (at.%) alloys were produced by vacuum arc melting and the cyclic hydrogen absorption-desorption characteristics were evaluated.[93] Cyclic hydrogen capacity values of 2.5 wt% and 2.0 wt% were obtained (even after 15 cycles) for TiCrV and $Ti_{0.8}Cr_{1.2}V$ alloys respectively. This is in agreement with the work of Wang *et al.,*[181] in that decreasing Ti/Cr ratio led to a decrease in hydrogen uptake.

Tominaga *et al.*[74] (cited in Akiba and Okada [4]) reported Ti-(0-35)V-Cr alloys containing more than 15 at.% V were mainly bcc phase and absorption-desorption capacities of ~2.4 mass%, but alloys with less than 10% V contained Laves phase and hydrogen capacities of less than 1.8 mass%.

Okada *et al.*[75] reported the highest hydrogen capacity of 3.0 mass% in Ti-(5-7.5 at.%)V-Cr alloys, similar to Ti-Cr-(1-25 at.%)-Mo alloys reported by Kamegawa *et al.*[77] (cited in Akiba and Okada[4]). This capacity is the highest reported so far for the 313 K isotherm.

Research was carried out on the use of ferrovanadium to substitute for vanadium to reduce the cost of a $Ti_{34}Mn_{18}Cr_{16}V_{32-5x}(V_4Fe)_x$ alloy where x = 0, 2, 3, 4, 5 (at.%). Hydrogen

desorption capacity increased with increasing x from 0 to 3, and decreased with further increase in x from 3 to 5 [76]. The best PCT (pressure-composition-temperature) performance with an effective hydrogen desorption capacity of 1.93 wt% and low cost was found at $x = 3$.

In the study of hydrogen storage characteristics of $TiMn_{2-x}V_x$ (x = 0.8, 1, 1.2) alloys, it was observed that the hydrogen storage capacity increased with increasing x [77]. Increasing the V content promoted the transition from coexisting Laves and V-based bcc phases to single phase V-based bcc.

It was found that partial substitution of Cr by VFe improved the reversible capacity of $TiCr_{1.8-x}(VFe)_x$ (x = 0, 0.2, 0.4, 0.6, 0.8) at.% alloy at low x and then slightly decreased it when VFe exceeded 0.6 [78]. The maximum hydrogen storage capacity was 3.4 wt% at x = 0.8. With increased VFe substitution for Cr, the phase structure changed from Laves to bcc and the crystal cell parameters of the bcc phase increased.

Miyamura *et al.*[217] studied the effect of partial substitution of Fe and Ti by V on hydrogen storage properties of Ti-Fe alloys by producing $TiFeV_3$, Ti_3FeV, TiFeV, $TiFeV_{0.7}$, $Ti_{0.3}Fe_{0.6}V_{0.1}$ and $TiFe_{0.3}V$ (at.%) alloys. It was found that vanadium additions increased the hydrogen storage capacity of the alloy, by lowering the equilibrium pressure of hydrogen. The highest absorption capacity, in terms of hydrogen-to-metal ratio (H/M), at 60°C was 1.0 wt% for $TiFeV_{0.7}$

Work on $V_x(Ti,Cr,Fe)_{100-x}$ alloys (Ti/Cr+Fe = 1.0, Cr/Fe = 2.5, x = 20–55 at.%) [199] showed that with increasing V content, the hydrogen absorption capacity and desorption capacity both increased, and the plateau pressure decreased. BCC and Laves phases appeared when $x < 30$ and a single bcc phase appeared when $x \geq 30$. While investigating the effect of Cr content on hydrogen storage properties of $TiV_{25}Cr_x\ Mn_{35-x}$ (x = 0 – 30 at.%), it was found that the incubation time was very short (10 – 90 s) for alloys with $x = 0$ and $x = 10$, but was 250 – 300 s for x = 20 and 30 [79]. The time to reach maximum capacity increased with increasing chromium content.

Considering the influence of Cr on hydrogen storage properties of Ti-rich ternary alloys $Ti_{0.7}V_{0.3-x}Cr_x$ (x = 0.2 – 0.3) and $Ti_{0.8}V_{0.2-x}Cr_x$ (x = 0.07 – 0.2 at.%), it has been shown that the alloy with the lowest content of chromium, $Ti_{0.8}V_{0.13}Cr_{0.07}$, fast/immediate hydrogenation occurred at room temperature[159]. However, increase in the Cr content led to

slower hydrogen absorption kinetics and an increase in the incubation time, and reduced the apparent activation energy of hydrogen desorption.

It was found that factors affecting the plateau pressure and hydrogen absorption and desorption of $V_{30}Ti_{32}Cr_{31.91}Fe_{6.09}$ alloy were: Ti/(Cr+Fe) ratio, Cr/Fe ratio, Ti/Cr ratio, lattice parameter and electron-to-atom *e*/*a* value[84]. It was also observed that lattice parameters and *e/a* value had a large influence on the hydrogenation properties. The critical value of *e/a* was found to be 5.25. When *e*/*a* < 5.25, the alloys had high absorption capacity, which decreased rapidly when *e*/*a* > 5.25.

The reversible desorption capacity of $V_{40}(TiCr)_{51}Fe_8Mn$ alloy was found to decrease with the cycle numbers from 2.2 wt% at the beginning to 1.86 wt% at the 10th cycle at 26°C. [89] It was also observed that during the first 10 cycles, oxides of the main elements formed rapidly and this led to deceleration of hydrogen uptake. Stability in desorption capacity after the 15th cycle was a result of formation of a dense, passive chromia layer around the alloy particle which hindered reversible desorption capacity.

The work of Cho *et al.* [90] on ternary Ti-V-Cr alloys showed that the hydrogen storage capacities and effective hydrogen uptake was strongly dependent on the Ti:Cr ratio, with the maximum value at Ti:Cr = 0.75. In addition, the lattice parameter increased with increasing Ti:Cr ratio.

The Zr-Fe-V-based alloys were systematically investigated for the possible use in hybrid storage devices[91]. $(Zr_{0.7}Ti_{0.3})_{1.04}Fe_{1.8}V_{0.2}$ shows the best overall properties with a reversible hydrogen capacity of 1.51 wt%, and hydrogen desorption pressure of 11.2 atm at 0 °C. The alloy also showed excellent stability without obvious capacity loss even after 200 hydrogen absorption/desorption cycles.

Wang *et. al.*[67] rapidly solidified $(NiMnAl)_{4.2}Co_{0.3}Fe_{0.5}$ at 900°C and found that the process can decrease the hydrogen equilibrium plateau pressure and the plateau slope. The activation time, discharge rate and discharge capacity was improved, but cycling performance was poor.

Studies into enhancement of hydrogen storage capacity of Ti-V-Cr-Mn bcc phase alloy were carried out by Yu *et al.* [86]. In the work Ti–*x*V–10Cr–(50−*x*)Mn (*x*= 20, 24, 28 and 32), alloys were prepared by magnetic levitation melting. The result of PCT analysis showed that

increasing the V content led to flattening of the hydrogen desorption plateau and depression of the hydrogen desorption plateau pressure. As V content increased, the two phases bcc and C14 Laves changed to a single phase bcc. The maximum and effective hydrogen storage capacities were 3.98 and 2.51 wt%, respectively when x=32.

Effect of Fe on Ti based alloys

In the study on the effect of iron substituting cobalt in $Ti_{12}Zr_{21.5}V_{10}Cr_{7.5}Mn_{8.1}Fe_xCo_{8-x}Ni_{32.2}Sn_{0.3}Al_{0.4}$ (x = 0 – 5) (at.%) it was observed that hydrogen storage characteristics were not really influenced by the addition of Fe [206]. This is in contrast to Murshidi *et al.*[101]. The work of Young[108] and Murshidi[101] implies that Fe may or may not influence hydrogen uptake, depending on the alloy in question.

It has been shown that substitution of V for Fe reduced hydrogen uptake in $Ti_{0.8}Zr_{0.2}V_{2.7-x}Mn_{0.5}Cr_{0.8}Ni_{1.0}Fe_x$ (x = 0 – 0.5) (at.%) [109]. In addition, it was noticed that with increased Fe content, the proportion of the C14 Laves phase gradually decreased, while that of the V-based solid solution phase increased.

The effect of desorption temperature and substitution of Fe for Cr on the hydrogen storage properties of arc-melted Ti-Cr-V alloys was investigated by Jeong-Hyun *et al.* [89]. When the H desorption was measured at seven temperatures, the usable hydrogen increased slightly with increase in temperature. For $Ti_{0.32}Cr_{0.43-x}V0.25Fe_x$ (x = 0, 0.03, 0.05, 0.08, 0.1) alloys, $Ti_{0.32}Cr_{0.35}V_{0.25}Fe_{0.08}$ alloy was the most promising for practical applications such as fuel cells.

A study on the effect of Fe addition on hydrogen storage characteristics of a $Ti_{0.16}Zr_{0.05}Cr_{0.22}V_{0.57}$ (at.%) alloy showed that there was a noticeable decrease in hydrogen uptake in alloys that contained 3-5 at.% Fe and the lattice parameter also decreased linearly [110].

Lee and Perng [92] found that the absorption rate of $TiFe_{1-x}M_x$ (M = Cr, Mn) alloys was strongly dependent on the Cr content and heat treatment. $TiFe_{0.9}Cr_{0.1}$ in the as-melted condition had the highest rate, while $TiFe_{0.95}Cr_{0.05}$ after annealing had the lowest rate. It was also observed that $TiFe_{0.9}Mn_{0.1}$ could absorb hydrogen without activation, although the absorption rates were much lower than those of $TiFe_{0.8}Mn_{0.2}$. The incubation time of $TiFe_{0.9}Mn_{0.1}$ was ~2 h and it took more than 2 days to reach the saturated value.

Homogenization treatment of $TiFe_{0.9}Mn_{0.1}$ did not substantially improve the hydrogenation rate.

Partial substitution of Cr with Fe on hydrogen storage properties of the $TiCr_{1.9}Mn_{0.1}$ alloy showed that hydrogen storage capacity decreased with increasing Fe content. The capacity was 1.78, 1.74 and 1.48 wt% for 0.4, 0.5 and 0.6 at.% Fe respectively. [111]

The study of microstructure and hydrogen storage properties of the titanium-rich $Ti_{0.8}Zr_{0.2}V_{2.7}Mn_{0.5}Cr_{0.8-x}Ni_{1.25}Fe_x$ (x = 0.0- 0.8) revealed that discharge capacity decreased from 350mAh/g at x=0 to 260mAh/g at x=0.8[112]. However, the cyclic stability and the high rate dischargeability increased firstly (from 60% at x = 0 to 69% at x = 0.3) and then decreased (to 65% at x = 0.4 and 30% at x = 0.8). Discharge capacity increased from 42% (x = 0) to 69% (x = 0.4) and then dropped to 21% (x = 0.8) after 200 cycles.

The Zr-Fe-V-based alloys were systematically investigated for the possible use in hybrid storage devices[113]. $(Zr_{0.7}Ti_{0.3})_{1.04}Fe_{1.8}V_{0.2}$ shows the best overall properties with a reversible hydrogen capacity of 1.51 wt%, and a hydrogen desorption pressure of 11.2 atm at 0°C. The alloy also showed excellent stability without obvious capacity loss even after 200 hydrogen absorption/desorption cycles.

Effect of PGMs on Ti based alloys

TiFe was produced by arc-melting and the surface modified with Pd. The effect of chemical surface modification with Pd on H_2 storage was then assessed. The work showed that Pd deposition improved hydrogenation properties at moderate H_2 pressure [188]. It has also been shown that surface modification of a TiFe alloy with Pd nanoparticles promoted hydrogenation of the alloy, even after exposure to air [35].

Typical of hydrides of Platinum Group Metals (PGMs), palladium hydride shows exceptional catalytic properties and kinetic reversibility of hydrogen, but gravimetric and volumetric H densities are low due to their high atomic mass and low n in MH_n (all known PGM hydrides have $n \leq 1$) .[45, 100, 115]

Work on the effect of palladium on hydrogenation behaviour of arc-melted $TiFe_{1-x}Pd_x$ ($0.05 \leq x \leq 0.30$) at.% alloys showed that the lattice constant increased with the increased in

palladium content[116]. The plateau pressure and activation temperature were lowered as *x* increased, although the hydrogenation capacity was not significantly affected. [193]

Zhang *et. al.*[7] ball milled $Mg_{67}Co_{33}$ and $Mg_{67}Co_{33}$–Pd for 120h and analysed the properties. High resolution transmission electron microscopy (HRTEM) and selected area electron diffraction (SAED) analyses showed that the alloys all had BCC structures. Introduction of 5.0 at.% Pd significantly increased the initial discharge capacity of $Mg_{67}Co_{33}$ (from 10 mAh g^{-1} to a maximum of 530 mAh g^{-1}). The hydrogen diffusion coefficient of the $Mg_{67}Co_{33}$ was enhanced with Pd.

In hydrogen absorption-desorption studies of $Ti_{33}V_{33}Cr_{34}$ (with 0, 0.05 and 0.5wt% Pd), increasing the Pd content improved the activation properties and steady absorption capacity, and resulted in a smaller desorption plateau [72].

Effect of Zr, Co, Ni, Al, Sn, B, Mn, Hf and Ce on Ti-based alloys

The maximum hydrogen storage capacity of TiMn hydrogen storage alloys when Zr was substituted at the Ti site and V, Fe, Cr and Al at the Mn site, was found to be 1.71 wt% at 25°C [121]. However, at higher temperature, the hydrogen sorption capacity decreased and the plateau increased. The ΔH and ΔS of hydrogen absorption were -21.7kJ/mol and 99.8J/mol.K. Desorption values were 25.4kJ/mol and 108.5J/mol./K; indicating a significant hysteresis effect. All the alloys were found to contain the hexagonal C14 Laves phase.

Pickering[102] produced ten alloys from the Ti-V-Mn, Ti-V-TM-Mn and Ti-V-Nb-Mn systems. The highest reversible hydrogen capacity of 1.56 wt% was found in $Ti_{0.50}V_{0.51}Mn_1$, with enthalpy and entropy values of -26.63 kJ/mol.H_2 and 111.77 J/mol.H_2. The $Ti_{0.55}V_{0.42}Cr_{0.11}Mn_1$ had the lowest reversible capacity of 1.06 wt%, with a ΔH of -27.73 kJ/mol.H_2 and a ΔS of 103.93 J/mol.H_2

Addition of Al and V to Ti improved the mechanical properties and hydrogen uptake [103]. Ti and a Ti–6Al–4V alloy were hydrogenated at different temperatures between 150°C and 750°C using elastic recoil detection analysis (ERDA) with 3 MeV particles and Rutherford backscattering spectrometry (RBS) with 6.585 MeV particles. It was observed that hydrogen absorption began at 550°C in Ti and at a slightly higher temperature in Ti–6Al–4V. Titanium showed cracks after the hydrogenation process, but the Ti–6Al–4V samples were more mechanically stable. A natural hydrogen desorption was observed in both materials

with time; the desorption from 100 - 20% took place within 40 days in Ti–6Al–4V hydrogenated at 750°C and for the Ti alloy hydrogenated at 600°C, dehydrogenation to 75% concentration occurred within 140 days and then remained stable.

Hydrogen absorption/desorption properties of Ti-M-V-B (M=Cr, Mn) were examined by Uno *et al.* [104] at hydrogen pressures of 0.01-7MPa and a temperature of 30°C. The $Ti_{37}Mn_{25}V_{38}B_x$ alloys were prepared by arc-melting, while $Ti_{31}Cr_{30}V_{39}B_x$ (x = 0, 6 at.%.) alloys were prepared by the suction casting method. XRD showed that $Ti_{37}Mn_{25}V_{38}$ had a bcc single phase and $Ti_{37}Mn_{25}V_{38}B_x$ (x = 2 - 10) comprised two or three phases indexed as a BCC phase and C14 Laves phase. The P-C isotherms revealed that the $Ti_{37}Mn_{25}V_{38}$ has the largest hydrogen capacity of 2.98 wt% at 6.3MPa, and the capacity decreased gradually with increased x. A similar trend was observed in $Ti_{31}Cr_{30}V_{39}B_x$ alloys, which suggests that boron reduces hydrogen uptake.

In the study of the effect of Sn substitution at the Ti site on the hydrogen storage properties of $FeTi_{1-x}Sn_x$ (x = 0.02 and 0.05), there were increases in plateau pressures, enthalpy (ΔH) and entropy (ΔS) values, but a decrease in hydrogen saturation contents [82]. Both FeTi and $FeTi_{0.98}Sn_{0.02}$ needed ~12 cycles of activation to attain the saturation hydride compositions of $FeTiH_2$ and $FeTi_{0.98}SnH_{1.6}$ respectively, while $FeTi_{0.95}Sn_{0.05}$ needed 1 to 2 cycles of activation to attain the saturation composition of $FeTi_{0.95}Sn_{0.05}H_{1.4}$.

Abrashev *et al.* [106] studied the microstructure and electrochemical properties of $TiFe_{1-x}Co_x$ (x = 0.1, 0.3) and $TiFe_{0.7}Ni_{0.2}Co_{0.1}$ (at.%) alloys produced by milling in a high-energy planetary mill for 15, 20 and 30 hours. The electrochemical cycle life of the electrodes showed that Co-containing alloys had lower discharge capacity and better corrosion stability compared with the TiFe alloy. Contrarily, the Ni-containing alloy did not show a significant difference in the discharge capacity and cycle performance for samples after varying milling times.

Chen *et al.* [107] synthesised $Ti_{1+x}Cr_{1.2}Mn_{0.2}Fe_{0.6}$ (x = 0, 0.02, 0.05, 0.1) alloys by induction levitation melting and investigated the hydrogen storage behaviour. The results showed that the unit cell volume expanded with increasing Ti content and $Ti_{1.02}Cr_{1.2}Mn_{0.2}Fe_{0.6}$ had the highest storage capacity of 1.61 wt%.

Copper was studied[108] as a modifier for $Ti_{12}Zr_{21.5}V_{10}Cr_{7.5}Mn_{8.1}Co_{8.0-x}Ni_{32.2}Cu_xSn_{0.3}Al_{0.4}$ (x = 0 to 5 at.%) alloys. As the Cu content increased, the maximum and reversible hydrogen

storage decreased, but the high rate dischargeability fluctuated. A maximum hydrogen uptake of 1.4 wt% was observed at $x = 0$, *i.e.* with no copper added.

The effect of aluminium on hydrogen storage of $(V_{30}Ti_{35}Cr_{25}Fe_{10})_{100-x}Al_x$ (x= 0.6 to 6 at.%) alloys was studied by Yigang *et al.* [109]. No significant reduction was found when the Al content was 0.6, 0.7, 0.8 and 0.9 at.%, but when the Al content was increased further, absorption and desorption of hydrogen decreased noticeably. The maximum hydrogen uptake was found to be 3.6 wt% at $x = 0$, *i.e.* $V_{30}Ti_{35}Cr_{25}Fe_{10}$ without Al.

The presence of Si and Al in $V_{55}Ti_{20.5}Cr_{18.1}Fe_{6.4}$ has been shown to have a positive effect on the cyclic capacity [110], promoting transformation from fcc to bcc and enhancing the pulverisation resistance. The maximum hydrogen uptake of $V_{54.8}Ti_{20.4}Cr_{18}Fe_{6.4}Si_{0.1}Al_{0.3}$ was 2.23 wt%.

$Ti_{10}V_{84-x}Fe_6Zr_x$ (x = 1 - 8) alloys were produced by induction levitation melting and its hydrogen uptake characteristics were investigated[111]. Zr substitution for V had the best hydrogen absorption/desorption capacity at $x = 1$. However, for $x = 2$ to 8, the activation behaviour improved, but the hydrogen absorption/desorption capacity decreased.

While investigating the hydrogen storage characteristics of $TiCr_{1.8}$ + x wt% $LaNi_5$ (x = 5, 10, 15 and 20), the hydrogen storage capacity decreased with increasing $LaNi_5$ content. [112] Storage capacities at $x = 5$ and $x = 10$ were almost the same, similarly the capacity at $x = 15$ and $x = 20$ were similar. However, electrochemical characteristics were greatly improved as x increased, with a maximum discharge capacity after 5 charge/discharge cycles of 55 mAh/g at $x = 20$.

A comparative study of the hydrogenation characteristics of two alloys shows that $Ti_{0.85}VFe_{0.15}$ (at.%) could absorb a maximum of 3.7 wt% hydrogen and $Ti_{0.85}V_{0.95}Fe_{0.15}Zr_{0.05}$ was able to absorb 3.5 wt%, showing that substituting Zr for V slightly reduced the hydrogen uptake. [113]

Excessive substitution of Co for Ni decreased the cycling stability of a $Ti_{0.8}Zr_{0.2}V_{2.7}Mn_{0.5}Cr_{0.8}Ni_{1.25-x}Co_xFe_{0.2}$ (x = 0.00, 0.05, 0.10, 0.15, 0.20 and 0.25) alloy[114]. As x increased, the discharge capacity decreased from 340.5 to 305.6 mAh/g and the high rate dischargeability (HRD) gradually decreased from 66.8% to 55.0%.

Addition of Ce was found to be an effective way to inhibit formation of the C14 Laves phase, improve the flatness of the plateau (*i.e.* the pressure at which H uptake begins), increased the hydrogen capacity and the H diffusion rate of $Ti_{27.25}Cr_{28.05}V_{37.25}Fe_{7.45}Ce_{1.0}$. [116] This work and that of Miao *et al.*[113] indicate that C14 Laves is detrimental to hydrogen storage in bcc alloys.

V–Ti based hydrogen storage electrode alloys with Zr, Mn, Cr Ni, Co and Fe alloying additions were produced by induction levitation melting[59]. Studies on the mechanisms for improving the cyclic stability of $Ti_{0.8}Zr_{0.2}V_{2.7}Mn_{0.5}Cr_{0.6}Ni_{1.25}Fe_{0.2}$, $Ti_{0.8}Zr_{0.2}V_{2.7}Mn_{0.5}Cr_{0.4}Ni_{1.25}Fe_{0.4}$, $Ti_{0.8}Zr_{0.2}V_{2.7}Mn_{0.5}Cr_{0.6}Ni_{1.15}Co_{0.1}Fe_{0.2}$ and $Ti_{0.8}Zr_{0.2}V_{2.7}Mn_{0.5}Cr_{0.6}Ni_{1.25}Fe_{0.8}$ (at.%) alloys showed that Cr and Co enhanced the cyclic stability, resistance to corrosion and pulverisation of these V-Ti based hydrogen storage electrode alloys [59].

It was established that Mn retarded hydrogen uptake in $TiFe_{0.9}V_x$ and $TiFe_{0.8}Mn_{0.1}V_x$ (x = 0, 0.05 and 0.1 at.%) as the hydrogen absorption increased with increased vanadium content, although the increase was more significant without the presence of Mn [47].

Addition of V to FeTi intermetallic significantly increased the hydrogen absorption kinetics at the cost of a marginal increase reduction of hydrogen storage capacity[151]. The maximum storage capacity was found to be ~1.2 and 1.1 mass% for the FeTi intermetallic and FeTi-3.1 mass% V respectively.

An Investigation conducted on effect of partial substitution of Cr with Mn on hydrogen storage properties of $TiCr_{1.4-y}Mn_yFe_{0.6}$ (y= 0.1, 0.2, 0.3) alloys showed that Mn reduced hydrogen storage capacity[90]. Increasing Mn content from 0.1 to 0.3 at.% reduced hydrogen storage capacity from 1.48 to 1.26 wt%

Work by Chao *et al.* [156] on $Ti_{0.33-x}Zr_xCr_{0.47}V_{0.20}$, $Ti_{0.27-x}Zr_xCr_{0.36}V_{0.37}$ and $Ti_{0.20-x}$ $Zr_xCr_{0.25}V_{0.55}$ (at.%) alloys produced by arc-melting showed that substituting zirconium for titanium decreased hydrogen storage capacity and increased the slope of the isotherm.

When Hf was substituted for Zr in $Ti_{40}Hf_{40}Ni_{20}$ and $Ti_{45}Zr_{38}Ni_{17}$ (wt%) alloys, it was found that Zr was a better substitute for Hf [162] as the hydrogen uptake for $Ti_{40}Hf_{40}Ni_{20}$ and $Ti_{45}Zr_{38}Ni_{17}$ was 1.4 and 1.5 wt% respectively.

In a study of hydrogen absorption characteristics of $Ti_{0.42}Zr_{0.08}Fe_{0.50}$ and its comparison with TiFe and $Ti_{0.45}Fe_{0.45}B_{0.1}$ (at.%) [134], it was observed that the maximum solubility of hydrogen (H/M ratio) was 0.065 - 0.07 for $Ti_{0.42}Zr_{0.08}Fe_{0.50}$, 0.04 - 0.05 for TiFe and 0.08 - 0.09 for $Ti_{0.45}Fe_{0.45}B_{0.1}$, which suggested that B promoted hydrogen uptake.

Zhao *et al.* [63] studied part substitution of Ti by Zr in $Ti_{2-x}Zr_xNi$ (x = 0, 0.2, 0.4) (at.%). Results showed that Zr retarded the discharge capacity, which is in agreement with Basak *et al.* [112] and Murshidi *et al.* [101].

Hydrogen absorption/desorption properties of (40-x)Ti-40V-10Cr-10Mn-xSc (x=0, 5, 10, 15) were investigated[212]. It was observed that hydrogen absorption capacity of a Sc-free sample was larger than the Sc-containing samples. The absorption/desorption capacity increased with increasing Sc content and the maximum absorption capacity of 3.577 wt% was obtained at 15 at.% Sc.

Investigation on the structure and hydrogen storage properties of $TiMn_{2-5x}(V_4Fe)_x$ (x = 0.30, 0.35) (at.%) showed that $TiMn_{0.50}(V_4Fe)_{0.30}$ had better hydrogenation properties than a $TiMn_{0.25}(V_4Fe)_{0.35}$ alloy, implying that higher Mn : V_4Fe favoured hydrogen uptake [152].

Lee and Perng [123] investigated the effect of boron and carbon on hydrogenation properties of TiFe, $TiFeC_{0.001}$, $TiFeB_{0.001}$, $Ti_{1.1}Fe$, $Ti_{1.1}FeC_{0.001}$ and $Ti_{1.1}FeB_{0.001}$ (at%). Results of the investigation showed that B and C slowed down activation rates of hydrogen uptake.

Martínez and Santos[169] found that the hydrogen storage capacity attained a value of 3.6 wt. (%) for $TiCr_{1.1}V_{0.9}$ alloy in a time of 9 minutes, 3.3 wt. (%) for a $TiCr_{1.1}V_{0.45}Nb_{0.45}$ alloy in a time of 7 minutes, and 3.6 wt. (%) for $TiCr_{1.1}V_{0.9}$ + 4%Zr_7Ni_{10} with an increase of the hydrogen absorption kinetics attained in 2 minutes. This indicates that the addition of Nb and 4%Zr_7Ni_{10} to the TiCrV alloy acts as catalysts to accelerate the hydrogen absorption kinetics.

Arc-melting of $Ti_{25}V_{35}Cr_{40}M_x$ (M = B or C and x = 0, 0.1, 1, or 5**)** alloys were carried out by Shen *et al.* [208]to investigate the effect of interstitial boron and carbon on hydrogenation properties. The effective hydrogen desorption capacities were increased from 0.80 H/M for the sample without doping to 0.86 H/M for $Ti_{25}V_{35}Cr_{40}B_1$ and 0.87 H/M for $Ti_{25}V_{35}Cr_{40}C_{0.1}$.

Towata *et al.* [127] investigated the effect of partial niobium and iron substitution on short-term cycle durability of Ti-Cr-V hydrogen storage. The investigation revealed that partial

substitution of iron improved the durability and reduced the hydrogen storage capacity of $Ti_{16}Cr_{34}V_{50.}$ Contrarily, partial substitution of niobium improved durability, but did not affect the hydrogen storage; a similar result was obtained for $Ti_{25}Cr_{50}V_{25.}$ After 10 cycles of hydrogen absorption and desorption, the effective hydrogen absorption and desorption decreased to 84.9% of its initial values for $Ti_{25}Cr_{50}V_{25}$ and 94.2% for $Ti_{16}Cr_{34}V_{50}$.

The reviewed literature is summarised in Table 2.3

2.4.1. Effect of production methods on hydrogen storage alloys

Alloys can be produced from metallic oxide by first reducing the oxide to the metallic states and the metals are then mixed, melted and pulverized[127]. In order to shorten this long expensive route, Ryosuke and Yoshinori [128] examined a shorter method of forming a Ti-V-Cr alloy by first reducing the most stable oxides powder, V_2O_5 and TiO_2, (both <1μm in particle size) using liquid Ca and CaCl (independently) in a sealed stainless vessel and the reduced oxides were mechanically mixed in a mortar. They later used a similar reduction method to produce binary alloy Ti-V from a high melting V_2O_3 in place of V_2O_5. From this work it was observed that by using calcium as reductant, high purity titanium with only 500 ppm oxygen could be obtained even from titanium oxide containing 40% oxygen.

Ryosuke and Yoshinori[128] also studied binary Ti-V alloys and the intermetallic $TiCr_2$ compound, aiming at a ternary Ti-V-Cr alloy in the future. The well-homogenized Ti-V solid solution and $\alpha TiCr_2$ were obtained from a mechanical mixture of V_2O_3 and TiO_2 and of Cr_2O_3 and TiO_2, respectively. The by-product CaO was removed *in-situ* by dissolving it into molten $CaCl_2$ to complete the reaction. The morphology of the powders was commonly coral-like, slightly sintered fine particles. Their large surface areas seemed suitable for hydrogen absorption. These alloy powders showed a hydrogen storage capacity of 1.8 wt% after the normal activation treatment.

Table 2.1 Effect of alloying additions on hydrogenation properties.

Element	Alloy(s) produced	*x* (at.%)	Phases	Effects
V	$(TiCr)_{95}V_5$, $(TiCr)_{90}V_{10}$ $(TiCr)_{65}V_{35}$	5, 10, 35	fcc, bcc, hcp Cr_2Ti	Increasing V: increased H uptake.
V	$TiMn_{2-x}V_x$	0.8, 1, 1.2	BCC and Laves	Storage capacity increased with x
V	$TiFeV_3$, Ti_3FeV, $TiFeV_{0.7}$, TiFeV, $Ti_{0.3}Fe_{0.6}V_{0.1}$, $TiFe_{0.3}V$	0.1, 0.7, 1, 3	C14 laves	V increased storage capacity
V	$V_x(Ti, Cr, Fe)_{100-x}$	Ti/Cr+Fe=1 Cr/Fe = 2.5 x = 20–55	x <30: bcc + Laves. x≥30 BCC	Absorption and desorption capacity increased with V increase
V	Ti–xV–10Cr–(50−x)Mn	20, 24, 28 and 32	BCC and C14 Laves	H uptake increased and plateau pressure reduced with V increase.
Ti:Cr	TiCrV and $Ti_{0.8}Cr_{1.2}V$	50:50, 40:60	BCC (V) and FCC	Decreasing Ti:Cr ratio decreased hydrogen uptake.
V_4Fe	$Ti_{34}Mn_{18}Cr_{16}V_{32-5x}(V_4Fe)_x$	0, 2, 3, 4, 5	BCC and Laves	Desorption capacity increase with x≤3, decreased for x>3.
VFe	$TiCr_{1.8-x}(VFe)_x$	0, 0.2, 0.4, 0.6, 0.8	BCC and Laves	x<0.6 Improved reversible capacity storage capacity increased with x
Pd	TiFe	Pd deposition on surface	BCC TiFe	Pd deposition on surface improved hydrogenation properties.
Pd	$TiFe_{1-x}Pd$	0.05≤x≤0.3	BCC (V)	Plateau pressure + activation T reduced with increase in x
Pd	$Ti_{33}V_{33}Cr_{34}$	0, 0.05 and 0.5	BCC (V)	Pd favoured Hydrogenation.
Zr, V, Fe, Cr, Al	$Ti_{0.97}Zr_{0.019}V_{0.439}Fe_{0.097}Cr_{0.045}Al_{0.026}Mn_{1.5}$	0.019, 0.439, 0.045, 0.026, 0.097	hcp C14 Laves	Max. storage capacity at is 1.71 wt% but 1.86 wt% for the pure $TiMn_{1.5}$ system.
Cr, Mn	$Ti_{37}Mn_{25}V_{38}B_x$ and $Ti_{31}Cr_{30}V_{39}B_x$	0 and 6	BCC at x=0; x=6: BCC+Laves	Boron reduced H uptake.
Cr	$Ti_{0.7}V_{0.3-x}Cr_x$ (A) and $Ti_{0.8}V_{0.2-x}Cr_x$ (B)	0.2 - 0.3 (A) 0.07 - 0.2 (B)	FCC and BCC.	For B with 0.07 Cr - immediate hydrogenation. Increase in Cr: slow H absorption kinetics and increased incubation time
Cr	$TiV_{25}Cr_x$ Mn_{35-x}	0-30	C14 and C15 Laves	Cr slows down absorption rate
Fe	$Ti_{12}Zr_{21.5}V_{10}Cr_{7.5}Mn_{8.1}Fe_xCo_{8-x}Ni_{32.2}Sn_{0.3}Al_{0.4}$	0-5	hcp C14 Laves + BCC	Fe has no effect on H storage characteristics
Fe	$Ti_{0.8}Zr_{0.2}V_{2.7-x}Mn_{0.5}Cr_{0.8}Ni_{1.0}Fe_x$	0 - 0.5	C14 Laves and BCC	Fe reduced H uptake.
Fe	$Ti_{0.32}Cr_{0.43-x}V_{0.25}Fe_x$	0, 0.03, 0.05, 0.08, 0.1	BCC and Laves	Useable H slightly increased to maximum at 0.08.
Fe	$Ti_{0.16}Zr_{0.05}Cr_{0.22}V_{0.57-x}Fe_x$	0-0.5	BCC and C14 Laves	H uptake decreased with increase in Fe
Fe	$Ti_{0.8}Zr_{0.2}V_{2.7}Mn_{0.5}Cr_{0.8-x}Ni_{1.25}Fe_x$	0.0–0.8	C14 laves	Discharge capacity increased for x ≤0.4) and then dropped for x>0.4.
Ni, Fe	$Ti_{16}Cr_{34}V_{50}$	0.11	BCC (V)	Fe retarded H uptake; Ni - no effect

Table 2.1 (cont.)

Element	Alloy(s) produced	*x* (at.%)	Phases	Effects
M = Cr, Mn	$TiFe_{1-x}M_x$	0.05, 0.1		Mn slows down activation rate; Cr improves absorption rate
Al, V	Ti–6Al–4V		αTi phase	Mechanic and H uptake properties improved.
Sn	$FeTi_{1-x}Sn_x$	0.02 and 0.05	BCC TiFe phase	Sn increased plateau pressures, ΔH and ΔS, decreased hydrogen saturation contents
Co	$TiFe_{1-x}Co_x$, $TiFe_{0.7}Ni_{0.2}Co_{0.1}$	0.1, 0.3	BCC TiFe phase	Co lowers discharge capacity, Ni has no real effect on H uptake.
Cu	$Ti_{12}Zr_{21.5}V_{10}Cr_{7.5}Mn_{8.1}Co_{8.0-x}Ni_{32.2}Cu_x\ Sn_{0.3}Al_{0.4}$	0 to 5	hcp C14 + BCC	Cu decreased H uptake.
Al	$(V_{30}Ti_{35}Cr_{25}Fe_{10})_{100-x}Al_x$	0.6 to 6	FCC and BCC	Al decreased H uptake.
Si, Al	$V_{55}Ti_{20.5}Cr_{18.1}Fe_{6.4}$, $V_{54.8}Ti_{20.4}Cr_{18}Fe_{6.4}Si_{0.1}Al_{0.3}$	0.1, 0.3	FCC and BCC	Si and Al improved cyclic capacity.
Ce	$Ti_{27.25}Cr_{28.05}V_{37.25}Fe_{7.45}Ce_{1.0}$	1	CeO_2, BCC (V) and C14 Laves	Ce improved plateau flatness, enlarged hydrogen capacity and increase the H diffusion rate.
Cr, Co	$Ti_{0.8}Zr_{0.2}V_{2.7}Mn_{0.5}Cr_{0.6}Ni_{1.25}Fe_{0.2}$/ $Fe_{0.4}$ /$Ni_{1.15}Co_{0.1}Fe_{0.2}$ /$Fe_{0.8}$	0.4, 0.6Cr; 0.1Co	BCC(V) and C14 Laves	Cr and Co enhanced cyclic stability
Co	$Ti_{0.8}Zr_{0.2}V_{2.7}Mn_{0.5}Cr_{0.8}Ni_{1.25-x}Co_xFe_{0.2}$	0.00 - 0.25	C 14 Laves and BCC (V)	Increase in Co: Cycling stability + discharge capacity reduced.
Mn	$TiFe_{0.9}V_x$ and $TiFe_{0.8}Mn_{0.1}V_x$	0, 0.05, 0.1	cubic TiFe; Ti and Ti_2Fe	Mn retards H uptake.
Zr	$Ti_{0.33-x}Zr_xCr_{0.47}V_{0.20}$, $Ti_{0.27-x}Zr_x\ Cr_{0.36}V_{0.37}$ and $Ti_{0.20-x}\ Zr_xCr_{0.25}V_{0.55}$		BCC(V) C14 Laves	addition of Zr: H storage capacity decrease, plateau pressure increase
Zr	$Ti_{10}V_{84-x}Fe_6Zr_x$	1 – 8	x=1:BCC (V) x=2-8: BCC (V) and Laves	Zr improved activation behavior but reduce H absorption capacity
Zr	$Ti_{0.85}VFe_{0.15}$ $Ti_{0.85}V_{0.95}Fe_{0.15}Zr_{0.05}$	0.05	C 14 Laves and BCC (V)	Zr slightly reduced H uptake
Zr	$Ti_{40}Hf_{40}Ni_{20}$ $Ti_{45}Zr_{38}Ni_{17}$			Hydrogen uptake for $Ti_{40}Hf_{40}Ni_{20}$ and $Ti_{45}Zr_{38}Ni_{17}$ was 1.4 and 1.5 wt% respectively.
B, Zr	$Ti_{0.42}Zr_{0.08}Fe_{0.50}$, TiFe, and $Ti_{0.45}Fe_{0.45}B_{0.1}$	0.1, 0.08		Zr retarded and B promoted H uptake
Zr	$Ti_{2-x}Zr_xNi$	0, 0.2, 0.4		Zr retarded H uptake.
$LaNi_5$	$TiCr_{1.8}$ + x wt%$LaNi_5$	5, 10, 15, 20	C14 Laves	increase in $LaNi_5$: Storage capacity reduced, discharge capacity improved
Mn:VFe	$TiMn_{2-5x}(V_4Fe)_x$	0.30, 0.35	BCC (V) and Laves	higher Mn : V_4Fe favoured hydrogen uptake.
B, C	TiFe, $TiFeC_{0.001}$, $Ti_{1.1}Fe$, $TiFeB_{0.001}$, $Ti_{1.1}FeC_{0.001}$ and $Ti_{1.1}FeB_{0.001}$	0.001	TiFe and $TiFe_2$	B and C slow down activation rate.
B, C	$Ti_{25}V_{35}Cr_{40}M_x$	0, 0.1, 1, or 5	BCC. Small ppt. removed after anneal	B, C slightly improved desorption capacity.

The effect of preparation method on hydrogen storage of a Ni/MH battery alloy by centrifugal casting and gas atomization was investigated by Young *et al.* [129]. It was discovered that alloys produced by centrifugal casting had a better cycle life, improved low temperature performance, but were slower in activation. The production cost was found to be lower in case of gas atomisation; it also had the advantage of high cycle life and charge retention, but suffers from higher bulk oxygen content and thicker surface oxide, thus, inferior battery performance characteristics.

In the work of Abe and Kuji [130] on the hydrogen absorption properties of a TiFe alloy synthesized by ball milling and post-annealing, the two samples prepared by ball milling for 10 and 40 h were able to absorb hydrogen readily after heat treatment at 573K for 3 h. However, the TiFe milled for 40 h could not desorb hydrogen completely. This indicated that the hydride of TiFe synthesized for a longer milling time is stable, corresponding to a lower plateau pressure. However post-annealing between 500°C and 600°C was found effective for achieving a wide plateau area without reducing the hydrogen capacity. The maximum plateau pressure was ~1.0MPa for TiFe.

Hu *et al.* [131] prepared a metastable $TiCr_2$ alloy by both mechanical grinding (MG) and mechanical alloying (MA). Result of PCT tests revealed that the maximum hydrogen absorption and desorption capacities for the MA sample were ~1.0 and ~0.4 wt% at 50°C (2.5 MPa hydrogen pressure) and those for the MG sample were ~0.7 and ~0.5 wt%. Therefore, MA was superior to MG in processing $TiCr_2$ alloy for hydrogen storage.

Wang [180] prepared a $Ti_{0.37}V_{0.38}Mn_{0.25}$ alloy by MA and vacuum arc-melting (VAM) to study the differences in hydrogen storage capacities. The alloy samples produced by MA showed an amorphous structure and maximum hydrogen absorption of 1.76 wt%, while those prepared by VAM exhibited a single phase BCC structure with no Laves phase, and maximum hydrogen absorption of 3.62 wt%. It was also observed that after 100 absorption/desorption cycles, the MA powders, which did not pulverize as much as those of the VAM powders, showed a smaller decline in hydrogen-absorption capability.

The influence of melting methods and heat treatment on microstructure and hydrogen absorption properties of Ti-V-Cr and Ti V-Cr-Fe alloys were examined. The $Ti_{30}Cr_{50}V_{20}$

alloy (A) was prepared by arc-melting, and the $Ti_{27.8}Cr_{42.2}V_{25}Fe_5$ (B) alloy was produced by vacuum induction melting (VIM). After heat treatment at 1200-1400°C for 1 min to 6 hours, alloy A was water quenched and B was gas quenched in the furnace. The lattice constant and microstructure on surface and side of crucible was found to be different for alloy A[69]. The absorption capacities and thermodynamic properties did not vary much between alloys A and B. High temperature heat treatment improved homogeneity: the fast cooling rate refined the grain size and increased the lattice constant.

Neutron diffraction measurement on $Ti_{(1-y)}V_yH_x$ ($0 \leq y \leq 0.5$; $1.6 \leq x \leq 1.92$) showed that the transition from the cubic gamma-phase to the tetragonal delta-phase observed in the system was strongly influenced by a partial substitution of titanium by vanadium [122]. The tetragonal phase did not occur for $y = 0.35$ and 0.50.

Microstructures of Ti-rich alloys are either α, near α, β or α+β titanium[30]. Ibaraki *et al.* [136] discovered that when a Ti-6Al-4V titanium alloy was heat treated in vacuum or a neutral atmosphere (from room temperature to a 3 cycle treatment of 930°C-500°C, then furnace cooled), the hydrogen storage capacity, toughness, formability, and creep resistance improved, and the microstructure changed from abnormal to normal α-Ti or α+β Ti. The microstructure is termed abnormal α, near α, β or α+β structure if it looks like, but is not the same as α, near α, β or α+β respectively.

In the investigation on hydrogenation properties of Pd-Ti and Pd-Ti-H (0 - 30 at.% Ti) alloys, it was discovered that the hardness of the alloys hydrogenated at high pressure were higher than the non-hydrogenated alloy, and that the α-phase Pd-Ti-H alloys had higher hardnesses than the β-phase or α+β-phase alloys [39]. This was attributed to a pre-precipitation effect of H gas, which was consistent with the observed X-ray line broadening for these alloys.

Annealing (i.e. homogenisation treatment) of arc-melted $TiFe_{0.9}Mn_{0.1}$, $TiFe_{0.8}Mn_{0.2}$, $TiFe_{0.95}Cr_{0.05}$ and $TiFe_{0.9}Cr_{0.1}$ (at.%) alloys at 900°C in vacuum for 80 h eliminated segregation [92]. It was reported that the hydrogenation incubation time of these alloys was ~2 h. It took more than 2 days to reach the saturated value, implying that annealing slowed down, rather than improved, the hydrogenation rate. However, for the subsequent hydrogenation cycles, the rates of hydrogen absorption were very rapid and the saturated contents were reached in 10 minutes for all as-cast and annealed samples.

A $V_3TiNi_{0.56}$ alloy was produced by arc-melting then heat treated in temperature range 700-1200°C for 24 hours, followed by furnace cooling to room temperature[171]. It was observed that heat treatment at 700°C had the same plateau pressure as for the as-cast alloy. Heat treatments between 800°C and 1000°C brought about a flatter plateau pressure. For temperatures above 900°C, it was observed that the grain size of the major phase (V-based BCC solid solution) increased and the network structure of the TiNi secondary phase, which favours hydrogen uptake, was degraded, thereby causing a decrease in the high rate capability and the cycle life. The optimum heat treatment temperature for the alloy was 800 - 890°C.

A Ti-Zr-Ni-V-Cr-Mn-Fe alloy was prepared by Chuang *et al.* [140] and the influence of heat treatment at: 450°C, 650°C, 850°C or 1050°C for 4 hours on the hydrogenation properties of the alloy investigated. It was shown that heat treatments at all the temperatures investigated increased the degree of crystallisation of the atomised powder. The discharge capacity was also enhanced, but the hydrogenation properties were best with a heat treatment at 850°C.

In order to investigate the influence of Ce and heat treatment on plateau property of $Ti_{32}Cr_{46}V_{22,}$ Liu *et al.*[141] produced $Ti_{32}Cr_{46}V_{22}$ and $Ti_{32}Cr_{46}V_{22}Ce_{0.4}$ (at.%) by magnetic levitation melting and heated them to 1400°C for 5 minutes, then quenched into iced water. Their work revealed that Ce addition and heat treatment effectively improved the flatness of plateau and enlarged the hydrogenation capacity of the $Ti_{32}Cr_{46}V_{22}$ alloy, due to both lowering the oxygen concentration and homogenisation of composition and microstructure.

At low hydrogen pressure and temperature, palladium-nickel (Pd-Ni) co-deposition by electroless plating significantly improved the kinetics of hydrogen charging of $La_{0.40}Ce_{0.48}(Nd,Pr)_{0.16}Ni_{3.34}Co_{0.64}Al_{0.63}Mn_{0.58}$ at.% AB_5-type alloys [142].

A $Ti_{0.32}Cr_{0.43}V_{0.25}$ (at.%) alloy was ball milled using tungsten carbide and stainless steel balls and heat treated at 1200°C for 2 hours, 1200°C for 8 hours, 1000°C for 2 hours and then 800°C for 2 hours. Heat treatment improved the hydrogen storage properties, such as hysteresis in the hydrogen absorption curve and phase transformation [143], especially for heat treatment at 1200°C.

Hang *et al*[144]. produced $Ti_{10}V_{77}Cr_6Fe_6Zr$ (at.%) by induction levitation melting, then heat treated it at 1100°C for 8 hours, 1250°C for 5 minutes and quenched in water. The sample heat treated at 1250°C had the best overall hydrogen storage properties[54], with a hydrogen

desorption capacity of 1.82 wt%, a dehydriding plateau pressure of 0.75 MPa and a plateau slope factor of 0.1. The slope factor, which is a measure change in the H/M ratio, could be caused by change in pressure (P), is expressed as:

$$S_f = \frac{d(ln\ P)}{d(ln\ H/M)} \quad \text{.....} \quad (2.6)$$

Alloys having a low S_f are preferred, as this indicates that a small increase in pressure results in an increase in H/M ratio.

Yamamoto and Kanda [145] investigated the corrosion behaviour of AB_5 type hydrogen storage alloy in alkaline solution. The work revealed that the effect of heat treatment on corrosion resistance is not significant.

2.4 PHASE DIAGRAMS IN THE TI-V-CR SYSTEM

After a review of literature on Ti-based alloys, the decision was made to study alloys from Ti-V-Cr system. The major constituents of alloys in this work are titanium, chromium and vanadium, so the binary (Ti-V, Cr-Ti, Cr-V) and pseudo-binary (TCr_2 - V) and ternary phase diagrams are reviewed. Other minor constituents are iron (≤ 6 at.%), rhodium (≤ 0.1 at.%) and palladium (≤ 0.1 at.%).

2.4.1. Binary systems

According to Enomoto[39], the binary Ti-V phase diagram in Figure 2.1 shows that the (βTi) and (V) phases form a continuous bcc solid solution above ~880°C. The monotectoid reaction: (βTi) ↔ (αTi) + (V) occurs below 850 °C because of the miscibilty gap in the (βTi) phase.

Wei and Flower[34] reported that neither the gap nor a stable monotectoid reaction was likely to occur in the binary Ti-V system, and that the reported miscibility gap in the phase was possibly due to oxygen impurity.

In the binary Cr-Ti phase diagram (Figure 2.2)[39], Cr-Ti alloy solidifies as a continuous isomorphous bcc solid solution (βTi,Cr). The phase diagram contains three equilibrium solid phases, two solid solutions, (αTi) and (βTi,Cr); and an intermetallic compound, $TiCr_2$, where the compound phases are designated α-, β- and γ$TiCr_2$. The $TiCr_2$ phases are the Laves phases C14, C15 and C36 respectively.

Smith[36] showed that the binary Cr-V phase diagram (Figure 2.3) contained a completely miscible bcc solid solution (V,Cr) where no intermediate compounds exist.

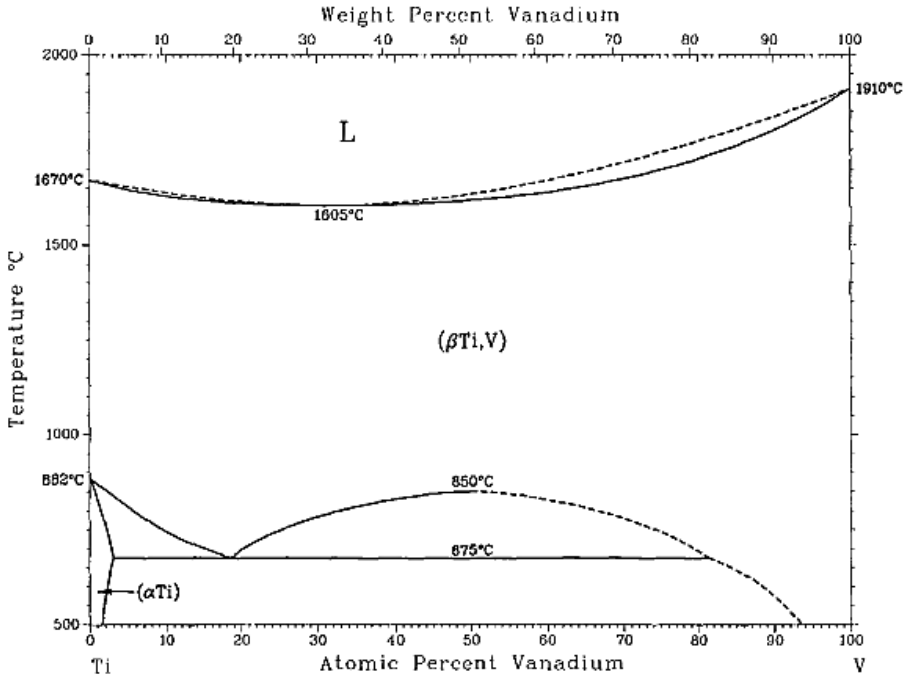

Figure 2.2 Ti-V phase diagram.[39]

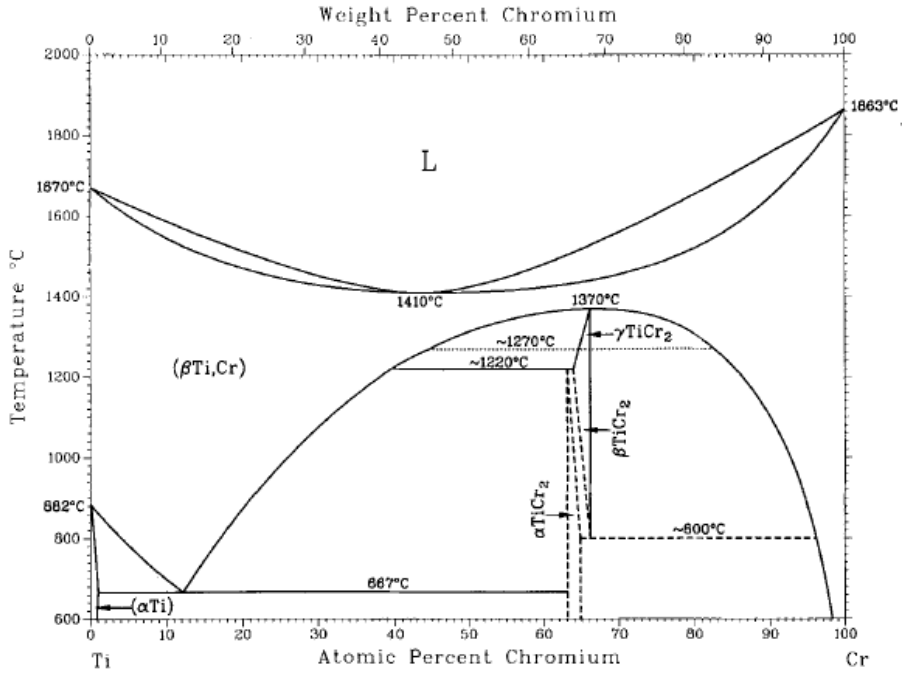

Figure 2.3 Ti-Cr phase diagram.[39]

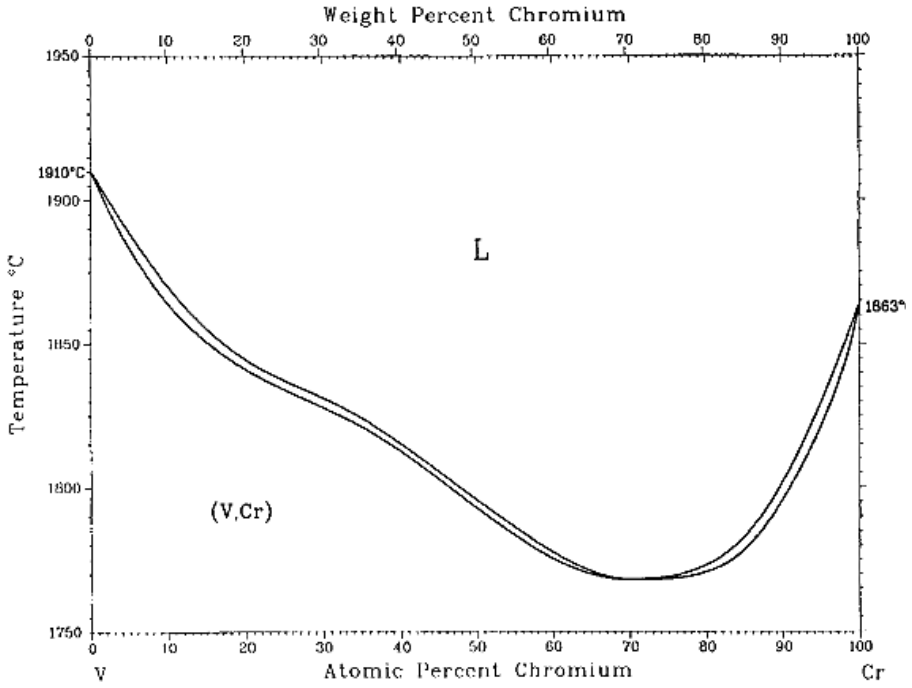

Figure 2.4 V-Cr phase diagram.[39]

2.4.2. $TiCr_2$ - V pseudobinary system

The pseudobinary system in Figure 2.4 through $TiCr_2$-V was reported by Samsonova[37]. The alloys were produced from iodide Ti, high purity electrolytic Cr (99.99%) and carbothermic V (99.75%). A combination of thermal analysis, powder XRD, powder X-ray diffractometry and metallography was used for thermal analysis of the alloy.

The system shows the peritectoid reaction $\beta TiCr_2 + \beta \leftrightarrow \alpha TiCr_2$. $\beta TiCr_2$ and $\alpha TiCr_2$ correspond to ternary hexagonal C14 (β) and cubic C15 (α) Laves phases respectively. Crystallographic parameters for $\gamma TiCr_2$ were not available[38]. The $TiCr_2$–V system is not consistent with the phase boundaries in Figure 2.2 because it shows allotropic transformation from β to $\alpha TiCr_2$ at ~1220°C.

A list of solid phases in this system adapted from Enomoto[39] is shown in Table 2.1. According to Murray[40], the $\alpha TiCr_2$ compound is a cubic C15 Laves phase, the $\beta TiCr_2$ (C14) compound is a higher temperature form of $TiCr_2$ with a higher Cr content than $\alpha TiCr_2$ and the $\gamma TiCr_2$ (C36) compound can only be found above ~1270°C.

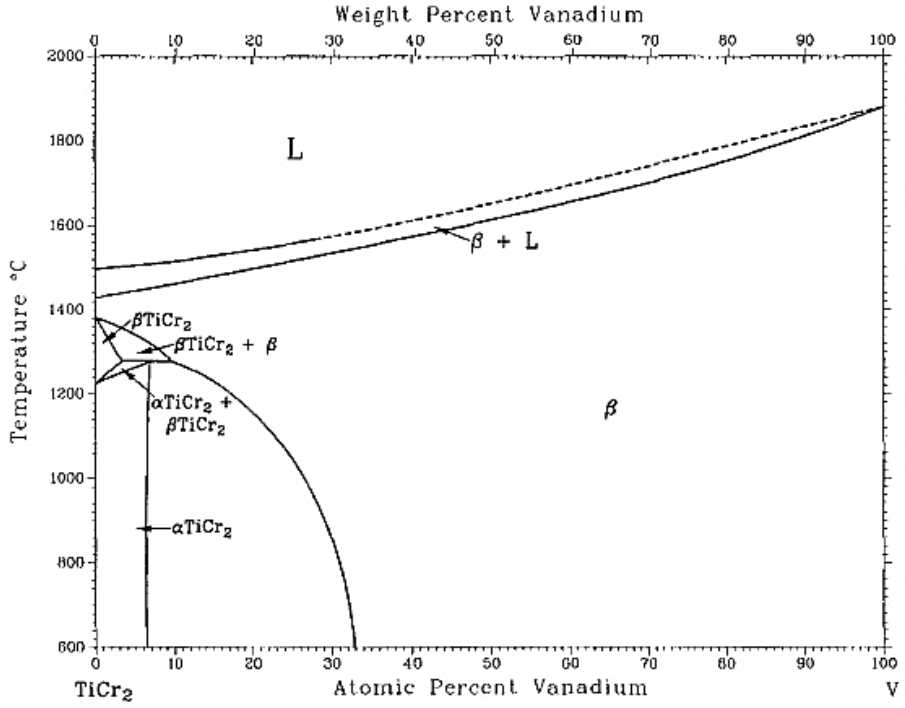

Figure 2.5 Pseudobinary $TiCr_2$ section through the Cr-Ti-V phase diagram.[37,38]

Table 2.2 Cr-Ti-V crystal structure and lattice parameter data.[38]

Phases	**Composition range, at.%**	**Pearson symbol**	**Space group**	**Strukturbericht designation**	**Lattice parameters, nm**	
					a	***c***
(αTi)	0 - 0.2Cr 0 - ~ 3V	*hP_2*	*$P6_3/mmc$*	A3	0.29506	0.46835
(βTi)	0 – 100Cr 0 – 100V	*cl2*	*Im3m*	A2	0.33065	
$\alpha TiCr_2$	63 – 65Cr [118] 0 – 7.5V [139,140]	*cF24*	*Fd3m*	C15	0.6957	
$\beta TiCr_2$	64 – 66Cr [65, 66] 0 – 4V	*hP12*	*$P6_3/mmc$*	C14	0.4921	0.7945
$\gamma TiCr_2$	64 – 66Cr	*hP24*	*$P6_3/mmc$*	C36	-	-

The cell volumes of different Ti-Cr phases obtained from AtomWorks are: (αTi) – 35.66 $Å^3$; C14 – 168.17 $Å^3$; C15 – 333.10 $Å^3$ and C36 – 327.5 $Å^3$. All belong to the same space group (*$P6_3/mmc$*), except for C15, which belongs to the *Fd3m* space group. Information from other references listed in Table 2.2 show that the cell volumes may vary, *e.g.* the range for C14 Laves could be: 161-171 $Å^3$; C15: 332-335 $Å^3$; αTi: 35.16-36.24 $Å^3$. The isothermal sections through Ti-V-Cr system at 1000°C is shown in Figure 2.6.

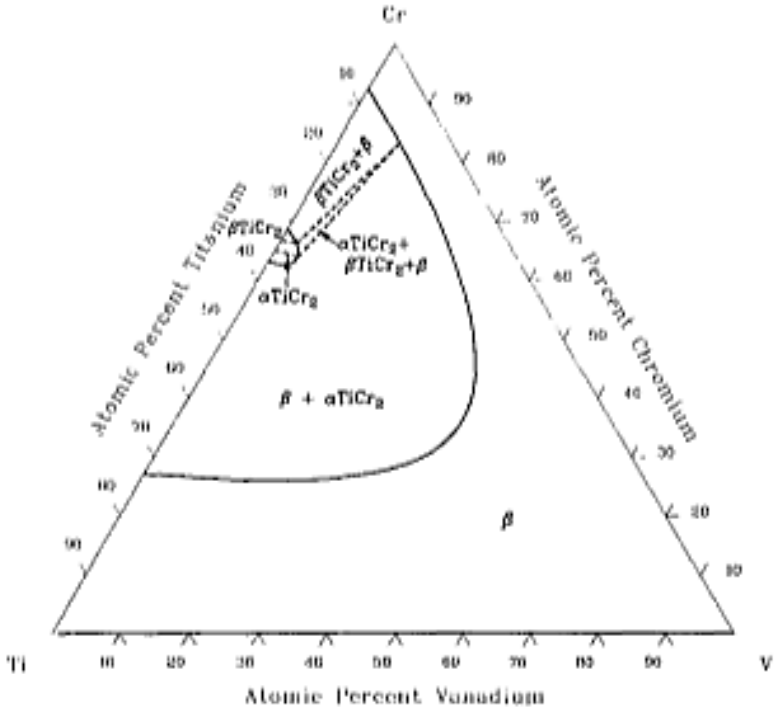

Figure 2.6. Isothermal sections through Ti-V-Cr system at 1000°C[39]

Table 2.3. Possible cell volume of Laves and other phases.

S/NO	Space group	Element/ Compound	Cell volume ($Å^3$)	Ref.
1	*P6₃/mmc*	αTi	35.22	[51]
2	*P6₃/mmc*	$Ti_{0.981}V_{0.011}$	35.33	[114]
3	*P6₃/mmc*	$Ti_{0.981}V_{0.019}$	36.24	[126]
4	*P6₃/mmc*	$Ti_{1.03}V_{1.97}$	168.17	[101]
5	*P6₃/mmc*	$Cr_{1.93}Ti_{1.07}$	167.81	[15]
6	*P6₃/mmc*	V(TiFe)	164.17	[170]
7	*P6₃/mmc*	$Ti(Cr_{0.986}Ti_{0.014})_2$	332.13	[170]
8	*P6₃/mmc*	$Ti(Cr_{0.964}Ti_{0.036})_2$	335.46	[13]
9	*P6₃/mmc*	$Ti_{1.11}V_{0.78}Fe_{1.11}$	166.45	[117]
10	*P6₃/mmc*	$TiV_{0.84}Fe_{1.16}$	165.92	[197]
11	*P6₃/mmc*	(CrFe)Ti	161.7	[178]
12	*P6₃/mmc*	$Ti_{0.801}Fe_{0.197}$	35.16	[48]
13	*P6₃/mmc*	$(Cr_{1.6}Fe_{0.4})Ti$	163.15	[22]
14	*P6₃/mmc*	$TCr_{1.56}Fe_{0.44}$	163.63	[80]
17	*P6/mmm*	$Ti_{0.8}V_{0.2}$	49.91	[114]
18	*Fd3m*	$TiCr_2$	336.28	[81]
19	*Fm3m*	Ti	67.97	[182]
20	*Fd3m*	$Ti_{1.07}Cr_{1.97}$	334.39	[15]
21	*Fd3m*	Cr_2Ti	334.50	[78]

The Laves phase is an intermetallic compound with the AB_2 stoichiometry. It can exist as the cubic C15 (3C), hexagonal C14 (2H) or dihexagonal C36 (4H) structures. Annealing at elevated temperatures for long times sluggishly transforms the metastable C14 phase in Ti-V-Cr system to the intermediate stability C36 structure or alternately, to the stable C15 phase[36].

Maeland *et al.* [42] found that the structure of titanium, which is hcp at room temperature, can react with hydrogen at an appreciable rate only at elevated temperatures. Rapid reactions at room temperature of these stable bcc solid solution phases with hydrogen were observed when small amounts of a third element with a radius more than 5% smaller than that of titanium was introduced.

The focus of this work was to develop titanium alloys (Ti-Cr-V based) for hydrogen storage. Titanium was discovered in Cornwall in 1791 by William Gregor[43], an English priest. Titanium is a bright silvery metal and, when polished, resembles steel in appearance. In its pure form, it has relatively low tensile strength (216 MPa) and a high ductility (50%) but the commercial grade contains some impurities which raise the tensile strength to as much as 700MPa and reduce ductility by 20% [43]. Because of its high fatigue strength and creep properties, titanium (in commercially pure and alloyed forms) has become an increasingly important engineering material in the aircraft industry. Its high melting point (1725°C) has contributed to its use as a component in jet engine construction[94].

2.5 ELECTROCHEMICAL CORROSION MEASUREMENT

Most metal corrosion occurs through electrochemical reactions at the interface between the metal and an electrolyte[44]. The rate of the reaction is evaluated in terms of the corrosion current. The natural logarithm of the absolute value of the corrosion current versus the potential is plotted as a Tafel curve, as shown in Figure 2.7.

The corrosion current values can be transformed to corrosion rate values (e.g. mm/y) using Equation 2.9[44]:

$$CR = K \frac{i_{corr}}{\rho} EW \ldots\ldots\ldots\ldots\ldots\ldots\ldots\ldots\ldots\ldots\ldots\ldots\ldots\ldots\ldots\ldots\ldots\ldots\ldots\ldots\ldots\ldots\ldots\ldots\ldots\ldots.. (2.7)$$

where K is a constant that depends on the unit of corrosion rate;

$K = 3272$ for mm/y (mmpy), or $= 1.288 \times 10^5$ for milli-inches/y (mpy)

i_{corr} = corrosion current density, μA/Cm^2

ρ = alloy density

EW = Equivalent weight = 1/electron equivalent (Q) where:

$$Q = \sum \frac{n_i f_i}{W_i} \dots\dots\dots\dots\dots\dots\dots\dots\dots\dots\dots\dots\dots\dots\dots\dots\dots\dots\dots\dots\dots\dots\dots\dots\dots\dots\dots (2.8)$$

where n_i = the valence if i^{th} element of the alloy

f_i = the mass fraction of the i^{th} element in the alloy

Wi = the atomic weight of the i^{th} element in the alloy.

Inserting Equation 2.8 in 2.7, the penetration rate (corrosion rate) CR or mass loss (ML) of an alloy is given by:

$$CR = K_1 \frac{i_{corr}}{\rho \sum \frac{n_i f_i}{W_i}} \dots\dots\dots\dots\dots\dots\dots\dots\dots\dots\dots\dots\dots\dots\dots\dots\dots\dots\dots\dots\dots\dots\dots\dots\dots .. (2.9)$$

$$ML = K_2 i_{corr} EW \dots\dots\dots\dots\dots\dots\dots\dots\dots\dots\dots\dots\dots\dots\dots\dots\dots\dots\dots\dots\dots\dots\dots\dots . (2.10)$$

The values of constants for use in the equations above are given in Table 2.4

.

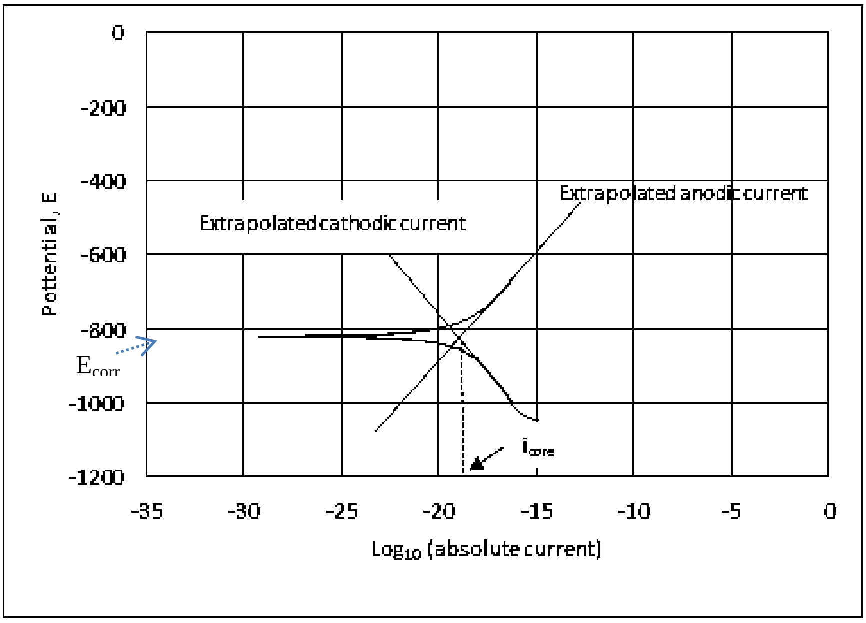

Figure 2.7. Classic Tafel curve. [44]

Table 2.4 Value of constants used in corrosion rate calculations[44].

Penetration rate units (CR)	**I_{corr} units**	**ρ units**	**K_1**	**Unit of K_1**
m/y	$\mu A/cm^2$	g/cm^3	0.1288	mpy g/μA cm
mm/y	$\mu A/cm^2$	g/cm^3	0.03272	mm g/μA cmy

CHAPTER 3: Experimental procedure

3.1. Overview

This chapter describes the experimental procedures that were followed to produce, characterise and evaluate the mechanical properties of the alloys. The materials used, the alloy production and heat treatment processes employed are described. The equipment used for the experimental work, the material preparation for metallography, the corrosion tests and the pressure-composition-isotherm tests are also given. The use of Thermo-Calc programming for calculating the equilibrium phases in the alloys concludes the chapter.

3.2. Choice of alloy composition

In accordance with the main aim of this work, *i.e.* to develop and assess titanium alloys based on the Ti-Cr-V system for hydrogen storage, relevant literature was reviewed. In the work of Cho *et al.*[147], a composition region was identified in the Ti-V-Cr phase diagram as having the highest hydrogen uptake. This informed the choice of the base alloy $Ti_{25}V_{40}Cr_{35}$. The research gaps in their work are: no other alloying additions were made and the alloys were not heat treated, but only assessed in the as-cast condition.

South Africa has the world's third largest reserves of vanadium deposits, and was the second largest producer of vanadium, as titaniferous magnetite ore in 2014, behind China[148, 149]. Vanadium slag is produced from the steelmaking process, and is then refined to ferrovanadium.

The choice of adding iron to the Ti-V-Cr alloy was made because the relatively low cost of ferrovanadium compared to refined vanadium would make partial substitution of V with FeV a financially viable option if the hydrogen storage capacity wass not substantially reduced by iron. The prices in October 2015 are:
Ferrovanadium - 13.5 USD/kg
Vanadium metal (99.9% pure) – 2200 USD/kg

The platinum group metals (PGMs) Rh and Pd were chosen for their relative abundance in South Africa. Pd and Rh are among the economically significant PGMs, as South Africa is the world's leading Rh producer and the second largest Pd producer after Russia.[150]

Literature showed that heat treatment has varying effects on hydrogenation characteristics of alloys[151,153-156], therefore, there is a need to investigate effects of heat treatment on Ti-V-Cr, Ti-V-Cr-Fe, Ti-V-Cr-Rh, Ti-V-Cr-Pd alloys.

3.3. Materials processing and procedure

Alloy compositions are usually measured by weight % or atomic %. Equation 1 shows how to convert from atomic weight composition to atomic mass and vice-versa in binary alloy [64].

$$\left.\begin{aligned} wt\ \%\ A &= \frac{at.\%\ A \times at.\ weight\ of\ A}{(at.\%\ A \times at.\ weight\ of\ A)+(at.\%\ B \times at.\ weight\ of\ B)} \times 100 \\ at\ \%\ A &= \frac{wt\ \%\ \frac{A}{at}.weight\ of A}{(wt\ \%\ A/at.weight\ of A) + (wt\ \%\ B/at.weight of B)} \times 100 \end{aligned}\right\} \quad 3.1)$$

The equation for converting from atomic % to weight % in higher order alloys is similar to that of binary systems, except that an additional term is added to the denominator for each additional components[64] e.g. for quaternary alloy as in the case of this research work.

$$\left.\begin{aligned} wt\ \%\ A &= \frac{at\ \%\ A \times at\ wt.\ of\ A}{(at\ \%\ A \times at\ wt\ .of\ A)+(at\ \%\ B \times at\ wt.\ of\ B)+(at\ \%\ C \times at\ wt.\ of\ C)+(at\ \%\ D \times at\ wt.\ of\ D} \times 100 \\ at\ \%\ A &= \frac{wt\ \%\ A/atweight of A}{(wt\ \%/at.\ wt\ of\ A) + (wt\ \%\ B/at.wt\ of\ B) + (wt\ \%/at.\ wtof\ C) + (wt\ \%\ D/at.wtof\ D} \times 10 \end{aligned}\right\} \quad ..3.2$$

The compositions from weight to atomic % calculations for four and higher order systems was done on a computer spreadsheet.

The starting materials for the alloys were powders: iron (325-290 mesh, 99% purity, 0.01% C and 0.015% P and S); chromium (<0.3mm, 99.8% purity) vanadium (-325 mesh, 99.5% purity), titanium (-325 mesh, 99.5% purity), Rhodium (99.9% purity) and palladium (99.9% purity).

The required mass of each powder was weighed out on an electronic scale, as listed in Table 3.1. Before melting, the powder constituents were compacted using a 20mm diameter die under a pressure of 220 kPa.

3.4. Alloy production

Prior to melting, the furnace was evacuated and filled with argon gas 3 times to extract oxygen. Melting of the alloy compacts was done in a water-cooled, copper-crucible arc-melting furnace (Figure 3.1) under argon atmosphere. The ingots were turned over and remelted three times to ensure homogeneity. After melting, the ingots were cut to three pieces. Two cut samples were vacuum sealed in separate silica glass ampoules in readiness for heat treatment.

Table 3.1 Mass of elements for arc-melting of 10g samples.

		Mass (g)					
Alloy no.	**Composition (at. %)**	**Ti**	**V**	**Cr**	**Fe**	**Rh**	**Pd**
A1	$Ti_{25}V_{40}Cr_{35}$	2.37	4.03	3.60	-	-	-
A2	$Ti_{24}V_{40}Cr_{34}Fe_{2}$	2.27	4.02	3.49	0.22	-	-
A3	$Ti_{23}V_{40}Cr_{33}Fe_{4}$	2.17	4.01	3.38	0.44	-	-
A4	$Ti_{22}V_{40}Cr_{32}Fe_{6}$	2.07	4.00	3.27	0.66	-	-
A5	$Ti_{24.975}V_{40}Cr_{34.975}Rh_{0.05}$	2.37	4.03	3.60	-	0.01	-
A6	$Ti_{24.95}V_{40}Cr_{34.95}Rh_{0.1}$	2.36	4.03	3.59	-	0.02	-
A7	$Ti_{24.975}V_{40}Cr_{34.975}Pd_{0.05}$	2.37	4.03	3.60	-	-	0.01
A8	$Ti_{24.95}V_{40}Cr_{34.95}Pd_{0.1}$	2.36	4.03	3.59	-	-	0.02

(a) Exterior (b) Interior

Figure 3.1. Photographs of water-cooled copper-crucible furnace (Mintek, South Africa).

3.5. Heat treatment of samples

Heat treatment processes (Section 2.5.3) having positive effects on Ti-V-Cr alloys with similar compositions to the alloys in this work were closely examined. For instance, heat treatment at 1400°C for 5 minutes was found to effectively improve the flatness of the plateau and enlarge the hydrogenation capacity of a $Ti_{32}Cr_{46}V_{22}$ alloy[96]. According to Cho et al.[143], heat treatment at 1200°C for 2 hours improved the hydrogen storage properties of $Ti_{0.32}Cr_{0.43}V_{0.25}$. Itoh et al.[133] found that high temperature heat treatment improved homogeneity, a fast cooling rate refined the grain size and increased the lattice constant of $Ti_{30}Cr_{50}V_{20}$ and $Ti_{27.8}Cr_{42.2}V_{25}Fe_5$ alloys. According to the pseudo-binary $TiCr_2$-V phase diagram[139, 140] (Figure 2.4), the alloys and the heat treatment temperatures in the examined literature fall within the β phase, hence the choice of heat treatment temperature of 1000°C for $Ti_{25}Cr_{35}V_{40}$.

The specimens sealed in the evacuated quartz ampoules were loaded in two batches in a heat treatment oven and heated to 1000 °C for 1 hour. The first set of ampoules were immediately removed and broken in cold water to quench the alloy. The second batch was loaded into the furnace, heated to 1000 °C for 1 hour and then slowly furnace-cooled.

3.6. Metallographic preparation

3.6.1 Mounting

Mounting of the specimens was done on a Struers CitoPress10®. The resins used were PolyFast phenolic hot mounting resin with carbon filter and ClaroFast hot mounting acrylic resin containing methy methacrylate for transparent embedding of specimens.

3.6.2 Grinding and polishing

Grinding of the specimens was done on a Leco Spectrum System 2000 Autogrinder®. The machine was set to a grinding speed of 150 rpm for 5 minutes under a pressure of 20 N and water was used as lubricant on silicon carbide abrasive papers. These grinding parameters were maintained for successive grinding using 1200, 2400 and 4000 grit. The specimens were cleaned of grinding particles under running tap water between each stage. After grinding, the specimens were polished with 0.15 µm with Buehler MasterMet non crystalising colloidal silica suspension for 2 minutes under a pressure of 10 N and wheel speed of 100 rpm.

3.7. Characterisation of the alloys

The alloys (both as-cast and heat treated) were characterised for phase identification using optical microscopy, X-ray diffraction (XRD), and scanning electron microscopy (SEM) with energy dispersive X-ray spectroscopy (EDX) using an Oxford® system.

3.7.1 Optical microscopy

After polishing, the specimens were etched with HF by swabbing for 5 to 7 seconds. The microstructure of the alloys was examined under a Leica Microsystems Compound Microscope® DMi8.

3.7.2 XRD

Phases of the as-cast and heat-treated alloys were determined by XRD analysis, using Xpert High Score® phase identification software on a Bruker D2_Phaser X-ray® diffraction machine with Cu-Kα radiation from $2\theta = 10^{o}$ to 90^{o}.

3.7.3 SEM

Analysis of the alloys was done using a FEI Nova NanoSEM 200® scanning electron microscope (SEM) fitted with EDAX® advanced microanalysis solution and a Zeiss Sigma FE-SEM with a low kV optimised backscatter detector, HD BSD, for the samples at low acceleration voltages (750V to 3kV) and low probe currents. The samples were viewed using backscattered electron imaging (BSE) to distinguish between the phases. EDX was performed on selected areas to analyse compositional variations in the alloys. The approximate amount of the phases was determined by image analysis using ImageJ freeware[179].

3.8. Hardness test

A FutureTech FT FM700®, Microhardness tester (Figure 3.7) was used for the Vickers hardness tests with a 2 kg load. The hardness values were measured five times for the as-cast and heat treated samples and the average values were recorded.

3.9. Corrosion tests

Potentiostatic corrosion tests on the alloys were performed using an AutoLab® corrosion test apparatus and electrochemical cell in Figure 3.8. The electrochemical cell consisted of a tri-electrode: platinum reference electrode Ag/AgCl counter electrode, and test alloy as the working electrode in 6 M KOH aqueous solution as the electrolyte.

The alloy samples were cut into rectangles and a copper wire of suitable length was attached to one side of the specimen with aluminium tape and covered in cold-resin for 24 hours, leaving only the test surface exposed. When cured, the test surface was ground to 120 grit. The corrosion experiments were performed at 25°C, and potentiodynamic Tafel curves were recorded from -1.4V to -0.2V with a scanning rate of 1mV/s.

3.10. Pressure Composition Temperature PCT measurements

Before the PCT test, an initial activation process was performed by evacuating the Sievert's apparatus at 673 K for 30 minutes. After the activation process, a Sieverts-type apparatus was used for the measurement of the pressure composition (PCT) curves. After crushing the samples into particles <75 μm diameter, 1 g of each alloy was sealed into a stainless steel reactor. The samples were heated up to 573 K, and hydrogen at 3 MPa was introduced into the apparatus for 30 minutes. This was followed by slow cooling to room temperature in hydrogen. The alloys absorbed most of the hydrogen and pulverized in this step. After the absorption process, the samples were heated up to 573 K and chamber was evacuated with a mechanical pump for 1 hour to dehydrogenate completely for PCT measurements at 303, 333 and 363 K.

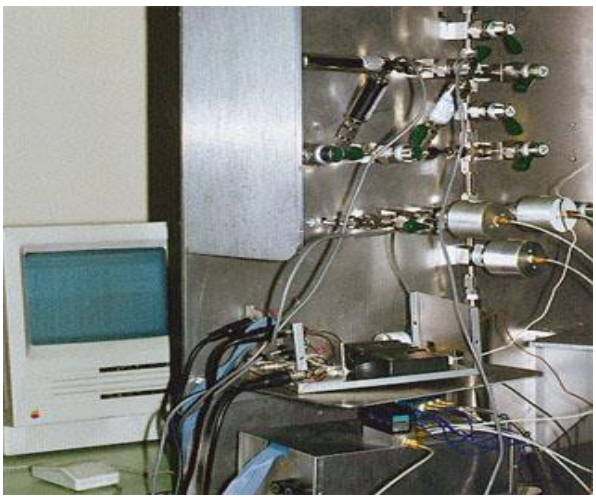

Figure 3.2. Computer controlled Sievert's apparatus.

3.11.Thermo-Calc modelling

ThermoCalc modelling is included in this work to enable prediction of the expected phases, determine the equilibrium conditions and the amount of phases in the alloys.

The Titanium database (TTTI3) and the solid solution database (SSOL4) were used for the Thermo-Calc modelling. A Thermo-Calc code/template (.tcm) shown in Figur 3.2 below was used for modelling the equilibrium phases in Ti-V-Cr system using TTTI3 database, 1 degree of freedom and 40 at.% V and 35 at.% Cr composition. Indented lines were edited appropriately depending on the alloy system, the alloy composition and the database to be used in the model.

```
go data
      sw ttti3 (ttti3-titanium
database, ssol4-general database)
def-sys
      ti v cr (alloy system)
l-s
CONSTITUENT
get
go p-3
s-c n=1
s-c p=101325
s-c t=1200
      s-c x(v)=.40  at.%
                    composition
      s-c x(cr)=.35
l-c
@&
c-e
s-a-v
1
T
473
2173
3
save
                              (cont.)
```

```
      Cont.)

      A1 ttti3 (File name)
step
NORMAL
post
s-d-a x T-c
s-d-a y np(*)
plot
SCREEN
set-tit
      Ti25V40Cr35     (Title of plotted
diagram)
plot
SCREEN
set-label
d
s-t-m-s
x
s-s x n 250 2000
plot SCREEN
set-interactive
```

CHAPTER 4: Results

Overview

The results are presented in six sections. The first section presents the analysed compositions of the as-cast alloys compared with the nominal (targeted) compositions. The next four sections present the following results for as cast and heat treated alloys A1 – A8: the microstructures and phase information, hardness, corrosion properties and hydrogen storage characteristics. The sixth section presents the Thermo-Calc calculations of phases in each of the alloys.

4.1. Comparison of the actual and nominal compositions of all alloys

The targeted (nominal) and the actual compositions analysed by EDX are listed in Table 4.1. All the subsequent alloys (A2-A7) were based on the Ti-V-Cr alloy A1.

Table 4.1. Targeted and analysed compositions of the alloys.

	Compositions (at.%)	
Alloys	**Targeted**	**Analysed**
A1	$Ti_{25}:V_{40}:Cr_{35}$	$Ti_{25.3}:V_{38.4}:Cr_{36.3}$
A2	$Ti_{24}:V_{40}:Cr_{34}:Fe_2$	$Ti_{21.9}:V_{40}:Cr_{35.6}:Fe_{2.6}$
A3	$Ti_{23}:V_{40}:Cr_{33}:Fe_4$	$Ti_{24.4}:V_{37.4}:Cr_{33.0}:Fe_{5.2}$
A4	$Ti_{22}:V_{40}:Cr_{32}:Fe_6$	$Ti_{24.6}:V_{36.0}:Cr_{33.1}:Fe_{6.3}$
A5	$Ti_{24.98}:V_{40}:Cr_{34.97}:Rh_{0.05}$	$Ti_{29.8}:V_{36.0}:Cr_{34.1}$*
A6	$Ti_{24.95}:V_{40}:Cr_{34.95}:Rh_{0.1}$	$Ti_{21.4}:V_{41.4}:Cr_{37.1}$*
A7	$Ti_{24.98}:V_{40}:Cr_{34.97}:Pd_{0.05}$	$Ti_{23.8}:V_{41.2}:Cr_{35.0}$*
A8	$Ti_{24.95}:V_{40}:Cr_{34.95}:Pd_{0.1}$	$Ti_{28.0}:V_{36.0}:Cr_{35.6}:Pd_{0.5}$*

*Analysed compositions of Rh and Pd are not given, as the detection limit of the SEM EDX is 0.2 at.%.

4.2. Microstructures of alloys A1 to A8

4.2.1. Microstructures and phase analysis of alloy A1 ($Ti_{25}:V_{40}:Cr_{35}$)

The optical and SEM micrographs of as-cast, annealed and quenched alloy A1 are shown in Figure 4.1, the XRD results are in Figure 4.2 and the EDX composition and XRD measured crystallographic parameters are listed in Table 4.2.

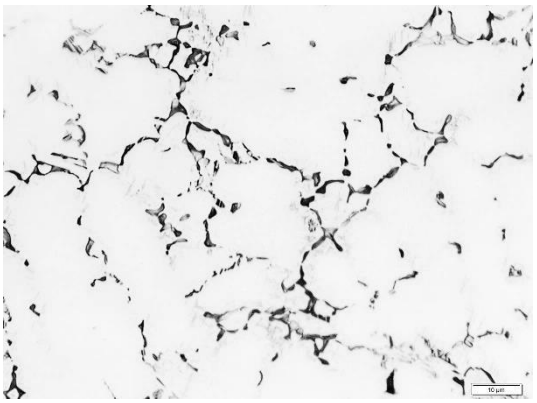

a) Optical micrograph

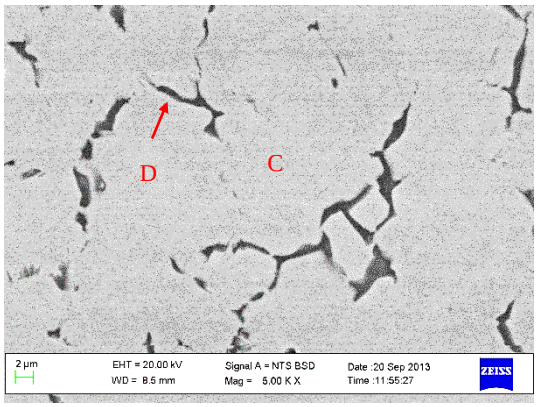

b) SEM-BSE micrograph

As-cast (A1)

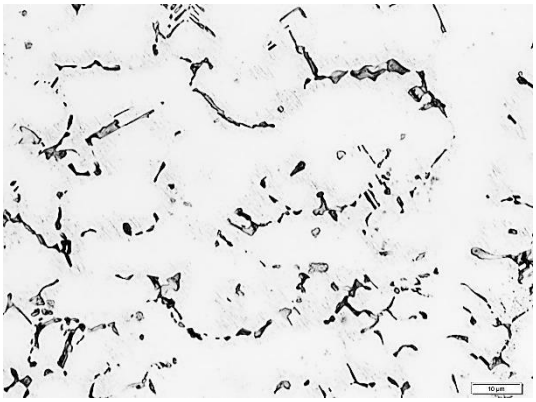

c) Optical micrograph

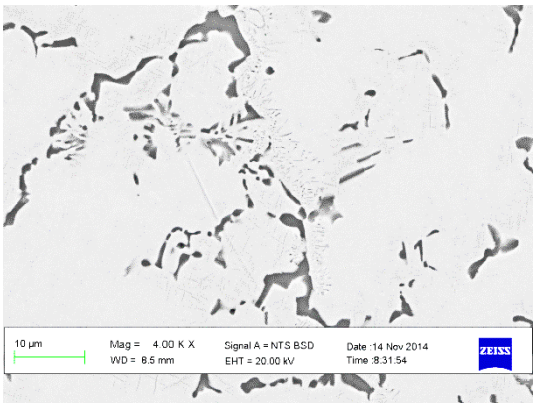

d) SEM-BSE micrograph

Annealed (A1A)

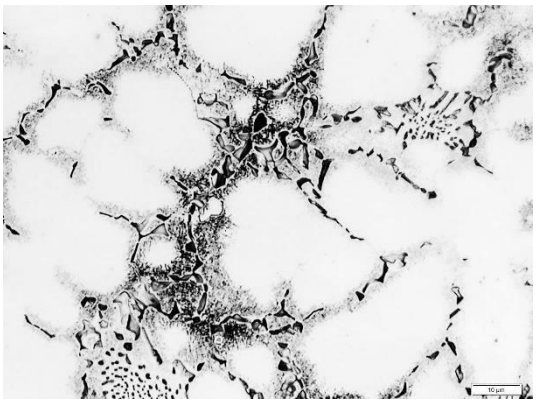

e) Optical micrograph

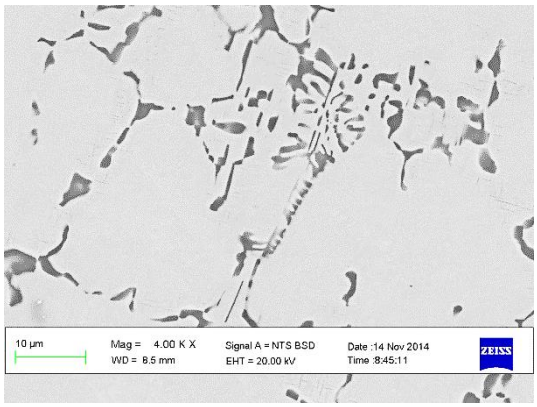

f) SEM-BSE micrograph

Quenched (A1B)

Figure 4.1. Microstructures of alloy A1 (Ti_{25}:V_{40}:Cr_{35}).

The microstructure of Alloy A1 (Figure 4.1) was a primary, light grey, bcc (V) matrix phase (C- confirmed by XRD) and a mixture of darker, intergranular phases (D). The bcc (V) phase in all three samples i.e. as-cast, annealed and quenched, contained 18-25 at.% Ti, 40-46 at.% V and ~35 at.% Cr. As listed in Table 4.2, all three A1 samples contained a black hcp α-Ti phase, while in the annealed sample, a small amount of a hcp C14 Laves phase was also identified by XRD (Figure 4.2). It is difficult to distinguish between the secondary phases by microscopy and EDX, as the phases are small, so analyses may be diluted by the (V) matrix.

The Ti-rich phases in the as-cast and annealed samples had similar compositions. As shown in Table 4.2, annealing introduced a C14 Laves phase, decreased the bcc (V) unit cell volume, while the hcp αTi volume was unchanged. Quenching removed the αTi phase, but slightly increased the bcc (V) unit cell volume, and introduced a hexagonal ωTi phase. Jafari *et al.*[70] reported that phase transition of α to ω-Ti can be obtained at 0 GPa and 0 K.

The as-cast sample contained ~90% bcc (V) phase, which was slightly decreased to 86.5% after annealing and 85.7% after quenching. Fine secondary precipitation is visible in the optical micrograph of the quenched (Figure 4.1 e).

The Ti/Cr ratio in the primary bcc phase did not change much: decreasing slightly from 0.6 to 0.5 after annealing, and increasing to 0.7 after quenching. The Ti/Cr ratio in the secondary phases changed from 4.4 to 5.4 after annealing and 2.4 after quenching.

Table 4.2. EDX compositions and XRD crystallographic parameters of phases in alloy A1 (Ti_{25}:V_{40}:Cr_{35}).

Sample	Phase (tag in BSE micrograph)	Composition (at.%)*				Phase proportion (% area)		Crystallographic description				
		Ti	V	Cr	Ti/Cr ratio	SEM BSE	Optical	Phases XRD	Space group (no.)	a (*Å*)	c (*Å*)	Cell vol. ($Å^3$)
As-cast	Primary light grey (C)	22.0 (0.7)	42.8 (0.4)	35.2 (0.8)	0.6	89.7	89.5	BCC (V)	$Im\bar{3}m$ (229)	3.0246	-	27.67
	Intergranular black (D)	66.1 (1.6)	18.9 (1.2)	15.0 (0.8)	4.4	10.3	11.5	αTi	$P6_3/mmc$ (194)	2.98	4.72	36.24
Annealed	Primary light grey (C)	18.0 (1.2)	46.1 (0.8)	35.9 (1.9)	0.5	86.5	90.8	BCC (V)	$Im\bar{3}m$ (229)	3.0235	-	27.64
	Intergranular black (D)	70.8 (5.6)	16.2 (3.2)	13.1 (2.6)	5.4	13.5	9.2	αTi	$Fm\bar{3}m$ (225)	2.98	4.73	36.24
								C14 Laves	$P6_3/mmc$ (194)	4.93	7.96	167.81
Quenched	Primary light grey (C)	25.1 (2.4)	40.4 (3.5)	34.5 (4.4)	0.7	85.7	73.6	BCC (V)	$Im\bar{3}m$ (229)	3.0380	-	28.04
	Intergranular black (D)	53.8 (5.1)	23.8 (2.6)	22.4 (2.6)	2.4	14.3	26.4	ωTi	$P6/mmm$ (191)	4.55	2.78	49.91

* Standard deviation in parentheses

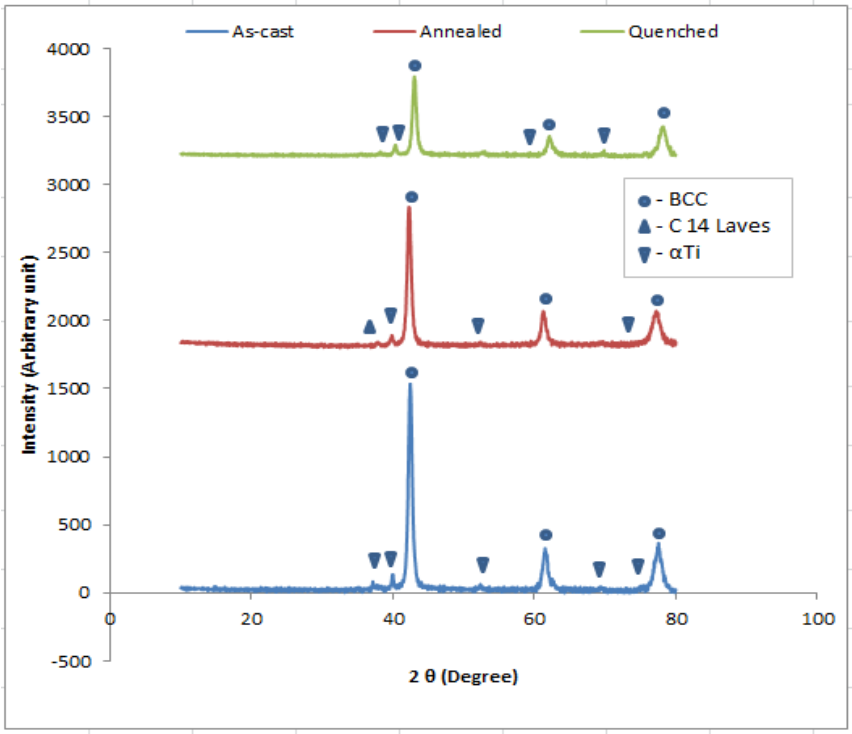

Figure 4.2. XRD patterns of as-cast and heat treated alloy A1.

4.2.2. Microstructures and phase analysis of alloy A2 (Ti24:V40:Cr34:Fe2)

The optical and SEM micrographs of as-cast, annealed and quenched alloy A2 are shown in Figure 4.3. The XRD patterns are shown in Figure 4.4 and the EDX composition and XRD measured crystallographic parameters are listed in Table 4.3.

The microstructure of Alloy A2 (Figure 4.3) was a primary, light grey, bcc (V) phase, with a black intergranular phase (D) in all three samples, and a dark grey intergranular phase in the as-cast and quenched samples. There were fine needle-like and spherical precipitates surrounding some of the black secondary phase particles (Figure 4.3 e)

Table 4.3 shows that the bcc (V) phase (C) in all the three samples The XRD analysis revealed that the sample also contained a small amount of C15 Laves which could not be detected by the SEM. The annealing treatment removed the dark grey fcc C15 and hcp C14 Laves phases and introduced the C36 Laves phase. Quenching introduced twinning in the secondary phase particles in Figure 4.3 iiib shown inside the circle (E). The C15 Laves in the as-cast and C36 Laves phase in the annealed sample were too small for EDX to analyse.

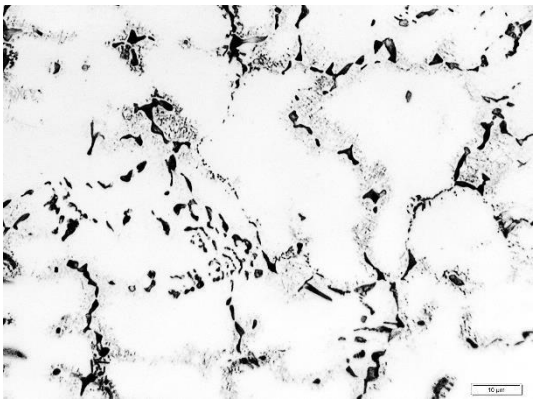

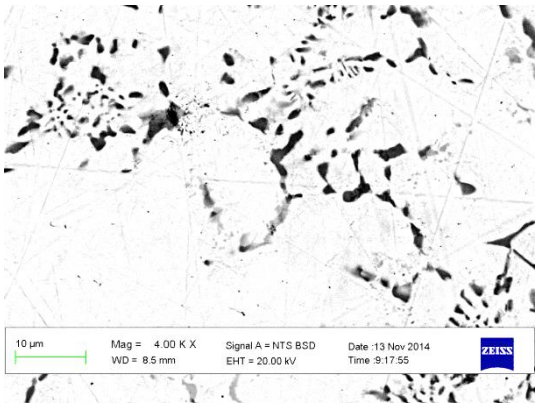

a) Optical micrograph b) SEM-BSE micrograph

As-cast (A2)

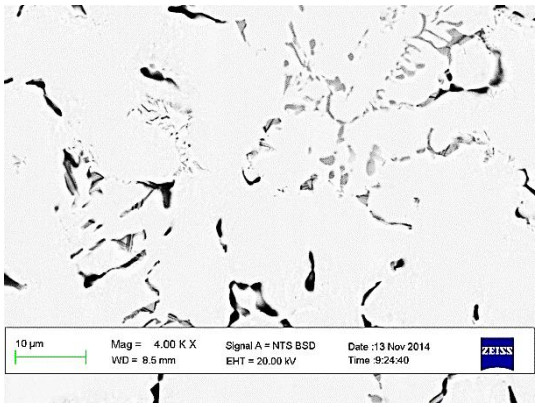

c) Optical micrograph d) SEM-BSE micrograph

Annealed (A2A)

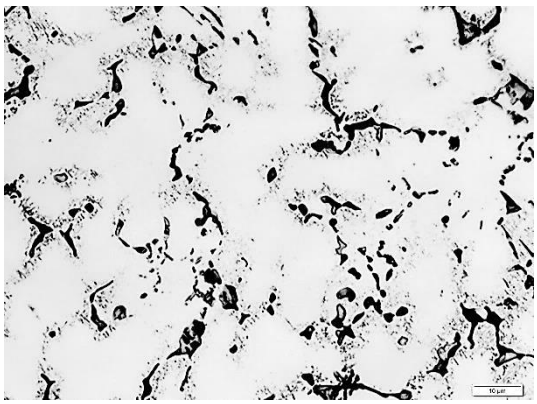

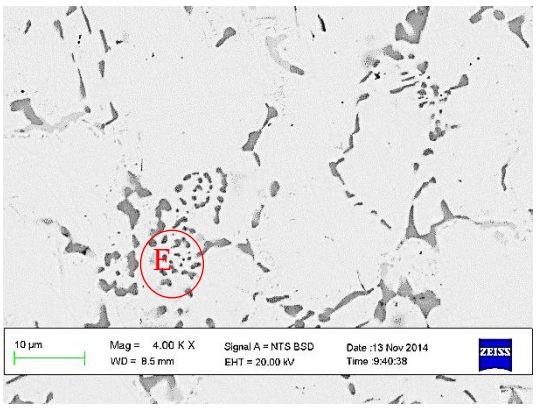

e) Optical micrograph f) SEM-BSE micrograph

Quenched A2B

Figure 4.3. Microstructure of alloy A2.

The optical and SEM BSE micrograph showed 71 - 85% bcc (V) phase, 15-27% dark phase and 1-2 % light grey phase. The proportion of the bcc (V) phase increased to ~82-85% after annealing and decreased to between 76 and 82% after quenching. The proportion of the dark phase reduced to between 15 to 18% after annealing and 16 to 22% after quenching.

Annealing had no effect on composition of the primary phase, but the cell volume increased marginally. The Ti content increased by ~5 at.% after quenching, and a significant increase in secondary cell volume was observed in the black intergranular (αTi) as it changed to hcp C36 Laves phase.

The Ti/Cr ratio in the bcc phase remained relatively constant at 0.5-0.6 for all three samples. The Ti/Cr ratio in the secondary phases increased from 0.6 to 4.4 after annealing and 2.2 after quenching.

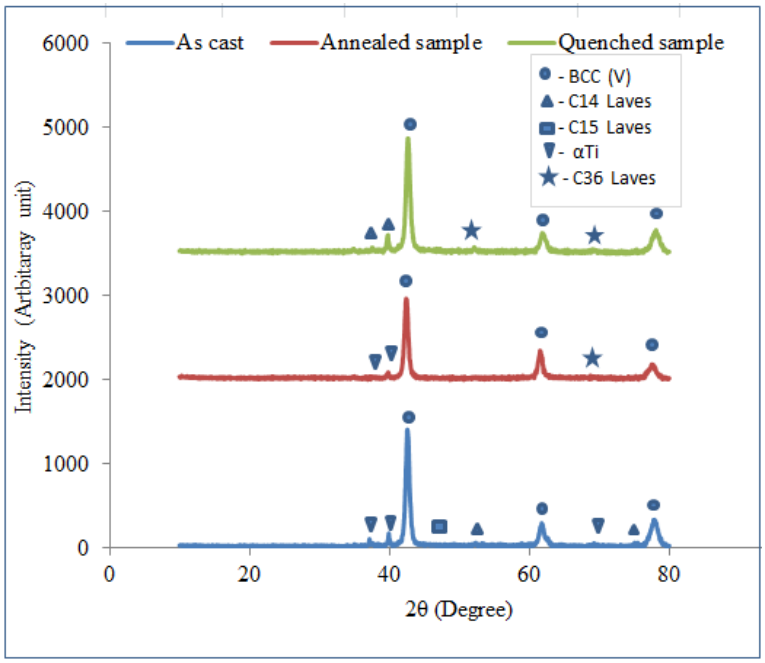

Figure 4.4. XRD patterns of as-cast and heat treated alloy A2.

Table 4.3. EDX compositions and crystallographic parameters of phases in alloy A2 (Ti_{24}:V_{40}:Cr_{34}:Fe_2).

Sample	Phase (tag in BSE micrograph)	Composition (at.%)*					Phase proportion (% area)		Crystallographic description				
		Ti	V	Cr	Fe	Ti/Cr ratio	SEM BSE	Optical	Phases XRD	Space group (no.)	*a* (Å)	*c* (Å)	Cell vol. ($Å^3$)
As-cast	Primary light grey (C)	17.7 (1.1)	43.5 (1.6)	36.5 (2.2)	2.3 (0.7)	0.5	78.5	71.2	BCC (V)	$Im\bar{3}m$ (229)	3.0030	-	27.08
	Black inter-granular (D)	23.0 (3.7)	41.4 (2.4)	35.5 (1.4)	2.0 (0.2)	0.6	20.2	26.7	α-Ti	$P6_3/mmc$ (194)	2.98	4.73	36.24
	Dark grey (E)	24.7 (0.8)	37.8 (0.7)	34.0 (0.4)	3.5 (0.3)	0.7	1.3	2.1	C14 Laves	$P6_3/mmc$ (194)	4.85	7.94	161.7
									C15 Laves	$Fd\bar{3}m$ (229)	6.94	-	334.4
Annealed	Primary light grey (C)	17.7 (1.9)	43.5 (1.3)	36.5 (2.9)	2.3 (0.2)	0.5	82.0	84.9	BCC (V)	$Im\bar{3}m$ (229)	3.0136	-	27.37
	Black inter-granular (D)	65.9 (5.2)	18.6 (2.8)	14.9 (2.2)	0.6 (0.2)	4.4	18.0	15.1	α-Ti	$P6_3/mmc$ (194)	2.98	4.73	36.24
									C36 Laves	$P6_3/mmc$ (194)	4.91	16.00	334.5
Quenched	Primary light grey (C)	21.8 (1.5)	40.0 (1.3)	35.6 (1.2)	2.6 (1.7)	0.6	81.5	76.0	BCC (V)	$Im\bar{3}m$ (229)	3.0136	-	27.37
	Black inter-granular (D)	49.1 (5.7)	26.8 (3.0)	22.7 (2.8)	1.3 (0.4)	2.2	16.5	22.0	C36 Laves	$P6_3/mmc$ (194)	8.81	4.57	354.54
	Dark grey (E)	47.3 (3.7)	21.6 (2.5)	24.7 (1.4)	6.4 (0.5)	1.9	2.0	2.0	C14 Laves	$P6_3/mmc$ (194)	4.93	7.96	167.8

* Standard deviation in parentheses

4.2.3. Microstructures and phase analysis of Alloy A3 (Ti_{25}:V_{37}:Cr_{33}:Fe).

The optical and SEM micrographs of the as-cast, annealed and quenched alloy A3 are shown in Figure 4.5, the XRD patterns are shown in Figure 4.6 and the EDX compositions and XRD measured crystallographic parameters are listed in Table 4.4.

The microstructure of Alloy A3 (Figure 4.5) was a primary, light grey, bcc (V) phase, intergranular α-Ti and dark grey Laves phases. The vanadium content of the bcc phase increased after heat treatment.

Both annealing and quenching increased the bcc cell volume of the as-cast sample from 26.95 to 27.08 $Å^3$ but had no effect on the volume of αTi. However, an additional phase (C15 Laves) with a large cell volume appeared after quenching.

The abundance of bcc (V) was increased by heat treatment, by 6.8% after quenching and by 22.5% after annealing. The secondary αTi phases are rich in Ti (49-67 at.%) and lean in other constituents when compared with the primary phase. However, the dark grey phase had a composition range of near-equiatomic proportions.

The Ti/Cr ratio in the primary phase decreased from 0.70 to 0.62 after annealing and 0.50 after quenching. There was a noticeable increase in the Ti/Cr ratio in the (αTi) phase from 8.80 to 43.60 after annealing, but less (to 9.9) after quenching, however, the ratio in the dark grey phase slightly decreased to 4.4 in annealed sample and 3.5 in quenched sample.

Table 4.4. EDX compositions and crystallographic parameters of phases in alloy A3.

Sample	Phase (tag in BSE micrograph)	Composition (at.%)*					Phase proportion (% area)		Crystallographic description				
		Ti	V	Cr	Fe	Ti/Cr ratio	SEM BSE	Optical	Phases XRD	Space group (no.)	a (Å)	c (Å)	Cell vol. ($Å^3$)
As-cast	Primary light grey (C)	24.4 (2.8)	37.4 (2.5)	33.0 (1.0)	5.2 (3.1)	0.7	67.5	81.2	BCC (V)	$Im\bar{3}m$ (229)	2.9981	-	26.95
	Black (D) intergranular	78.3 (5.4)	11.2 (2.9)	8.9 (2.0)	1.5 (0.6)	8.8	32.5	16.3	α-Ti	$P6_3/mmc$ (194)	2.98	4.73	36.24
									C14 Laves	$P6_3/mmc$ (194)	4.93	7.96	167.81
Annealed	Primary light grey (C)	21.6 (0.7)	39.3 (2.6)	34.9 (2.5)	4.3 (1.3)	0.62	90.0	84.0	BCC (V)	$Im\bar{3}m$ (229)	3.0030	-	27.08
	Black (D) intergranular	93.3 (1.0)	3.8 (0.7)	2.1 (0.2)	1.03 (0.9)	43.6	8.0	11.5	α-Ti	$P6_3/mmc$ (194)	2.98	4.73	36.24
	Dark grey	65.5 (6.7)	16.3 (3.1)	14.9 (3.5)	3.4 (0.8)	4.4	2.0	4.5	BCC (V)	$Im\bar{3}m$ (229)	3.05	-	28.26
Quenched	Primary light grey (C)	18.2 (2.0)	40.5 (1.8)	35.2 (2.0)	6.1 (2.6)	0.5	74.3	73.4	BCC (V)	$Im\bar{3}m$ (229)	3.0030	-	27.08
	Black (D) intergranular	78.5 (2.4)	9.8 (0.7)	7.9 (1.2)	3.8 (1.0)	9.9	20.0	21.5	α-Ti	$P6_3/mmc$ (194)	2.98	4.73	36.24
	Dark grey (E)	58.8 (9.3)	20.3 (4.4)	16.8 (4.4)	4.1 (1.1)	3.5	5.7	5.1	C15 Laves	$Fd3m$ (227)	6.94	-	334.39

* Standard deviation in parentheses

a) Optical micrograph

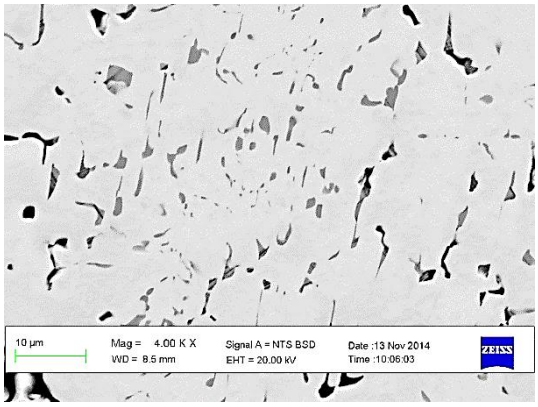

b) SEM BSE micrograph

As-cast A3

c) Optical micrograph

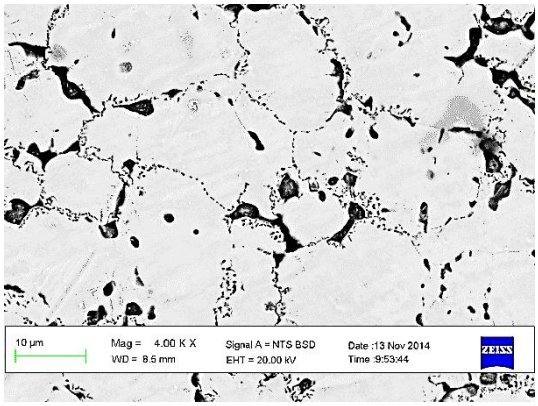

d) SEM BSE micrograph

Annealed A3A

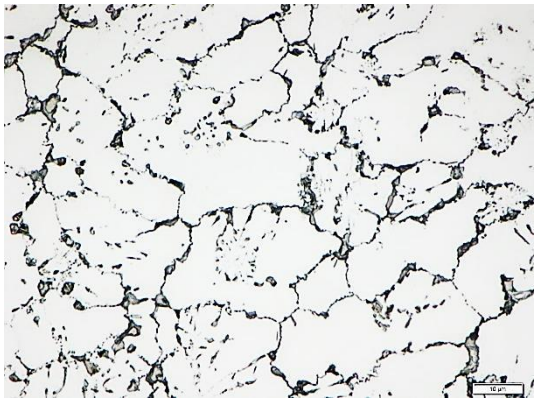

e) Optical micrograph

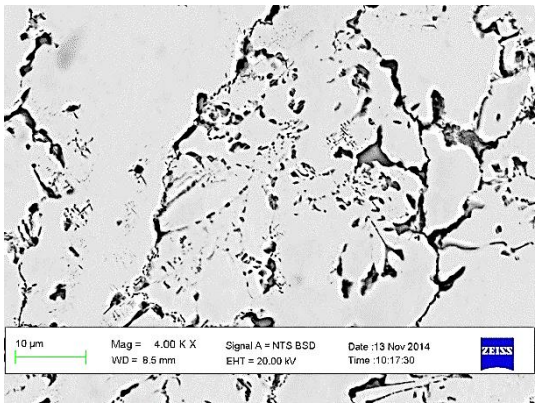

f) SEM BSE micrograph

Quenched A3B

Figure 4.5. Microstructures of as-cast and heat treated alloy A3.

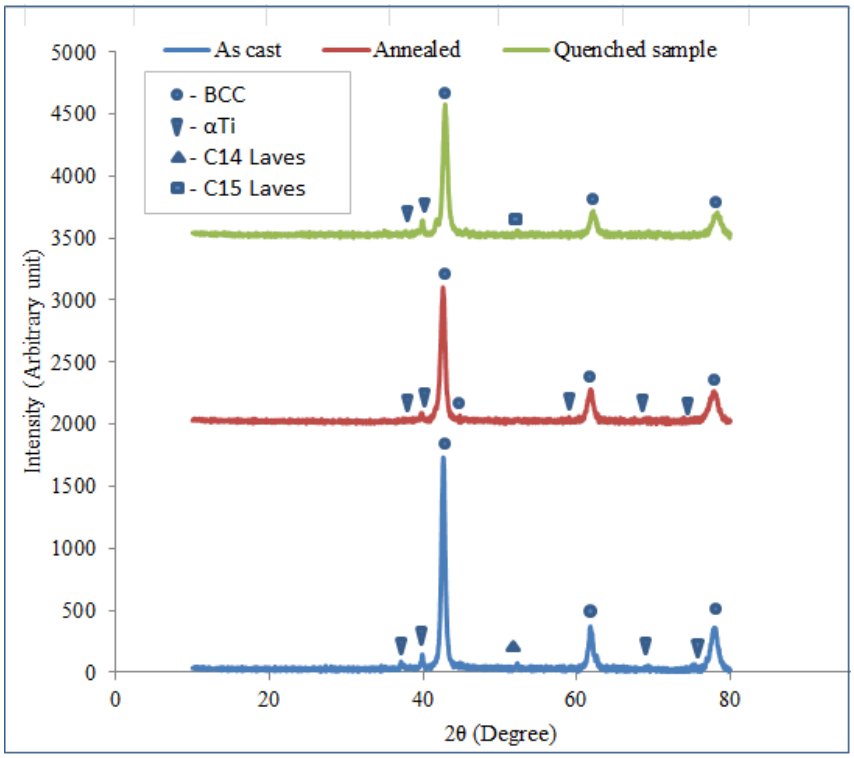

Figure 4.6. XRD patterns of as-cast and heat treated alloy A3.

4.2.4. Microstructures, and phase analysis of alloy A4

The optical and SEM micrographs of as-cast, annealed and quenched alloy A4 are shown in Figure 4.7, the XRD results are in Figure 4.8 and the EDX composition and XRD measured crystallographic parameters are listed in Table 4.5.

The microstructure of the alloy A4 samples (Figure 4.7) was a primary, light grey, bcc (V) matrix and dark grey intergranular phases. There is evidence of twinning in many of the dark intergranular phase particles. EDX analysis could not be done on the Laves phases in the as-cast and quenched samples, as the phases were too small.

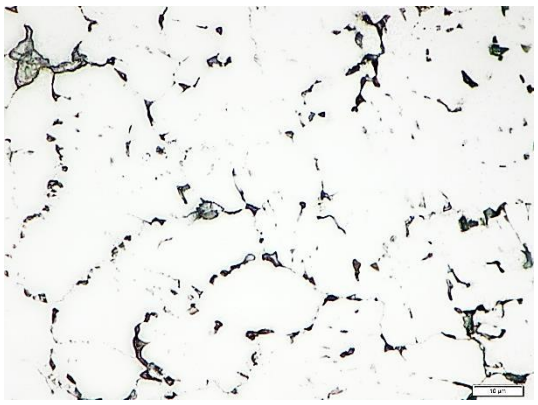

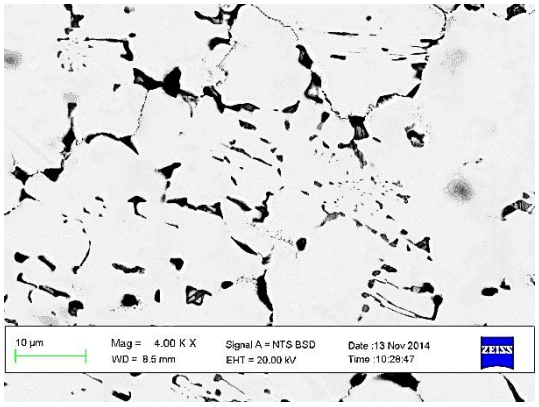

a) Optical micrograph b) SEM BSE micrograph

As-cast A4

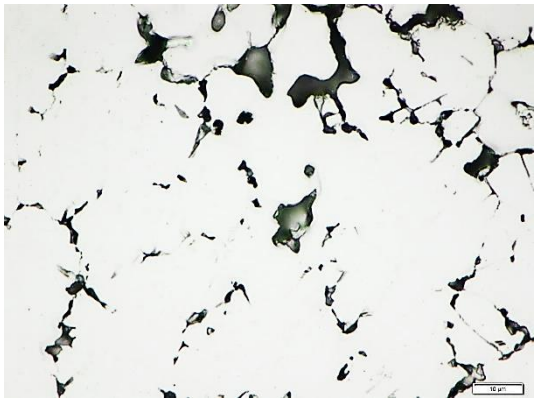

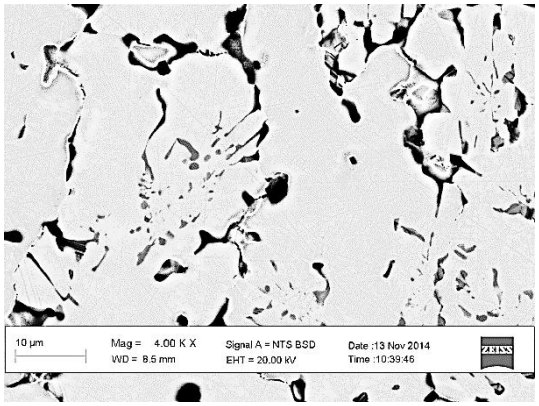

c) Optical micrograph d) SEM BSE micrograph

Annealed A4A

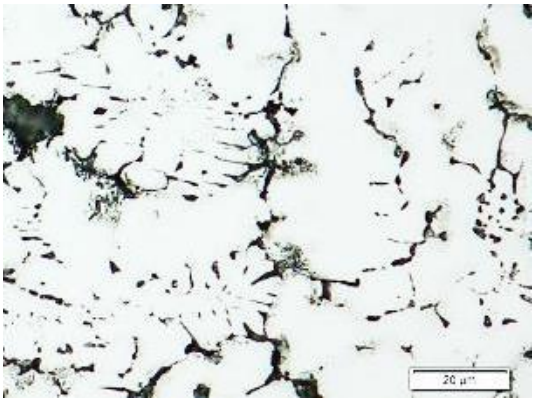

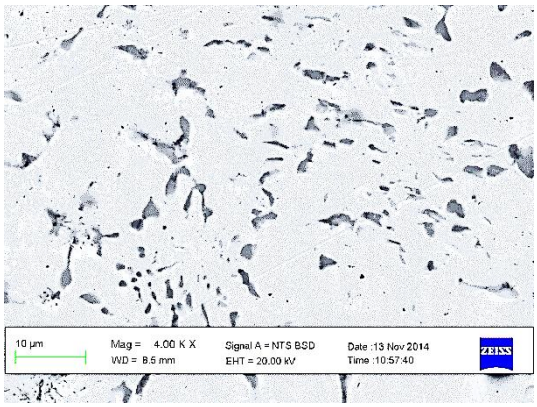

e) Optical micrograph f) SEM BSE micrograph

Quenched A4B

Figure 4.7. Microstructures of as-cast and heat treated alloy A4.

Table 4.5. EDX compositions and crystallographic parameters of phases in alloy A4.

Sample	Phase (tag in BSE micrograph)	Composition (at.%)*					Phase proportion (% area)		Crystallographic description				
		Ti	V	Cr	Fe	Ti/Cr ratio	SEM BSE	Optical	Phases XRD	Space group (no.)	a (*Å*)	c (*Å*)	Cell vol. ($Å^3$)
As-cast	Primary light grey (C)	15.5 (2.2)	44.0 (2.5)	35.5 (0.4)	5.0 (4.9)	0.40	85.5	88.0	BCC (V)	$Im\bar{3}m$ (229)	3.0000	-	27.00
	Black (D) intergranular	79.5 (5.4)	11.0 (2.7)	8.5 (2.5)	1.0 (0.2)	9.40	14.5	12.0	α-Ti	$P6_3/mmc$ (194)	2.98	4.73	36.24
									C14 Laves	$P6_3/mmc$ (194)	4.93	7.96	167.81
Annealed	Primary light grey (C)	15.5 (1.2)	44.1 (1.8)	35.5 (2.6)	4.9 (3.0)	0.44	73.5	73.2	BCC (V)	$Im\bar{3}m$ (229)	2.9981	-	26.95
	Black (D) intergranular	62.5 (3.8)	19.6 (2.5)	15.7 (1.5)	2.2 (0.3)	4.00	26.5	26.8	ω-Ti	$P6/mmm$ (191)	4.55	2.78	49.91
Quenched	Primary light grey (C)	17.5 (0.7)	42.3 (2.5)	34.6 (1.8)	5.6 (2.3)	0.57	76.4	64.5	BCC (V)	$Im\bar{3}m$ (229)	2.9892	-	26.71
	Black inter-granular (D)	66.5 (4.1)	17.2 (2.0)	14.3 (2.2)	2.0 (0.4)	4.70	23.6	35.5	ω-Ti	$P6/mmm$ (191)	4.6	2.82	51.68
									C36 Laves	$P6_3/mmc$ (194)	4.91	16.00	334.50

*Standard deviation in parentheses.

The primary phase proportion decreased from 85.5 to 73.5% after annealing and slightly increased to 76.4% after quenching, while the cell volume decreased from 27.00 to 26.95 $Å^3$ after annealing and 26.71 $Å^3$ after quenching. The cell volume of (αTi) increased from 36.24 $Å^3$ in the as-cast sample to 49.91 $Å^3$ after annealing and 51.68 $Å^3$ after quenching.

The primary phase showed a marginal increase in Ti/Cr ratio from 0.40 to 0.44 after annealing and 0.57 after quenching. Heat treatment reduced the Ti/Cr ratio in the α-Ti phase from 9.40 to 4.00 after annealing and 4.70 after quenching.

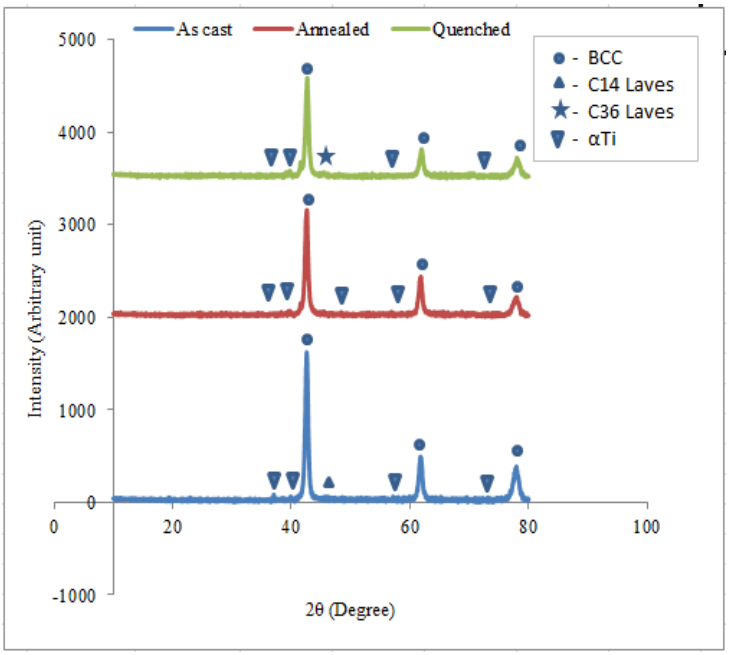

Figure 4.8. XRD patterns of as-cast and heat treated alloy A4.

4.2.5. Microstructures and phase analysis of alloy A5 ($Ti_{24.975}$:V_{40}:$Cr_{34.975}$:$Rh_{0.05}$)

The optical and SEM micrographs of as-cast, annealed and quenched alloy A5 are shown in Figure 4.9, the XRD results are in Figure 4.10 while the EDX composition and XRD measured crystallographic parameters are listed in Table 4.6.

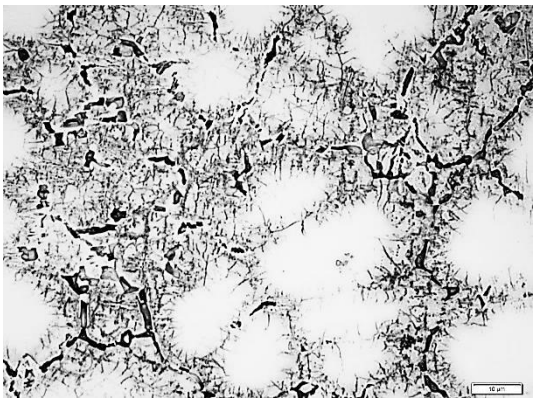

a) Optical micrograph

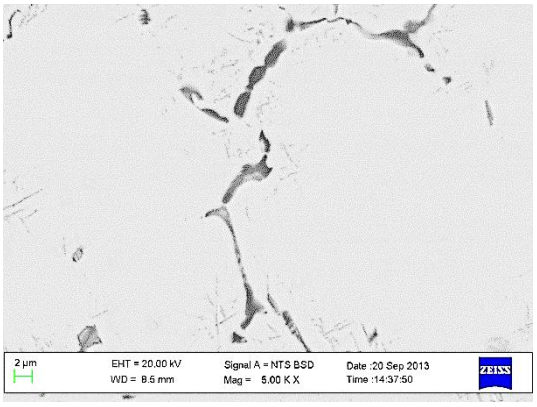

b) SEM BSE micrograph

As-cast A5

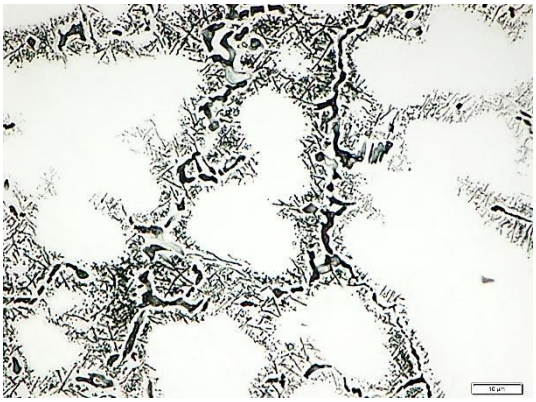

c) Optical micrograph

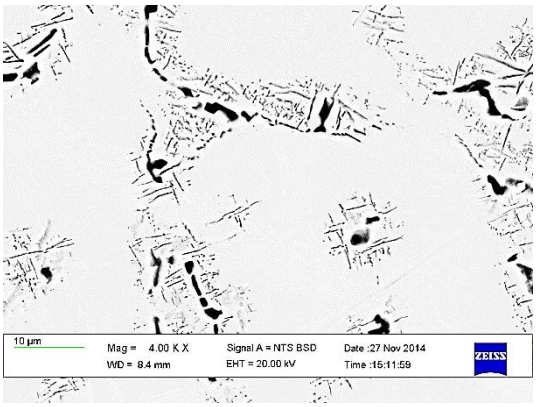

d) SEM BSE micrograph

Annealed A5A

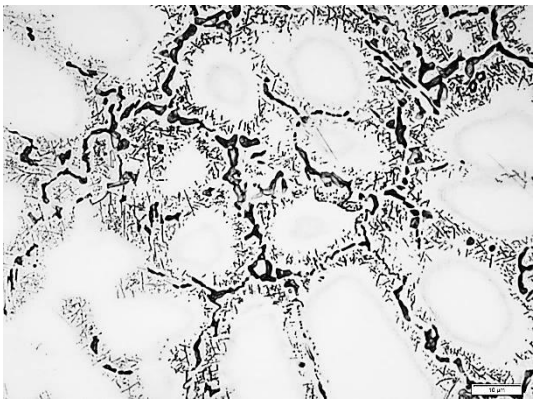

e) Optical micrograph

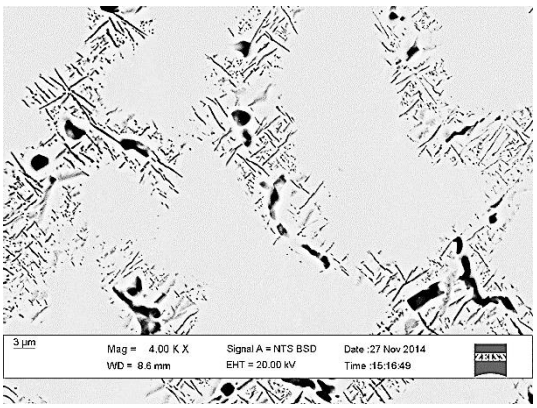

f) SEM BSE micrograph

Quenched A5B

Figure 4.9. Microstructures of alloy A5.

The microstructure of A5 is a primary, light grey, bcc (V) with intergranular Laves phases. In the quenched sample, the Ti content in the primary phase decreased slightly to 24.1 at.%, while V and Cr increased to 41.6 and 34.3 at.% respectively.

Heat treatment had no effect on the amount of primary phase (from 82.2 to 81.8% in the annealed sample and 82% in quenched sample).

Annealing increased the cell volume of the bcc (V) phase from 27.37 to 28.09 $Å^3$ and of the secondary phases from 36.25 in the as-cast sample to 167.81 $Å^3$. Quenching increased the Laves cell volume to 49.99 $Å^3$ but had no effect on the bcc (V) cell volume.

Annealing decreased the Ti/Cr ratio from 0.9 to 0.8 in the bcc (V) phase, while quenching decreased it to 0.7. There was an observed decrease in the Ti/Cr ratio for the secondary phase after heat treatment, from 5.3 after casting to 4.4 after annealing and 4.0 after quenching. An acicular (αTi) phase was found near the bcc (V) grain boundaries.

Table 4.6. EDX compositions and crystallographic parameters of phases in alloy A5.

Sample	Phase (tag in BSE micrograph)	Composition (at.%)*					Phase proportion (% area)		Crystallographic description				
		Ti	V	Cr	Rh	Ti/Cr ratio	SEM BSE	Optical	Phases XRD	Space group (no.)	a (*Å*)	c (*Å*)	Cell vol. ($Å^3$)
As-cast	Primary light grey (C)	28.5 (3.8)	38.8 (2.2)	32.7 (1.7)	-	0.9	82.2	24.3	BCC (V)	$Im\bar{3}m$ (229)	3.0257	-	27.70
	Black inter-granular (D)	71.8 (5.8)	14.6 (3.0)	13.5 (2.8)	0.5 (0.4)	5.3	17.8	75.7	α-Ti	$P6_3/mmc$ (194)	2.98	4.73	36.25
Annealed	Primary light grey (C)	26.5 (1.9)	40.0 (2.0)	33.5 (3.8)	-	0.8	81.8	54.5	BCC (V)	$Im\bar{3}m$ (229)	3.0398	-	28.09
	Black inter-granular (D)	68.0 (4.4)	16.5 (2.7)	15.4 (2.7)	-	4.4	18.2	45.5	C14 (Laves)	$P6_3/mmc$ (194)	4.93	7.96	167.81
Quenched	Primary light grey (C)	24.1 (1.1)	41.6 (1.4)	34.3 (2.0)	-	0.7	82.0	64.0	BCC (V)	$Im\bar{3}m$ (229)	3.0136	-	27.37
	Black inter-granular (D)	66.6 (4.1)	16.6 (2.4)	16.8 (1.7)	-	4.0	18.0	36.0	ω-Ti	$P6/mmm$ (191)	4.55	2.78	49.99

*Standard deviation in parentheses

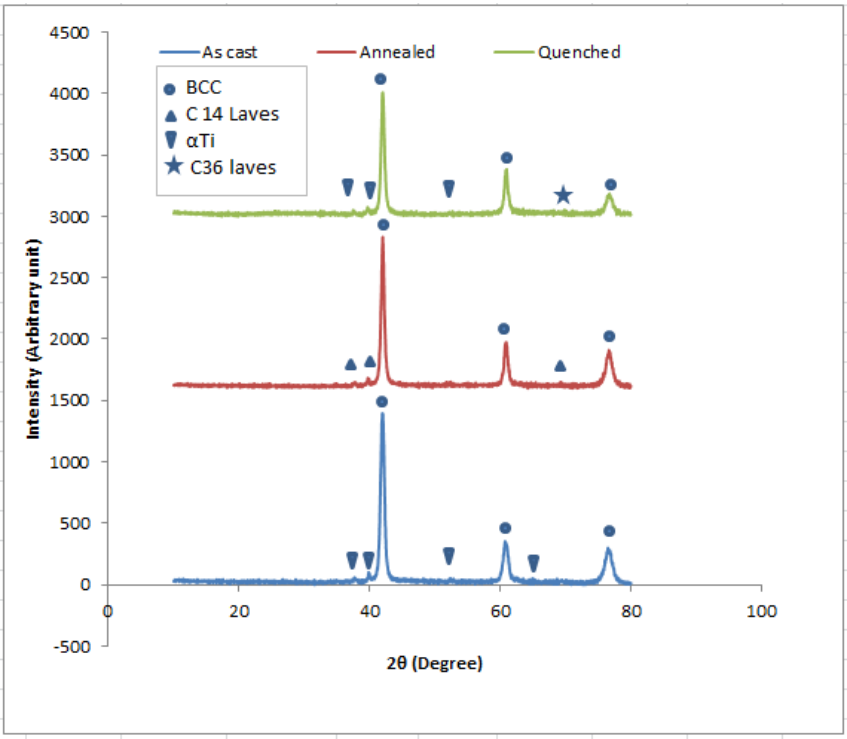

Figure 4.10. XRD patterns of as-cast and heat treated alloy A5.

4.2.6. Microstructures and phase analysis of alloy A6 ($Ti_{24.95}$:V_{40}:$Cr_{34.95}$:$Rh_{0.1}$)

The optical and SEM micrographs of as-cast, annealed and quenched alloy A6 are shown in Figure 4.11, the XRD results in Figure 4.12 and the EDX composition and XRD measured crystallographic parameters are presented in Table 4.7.

The microstructure of A6 (Figure 4.11) was a primary, light grey, bcc (V) and black intergranular secondary phase(s). Table 4.7 shows the composition of the phases. There was no significant change in the phase proportions of both bcc and secondary phases after either heat treatment.

The cell volume of bcc (V) was unchanged after heat treatment. The secondary phase volume increased from 34.48 to 167.8 $Å^3$ after annealing and to ~50 $Å^3$ after quenching.

Table 4.7. EDX compositions and crystallographic parameters of phases in alloy A6.

Sample	Phase (tag in BSE micrograph)	Composition (at.%)*					Phase proportion (% area)		Crystallographic description				
		Ti	V	Cr	Rh	Ti/Cr ratio	SEM BSE	Optical	Phases XRD	Space group (no.)	a (*Å*)	c (*Å*)	Cell vol. ($Å^3$)
As-cast	Primary light grey (C)	28.5 (3.8)	38.8 (2.2)	32.7 (1.7)	-	0.9	84.8	78.7	BCC (V)	$Im\bar{3}m$ (229)	3.0275	-	27.75
	Black inter-granular (D)	62.3 (6.3)	19.1 (3.4)	18.6 (3.2)	0.5 (0.4)	3.3	15.2	21.3	α-Ti	$P6_3/mmc$ (194)	2.92	4.67	34.48
Annealed	Primary light grey (C)	26.5 (1.9)	40.0 (2.0)	33.5 (3.8)	-	0.8	82.5	76.0	BCC (V)	$Im\bar{3}m$ (229)	3.0398	-	28.09
	Black inter-granular (D)	57.3 (2.3)	22.9 (0.7)	19.8 (1.8)	-	2.9	17.5	24.0	C14 Laves	$P6_3/mmc$ (194)	4.93	7.96	167.81
Quenched	Primary light grey (C)	24.1 (1.1)	41.6 (1.4)	34.3 (2.0)	-	0.7	83.0	77.0	BCC (V)	$Im\bar{3}m$ (229)	3.0275	-	27.75
	Black inter-granular (D)	58.5 (7.0)	22.3 (3.9)	19.2 (3.2)	-	3.0	17.0	23.0	ω-Ti	$P6/mmm$ (191)	4.55	2.78	49.99
	-	-	-	-	-	-	-	-	C36 Laves	$P6_3/mmc$ (194)	4.91	16.00	334.50

* Standard deviation in parentheses

The vanadium content in the bcc phase was 38.8 at.% (as-cast), and increased slightly after annealing and quenching. Quenching had no effect on the cell volume of bcc (V) and the abundance of the phase was not significantly affected. The SEM and optical images of alloy A6 (Figure 4.11) show a predominantly bcc (V) phase. Table 4.7 shows that the area proportion of bcc (V) was 82-85%.

Table 4.7 shows that after heat treatment, the Ti/Cr ratio in both the primary phase and secondary phases decreased. In the primary phase, a marginal decrease from 0.9 to 0.8 was observed in annealed sample and 0.7 in quenched sample. The Ti/Cr ratio in the secondary phase decreased from 3.3 to 2.9 after annealing and to 3.0 after quenching. This could imply formation of a small, Ti-rich phase that was not observed by SEM. The SEM-BSE micrographs show the formation of acicular precipitates near the boundary of bcc/secondary phases after heat treatment.

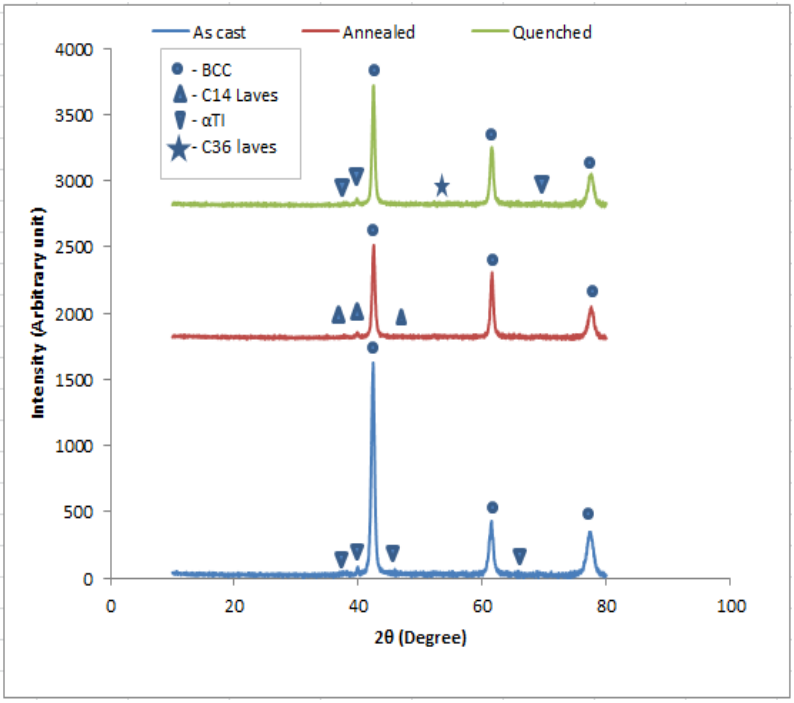

Figure 4.11. XRD patterns of alloy A6.

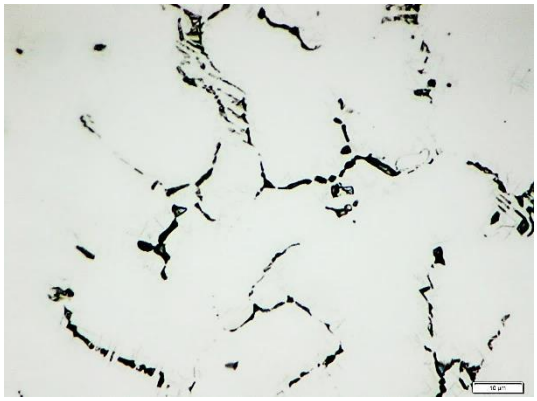

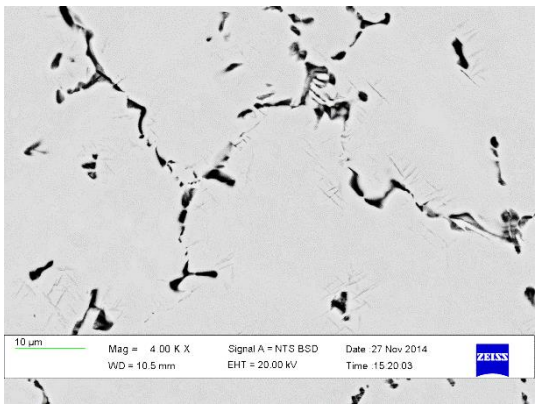

a) Optical micrograph b) SEM BSE micrograph

As-cast A6

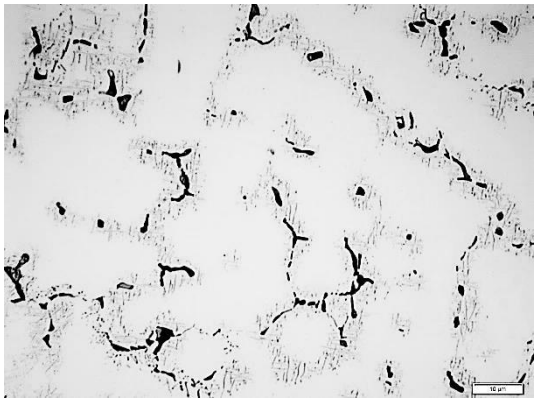

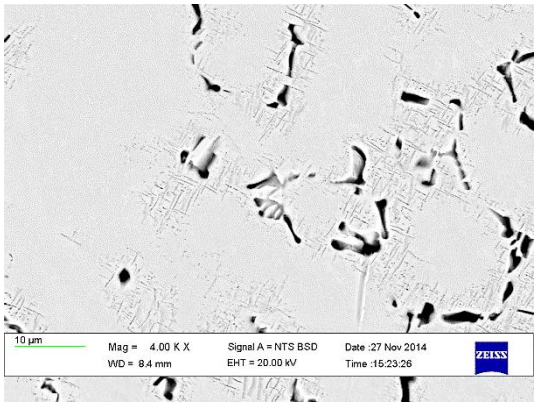

c) Optical micrograph d) SEM BSE micrograph

Annealed A6A

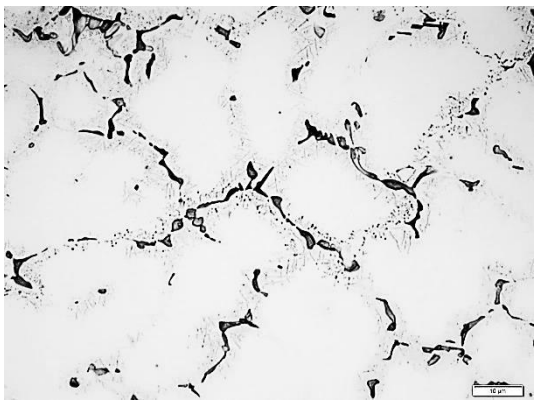

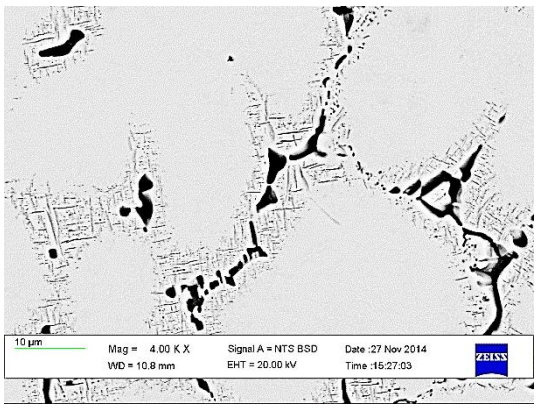

e) Optical micrograph f) SEM BSE micrograph

Quenched A6B

Figure 4.12. Microstructures of alloy A6.

4.2.7. Microstructures and phase analysis of alloy A7 ($Ti_{24.98}$:V_{40}:$Cr_{34.97}$:$Pd_{0.05}$)

Optical and SEM micrographs of as-cast, annealed and quenched alloy A7 are shown in Figure 4.13, the XRD results are in Figure 4.14 and the EDX composition and XRD measured crystallographic parameters are listed in Table 4.8.

The microstructure of alloy A7 was a primary, light grey, bcc (V) phase with minor, dark intergranular phases. Heat treatment increased the proportion of secondary phase from 17.5 to ~20% in the optical micrographs but for SEM BSE micrograph the proportion increased from 11.5 to 14.0 area % after quenching and decreased slightly to 10.5% after annealing.

Annealing decreased the cell volume of the Laves phase from 59.68 to 49.99 $Å^3$ but had no effect on the bcc phase. Quenching increased the bcc cell volume from 27.75 to 28.09 $Å^3$ but decreased the volume of the secondary phases from 59.68 to 52.09 $Å^3$.

The area proportion of the bcc (V) phase was found to be 86-90%, while the black intergranular secondary phase occupied the remaining 10-14 area % (Table 4.8).

The Ti/Cr ratio in the dark phase increased from 2.1 to 4.0 after both treatments. Annealing had no effect on the Ti/Cr ratio in primary bcc (V) phase, while quenching marginally increased it from 0.5 to 0.6. Precipitation of the secondary phase at the bcc (V) grain boundaries increased after heat treatment.

Table 4.8. EDX compositions and crystallographic parameters of phases in alloy A7.

Sample	Phase (tag in BSE micrograph)	Composition (at.%)*					Phase proportion (% area)		Crystallographic description				
		Ti	V	Cr	Pd	Ti/Cr ratio	SEM BSE	Optical	Phases XRD	Space group (no.)	a (*Å*)	c (*Å*)	Cell vol.($Å^3$)
As-cast	Primary light grey (C)	18.6 (1.4)	44.8 (2.2)	36.6 (1.3)	-	0.5	88.5	82.5	BCC (V)	$Im\bar{3}m$ (229)	3.0275	-	27.75
	Black (D) intergranular	50.5 (4.8)	25.7 (2.4)	23.8 (2.5)	0.4 (0.1)	2.1	11.5	17.5	C15 (Laves)	$Fd\bar{3}m$ (225)	3.91	-	59.68
Annealed	Primary light grey (C)	18.1 (1.9)	45.7 (4.1)	36.2 (2.7)	-	0.5	89.5	80.2	BCC (V)	$Im\bar{3}m$ (229)	3.0275	-	27.75
	Black (D) intergranular	66.0 (4.9)	17.6 (3.2)	16.4 (1.8)	-	4.0	10.5	19.8	ω-Ti	$P6/mmm$ (191)	4.55	2.79	49.99
Quenched	Primary light grey (C)	21.6 (0.8)	42.6 (1.0)	35.8 (1.4)	-	0.6	86.0	81.2	BCC (V)	$Im\bar{3}m$ (229)	3.0398	-	28.09
	Black (D) intergranular	65.3 (1.7)	18.3 (0.8)	16.4 (1.0)	0.4 (0.0)	4.0	14.0	19.8	ω-Ti	$P6_3/mmm$ (191)	4.61	2.83	52.09

* Standard deviation in parentheses

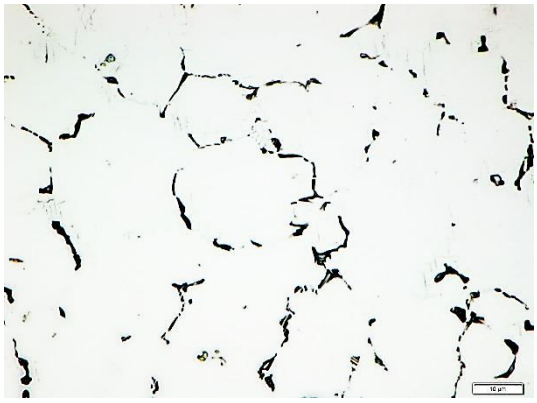

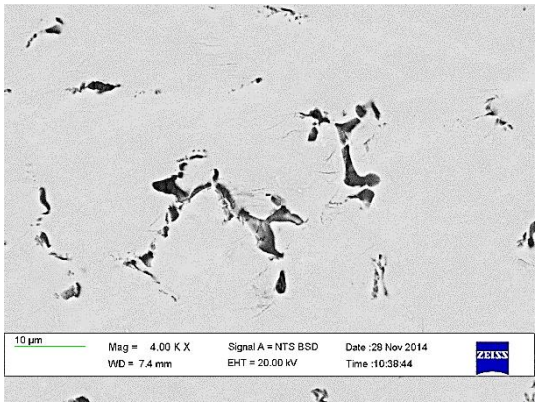

a) Optical micrograph b) SEM BSE micrograph

As-cast A7

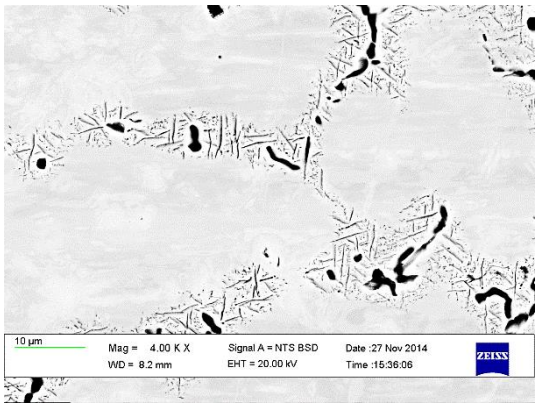

c) Optical micrograph d) SEM BSE micrograph

Annealed A7A

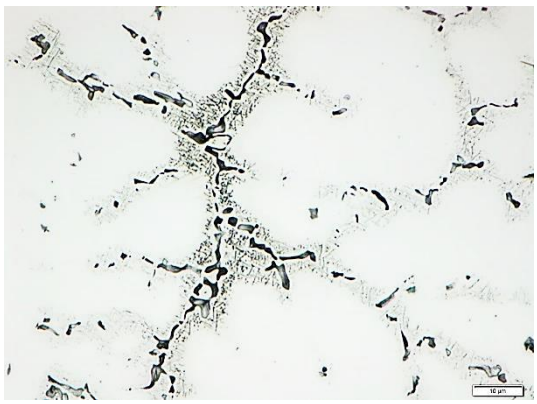

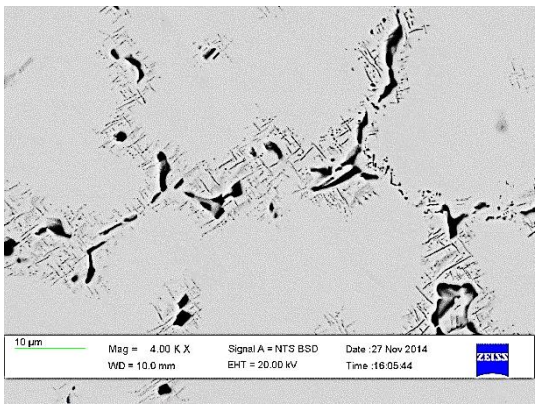

e) Optical micrograph f) SEM BSE micrograph

Quenched A7B

Figure 4.13. Microstructure of alloy A7.

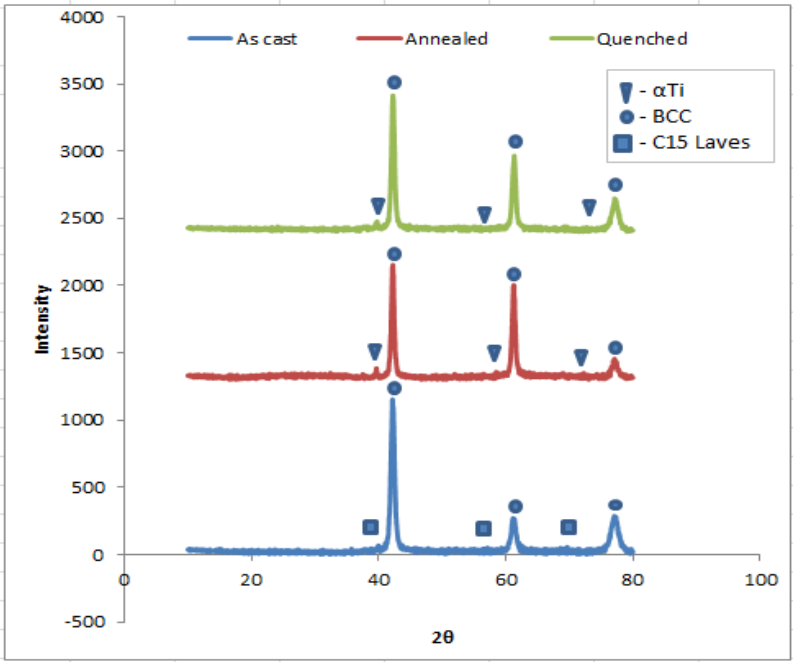

Figure 4.14. XRD patterns in alloy A7.

4.2.8. Microstructures and phase analysis of alloy A8 ($Ti_{25}:V_{40}:Cr_{34.9}:Pd_{0.1}$)

The optical and SEM micrographs of as-cast, annealed and quenched alloy A8 are shown in Figure 4.15, the XRD results are in Figure 4.16 and the EDX composition and XRD measured crystallographic parameters are listed in Table 4.9.

The microstructure of Alloy A8 was a primary, light grey, bcc (V) phase and intergranular secondary phases. The bcc (V) phase in the as-cast sample contained 19 at.% Ti, 44 at.% V and 37 at.% Cr. The annealed and quenched samples had similar compositions.

Table 4.9. EDX compositions and crystallographic parameters of phases in alloy A8.

Sample	Phase (tag in BSE micrograph)	Composition (at.%)*					Phase proportion (% area)		Crystallographic description				
		Ti	V	Cr	Pd	Ti/Cr ratio	SEM BSE	Optical	Phases XRD	Space group (no.)	a (*Å*)	c (*Å*)	Cell vol. ($Å^3$)
As-cast	Primary light grey (C)	19.1 (0.8)	43.6 (3.6)	37.3 (4.6)	-	0.5	91.4	88.5	BCC (V)	$Im\bar{3}m$ (229)	3.0275	-	27.75
	Black (D) intergranular	63.7 (1.4)	18.5 (1.1)	17.8 (0.6)	-	3.6	8.6	11.5	α-Ti	$P6_3/mmc$ (194)	2.95	4.69	40.72
Annealed	Primary light grey (C)	22.2 (1.1)	40.8 (1.4)	37.0 (2.2)	-	0.6	90.0	83.8	BCC (V)	$Im\bar{3}m$ (229)	3.0275	-	27.75
	Black (D) intergranular	70.2 (4.5)	14.8 (2.2)	15.0 (2.3)	-	4.7	10.0	6.2	α-Ti	$P6_3/mmc$ (194)	2.95	4.67	35.22
Quenched	Primary light grey (C)	22.2 (2.7)	40.3 (2.5)	37.5 (3.5)	-	0.6	94.9	92.6	BCC (V)	$Im\bar{3}m$ (229)	3.0275	-	27.75
	Black (D) intergranular	63.4 (4.4)	18.8 (2.8)	17.9 (1.7)	-	3.5	5.1	7.4	C14 (Laves)	$P6_3/mmc$ (194)	3.30	11.80	128.50

* Standard deviation in parentheses

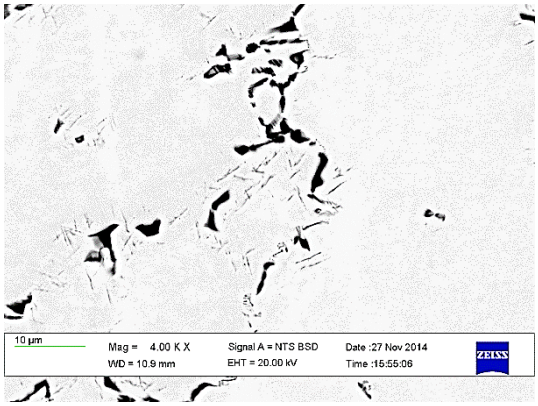

a) Optical micrograph b) SEM BSE micrograph

As-cast A8

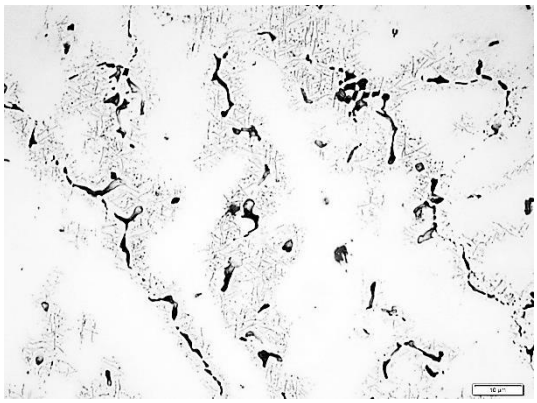

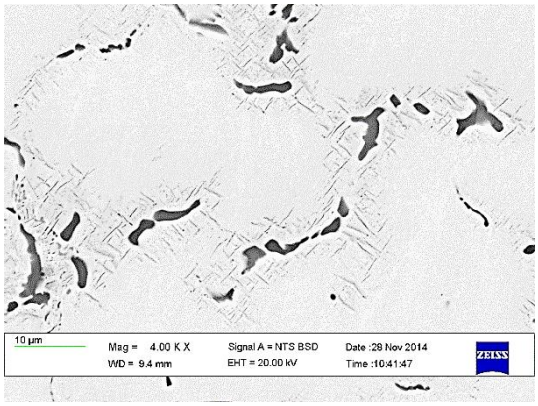

c) Optical micrograph d) SEM BSE micrograph

Annealed A8A

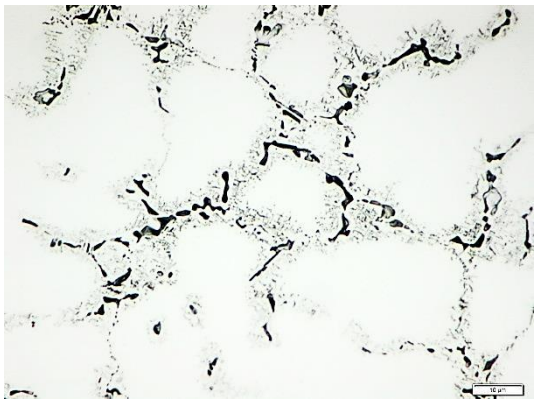

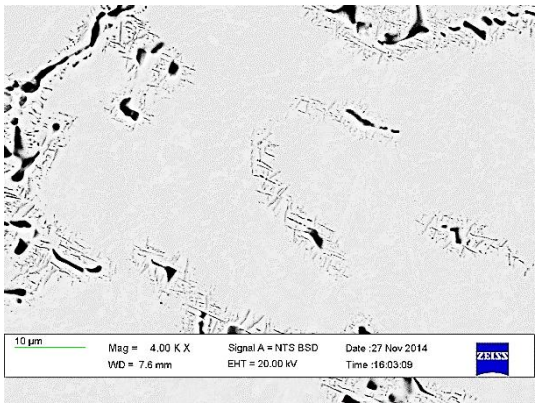

e) Optical micrograph f) SEM BSE micrograph

Quenched A8B

Figure 4.15. Microstructures of alloy A8.

Annealing reduced the vanadium content in both phases. Quenching had no significant effect on the V content in the second phase, but slightly decreased it from 43.6 to 40.3 at.% in the BCC phase. The abundance of the bcc (V) phase increased by 3.5 at.% after quenching, but the volume was not affected by heat treatment. However, the secondary phase unit cell volume decreased by 5.5 $Å^3$ after annealing (αTi) and increased by 87.78 $Å^3$ after quenching (C14 Laves).

Table 4.9 shows that the proportion of the bcc phase was 90-95%. The Ti/Cr ratio in the primary phase was the same (0.6) for both quenched and annealed samples, but 0.5 in the as-cast alloy. Quenching had no significant effect on the Ti/Cr ratio in the secondary phase, while annealing increased it from 3.6 to 4.7. After heat treatment, the acicular secondary phase formed fine precipitates around the grain boundaries.

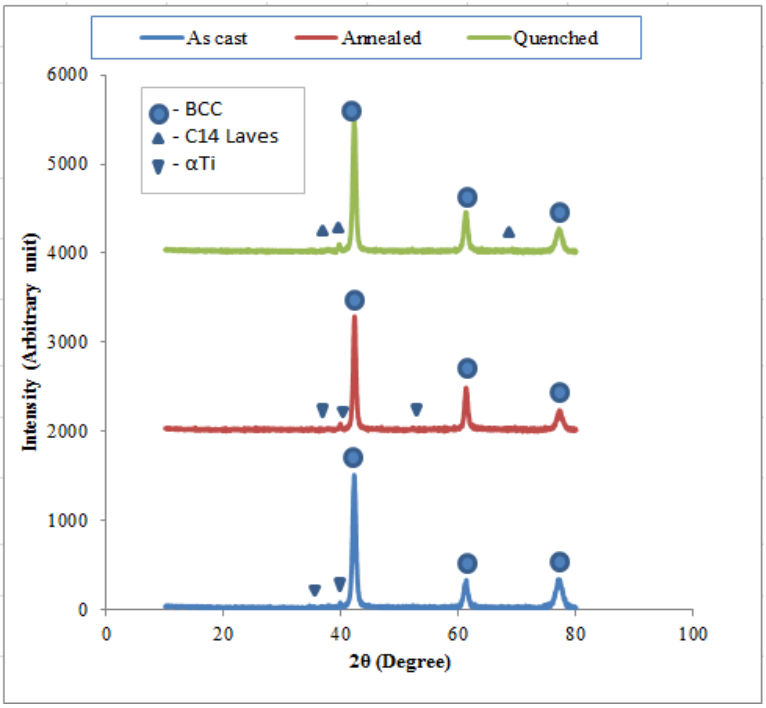

Figure 4.16. XRD patterns of alloy A8.

4.3. Hardness of alloys A1 to A8

The Vickers hardness (HV_2) values of the as-cast, annealed and quenched alloys are shown as follows:

- Base alloy A1 and the iron containing alloys (A2-A4) in Figure 4.17
- Rhodium containing alloys (A5 and A6) in Figure 4.18
- Palladium containing alloys (A7 and A8) in Figure 4.19

In the base alloy A1, heat treatment slightly reduced the hardness from 415 HV_2 (as-cast) to 408 HV_2 after annealing and to 405 HV_2 after quenching, as shown in Figure 4.17 a. In the alloys with iron added, annealing increased the hardness slightly, while quenching caused a larger increase in hardness.

In alloy A2 (2 at.% Fe), heat treatment increased the hardness (Figure 4.17 b). The quenched sample had the highest hardness of 440 HV2, while the as-cast and annealed samples had hardness values of 430 and 436 HV_2 respectively. With the addition of 5 at.% Fe (alloy A3), the as-cast and annealed hardnesses were the same at ~421 HV_2. However, there was a noticeable increase to 460HV_2 after quenching, as shown in Figure 4.17 (c)

The hardness of the as-cast alloy containing 6 at.% Fe increased from 425 to 438 HV_2 after annealing and to 446 HV_2 after quenching (Figure 4.17 d).

Among the samples of the iron-containing alloys ($Ti_{25-0.5x}V_{40}Cr_{35-0.5x}Fe_x$, x = 0, 2, 5, 6 at.%), the quenched base alloy had the lowest hardness and the 5 at.% Fe quenched sample had the highest hardness.

Heat treatment marginally increased the hardness of samples containing 0.05 at.% Rh from 409 to 414 HV_2 after annealing and to 413 HV_2 after quenching (Figure 4.18 a). However, with an addition of 0.10 at.% Rh (Figure 4.18 b), heat treatment decreased the hardness from 410 to 388 HV_2 after annealing and to 395 HV_2 after quenching. The heat treated 0.05 at.% Rh samples had the highest hardness ~414 HV_2, while the annealed 0.10 at.% Rh sample had the lowest hardness of the rhodium containing alloys.

For the 0.05 at.% Pd alloy (Figure 4.19 a), the hardness decreased slightly from 410 to 402 HV_2 after annealing and to 406 HV_2 after quenching. In the 0.10 at.% Pd alloy, the hardness was reduced from 425 to 392 HV_2 after annealing and to 405 HV_2 after quenching. The as-cast 0.10 at.% Pd sample had the highest hardness and the annealed 0.10 at.% Pd sample had the lowest hardness of the palladium containing alloys (Figure 4.19 b).

Overall, the quenched 5 at.% Fe sample had the highest hardness of 460 HV_2, while the annealed 0.10 at.% Rh sample had the lowest hardness of 392 HV_2.

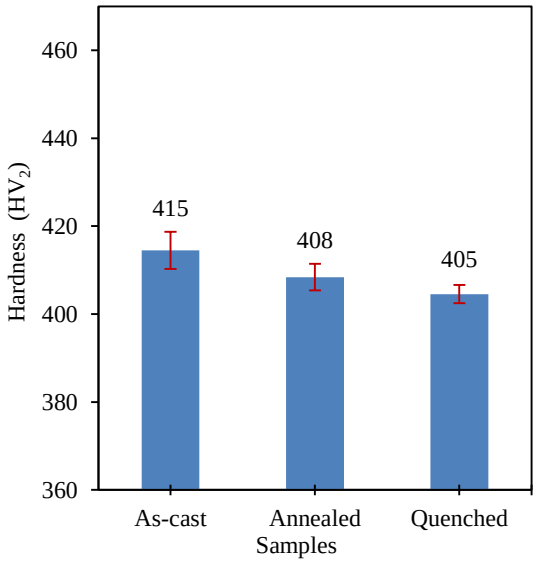

a) A1 (0 at.% Fe)

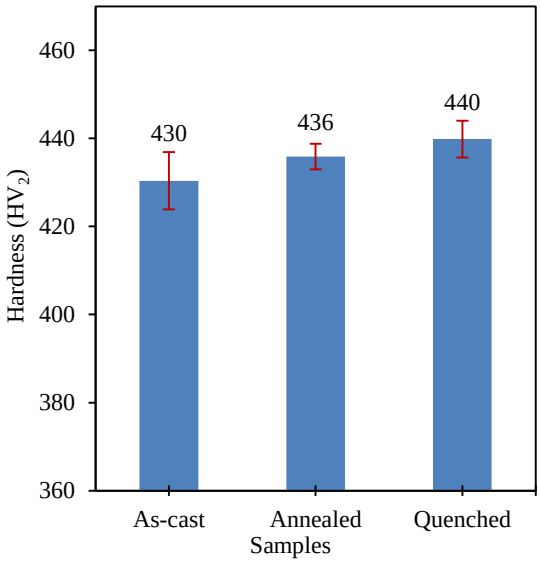

b) A2 (2 at.% Fe)

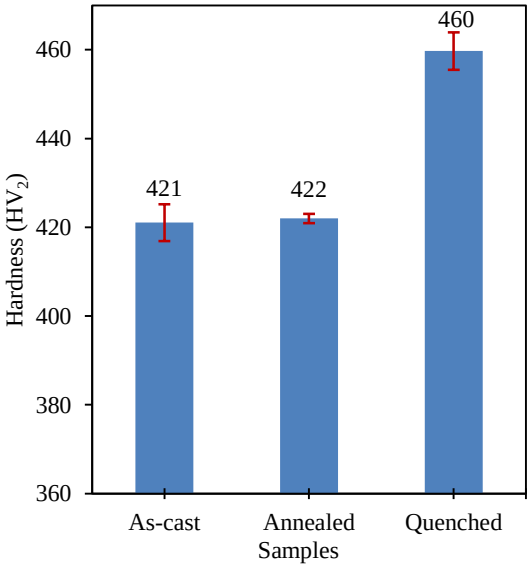

c) A3 (5 at.% Fe)

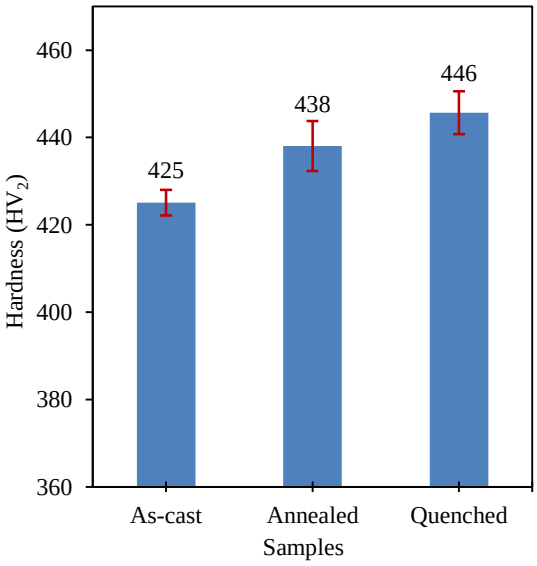

d) A4 (6 at.% Fe)

Figure 4.17 Hardness (HV_2) of as-cast and heat treated $Ti_{25-0.5x}V_{40}Cr_{35-0.5x}Fe_x$ (x = 0, 2, 5, 6 at.%) alloy.

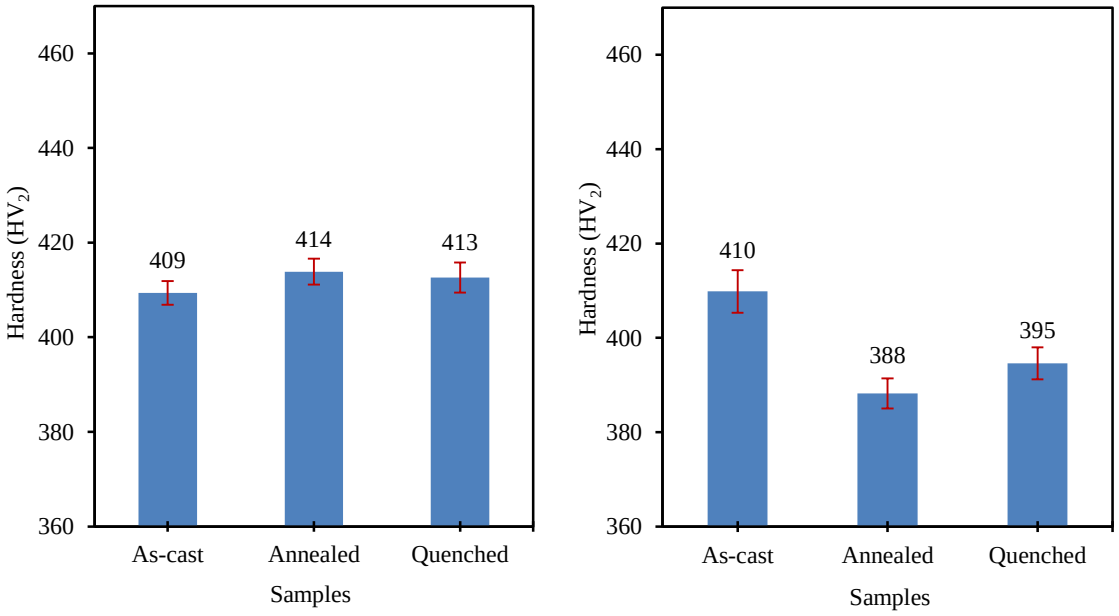

a) A5, 0.05 at.% Rh b) A6, 0.10 at.% Rh

Figure 4.18 Hardness (HV_2) of as-cast and heat treated $Ti_{25-0.5x}V_{40}Cr_{35-0.5x}Rh_x$ (x = 0.05, 0.10 at.%) alloy.

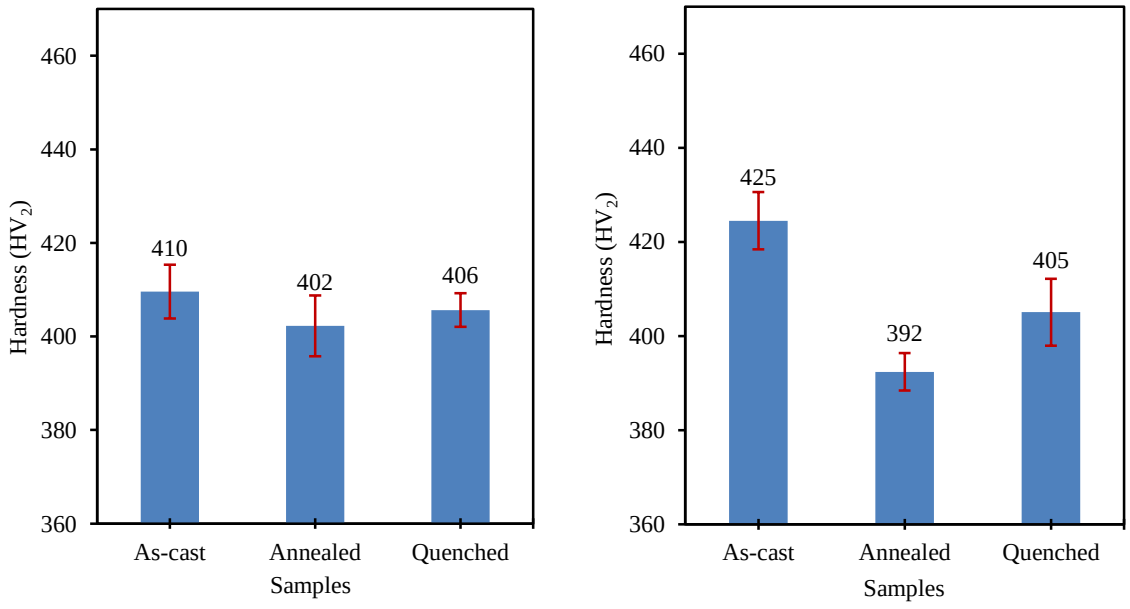

a) A5, 0.05 at.% Pd b) A6, 0.10 at.% Pd

Figure 4.19. Hardness (HV_2) of as-cast and heat treated $Ti_{25-0.5x}V_{40}Cr_{35-0.5x}Pd_x$ (x = 0.05, 0.10 at.%) alloy.

4.4. Corrosion behaviour of as-cast and heat treated alloys in KOH solution

4.4.1. Potentiodynamic behaviour in 6M KOH solution

The potentiodynamic behaviour of the iron-containing as-cast, annealed and quenched samples in a solution of 6M KOH are presented in Figure 4.20. The curves of the rhodium containing alloys are shown in Figure 4.21, while those of the palladium containing alloys are shown in Figure 4.22.

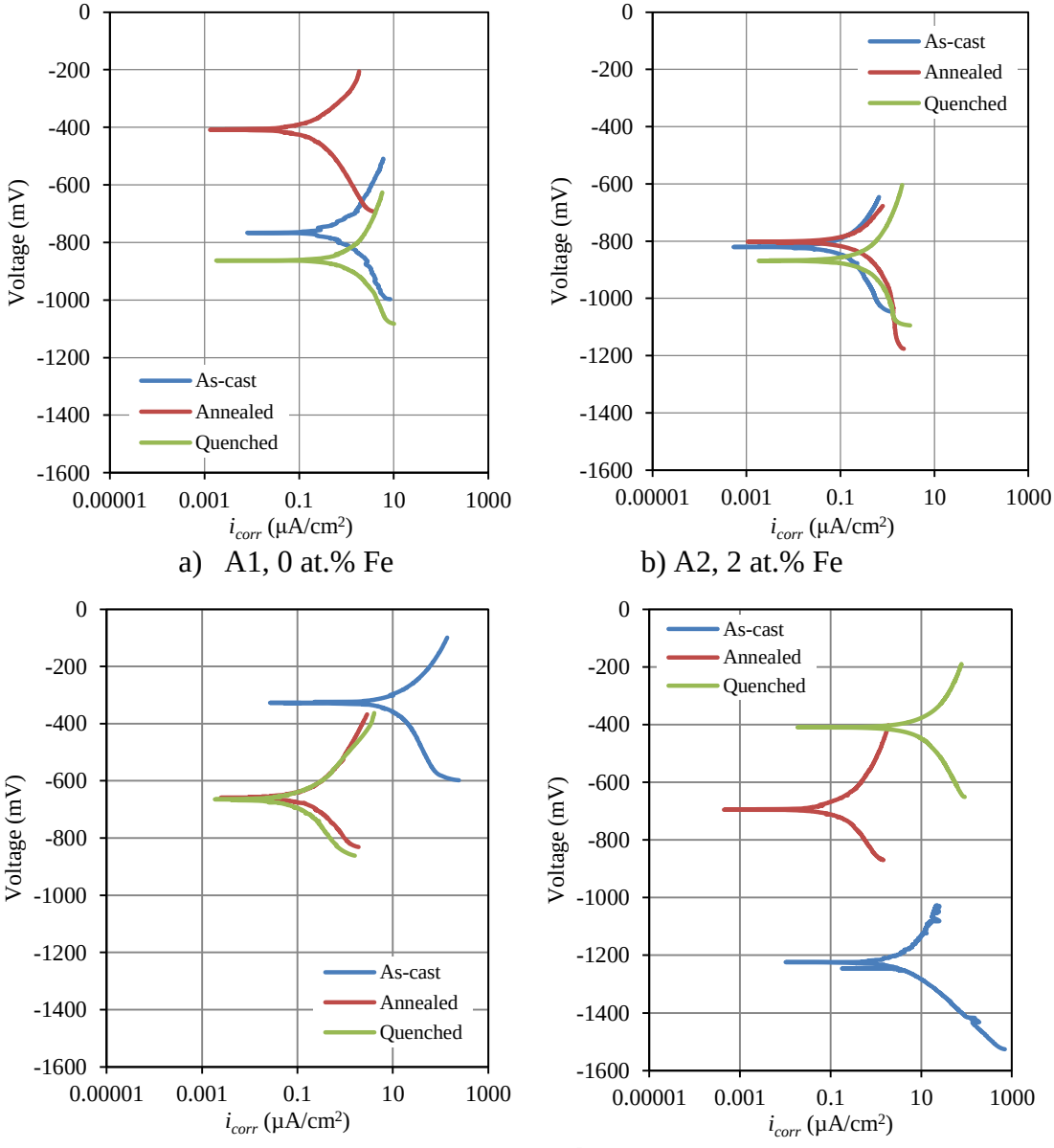

a) A1, 0 at.% Fe b) A2, 2 at.% Fe

c) A3, 5 at.% Fe d) A4, 6 at.% Fe

Figure 4.20. Potentiodynamic curves of as-cast and heat treated $Ti_{25-0.5x}V_{40}Cr_{35-0.5x}Fe_x$ (x = 0, 2, 5, 6 at.%) alloy.

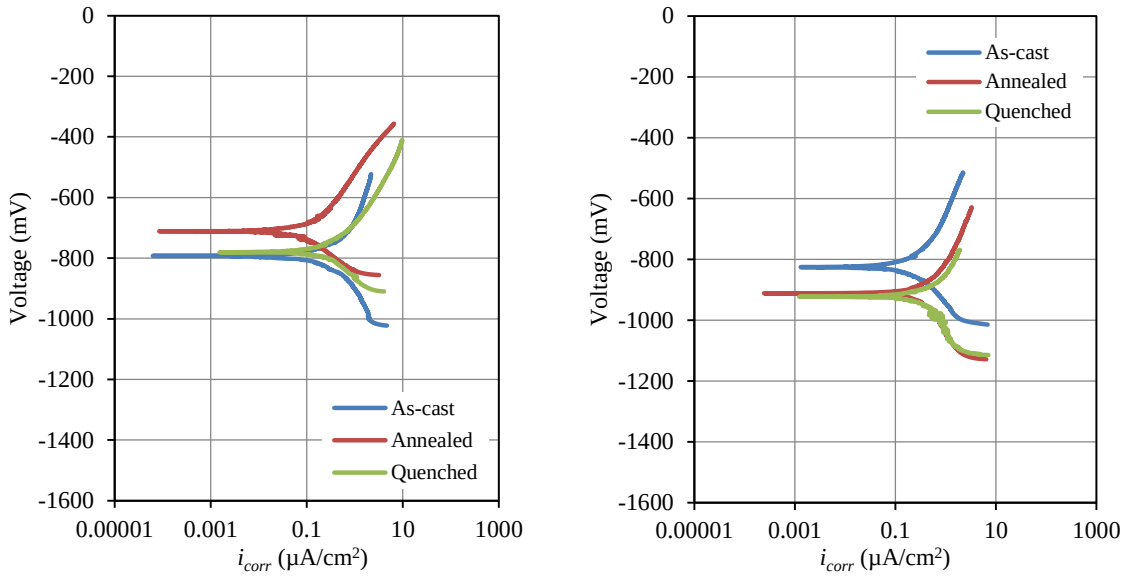

a) A5, 0.05 at.% Rh b) A6, 0.10 at.% Rh

Figure 4.21. Potentiodynamic curves of as-cast and heat treated $Ti_{25-0.5x}V_{40}Cr_{35-0.5x}Rh_x$ (x = 0.05, 0.10 at.%) alloys.

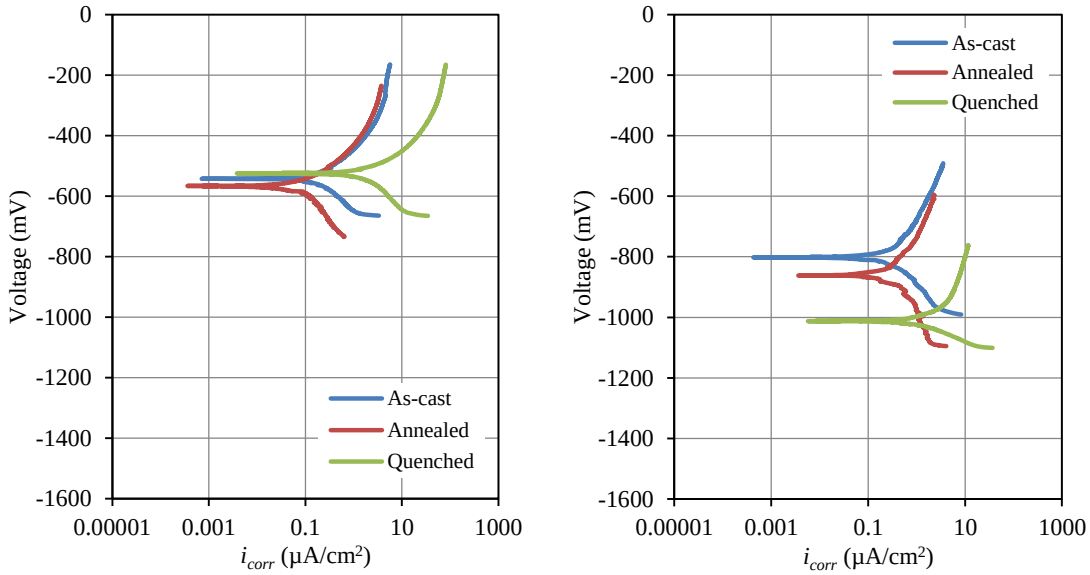

a) A7, 0.05 at.% Pd b) A8, 0.10 at.% Pd

Figure 4.22. Potentiodynamic curves of as-cast and heat treated $Ti_{25-0.5x}V_{40}Cr_{35-0.5x}Pd_x$ (x = 0.05, 0.10 at.%) alloys.

4.4.2. Corrosion rates of the alloys in 6M KOH solution

The corrosion rates (Figures 4.23 to 4.25) were calculated from the corrosion current densities in Figures 4.20 to 4.22 and Equations 2.7 to 2.10.

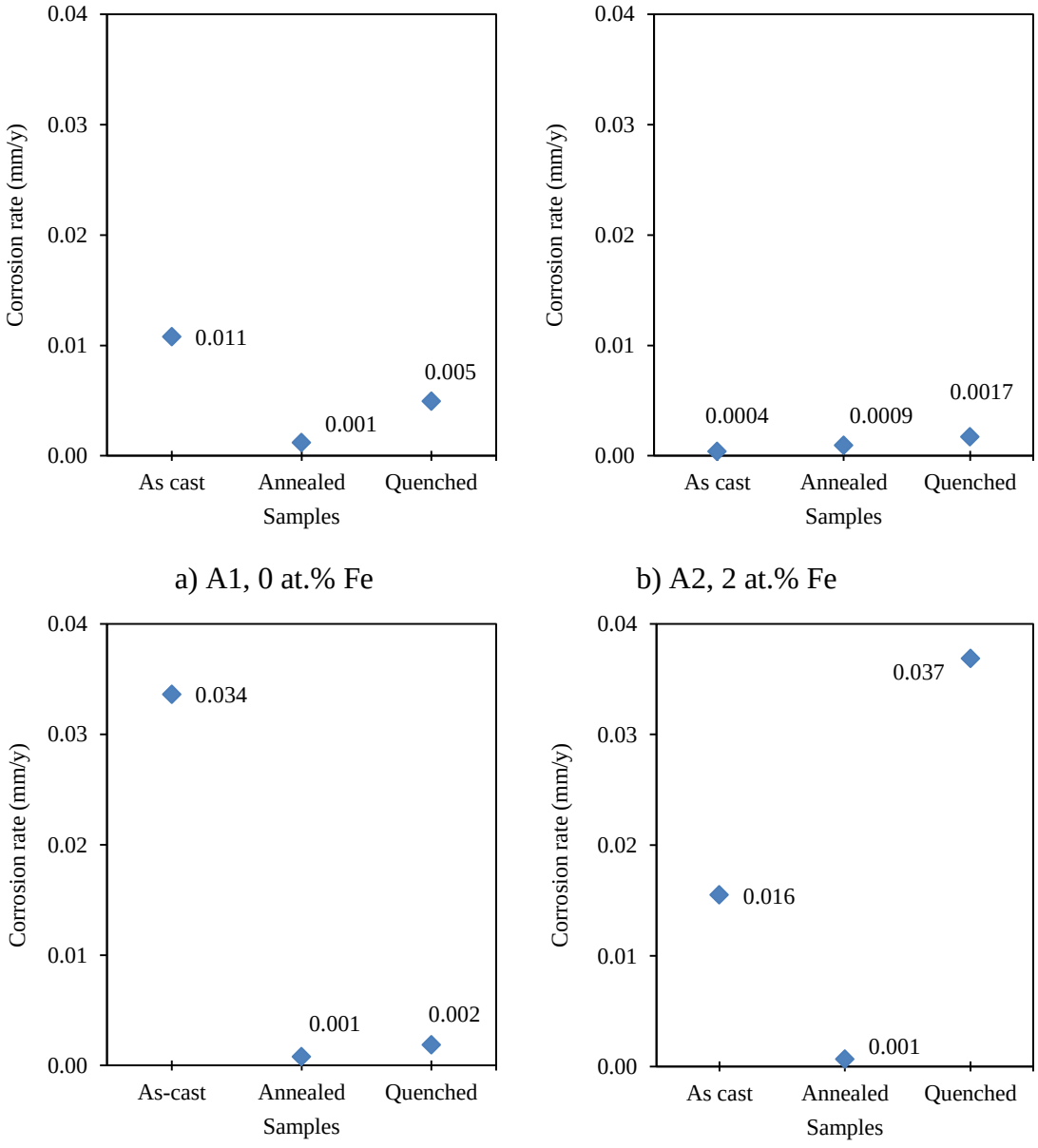

Figure 4.23. Corrosion rates of as-cast and heat treated $Ti_{25-0.5x}V_{40}Cr_{35-0.5x}Fe$ (x = 0, 2, 5, 6) at.% alloy.

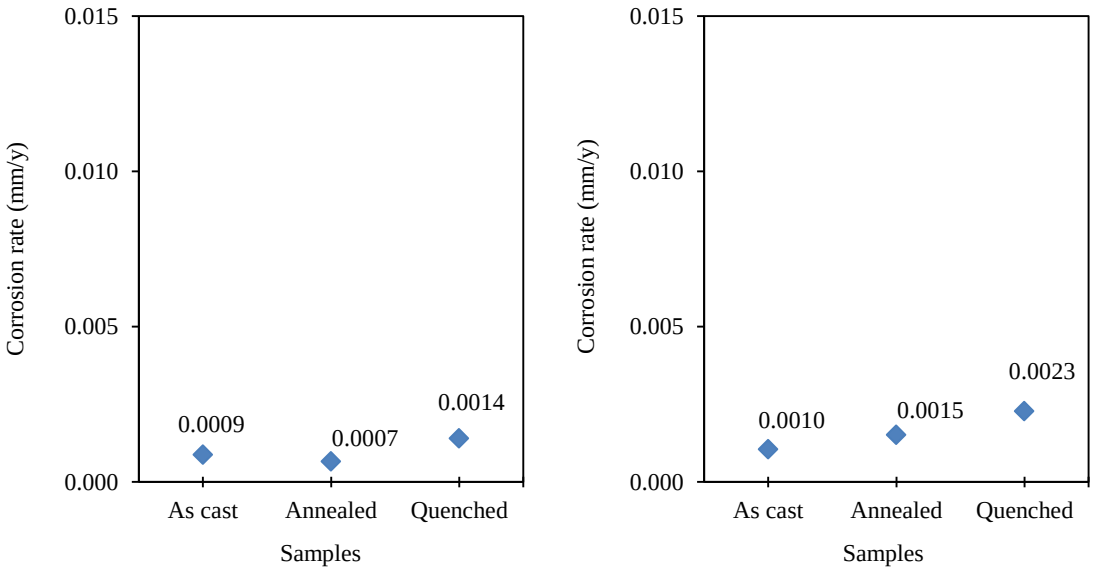

a) A5, 0.05 at.% Rh b) A6, x = 0.10 at.% Rh

Figure 4.24. Corrosion rates of as-cast and heat treated $Ti_{25-0.5x}V_{40}Cr_{35-0.5x}Rh_x$ (x = 0.05, 0.10 at.%) alloy.

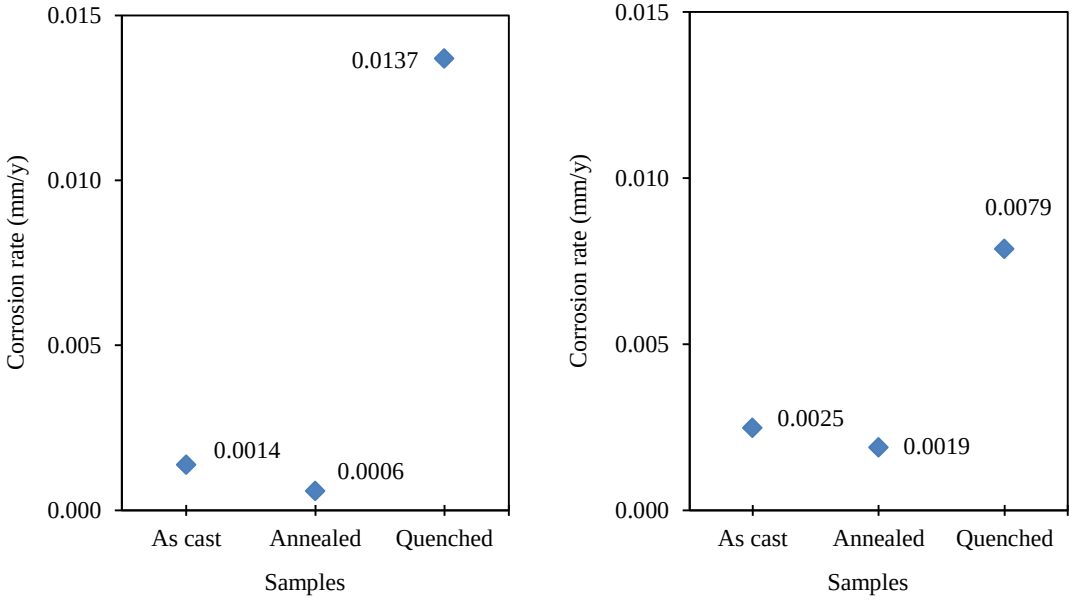

a) A7, 0.05 at.% Pd b) A8, 0.10 at.% Pd

Figure 4.25. Corrosion rates of as-cast and heat treated $Ti_{25-0.5x}V_{40}Cr_{35-0.5x}Pd_x$ (x = 0.05, 0.10 at.%) alloy.

In the Fe-free alloy Ti_{25}:V_{40}:Cr_{35} (Figure 4.20 a), the lowest E_{corr} of -860 mV occurred in the quenched sample, while the highest value of -410 mV was found in the annealed sample. The as-cast sample had the highest i_{corr} of 1.00 µA/cm^2 and the lowest value of 0.11 µA/cm^2 was recorded for the annealed sample. The annealed sample had the lowest corrosion rate of 0.001 mm/y, while the as-cast sample had the highest corrosion rate of 0.011 mm/y (Figure 4.23 a).

With addition of 2 at.% Fe, the Tafel behaviour of as-cast and heat treated samples were similar (Figure 4.20 b). The E_{corr} decreased from -821 to -869 mV after quenching but increased slightly to -800 mV after annealing. Both heat treatments marginally increased the corrosion rates, which was highest (0.0017 mm/y) in the quenched sample and lowest (0.0004 mm/y) in the as-cast sample (Figure 4.23 b).

The E_{corr} for the as-cast 5 at.% Fe sample was -327 mV, while the E_{corr} for the annealed and quenched samples were similar at -660 and 670 mV respectively (Figure 4.20c). The as-cast sample had the highest corrosion rate of 0.034 mm/y (Figure 4.23c), while the annealed and the quenched samples had much lower corrosion rates of 0.001 and 0.002 mm/y.

The E_{corr} of the as-cast, annealed and quenched 6 at.% Fe samples were -1220, -700 and -410 mV respectively, with the corresponding i_{corr} values of 1.43, 0.06 and 4.66 µA/cm^2 (Figure 4.20 d). Figure 4.23 d shows that the lowest corrosion rate of 0.002 mm/y was found in the annealed sample, while the quenched sample had the highest value of 0.037 mm/y.

In the 0.05 at.% Rh alloy, the E_{corr} for the as-cast, annealed and quenched samples were very similar at -790, -711 and -780 mV, while the corresponding i_{corr} values were 0.081, 0.061 and 0.13 µA/cm^2 (Figure 4.21 a). The addition of rhodium caused a reduction in the corrosion rates. The annealed sample had the lowest corrosion rate of 0.0007 mm/y and the highest corrosion rate of 0.0014 mm/y was found in the quenched sample, as shown in Figure 4.24 a.

The E_{corr} values were slightly lowered with addition of 0.10 at.% Rh and further reduced with heat treatment: -830 mV for the as-cast sample, -910 mV for the annealed

and a similar -920 mV for the quenched sample (Figure 4.21 b). Heat treatment marginally increased the corrosion rate. Figure 4.24 b shows that the as-cast sample had the lowest corrosion rate (0.0010 mm/y), followed by the annealed sample (0.0015 mm/y) and the quenched sample (0.0023 mm/y).

With addition of 0.05 at.% Pd, the E_{corr} range was ~40 mV, with the lowest at -566 mV (annealed) and the highest at -525mV (quenched), as shown in Figure 4.22 a. The highest corrosion rate of 0.0137 mm/y was found in the quenched sample, while low rates were found for the as-cast and annealed samples (0.0014 and 0.0006 mm/y respectively), indicating that the annealed sample was more resistant to corrosion (Figure 4.25 a).

An increase in palladium content to 0.10 at.% Pd decreased the E_{corr} substantially for all three samples: to -802 mV (as-cast), -862 mV (annealed) and the lowest at -1013 mV (quenched), as shown in Figure 4.22 b. The lowest corrosion rate was found in the annealed sample (0.0019 mm/y) and the highest (0.008 mm/y) in the quenched sample. The corrosion rate of the as-cast sample was 0.0025 mm/y.

Comparing all the as-cast and heat treated alloys (A1 to A8), the highest E_{corr} of -400 mV occurred in the 6 at.% Fe quenched sample, while the lowest value of -1240 mV was found in the as-cast sample of the same alloy. The highest i_{corr} of 4.66 µA/cm^2 and corresponding corrosion rate of 0.0369 mm/y was found in the quenched sample with 6 at.% Fe, with the second highest corrosion rate of 0.034 mm/y in the 5 at.% Fe as-cast sample.

The lowest i_{corr} value of 0.035 µA/cm^2 and corresponding corrosion rate of 0.0004 mm/y was recorded for the as-cast 2 at.% Fe sample.

4.5. Hydrogen storage characteristics of the Ti_{25}:V_{40}:Cr_{35} alloys

4.5.1. Absorption/desorption behaviour

The pressure-composition-temperature (PCT) data tested at 303, 333 and 363K is captured in Figures 4.26 to 4.28 and the data are summarised in Table 4.10.

Overall, the best desorption results were found at 303K for all samples. The desorption curves are shown in Figures 4.26 to 4.28. The hydrogen storage properties were then calculated from the desorption data and graphs.

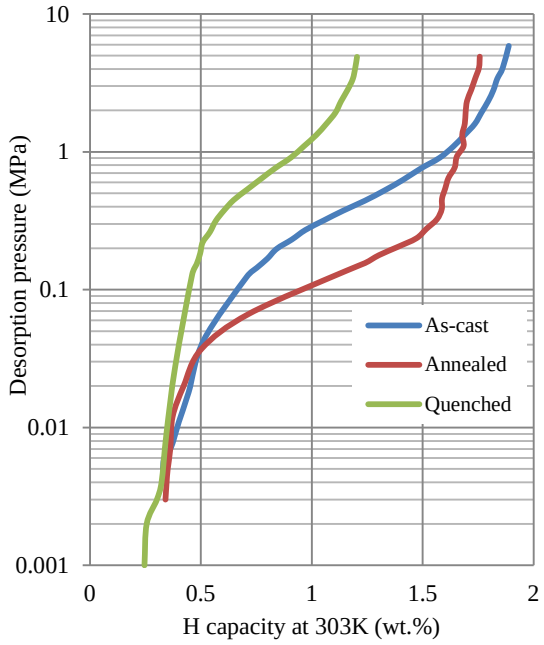

a) A1, 0 at.% Fe

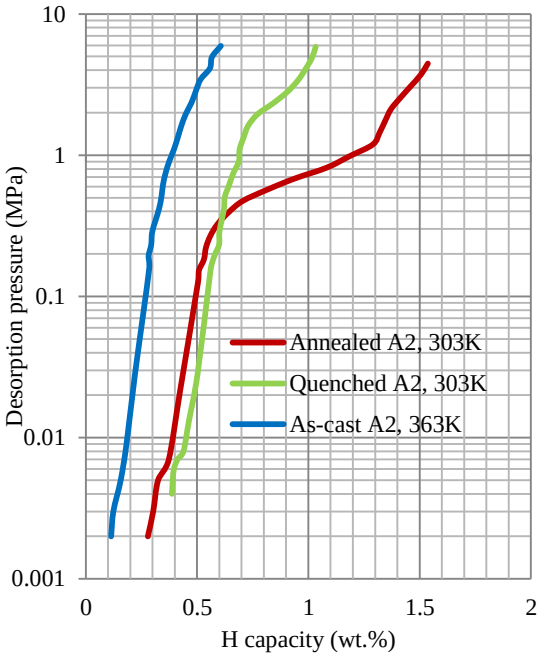

b) A2, 2 at.% Fe

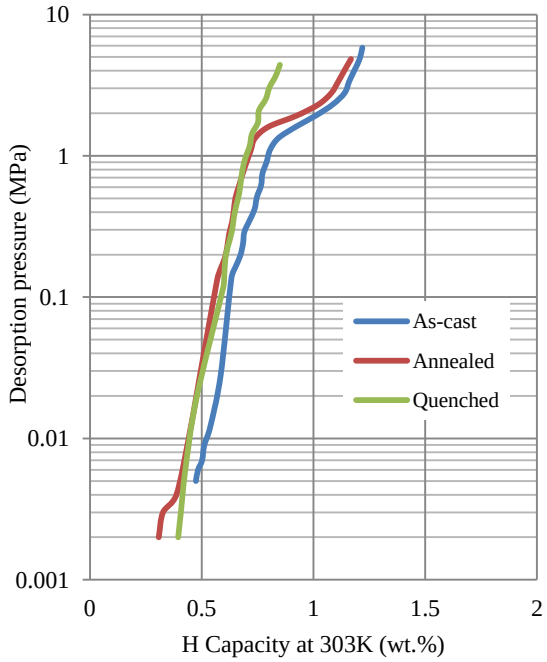

c) A3, 5 at.% Fe

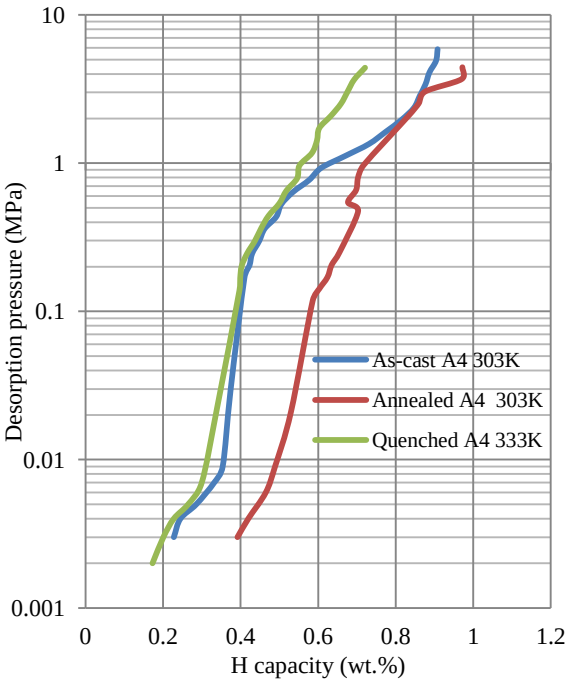

d) A4, 6 at.% Fe

Figure 4.26. Selected desorption curves of as-cast and heat treated $Ti_{25-x}V_{40}Cr_{35-x}Fe_x$ (x = 0, 2, 5, 6 at.%) alloy.

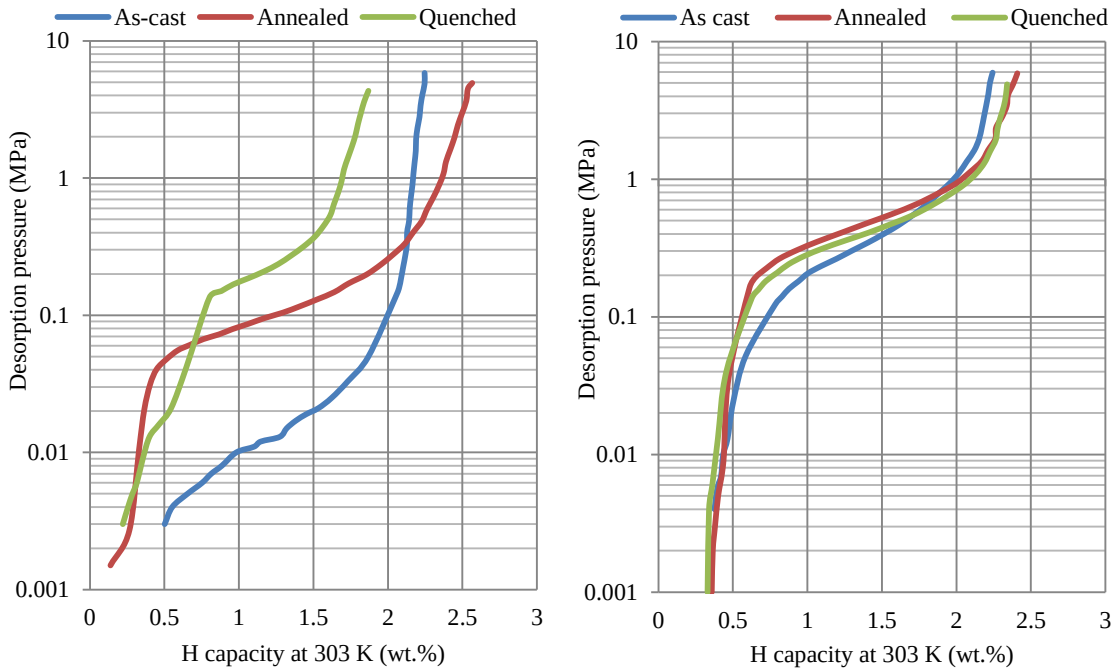

a) A5, 0.05 at.% Rh b) A6, 0.10 at.% Rh

Figure 4.27. The desorption curves of as-cast and heat treated $Ti_{25-0.5x}V_{40}Cr_{35-0.5x}Rh_x$ (x = 0.05, 0.1 at.%) alloy at 303K.

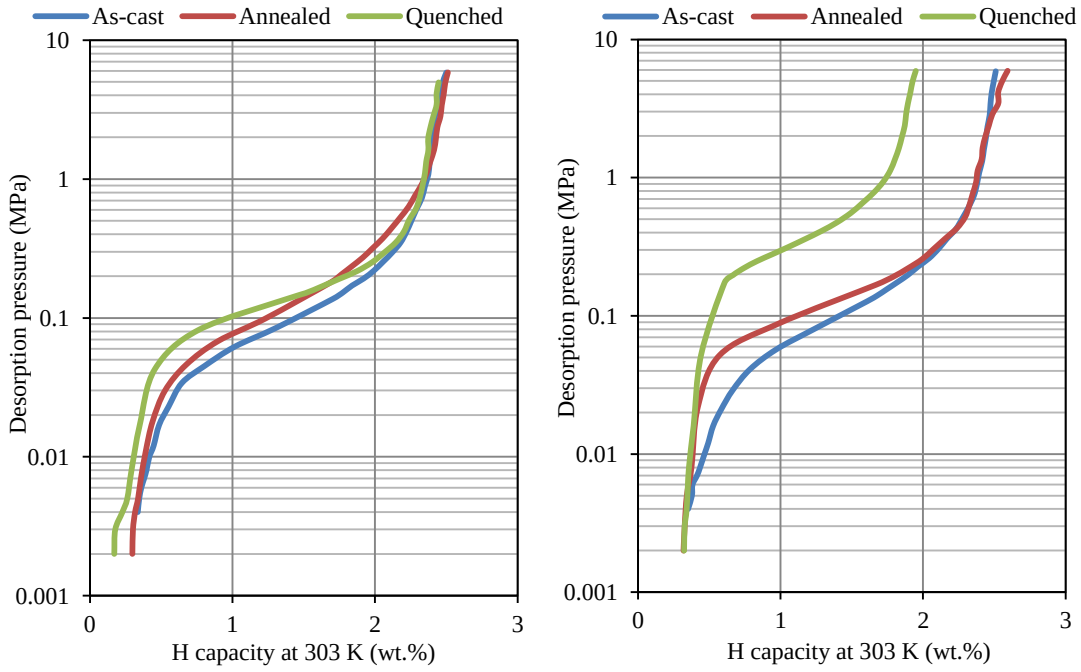

a) A7, 0.05 at.% Pd b) A8, 0.1 at.% Pd

Figure 4.28. The desorption curves of as-cast and heat treated $Ti_{25-0.5x}V_{40}Cr_{35-0.5x}Rh_x$ (x = 0.05, 0.1 at.%) alloy at 303K.

Table 4.10. Summary of absorption/desorption data for alloys A1 to A8.

Temperature		303K				333K				363K			
		H capacity (max.)		Useable H	Useable H (%)	H capacity (max.)		Useable H	Useable H (%)	H capacity (max.)		Useable H	Useable H (%)
		Absorbed	Desorbed			Abs.	Des.			Abs.	Des.		
A1	A1[1]	1.89	0.33	1.56	83	1.31	0.33	0.98	75	1.03	0.15	0.88	85
	A1A[2]	1.76	0.34	1.42	81	1.28	0.23	1.05	82	0.73	0.14	0.59	81
	A1B[3]	1.23	0.25	0.98	80	0.78	0.21	0.57	73	0.7	0.07	0.63	90
A2	A2	0.86	0.42	**0.44**	**51**	0.68	0.2	0.48	71	0.61	0.11	0.5	82
	A2A	1.54	0.28	1.26	82	0.88	0.32	0.56	64	0.75	0.23	0.52	69
	A2B	1.04	0.39	0.65	63	0.74	**0.35**	0.39	53	0.67	0.15	0.52	78
A3	A3	1.22	0.47	0.75	61	0.71	0.33	0.38	54	0.26	0.09	**0.17**	**65**
	A3A	1.17	0.31	0.86	74	0.81	**0.1**	0.71	88	0.72	0.14	0.58	81
	A3B	**0.85**	0.4	0.45	53	0.73	0.31	0.42	58	0.54	0.14	0.4	74
A4	A4	0.91	0.23	0.68	75	**0.36**	0.15	0.21	58	**0.23**	**0.01**	0.22	**96**
	A4A	0.97	0.39	0.58	60	0.74	0.17	0.57	77	0.6	0.17	0.43	72
	A4B	0.87	0.39	0.48	55	0.72	0.17	0.55	76	0.65	0.13	0.52	80
A5	A5	2.25	**0.75**	1.5	67	2.08	0.34	1.74	84	1.77	0.17	1.6	90
	A5A	2.57	0.32	2.25	88	**2.52**	0.26	2.26	90	**2.45**	0.17	**2.28**	93
	A5B	1.87	0.22	1.65	88	1.53	0.23	1.30	85	0.97	0.18	0.79	81
A6	A6	2.24	0.37	1.87	83	1.36	0.30	1.06	78	0.76	0.26	0.5	66
	A6A	2.41	0.36	2.05	85	1.39	0.31	1.08	78	0.92	**0.27**	0.65	71
	A6B	2.35	0.33	2.02	86	1.22	0.33	0.89	73	0.86	0.17	0.69	80
A7	A7	2.5	0.34	2.16	86	2.15	0.33	1.82	85	1.27	0.21	1.06	83
	A7A	2.51	0.3	2.21	88	2.18	0.32	1.86	85	1.28	0.18	1.1	86
	A7B	2.45	**0.17**	**2.28**	**93**	2.18	0.19	1.99	91	1.01	0.11	0.90	89
A8	A8	2.51	0.35	2.16	86	2.06	0.33	1.73	84	1.2	0.22	0.98	82
	A8A	**2.59**	0.32	2.27	88	2.27	0.27	2	88	1.26	0.20	1.06	84
	A8B	1.95	0.32	1.63	84	1.35	0.22	1.13	84	0.78	0.18	0.6	77
Maximum		**2.59**	**0.75**	**2.28**	**93**	**2.52**	**0.35**	**2.26**	**91**	**2.45**	**0.27**	**2.28**	**96**
Minimum		**0.85**	**0.17**	**0.44**	**51**	**0.36**	**0.1**	**0.21**	**53**	**0.23**	**0.01**	**0.17**	**65**

1 – As-cast
2 - Annealed
3 - Quenched

4.5.2. Reversible hydrogen storage capacity

The influence of heat treatment on reversible hydrogen storage capacity (RHSC) at 303, 333 and 363K for alloys A1 to A8 is shown in Figures 4.29 to 4.31. The thermodynamic properties of as-cast and heat treated alloys A1 to A8 are shown in Table 4.11.

For the iron-free base alloy A1, the plateau pressure of the as-cast sample at 303K decreased from 0.41 to 0.09 MPa by annealing and increased to 0.90 MPa by quenching. The highest RHSC of 1.56 wt% was found in the as-cast sample at 303K, as shown in Figure 4.29 a. The RHSC decreased at higher testing temperatures.

For the 2 at.% Fe alloy, the desorption curves for the annealed and quenched samples at 303 K and of the as-cast sample at 363 K , are plotted in Figure 4.26 b. The plateau pressure decreased from 1.30 MPa to 0.68 MPa after annealing, but increased to 2.34 MPa after quenching. The highest RHSC value of 1.26 wt% was found in the annealed sample at 303 K, while further increase in temperature decreased the RHSC to 0.56 at 333 K and further to 0.51 wt% at 363 K. The quenched samples showed a similar trend, with the second highest RHSC of 0.65 wt% at 303 K.

At 5 at.% Fe, the annealed sample had the highest RHSC of 0.86 wt%, while the lowest value of 0.46 wt.% was observed in the quenched sample (Figure 4.29 c). The plateau pressures of the as-cast and annealed samples were 1.92 and 1.86 MPa respectively, but there was no plateau after quenching (see Figure 4.26c).

For the 6 at.% Fe alloy, the as-cast sample showed the highest RHSC of 0.68 wt% at a testing temperature of 303K (Figure 4.29 d). The reduction in RHSC was more pronounced at higher testing temperatures for the as-cast samples compared to the heat treated samples. The plateau pressure of the as-cast sample was 1.34 MPa but there was no observed plateau after heat treatment.

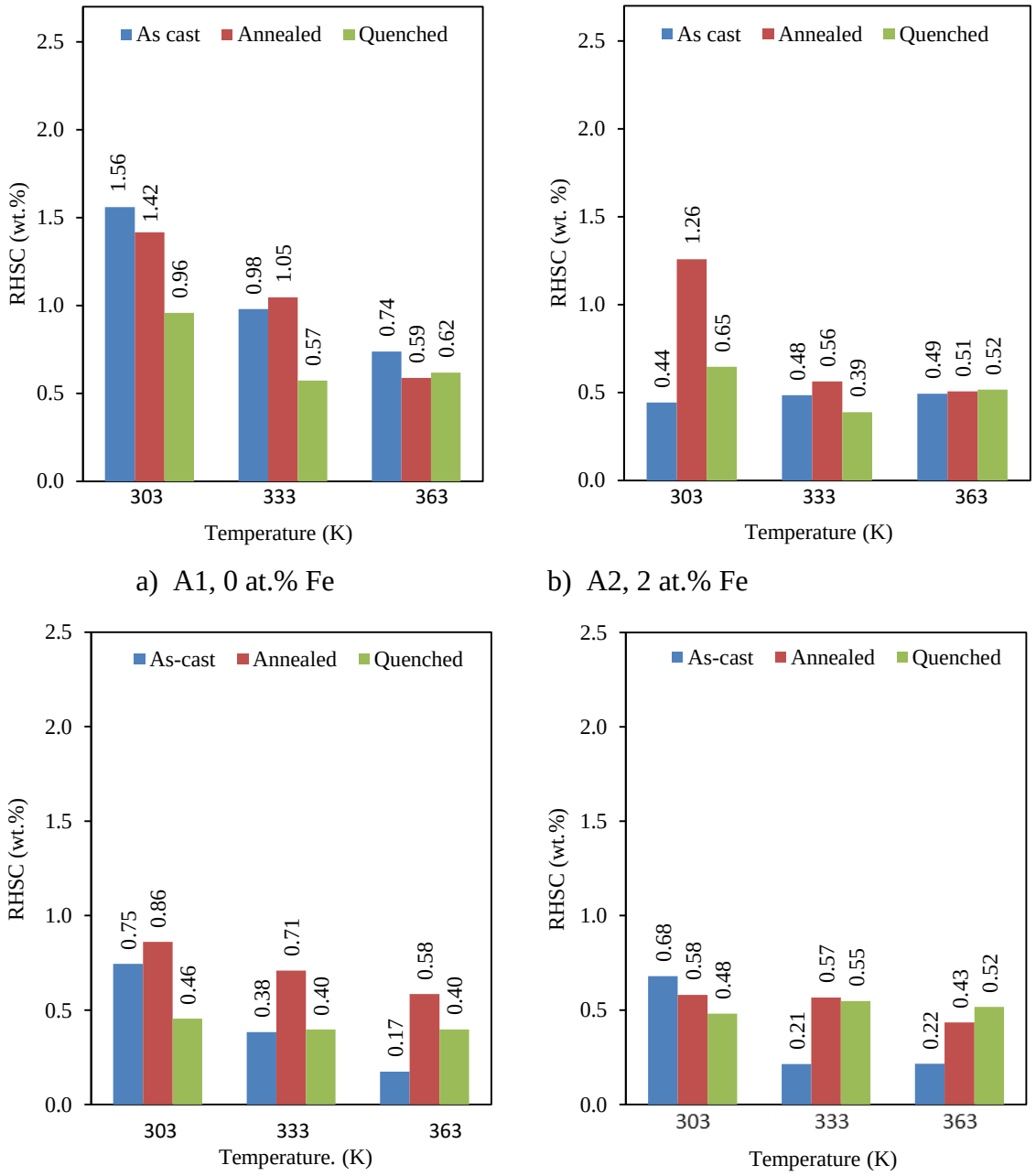

a) A1, 0 at.% Fe

b) A2, 2 at.% Fe

c) A3, 5 at.% Fe

d) A4, 6 at.% Fe

Figure 4.29. RHSC of the as-cast, annealed and quenched $Ti_{25-0.5x}V_{40}Cr_{35-0.5x}Fe_x$ (x = 0, 2, 5, 6 at.%) alloy.

With the addition of 0.05 at.% Rh, the optimum operating temperature for the alloy was surprisingly found to be 363 K for the annealed sample, with a RHSC of 2.28 wt% (Figure 4.30 a), while the RHSC at 363K was 1.60 and 0.79 wt% for the as-cast and quenched samples, respectively. Annealing had no effect on the plateau

pressure of the as-cast sample, although the plateau pressure increased to 0.21 MPa after quenching.

With an addition of 0.10 at.% Rh, the as-cast sample had the highest RHSC of 1.87 wt% at 303 K, while the RHSC was 2.05 and 2.01 wt% for the annealed and quenched samples respectively. The plateau pressure decreased from 0.29 MPa in the as-cast sample to 0.21 MPa in the annealed sample and 0.25 MPa in the quenched sample.

For the 0.05 at.% Pd alloy, increasing the testing temperature decreased the RHSC for all conditions (Figure 4.31 a). The RHSC was highest (2.28 wt%) in the quenched sample at 303 K and the lowest in the same sample at 363K. The plateau pressure increased from 2.16 to 2.21 MPa after annealing and to 2.28 MPa after quenching.

In the 0.10 at.% Pd alloy, the annealed samples had the highest RHSC at all three test temperatures (Figure 4.31 b). An increase in testing temperature decreased the RHSC for all conditions (Figure 4.31 b). The highest reversible storage capacity of 2.27 wt% was found in the annealed sample tested at 303K.

From all the PCT measured at 303K the annealed sample containing 0.10 at.% Pd had the highest RHSC of 2.28 wt%, while the lowest reversible capacity (0.46 wt%) was observed in the quenched 5 at.% Fe sample. The quenched 2 at.% Fe sample had the highest plateau pressure of 2.34 MPa. The as-cast sample with 0.05 at.% Rh had the lowest plateau pressure (0.02 MPa). The highest entropy of ~156 J/mol.K was found in the quenched 0.10 at.% Rh sample, while the as-cast 5 at.% Fe sample had the lowest entropy of 22.57 J/mol.K.

The entropy ΔS is an indication of how far the MH system is from a perfect, ordered condition. The theoretical value of ΔS is the entropy of hydrogen gas, which is approx. -135 J/mol.K); a higher value is an indication of higher degree of disorder in the MH system[204]. Table 4.11 showed a large difference between ΔS of the Fe-containing alloys and the theoretical values, implying a higher degree of disorder in the MH systems. The annealed base alloy showed the highest degree of order, while the as-cast sample with 5 at.% Fe showed the lowest degree of order.

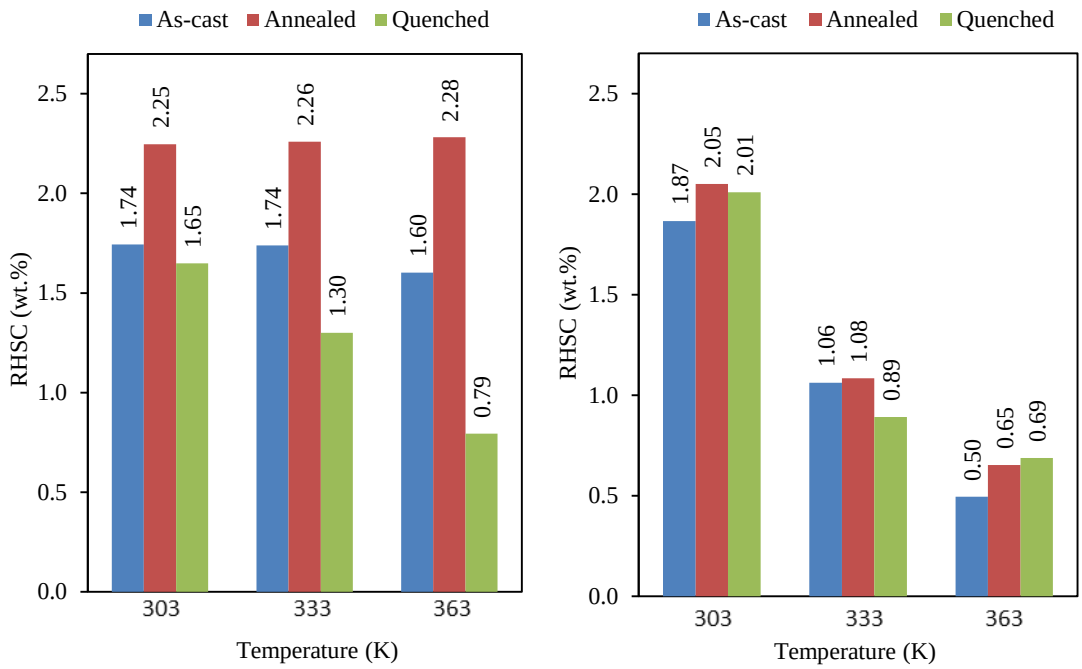

a) A5, 0.05 at.% Rh b) A6, 0.10 at.% Rh

Figure 4.30. RHSC of the as-cast, annealed and quenched $Ti_{25-0.5x}V_{40}Cr_{35-0.5x}Rh_x$ (x = 0.05, 0.10 at.%) alloy.

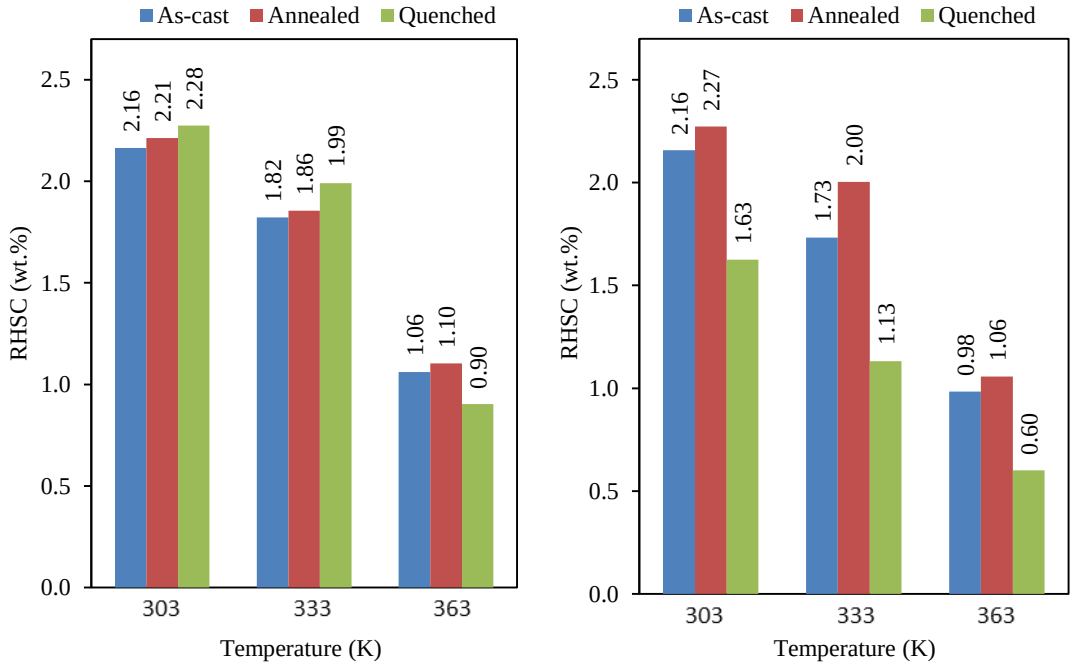

a) A7, 0.05 at.% Pd b) A8, 0.10 at.% Pd

Figure 4. 31. RHSC of the as-cast, annealed and quenched $Ti_{25-x}V_{40}Cr_{35-x}Pd_x$ (x = 0.05, 0.10 at.%) alloy.

Equations 2.2 and 2.3 show that two plateau pressures, P_1 and P_2, are required to calculate the enthalpy ΔH and entropy ΔS. These pressures were not calculated in the heat treated A2, A3 and A4 samples, as plateaus were only seen in one of the three isotherm curves.

Table 4.11. Thermodynamic properties of alloys A1 to A8.

Alloy no.	**Sample**	**Plateau pressure (MPa)**	**ΔH (kJ/mol)**	**ΔS (J/mol.K)**
A1 Base alloy	As-cast	0.41	40.59	121.49
	Annealed	0.09	45.90	131.90
	Quenched	0.90	27.43	89.60
A2 2% Fe	As-cast	1.30	110.40	36.00
	Annealed	0.68	-	-
	Quenched	2.34	-	-
A3 5% Fe	As-cast	1.92	51.80	22.57
	Annealed	1.86	-	-
	Quenched	-	-	-
A4 6% Fe	As-cast	1.34	31.50	106.20
	Annealed	-	-	-
	Quenched	-	-	-
A5 0.05% Rh	As-cast	0.02	41.79	104.11
	Annealed	0.12	44.20	110.18
	Quenched	0.21	37.21	110.13
A6 0.10% Rh	As-cast	0.35	41.98	128.19
	Annealed	0.49	42.77	142.32
	Quenched	0.43	46.74	155.58
A7 0.05% Pd	As-cast	0.11	31.92	87.24
	Annealed	0.15	32.83	91.68
	Quenched	0.15	32.83	91.68
A8 0.10% Pd	As-cast	0.14	32.06	88.01
	Annealed	0.13	35.48	100.76
	Quenched	0.45	37.37	114.42

4.6. Thermo-Calc calculations

The command file (Section 3.11) was run using the Solid Solution 4 (SSOL4) and Titanium (TTTI3) Thermo-Calc databases. Graphs were plotted to show the effect of temperature on phase proportion in the range 1900 to 250°C. The alloys and respective Figure numbers for the SSOL4 and TTTi3 graphs are summarised in Table 4.12.

Table 4.12. Figure numbers of the Thermo-Calc property diagrams showing calculation of the phases in alloys A1 to A8.

Alloy	Database	
	SSOL4	TTTi3
A1	Figure 4.32	Figure 4.33
A2	4.34	4.35
A3	4.36	4.37
A4	4.38	4.39
A5	4.40	4.41
A6	4.42	4.43
A7	4.44	4.45
A8	4.46	4.47

4.6.1 Calculation of phases in A1

Both SSOL4 and TTTI3 databases of Thermo-Calc software showed four phases in A1. SSOL4 predicts that only liquid phase exists beyond 1692°C: the liquid phase begins to solidify to BCC_A2#1 at 1692°C and the Liquid to BCC_A2#1 ratio is 1 at 1656°C. The solidification process ends at 1619°C. Further reduction in temperature does not change the phase until $610 \leq T(°C) \leq 627$ when some of the BCC_A2#1 transforms to BCC_A2#2. An HCP_A3 phase forms at 610°C and coexists with BCC_A2#1 until 250°C.

The TTTI3 database predicts that A1 will have only liquid phase for $T(°C) \geq 1543$. Solidification begins at 1543°C when BCC_A2 begins to form. At 1528°C, equal amount of liquid and BCC_A2 exists; but only the BCC_A2 phase exists between 1512°C and 815°C. The amount of BCC_A2 begins to decrease due to formation of a C15_FCC phase at 815°C, which grows until 392°C when HCP_A3 is formed. All three phases: BCC_A2, C15_FCC and HCP_A3 coexist until 250°C.

Experimentally, the four phases found in A1 were: BCC (V), C15 Laves, C14 Laves (Ti) and C14 Laves ($Cr_{1.93}Ti_{1.07}$). Only BCC was predicted correctly by the SSOL4 database while two phases, C15 and BCC, were predicted correctly by TTTI3.

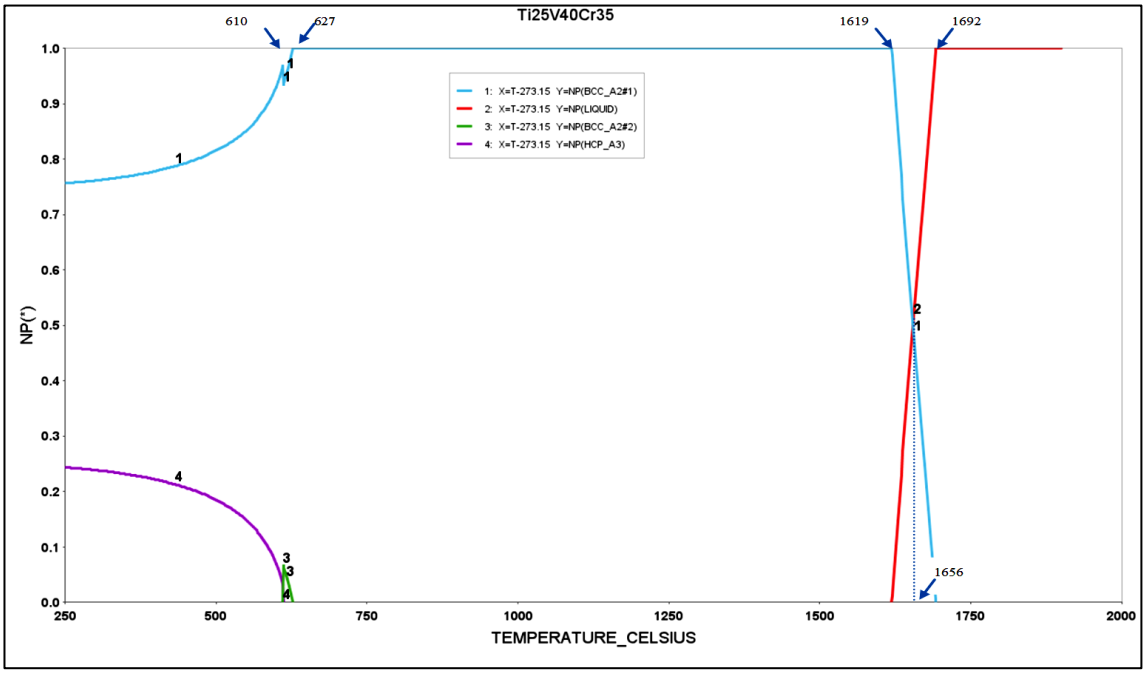

Figure 4.32. SSOL4 Thermo-Calc calculation of phases in A1.

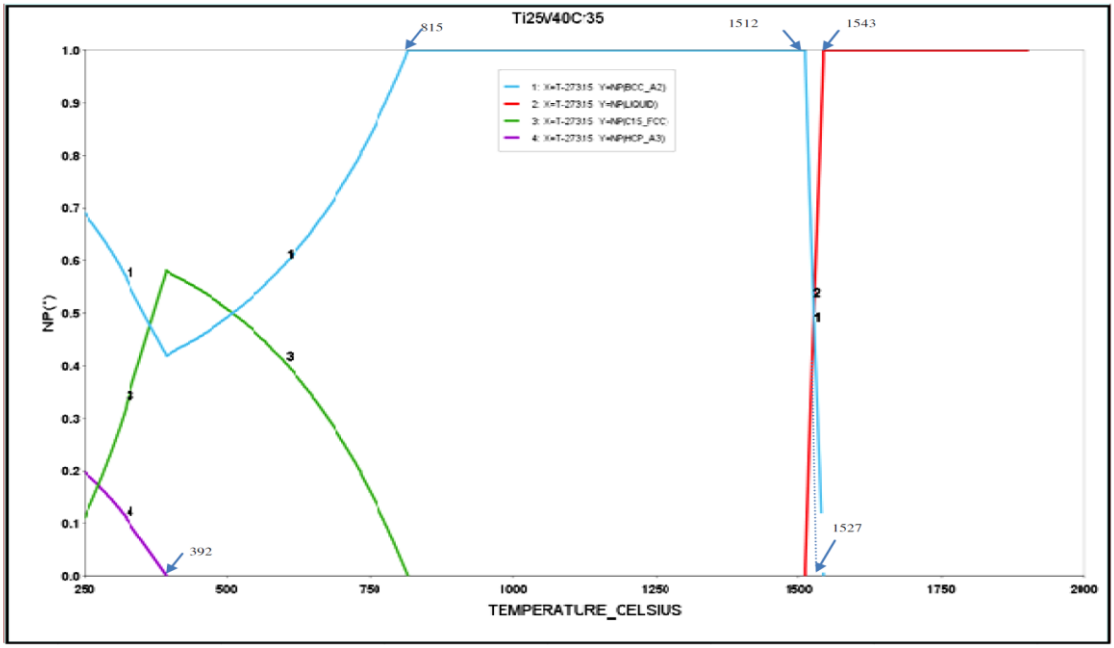

Figure 4.33. TTTI3 Thermo-Calc calculation of phases in A1.

4.6.2 Calculation of phases in A2

The SSOL4 database gave five phases in A2, while TTTI3 had four. Above 1685°C, SSOL4 database had only liquid phase in A2. The liquid phase starts solidifying to BCC_A2#1 at 1685°C until 1590°C when the solidification is complete. Only BCC_A2#1 exists between 1590°C to 731°C. BCC_A2#2 forms at 731°C due to depletion of BCC_A2#1. The new phase, BCC_A2#2 grows until 500°C when HCP-A3 forms. Four phases, BCC_A2#1, BCC_A2#2, HCP_A3 and FeTi coexist below 500°C.

In the TTTI3 database, only liquid phase exists beyond 1536°C, but both liquid and BCC_A2 coexist between 1536 and 1492°C. Only BCC_A2 was present between 1492 and 927°C. A new phase, C15_FCC forms at 927°C due to reduction in the amount of BCC_A2; the new phase grows till 354°C when the fourth phase, HCP_A3 forms. Three phases, C15_FCC, BCC_A2 and HCP_A3, coexist below 354°C.

Three phases, C14, C15 and Simple tetragonal were found experimentally. When compared with the results from Thermo-Calc models, none of the phases predicted by the SSOL4 database was found experimentally, while only C15 was found using TTTI3.

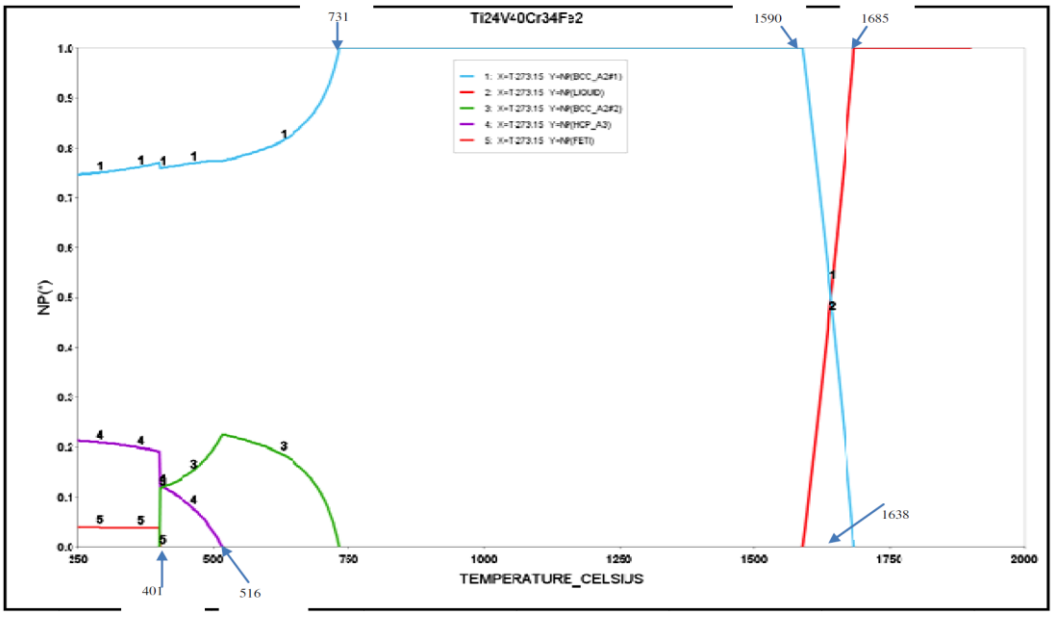

Figure 4.34. SSOL4 Thermo-Calc calculation of phases in A2

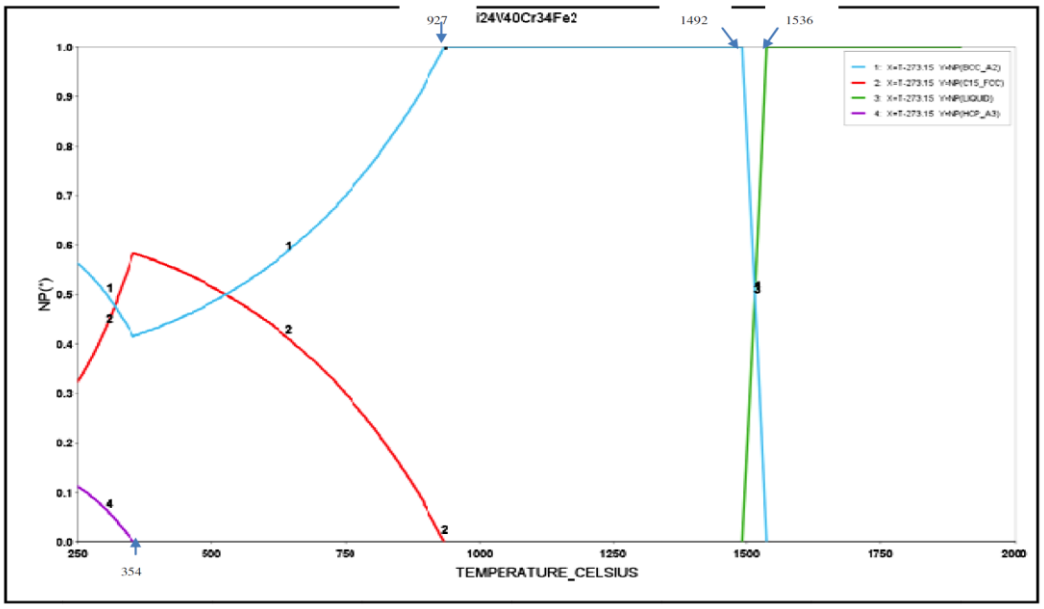

Figure 4.35. TTTI3 Thermo-Calc calculation of phases in A2.

4.6.3 Calculation of phases in A3

Both SSOL4 and TTTI3 databases had five phases in A3. According to SSOL4 database, only liquid phase was found at T > 1678°C. At 1678 ≤T≤ 1563, both liquid and BCC_A2#1 solid phase exist. The alloy consists of only BCC_A2#1 between 1563°C and 773°C. The third phase BCC_A2#2 forms at 773°C and grows (due to depletion of BCC_A2#1) until the temperature falls to 400°C. HCP_A3 and FETI phases form at 400°C and coexist with BCC_A2#2 till 200°C.

The TTTI3 database predicts that when temperature of A3 is greater than 1530°C, only liquid phase will exist, but both liquid and BCC_A2 will coexist between 1530°C and 1473°C. Between 1473°C and 927°C only BCC_A2 exists in A3. The C15_FCC phase forms at 927°C and the BCC_A2 starts depleting due to the growth of the new phase. HCP_A3 forms at 316°C and TIM_B2 was formed at 287°C. All except the liquid phase coexist from 316°C to 200°C.

The C14, C15 and αTi were found experimentally in A3. None (except αTi) of these three phases were found by the SSOL4 database but TTTI3 predicted formation of C15.

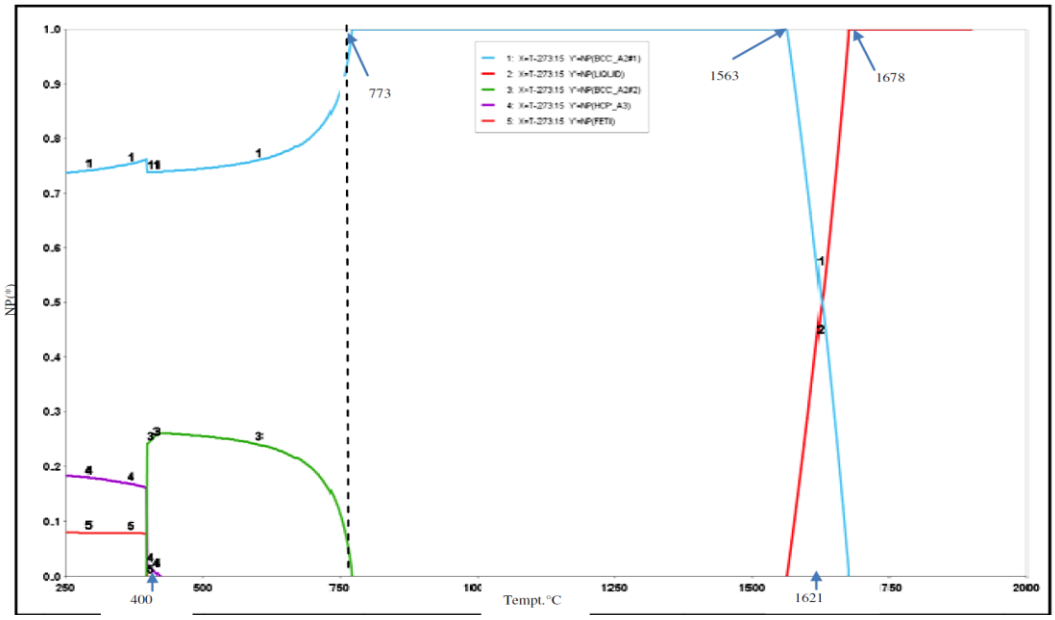

Figure 4.36. SSOL4 Thermo-Calc calculation of phases in A3.

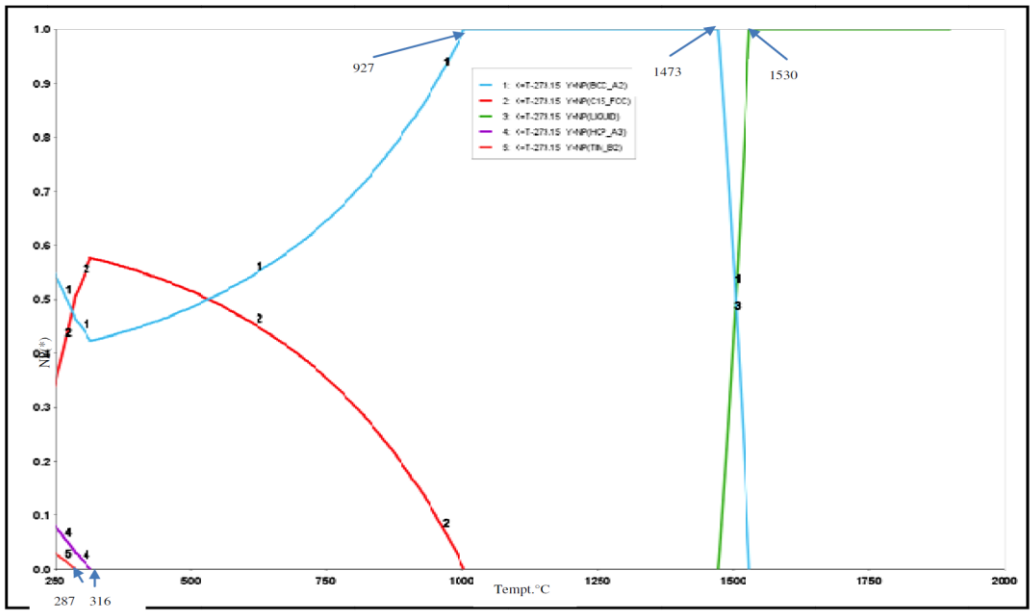

Figure 4.37. TTTI3 Thermo-Calc calculation of phases in A3

4.6.4 Calculation of phases in A4

Based on SSOL4 database, five phases were identified in A4. The liquid phase was observed above 1670°C where solidification to BCC_A2#1 begins. At 1604°C, the ratio of liquid to BCC_A2#1 becomes 50:50 and solidification is completed at 1538°C. BCC_A2#1 starts depleting at 796°C when the third phase, BCC_A2#2, forms. The fourth phase (FeTi) forms at 705°C and the fifth (αTi) at 398°C. All except the liquid phase coexist below 398°C.

Similar to the SSOL4 database, the TTTI3 database also identified 5 phases in A4. The Liquid phase was identified above 1524°C. Solidification to BCC_A2 begins at 1524°C and the ratio of BCC_A2 to the liquid phase is 50:50 at 1490°C. Solidification to BCC_A2 is completed at 1455°C. C15_FCC forms at 1051°C, TIM_B2 (TiFe) at 373°C and HCP_A3 (αTi) at 293°C.

C14 Laves, C15 Laves and bcc phases were found experimentally. Only C15 was predicted correctly in the TTTI3 database, while none of the phases predicted by the SSOL4 database correspond to the experimental results.

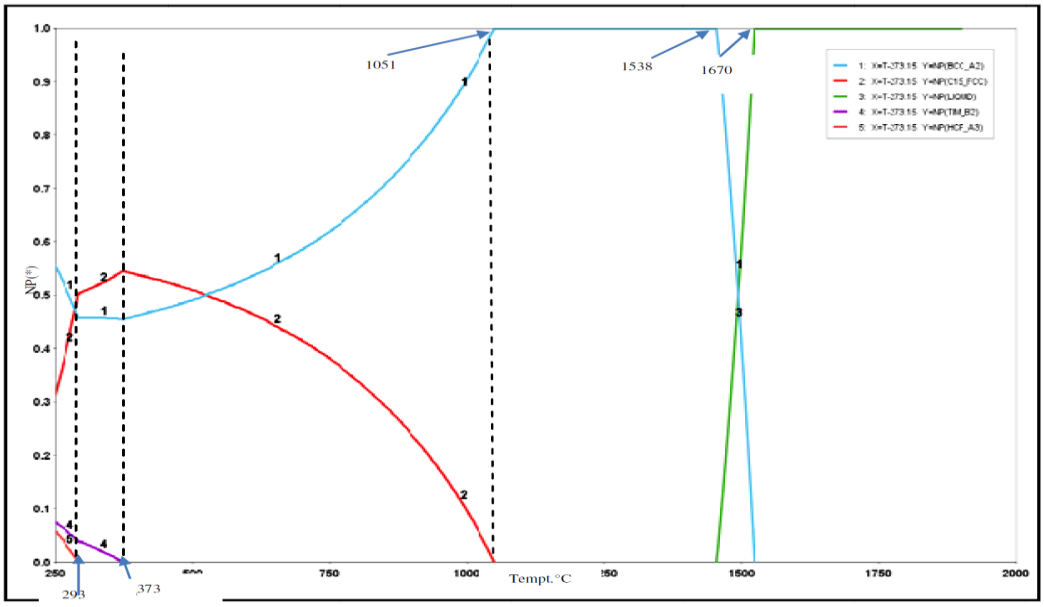

Figure 4.38. SSOL4 Thermo-Calc calculation of phases in A4.

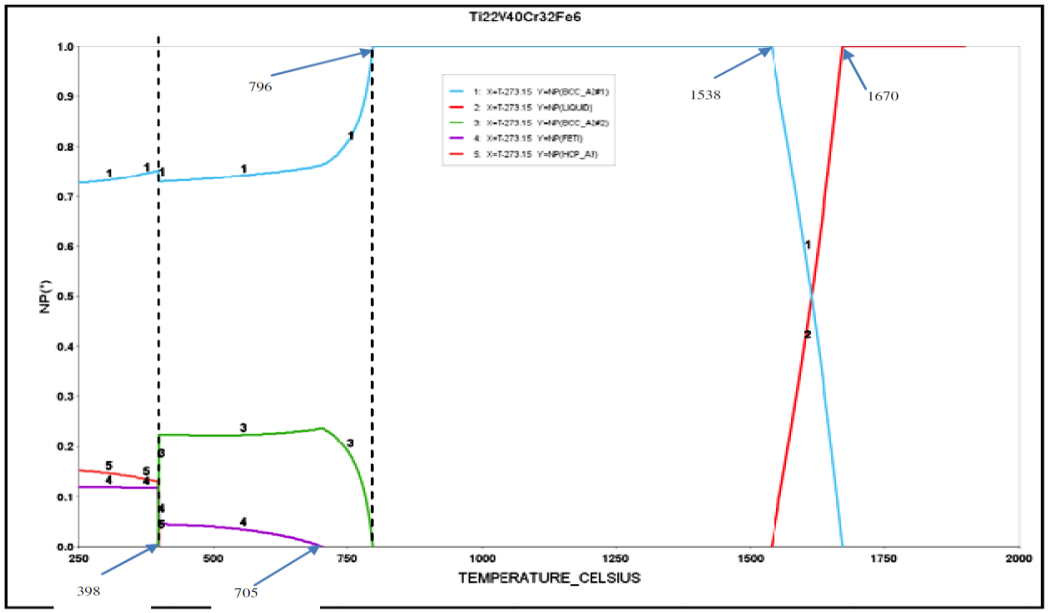

Figure 4.39. TTTI3 Thermo-Calc calculation of phases in A4.

4.6.5 Calculation of phases in A5

Both SSOL4 and TTTI3 databases calculated four phases in A5. SSOL4 shows the liquid phase above 1692°C, BCC_A2#1 only in the temperature range 626≤T(°C)≤ 1619, BCC_A2#2 in the range 613≤T(°C)≤626 and HCP_A3 from 613°C to 200°C. Solidification begins at 1692°C, while the ratio of the liquid phase to BCC_A2#1 is 50:50 at 1656°C.

The TTTI3 database shows the liquid phase above 1542°C, single BCC_A2 phase between 1511°C and 815°C, C15_ FCC from 815°C and HCP_A3 from 393°C. Solidification of the liquid phase begins at 1542°C and ends at 1511°C, and the quantities of the two phases become equal at 1527°C. The four phases coexist from and below 393°C. Phases found experimentally are BCC, αTi and C14 Laves.

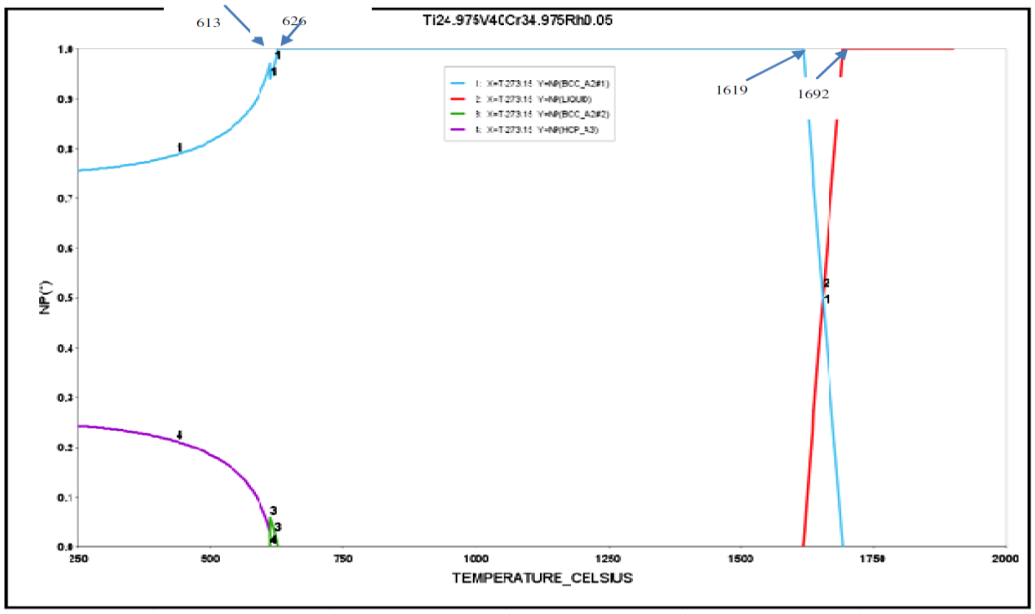

Figure 4.40. SSOL4 Thermo-Calc calculation of phases in A5.

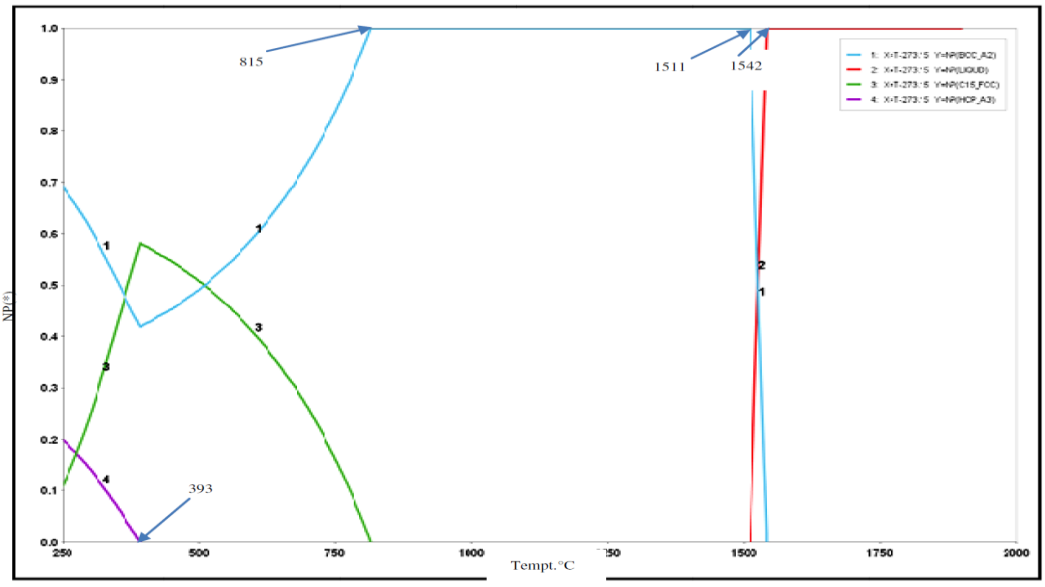

Figure 4.41. TTTI3 Thermo-Calc calculation of phases in A5.

4.6.6 Calculation of phases in A6

Based on the SSOL4 database, A6 is liquid above 1692°C. Solidification begins at 1692°C and ends at 1619°C. Only BCC_A2#1 forms between 1619°C and 626°C, BCC_A2#2 forms at 626°C and disappears at 613°C. HCP _A3 forms at 613°C and coexists with BCC_A2#1 until the program terminated at 250°C.

The TTTI3 database predicts three phases in A6; liquid phase above 1542°C, single BCC_A2 between 1511°C and 740°C and C15_FCC coexisting with BCC_A2 from 740°C. Solidification begins at 1542°C and ends at 1511°C. The quantity of BCC_A2 and liquid phase is equal at 1527°C.

Experimentally, the phases found in A6 were BCC and Laves (C14 and C36). The SSOL4 database did not predict C36 Laves, but the TTTI3 database predicted both BCC and C15 Laves phases.

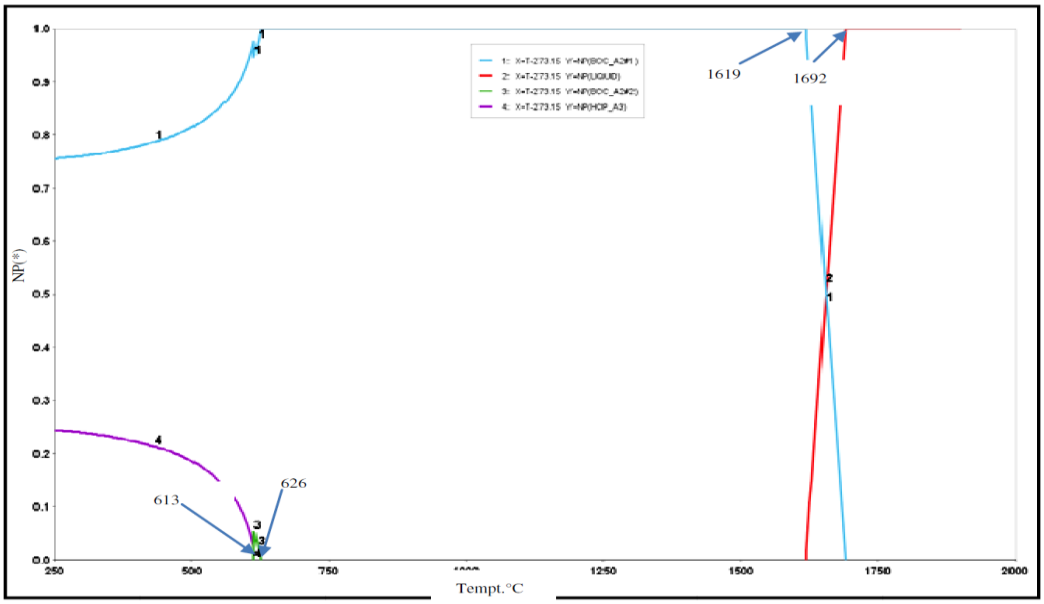

Figure 4.42. SSOL4 Thermo-Calc calculation of phases in A6.

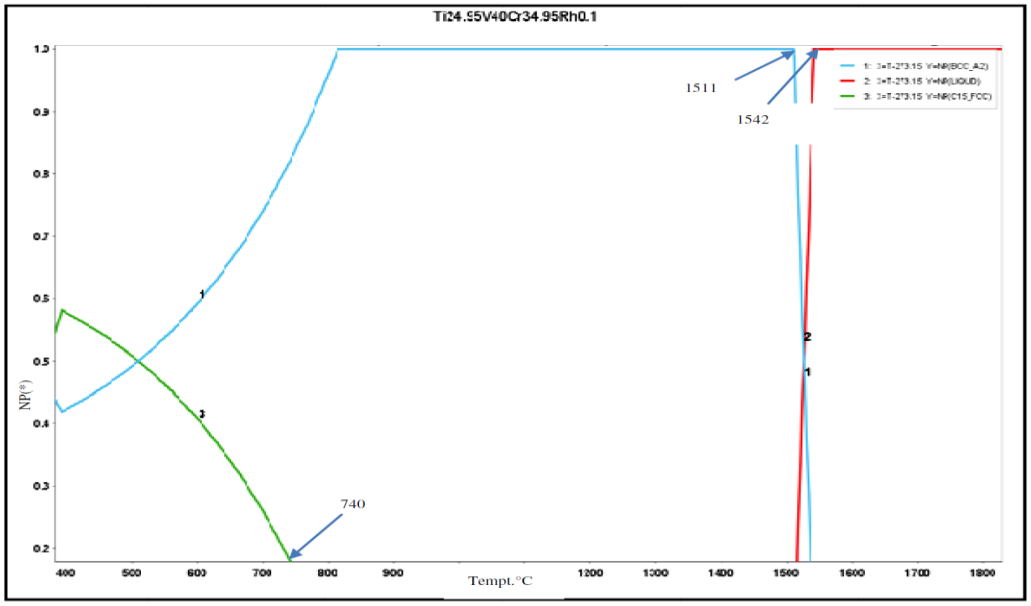

Figure 4.43. TTTI3 Thermo-Calc calculation of phases in A6.

4.6.7 Calculation of phases in A7

Both the SSOL4 and TTTI3 databases predict four phases in A7. SSOL4 shows liquid phase from 1692°C and above. Solidification to BCC_A2#1 begins at 1692°C and ends at 1619°C. Only the BCC_A2#1 solid phase was found in A7 from 1619°C to 625°C. BCC_A2#2 was formed at 625°C and disappears at 614°C where the fourth phase, HCP_A3, is formed.

The TTTI3 database found liquid phase at temperature above 1521°C, only solid BCC_A2 from 1512°C to 815°C, C15_FCC was formed at 815°C and HCP_A3 at 393°C. Ratio of liquid phase to BCC_A2 becomes 50:50 at 1517°C and all the phases coexisted from 393°C and below. Experimentally, BCC and Laves were found in A7. TTTI3 database also had the two phases but SSOL4 database did not calculate C15 Laves.

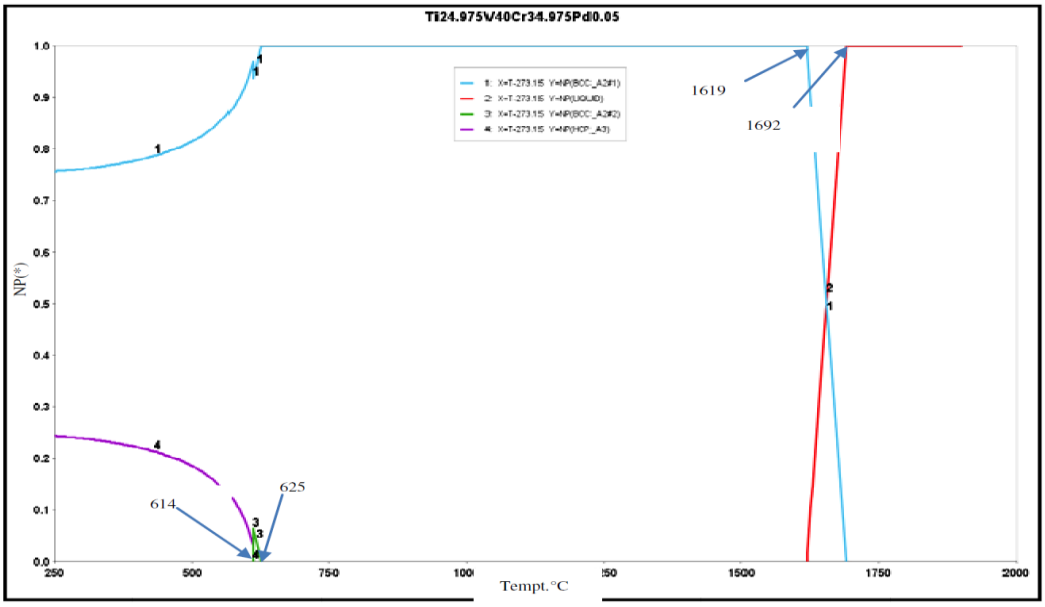

Figure 4.44. SSOL4 Thermo-Calc calculation of phases in A7.

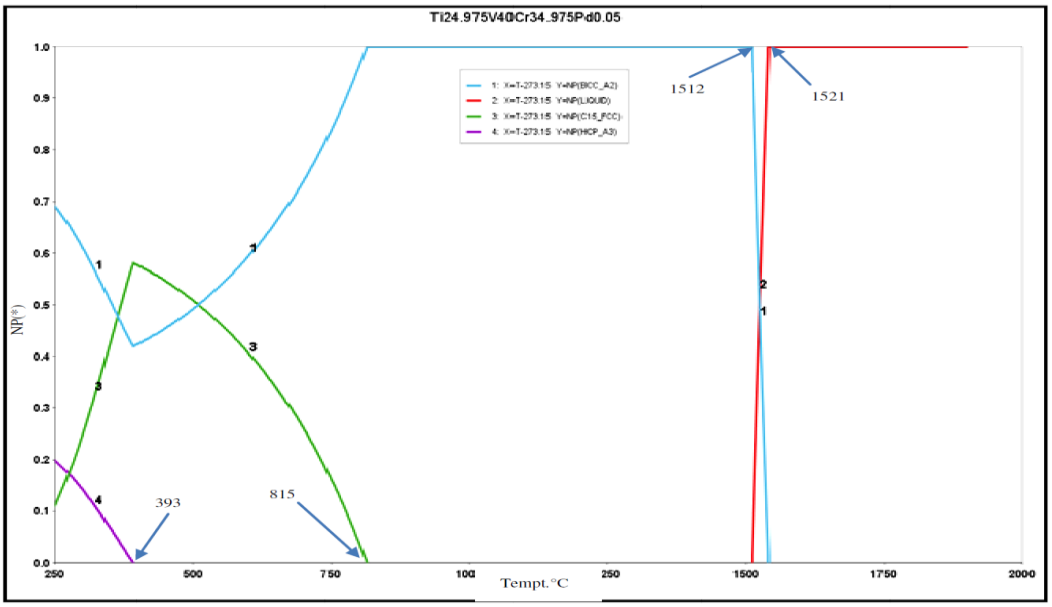

Figure 4.45. TTTI3 Thermo-Calc calculation of phases in A7

4.6.8 Calculation of phases in A8

Four phases were calculated using the SSOL4 and TTTI3 databases. The SSOL4 had Liquid, BCC_A2#1, BCC_A2#2 and HCP_A3 phases . Liquid phase formed beyond 1692°C, solidification to BCC_A2#1 starts at 1692°C and ends at 1618°C. Single phase BCC_A2#1 was between 1618 and 625°C, the quantity of the phase reduced due to formation of BCC_A2#2 between 625 and 611°C. The fourth phase HCP_A3 formed at 611°C and grows due to decline in quantity of BCC_A#2.

TTTI3 database had the liquid phase above 1542°C. Solidification to BCC_A2 begins at 1542°C and ends at 1512°C but only BCC_A2 was found between 1512°C and 815°C. The amount of BCC_A2 starts declining when the third phase C15_FCC was formed at 815°C. The decline reached a minimum value at 393°C when the fourth phase HCP_A3 was formed. All the three solid phases coexisted from 393°C to terminating temperature of 200°C.

BCC, and αTi were found experimentally, similar to SSOL4. The TTTI3 database predicted C15 Laves in addition to BCC and αTi.

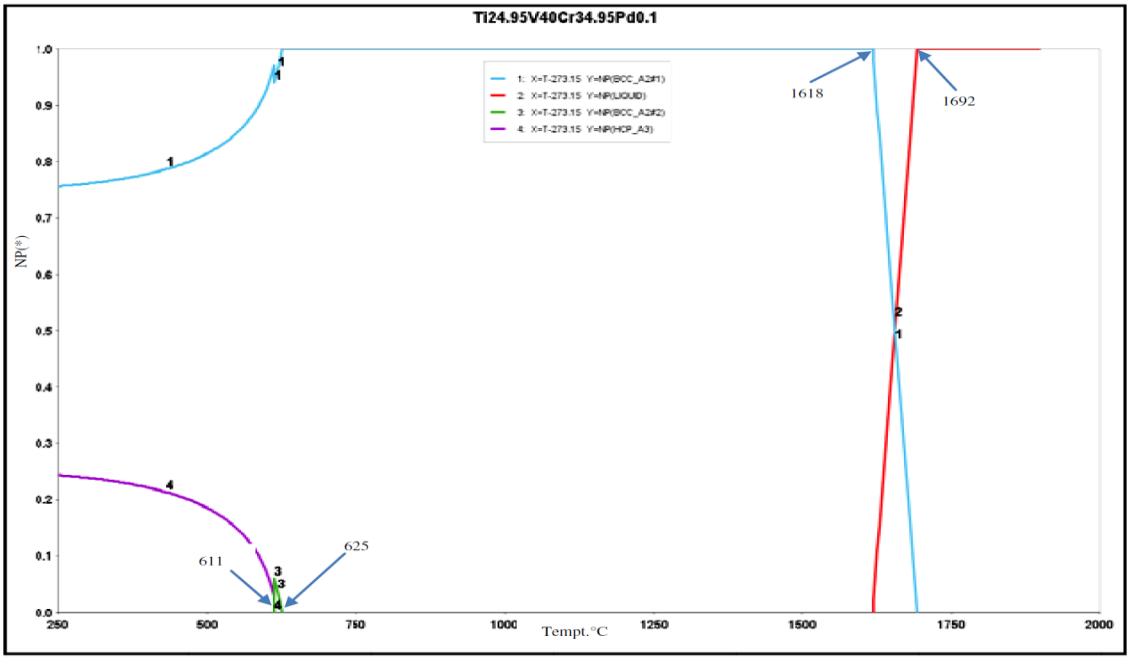

Figure 4.46. SSOL4 Thermo-Calc calculation of phases in A8.

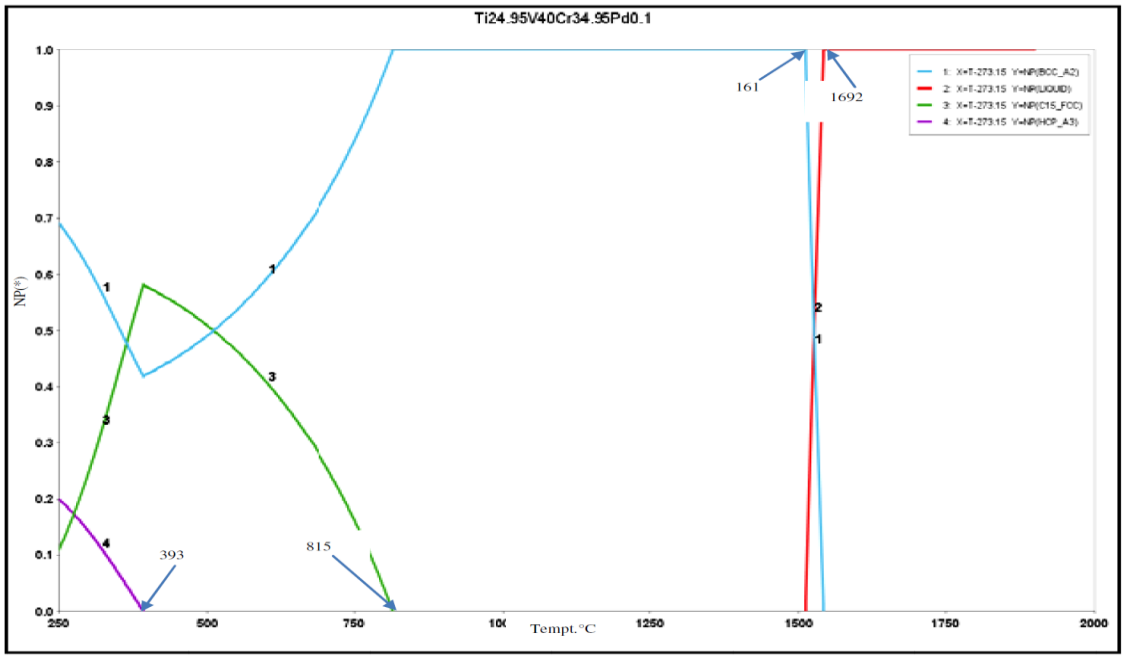

Figure 4.47. TTTI3 Thermo-Calc calculation of phases in A8.

Table 4.13. Summary of ThermoCalc calculations, listing the amount and composition of phase at 1000°C and 200°C in alloys A1 to A8.

Alloy	Data-base	Liquidus T (°C)	Solidus T (°C)	Structure	Phase	Start T (°C)	End T (°C)	1000°C					250°C				
								Amt (%)	Composition (at. %)				Amt (%)	Composition (at. %)			
									V	Ti	Cr	Fe		V	Ti	Cr	Fe
A1 $Ti_{25}V_{40}Cr_{35}$	SSOL4	1692	1619	BCC A2#1	-	1692		100	-	-	-	-	76		100.0	-	-
				BCC A2#2	-	627	610	-	-	-	-	-	0	-	-	-	-
				HCP A3	αTi	610	-	-	-	-	-	-	24	-	-	-	-
	TTTI3	1543	1512	BCC A2	BCC(V)	1543	-	100	40.3	23.7	36.0	0.0	69	53.1	0.9	46.0	--
				C15_ FCC	$\alpha TiCr_2$	815	-	-	-	-	-	-	11	10.2	32.0	57.8	-
				HCP A3	αTi	392	-	-	-	-	-	-	20	0.03	99.97		-
A2 $Ti_{24}V_{40}Cr_{34}Fe_2$	SSOL4	1685	1590	BCC A2#1	BCC(V)	1685		100	-	-	-	-	75	-	-	-	-
				BCC A2#2	-	750	401	-	-	-	-	-	0	-	-	-	-
				HCP A3	αTi	516	-	-	-	-	-	-	21	-	-	-	-
				FETI	FeTi	401	-	-	-	-	-	-	4	-	-	-	-
	TTTI3	1563	1492	BCC A2	BCC(V)	1536	-	100	40.2	22.7	34. 9	2.2	56	60.0	1.3	38.7	-
				C15_ FCC	$\alpha TiCr_2$	927	-	-	-	-	-	-	33	10.7	32.3	49.9	7.1
				HCP A3	αTi	354	-	-	-	-	-	-	11		100.0		
A3 $Ti_{25}V_{37}Cr_{33}Fe_5$	SSOL4	1678	1563	BCC A2#1	BCC(V)	1678	-	100	-	-	-	-	74	-	-	-	
				BCC A2#1	-	773	473	-	-	-	-	-	0	-	-	-	-
				HCP A3	αTi	400	-	-	-	-	-	-	18	-	-	-	-
				FETI	FeTi	400	-	-	-	-	-	-	8	-	-	-	-
	TTTI3	1530	1473	BCC A2	BCC(V)	1530	-	78	40.3	21.6	33.8	4.3	54	60.0	1.3	38.7	-
				C15_ FCC	$\alpha TiCr_2$	1000	-	22	21.7	33.2	35.1	10.0	35	10.7	32.3	49.9	7.1
				HCP A3	αTi	316	-	-	-	-	-	-	8	0.03	99.97	-	-
				TIM_B2	TiFe	287	-	-	-	-	-	-	3	-	46.2	-	53.8

Table 4.13 continued

Alloy	Data-base	Liquidus T (°C)	Solidus T (°C)	Structure	Phase	Start T (°C)	End T (°C)	1000°C					250°C				
								Amt (%)	Composition (at. %)				Amt (%)	Composition (at. %)			
									V	Ti	Cr	Fe		V	Ti	Cr	Fe
A4 $Ti_{22}V_{40}Cr_{32}Fe_6$	SSOL4	1670	1538	BCC A2#1	BCC(V)	1670	-	100	-	-	-	-	72	-	-	-	-
				BCC A2#2		796	398	0	-	-	-	-	0	-	-	-	-
				FETI	FeTi	705	-	0	-	-	-	-	12	-	-	-	-
				HCP A3	αTi	398	-	0	-	-	-	-	3	-	-	-	-
	TTTI3	1670	1538	BCC A2	BCC(V)	1670	-	90.4	42.1	19.4	32.7	5.8	55	60.0	1.3	38.7	
				C15_ FCC	$\alpha TiCr_2$	1000	-	9.6	20.6	33.2	32.8	13.4	32	10.7	32.3	49.9	7.1
				TIM_B2	TiFe	373	-	0	-	-	-	-	7	-	46.2	-	53.8
				HCP A3	αTi	293	-	0	-	-	-	-	6	0.03	99.97	-	
A5 $Ti_{24.97}V_{40}Cr_{34.98}Rh_{0.05}$	SSOL4	1692	1619	BCC A2#1	BCC(V)	1692	-	100	40.3	23.6	36.0	0.1	75	52.6	0.5	47.0	
				BCC A2#1		613	-	0	-	-	-	-	25	-	-	-	-
				HCP A3	αTi	626	613	0	-	-	-	-	0	0.06	99.50	0.01	0.45
	TTTI3	1542	1511	BCC A2	BCC(V)	1542	-	100	-	-	-	-	69	-	-	-	-
				C15_ FCC	$\alpha TiCr_2$	815	-	0	-	-	-	-	11	-	-	-	
				HCP A3	αTi	393	-	0	-	-	-	-	20	-	-	-	
A6 $Ti_{24.95}V_{40}Cr_{34.95}Rh_{0.1}$	SSOL 4	1692	1619	BCC A2#1	BCC(V)	1692	-	100	-	-	-	-	76	-	-	-	
				BCC A2#1	BCC(V)	626	613	0	-	-	-	-	0	-	-	-	
				HCP A3	αTi	613	-	0	-	-	-	-	24	-	-	-	
	TTTI3	1542	1511	BCC A2	BCC(V)	1542	-	100	-	-	-	-	43	-	-	-	
				C15_ FCC	$\alpha TiCr_2$	740	-	0	-	-	-	-	56	-	-	-	

Table 4.13 continued

Alloy	Data-base	Liquidus T (°C)	Solidus T (°C)	Structure	Phase	Start T (°C)	End T (°C)	1000°C					250°C				
								Amt (%)	Composition (at. %)				Amt (%)	Composition (at. %)			
									V	Ti	Cr	Fe		V	Ti	Cr	Fe
A7 $Ti_{24.975}V_{40}Cr_{34.975}Pd_{0.05}$	SSOL 4	1692	1619	BCC A2#1	BCC(V)	1692	-	100	-	-	-	-	76	-	-	-	-
				BCC A2#2	BCC(V)	625	614	0	-	-	-	-	0	-	-	-	-
				HCP A3	αTi	614	-	0	-	-	-	-	24	-	-	-	-
	TTTI3	1521	1512	BCC A2	BCC(V)	1512	-	100	-	-	-	-	69	-	-	-	-
				C15_ FCC	$\alpha TiCr_2$	815	-	0	-	-	-	-	11	-	-	-	-
				HCP A3	αTi	393	-	0	-	-	-	-	20	-	-	-	-
A8 $Ti_{24.95}V_{40}Cr_{34.95}Pd_{0.1}$	SSOL 4	1692	1618	BCC A2#1	BCC(V)	1692	-	100	-	-	-	-	75	-	-	-	-
				BCC A2#2	BCC(V)	625	611	0	-	-	-	-	0	-	-	-	-
				HCP A3	αTi	611	-	0	-	-	-	-	25	-	-	-	-
	TTTI3	1692	1618	BCC A2	BCC(V)	1692	-	100	-	-	-	-	69	-	-	-	-
				C15_ FCC	$\alpha TiCr_2$	815	-	0	-	-	-	-	11	-	-	-	-
				HCP A3	αTi	393	-	0	-	-	-	-	20	-	-	-	-

CHAPTER 5: Effect of Fe substitution and heat treatment on properties of as-cast $Ti_{25}V_{40}Cr_{35}$

Overview

This chapter assesses the effect of substituting equal amount of titanium and chromium with 2, 5 or 6 at.% iron on the microstructure, phases, hardness, corrosion behaviour and hydrogen storage characteristics of base alloy $Ti_{25}V_{40}Cr_{35}$. It also assesses the effect of heat treatment on these properties.

5.1. Effect of iron and heat treatment on the microstructure and phases

5.1.1 Effect of iron addition on microstructure and phases

The EDX analyses and crystallographic parameters of $Ti_{25-0.5x}V_{40}Cr_{35-0.5x}Fe_x$ (x = 0, 2, 5 6 at.%) alloys are shown in Table 5.1. The XRD patterns of the as-cast samples (from Figures 4.2, 4.4, 4.6 and 4.8) are presented in Figure 5.1.

The as-cast, Fe-free sample contained primary light grey and secondary dark phases (Table 5.1). The primary (V) phase contained ~43 at.% V while the dark phase had ~19 at.% V; their Ti/Cr ratios were 0.6 and 4.4 respectively. The primary phase constitute ~90 area % and the remaining ~10 area % is the secondary phase. The unit cell volume of the primary phase was 27.67 $Å^3$ while that of the secondary phase was 36.24 $Å^3$.

The V content in the main phase of the as-cast 2 at.% Fe sample increased marginally by 1.6%, but the Ti content decreased by 19.5% (Table 5.1). A C14 Laves phase with a higher Ti/Cr ratio was observed in the 2at.% Fe sample. The proportion of the main phase reduced from 89.7% in Fe-free sample to 78.5% in 2% Fe alloy; secondary phase increased to 20.2% while the remaining 1.3 area % was occupied by the third Phase. A reduction in cell volume from 27.67 to 27.08 $Å^3$ was observed in

the main phase of 2at.% Fe alloy due to lower atomic radius element Fe (1.72 Å^3) substituting larger atomic radius Cr (1.85 Å^3) and Ti (2 Å^3).

Table 5.1. EDX analyses and crystallographic parameters of as-cast $Ti_{35-0.5x}V_{40}Cr_{25-0.5x}Fe_x$ (x = 0, 2, 5, 6 at.%).

Fe content (at.%)	Phase	Composition (at.%)					Lattice parameters (Å)		Cell volume (Å^3)	Phase proportion (%)
		Ti	V	Cr	Fe	Ti/Cr ratio	a (Å)	c (Å)		
0	BCC	22.0 (0.7)*	42.8 (0.4)	35.2 (0.8)		0.6	3.0246	-	27.67	89.7
	αTi	66.1 (1.6)	18.9 (1.2)	15.0 (0.8)		4.4	2.98	4.72	36.24	10.3
2	BCC	17.7 (1.1)	43.5 (1.6)	36.5 (2.2)	2.3 (0.7)	0.5	3.003	-	27.08	78.5
	αTi	23.0 (3.7)	41.4 (2.4)	35.5 (1.4)	2.0 (0.2)	0.6	2.98	4.73	36.24	20.2
	C14 Laves	24.7 (0.8)	37.8 (0.7)	34.0 (0.4)	3.5 (0.3)	0.7	4.85	7.94	161.70	1.3
5	BCC	24.4 (2.8)	37.4 (2.5)	33.0 (1.0)	5.2 (3.1)	0.7	2.9981	-	27.00	67.5
	αTi	78.3 (5.4)	11.2 (2.9)	8.9 (2.0)	1.5 (0.6)	8.8	2.98	4.73	36.24	32.5
6	BCC	15.5 (2.2)	44.0 (2.5)	35.5 (0.4)	5.0 (4.9)	0.4	2.9981	-	26.95	75.0
	αTi	79.5 (5.4)	11.0 (2.7)	8.5 (2.5)	1.0 (0.2)	9.4	2.98	4.73	36.24	25.0

The V content in the primary phase of as-cast 5 at.% Fe decreased to 37.4 at.% while the Ti content increased to 24.4 at.%. The Ti content in the dark intergranular phase increased geometrically to 78.3 at.% thus increasing Ti/Cr ratio from 4.4 to 8.8 while the V content decreased to 11.2 at.%. The cell volume of the main phase was further reduced to 26.95 Å^3 because more of the smaller atomic radius Fe replaced larger radius Cr and V.

In the as-cast 6 at.% Fe sample, the V content in the main phase increased to 44 at.%, while the Ti content in the black intergranular αTi phase increased to 79.5 at.%, thus increasing the Ti/Cr ratio from 4.4 to 9.4 (Table 5.1). The variation of lattice parameter with Fe addition is shown in Figure 5.2.

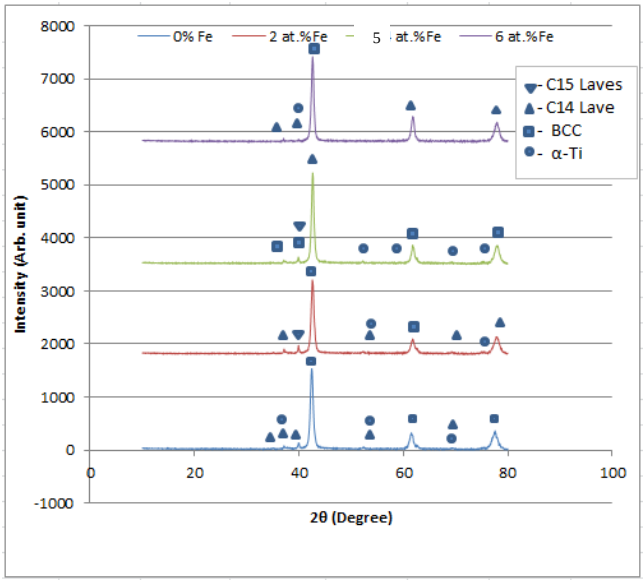

Figure 5.1. XRD patterns of as-cast $Ti_{25-0.5x}V_{40}Cr_{35-0.5x}Fe_x$ (x = 0, 2, 5, 6) alloys.

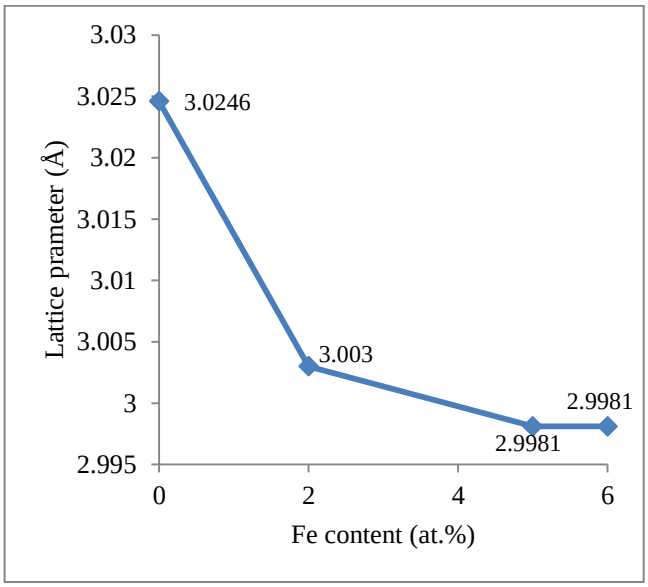

Figure 5.2. Variation of lattice parameter with Fe content.

The XRD patterns (Figure 5.1) showed the main peaks of vanadium BCC phase and minor peaks of C14-Laves, C15-Laves and (αTi) phases. Table 5.1 shows that addition of Fe reduced the primary phase cell volume but did not change that of the secondary phase. Image analysis of $Ti_{25}V_{40}Cr_{35}$ (using ImageJ 1.44 software [40]) revealed that the phase tagged "C" was dominant (~90 area %), with ~10 area % as

"D", therefore phase tagged C is the main peak of BCC (V) while D is the Laves phase.

Previous work shows that Laves, BCC and FCC are possible phases in Ti-V-Cr-Fe alloys. Jeong-Hyun[89] observed Laves and BCC phases in $Ti_{0.32}Cr_{0.43-x}V_{0.25}Fe_x$ ($0 \leq x \leq 0.10$), with the BCC phase dominating the structure of the alloys. Lin *et al.*[93] observed FCC and BCC structures in TiCrV and $Ti_{0.8}Cr_{1.2}V$ hydrogen storage alloys. Only the BCC (V) phase was observed in $Ti_{0.7}V_{0.3-x}Cr_x$ (x = 0.2 - 0.3) and $Ti_{0.8}V_{0.2-x}Cr_x$ (x = 0.07 - 0.2) alloys[159]. Huang *et al.*[171] found BCC and Laves phases in $TiCr_{1.8-x}(VFe)_x$. The XRD pattern of a Ti-25V-*x*Cr-(35-*x*)Mn alloy shows BCC and C14 Laves phases[208].

Similar to the findings in this work, Ulrich *et al.*[155] found BCC, C14 Laves and (αTi) in Ti-V-Cr-Fe alloys. The αTi cell volumes were: 41.54 $Å^3$ in $Ti_{30}V_{40}Cr_{22}Fe_8$; 41.43 $Å^3$ in $Ti_{32}V_{40}Cr_{20}Fe_8$ and 41.92 $Å^3$ in $Ti_{36}V_{40}Cr_{16}Fe_8$.

The observed phases in this work were also in agreement with those in the Ti-V-Cr ternary alloys of Itoh *et al.*[133] and Jeng *et al* [124], with a dominant BCC phase and secondary Laves phases in the ternary alloy.

In the work of Yan *et al.* [156], XRD patterns of V_x-$(Ti\text{-}Cr\text{-}Fe)_{100-x}$ (Ti/(Cr+Fe) = 1.0, Cr/Fe = 2.5, x = 20–55) alloys indicated BCC and Laves phases for < 30 at.% V and single phase (V) BCC for V ≥30 at.%. It was reported that 20 at.% V gave the highest amount of Laves phase which decreased and eventually disappeared as the V content increased.

Jeong-Hyun *et al.*[89] substituted Fe for Cr in $Ti_{0.32}Cr_{0.43-x}V_{0.25}$ ($0 \leq x \leq 0.10$) and found BCC and C14 Laves phases in the as-cast alloy. The Laves phase disappeared when the alloy was heat treated. Santos and Huot [65] found BCC solid solution and C14 Laves phase for all compositions of $Ti(FeV)_xCr_{1.2}$ (x= 0.4, 0.5, 0.6) at.%. With increased ferrovanadium substitution for chromium in $TiCr_{1.8-x}(VFe)_x$ (x = 0, 0.2, 0.4, 0.6, 0.8 at.%) alloy, Huang *et al.* [77] observed that the phase structure changed from single phase C14 Laves to BCC.

Table 4.3 shows that the primary phase of both the as-cast and annealed samples contained 2.3 at.% Fe, but the cell volume of the annealed sample was larger than that of the as-cast sample.

In Table 4.4, the amount Fe in the as-cast sample decreased from 5.2 to 4.3 at.% after annealing and increased to 6.1 at.% after quenching, whereas the cell volume of BCC phases of both heat treated samples were equal.

Modelling of phases in $Ti_{25-0.5x}V_{40}Cr_{35-0.5x}Fe_x$ (x = 0, 2, 5, 6 at.%) alloys

For comparison of predicted phases and the experimental phases, the liquid phase in Themo-Calc prediction was not considered because the samples were not heated to the melting point after the arc-melting. Secondly, only solid phases were determined by XRD. Phases labelled as BCC_A2#1 and BCC_A#2 were taken as BCC phase.

5.1.2. Effect of heat treatment on microstructure and phases

Figure 5.3 shows the effect of Fe and heat treatment on the phases of $Ti_{25-0.5x}V_{40}Cr_{35-0.5x}Fe_x$ (x = 0, 2, 5, 6 at.%) alloys. Figure 5.3 (a) showed that the Laves cell volume was unchanged after annealing the 0, 2 and 5 at.% Fe samples but increased in the 6% Fe sample. For both Fe-free and Fe-containing samples, the Laves cell volume increased after quenching, except in the 5% Fe alloy where the cell volume did not change. An increase in Laves cell volume was observed after quenching the 2% Fe alloy, while the increment was relatively small in the 0 and 6 at.% Fe samples.

Figure 5.3 (b) shows that the BCC cell volume of the as-cast 2 and 5 at.% Fe alloys increased after both heat treatments. However, the BCC cell volume decreased after annealing of the 0 and 6 at.% Fe alloys. Quenching increased the BCC cell volume in the 0 at.% Fe alloy, but decreased it in the 6 at.% Fe alloy.

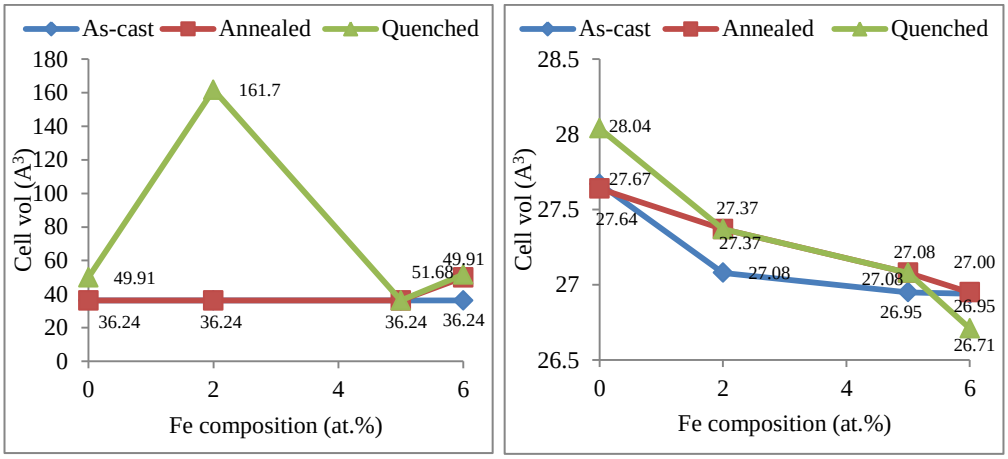

a) Laves phase b) BCC phase

Figure 5.3. Influence of Fe addition and heat treatment on cell volume.

For the Fe-free sample, Figure 5.3b shows that annealing marginally reduced the cell volume of BCC from 27.67 $Å^3$ in the as-cast sample to 27.64 $Å^3$, while quenching increased it to 28.04 $Å^3$. However, both annealing and quenching heat treatments increased the BCC cell volume to the same value in the 2 and 5% Fe alloys. The BCC cell volume in the 6 at.% Fe alloy reduced marginally after annealing, but relatively a high reduction was observed after quenching.

The atomic radius of Ti (2.00 Å) is greater than that of Cr (1.85 Å) and V (1.92 Å). Table 4.2 shows that the Ti content in the BCC phase decreased from 22 at.% (as-cast) to 18 at.% Ti in the annealed sample and increased to 25.1 at.% in the quenched sample. Therefore, the observed decrease in BCC cell volume after annealing could be attributed to decrease in Ti content in the phase, while the increase in cell volume after quenching was due to an increase in Ti content.

Table 4.2 shows that the Ti content in the Laves phase increased after annealing; the increase could have sufficiently compensated for the decrease in the at.% V and Cr in the phase, thereby suggesting the unchanged cell volume. After quenching the Fe-free sample, the total increase in Cr and V content was 21.5 at.%, while Ti decreased by 21.5 at.%, The combined effect of increase in at.% V and Cr compensate for the decrease in at.% Ti thereby leading to the observed increase in the Laves cell volume.

The EDX analysis of the 2 at.% Fe alloy in Table 4.3 shows that annealing dissolved the dark grey phase, increased the Ti content, and increased the Ti/Cr ratio from 0.6 to 4.4 in the Laves phase , and it is therefore surprising that the cell volume did not change. The composition of the main phase was not changed after annealing, although, the proportion and cell volume slightly increased. Quenching did not dissolve the third phase but increased its Ti content. The Ti/Cr ratio in all the three phases in the as-cast sample increased after quenching, suggesting the increase in cell volume.

In the as-cast 5 at.% Fe sample annealing led to the formation of (αTi) of the same cell volume as the C14 Laves (Table 4.4). A trace of an additional BCC phase having a cell volume of 28.26 $Å^3$ was also observed after annealing. The contents of both V and Cr in the BCC phase increased by 1.9, while that of Ti decreased by 2.8. The marginal increase in BCC cell volume therefore indicates that the combined increase in at.% V and Cr (3.8 at.%) more than compensates the effect of decrease in at.% Ti (2.8 at.%). A similar explanation applies to the increase in cell volume of BBC in the quenched sample of 5% Fe.

In Table 4.4, the αTi cell volume did not change after annealing because the decrease in at.% Cr and V was adequately compensated by the increase in Ti content. The compositions of Laves in as-cast and quenched samples were similar, hence giving the same cell volume, although quenching did not change the cell volume of Laves but reduced the abundance.

For the 6 %Fe alloy, annealing reduced the Ti/Cr ratio in the αTi phase, but had no significant effect on the EDX composition of the primary phase. The BCC cell volume reduced, while that of Laves increased after annealing. Quenching increased the αTi phase proportion, enriched V, Cr and Fe content but reduced at.% Ti in the phase.

Table 4.5 shows that the compositions of Ti, V and Cr were similar in annealed and as-cast samples of 6 at.% alloy, therefore the small decrease in the composition of Fe supports the marginal decrease in BCC cell volume after annealing. The increase in

composition of V, Cr and Fe compensates the decrease in Ti content, thereby explaining the observed increase in cell volume of αTi phase after quenching.

In Figure 5.3a the αTi cell volume is constant on the annealed and as-cast curves except in the 6 at.% Fe sample where a marginal increase was observed. However, on the quenched curve, the αTi cell volume fluctuates with increased Fe. Figure 5.3b shows that the BCC cell volume decreased with increased Fe content on all of the curves.

Short summary

The lattice parameters of the BCC in the base alloy decreased with increased Fe content. The SSOL4 calculations of the phases were closer to the experimental results than the TTTI3 database. Annealing increased the BCC cell volume, but had no effect on αTi cell volume in all compositions except for the annealed and quenched 6 at.% Fe alloy.

5.2 Effect of iron addition and heat treatment on hardness

5.2.1. Effect of iron addition on hardness of as-cast $Ti_{25}V_{40}Cr_{35}$ alloy

The averages of five Vickers hardness values of as-cast 0, 2, 5 and 6 at.% Fe samples are shown in Figure 5.4, while the effect of heat treatment on iron-containing samples is shown in Figure 5.5.

The Vickers hardness of $Ti_{25}V_{40}Cr_{35}$ increased from 415 to 430 HV_2 with addition of 2 at.% Fe (Figure 5.4). However, the hardness decreased slightly to 421 HV_2 at 5 at.% Fe and increased to 425 HV_2 at 6 at.% Fe.

The hardness value of Cr (1060 MPa) at room temperature is higher than V (628 MPa), Ti (970 MPa) and Fe (608 MPa).[105] Table 5.1 shows that the total Cr in the two phases of Fe-free sample is 50.2 at.% which decreases to ~ 42 at.% in the 5 at.% Fe alloy and 44 at.% in the 6 at.% Fe alloy. Therefore the reduction in Cr content promoted the decrease in hardness of 5 and 6 at.% Fe alloys. The highest hardness value observed in 2at.% Fe alloy was due to the high Cr content.

5.2.2. Effect of heat treatment on hardness

The effect of heat treatment on hardness of $Ti_{25-0.5x}V_{40}Cr_{35-0.5x}Fe_x$ (x = 0, 2, 5, 6 at.%) alloys are shown in Figure 5.4. Heat treatment decreased the hardness of the Fe-free sample, while the hardness of Fe-containing alloys increased after heat treatment. The increase was highest in the quenched 5 at.% Fe sample.

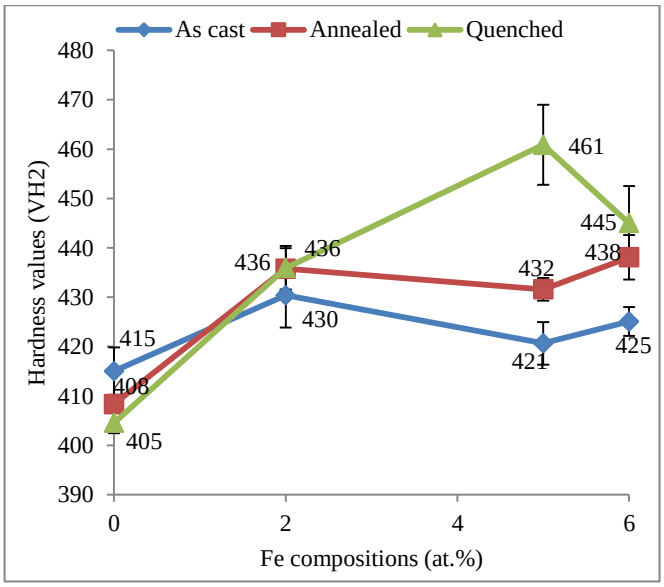

Figure 5.4. Effect of heat treatment on hardness values of $Ti_{25-0.5x}V_{40}Cr_{35-0.5x}Fe_x$ (x = 0, 2, 5, 6 at.%) alloys.

The hardness of the Fe-free sample reduced from 415 HV_2 in the as-cast sample to 408 HV_2 after annealing and 405 HV_2after quenching. Chromium had the highest hardness compared to Ti, Fe and V[105], thus a reduction in total Cr content after annealing could be responsible for the observed decrease in hardness.

For the 2% Fe alloy, an increase from 430 to 436 HV_2 was observed for both annealed and quenched samples. The hardness increased by 2.6% after annealing the 5% Fe alloy, although the increase was ~10% higher after quenching. For the 6at.% Fe alloy, the hardness increased from 425 HV_2in the as-cast sample to 438 $HV_2$and 445 HV_2 in the annealed and quenched samples respectively. The reason for the

increase in hardness, despite the reduction in Cr content in the alloy, needs further investigation.

Figure 5.4 shows that the hardness increased with increased Fe content (up to 5 at.% Fe) for the quenched samples, but addition of 6 at.% Fe decreased the hardness. However, the hardness values fluctuate with increased Fe content for the as-cast and annealed curves.

The effect of Fe on hardness of Ti-V-Cr alloy was not found in literature thus hindering any further comparison.

Short summary

Iron increased the hardness of the base alloy. Both annealing and quenching treatments increased hardness of the 2, 5, and 6 at.% Fe alloys, but reduced the hardness of the Fe-free sample.

5.3. Effect of iron addition and heat treatment on corrosion rate

5.3.1 Effect of iron addition on corrosion rate

The corrosion rates of $Ti_{25-x}V_{40}Cr_{35-x}$ (x = 0, 2 , 5, 6 at.%) alloys are shown in Figure 5.5. The corrosion rate decreased in the as-cast 2 at.% Fe sample, but increased in the 5 and 6 at.% Fe alloys. The Laves structures have been reported to have thinner oxide layers than BCC structures[55], and oxide layers are known for passivation[49, 150, 151]. It is therefore implied that for a dual-phase alloy like the alloys investigated, the corrosion rate will increase when the Laves phase proportion with thinner oxide layer increases. Therefore, the high proportion of Laves phases in the 5 and 6 at.% Fe samples suggests the reason for the observed increase in corrosion rate. Although the Laves phases proportion in the 2% Fe alloy was lower (Table 5.1), the alloy had a higher Cr content, which is well known for corrosion resistance[160], therefore the high Cr content could be responsible for the lower corrosion rate. The most corrosion resistant alloy was the as-cast 2 at.% Fe sample.

Literature on the effect of Fe on the corrosion rate of V-rich Ti-Cr-V alloys was not available, but the trend in this work (i.e. initial decrease in corrosion rate with 2 at.% Fe and increase in the rate with further addition of Fe) agrees with the findings of Tracy and Hungerford[160] and Swartzendruber and Bennett[161]: the rate of corrosion of a copper-rich Cu-Ni alloy could be reduced by adding a small amount of Fe (< 1.5 at.%), but further addition increased the corrosion rate.

5.3.2 Effect of heat treatment on corrosion rate

The Tafel curves for as cast, annealed and quenched $Ti_{25-0.5x}V_{40}Cr_{35-0.5x}Fe_x$ (x = 0, 2, 5, 6) alloys are presented in Figure 4.20 and the resulting corrosion rates in Figure 4.23. For ease of reference, the effect of heat treatment on corrosion rates of $Ti_{25-0.5x}V_{40}Cr_{35-0.5x}Fe_x$ (x = 0, 2, 5, 6) alloys is shown in Figure 5.5.

After annealing, the corrosion rates of 0, 5 and 6 at.% Fe alloys decreased, while the rate of the 2 at.% Fe increased. Quenching increased the corrosion rate of the 2 and 6 at.% Fe alloys but decreased the rate in the 0 and 5 at.% Fe alloys after quenching.

The corrosion rate of the Fe-free alloy decreased from 0.011 in the as-cast sample to 0.005 mm/y in the quenched sample and 0.001 mm/y in the annealed sample. Chromium is well known for inhibiting corrosion[160], therefore the decrease in Cr content in the as-cast sample (Table 4.2) after annealing suggests the decrease in corrosion rate.

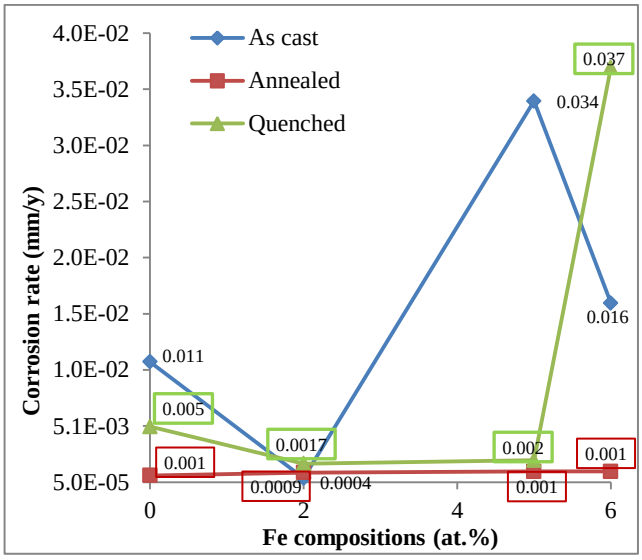

Figure 5.5. Effect of heat treatment on corrosion rate of $Ti_{25-0.5x}V_{40}Cr_{35-0.5x}Fe_x$ (x = 0, 2, 5, 6).

Table 4.3 shows that the as-cast 2 at.% Fe sample contained high Cr content, which suggests the reason for the observed low corrosion rate. However, the corrosion rate increased after heat treatment due to the decline in the total Cr contents.

It has been explained in Section 5.3.1 that Laves phases have low resistance to corrosion because of their thin corrosion passivating oxide layer; and BCC has a higher corrosion resistance due to the thicker oxide layer. Table 4.4 shows that the proportion of the BCC phase increased after heat treatment, thus explaining the observed decrease in corrosion rate in heat treated 5 at.% Fe alloy.

Table 4.5 shows that annealing increased the Cr content of the as-cast alloy, which could be responsible for the observed decrease in corrosion rate of the annealed 6 at.% Fe alloy. The Cr content in the quenched sample was higher than in the as-cast sample and the Laves phase proportion was lower. Combination of these two variables was expected to decrease the corrosion rate of quenched sample. Therefore, the reason for the increased corrosion rate should be subjected to further investigation.

The corrosion rate fluctuated with increased Fe composition in the as-cast curve. The rate initially decreased with increased Fe compositions on the quenched curve but

increased sharply at 6 at.% Fe sample, whereas the corrosion rate was similar between all Fe compositions.

Short summary

The highest corrosion rate was observed in the quenched 6 at.% Fe alloy and lowest in as-cast 2 at.% Fe alloy. The corrosion rate of the base alloy decreased with addition of 2 at.% Fe, but increased with the addition of 5 and 6 at.% Fe. Annealing increased the corrosion rate of the 2at.% Fe alloy, but decreased it in the 0, 5 and 6 at.% Fe samples. After quenching, the corrosion rates of the 0 and 5 at.% Fe alloys decreased, while the rate increased for the 2 and 6 at.% Fe alloys.

5.4. Effect of iron addition and heat treatment on hydrogen storage

5.4.1. Effect of iron addition on hydrogen storage properties of A1

Figure 5.6 shows the PCT ab/desorption isotherms measured at 303, 333 and 363 K for $Ti_{25-0.5x}V_{40}Cr_{35-0.5x}$ Fe_x (x = 0, 2, 5, 6 at.%) alloys. The pressure increased with hydrogen capacity on the absorption isotherms and decreased with hydrogen capacity on the desorption isotherms, similar to literature[97, 199, 202]. The trend is justified because, as the H pressure is increased by the Sievert apparatus, there are more H atoms that are absorbed onto the metal. When the H pressure is decreased during desorption, H atoms are released from the surface of the metal. For an alloy with a dual-phase structure, the phase with higher affinity attracts the H atoms first [10, 52, 55] *i.e.* the BCC phase is occupied before Laves.

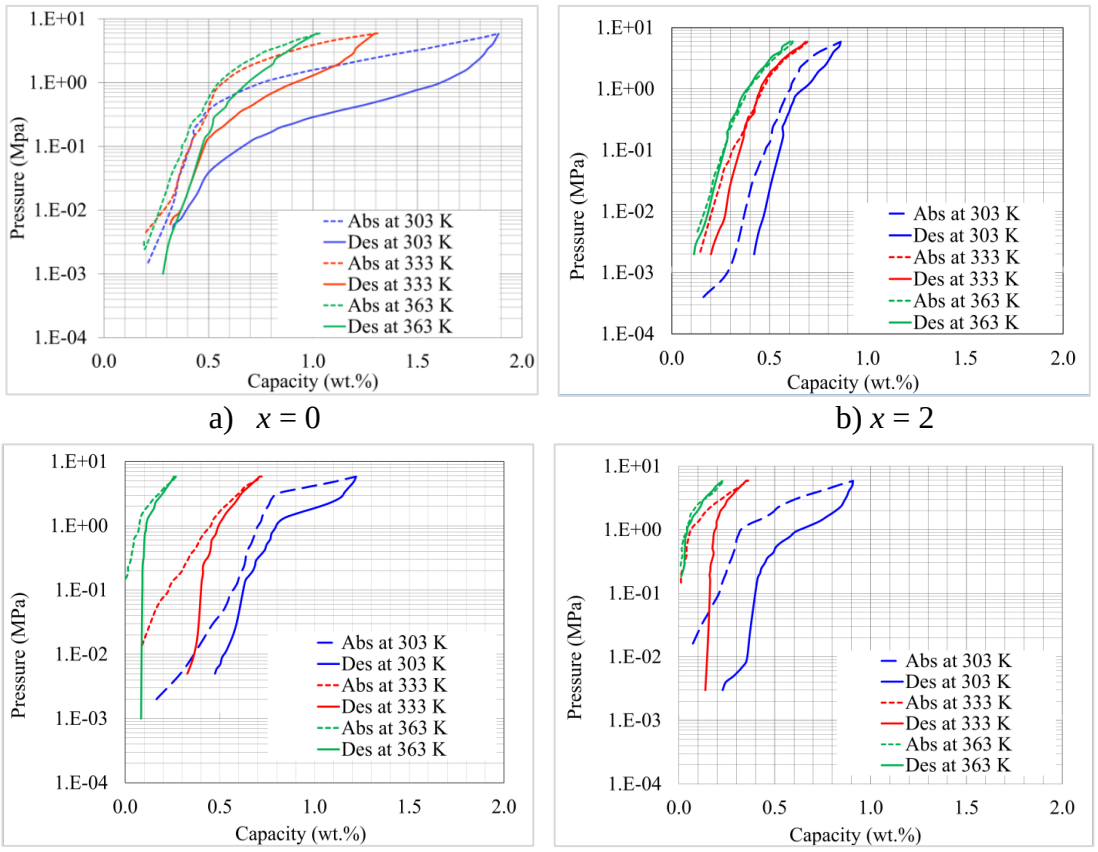

a) $x = 0$ b) $x = 2$

a) $x = 5$ d) $x = 6$

Figure 5.6. Absorption/desorption isotherms of $Ti_{25-0.5x}V_{40}Cr_{35-0.5x}Fe_x$ (x = 0, 2, 5, 6 at.%) alloys.

For practical applications in fuel cell, hydrogen desorption under ambient condition is desirable [5, 19, 67], therefore desorption curves of $Ti_{25-0.5x}V_{40}Cr_{35-0.5x}Fe_x$ (x = 0, 2, 5, 6 at. %) alloys at 303K are presented in Figure 5.7. The figure reveals that the plateau pressure rose with addition of Fe. It has already been shown in Figure 5.2 that the BCC cell volume decreased with increased Fe content in the alloy. The observed decrease in cell volume of BCC led to a reduction of H absorption sites, decrease in the distance between neighbouring hydrogen atoms and consequently the observed increase in plateau pressure. Earlier experimentalists[74, 110] also showed that increased BCC cell volume was favourable to H capacity and that Laves phases were detrimental to hydrogen absorption and desorption.

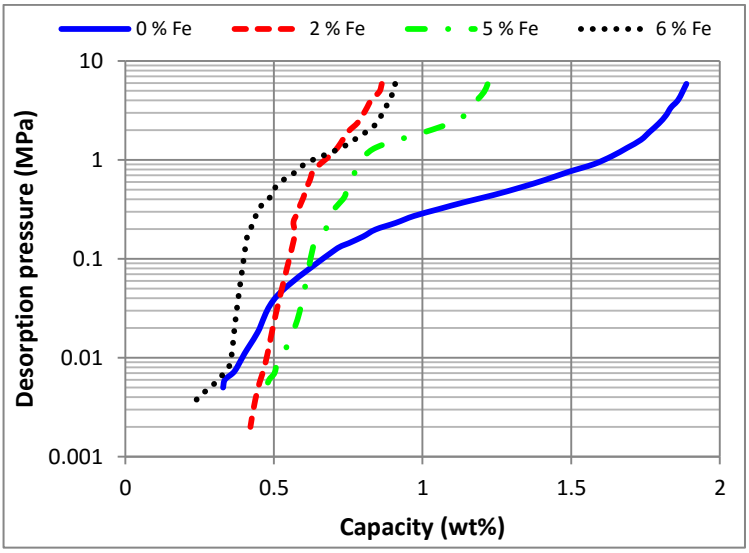

Figure 5.7. Effect of Fe on H desorption in $Ti_{25-0.5x}V_{40}Cr_{35-0.5x}Fe_x$ (x = 0, 2, 5, 6 at.%) alloys.

Table 5.2 shows that addition of Fe decreased the useful storage capacity. The Fe-free sample had the highest absorption capacity (1.89 wt%) and useful storage capacity (1.56 wt.%). The 2 at.% Fe sample had the lowest absorption and useful capacity of 0.89 and 0.44 wt% respectively; Yoo *et al.* [163] also found that substituting Fe for Cr was not favourable to hydrogen desorption. The effective capacity of Fe-free alloy (1.56 wt%) in this work is higher than an as-cast $Ti_{32}Cr_{46}V_{22}$ with an effective capacity of 1.35 wt%[96].

The Laves phases are known to be detrimental to H capacity, while the BCC phase promotes H capacity [63, 128, 198]. When there is an increase in the cell volume of BCC, the interstitial holes increase, thereby creating additional sites for H atoms to reside, consequently leading to higher H capacity. In this work, the increased Laves phase cell volumes decreased the H capacity. The high absorption and reversible capacity observed in the Fe-free sample could therefore be attributed to the high BCC cell volume, while the lowest storage capacity of 0.44 wt% at 2 at.% Fe was due to its large Laves cell volume (Table 5.1). This also explains the trend in Figure 5.8a, where the samples with large BCC cell volumes had high useful capacities and vice versa, while Figure 5.8b shows that samples with large Laves cell volumes had low useful capacities and vice versa.

Another observation fromn Table 5.2 is that the hydrogen capacity remaining as a percentage of the absorption capacity increased with Fe addition. During the absorption process in V-based alloys, two kinds of hydrides are formed *i.e.* mono-hydride (β-phase) and di-hydride (γ-phase) [172, 195]. The former are not easily decomposed, but the latter decompose easily under moderate conditions of temperature and pressure. Only ~17% of the absorbed hydrogen in the Fe-free alloy was not desorbed *i.e.* about 83 % was desorbed, implying that more γ-phase hydride was formed during the hydrogen absorption process (Table 5.2). The high capacity remaining in the 2 at.% Fe alloy implied that more mono-hydride was formed during the hydrogen absorption process.

Table 5.2. Hydrogen storage properties of $Ti_{25-0.5x}V_{40}Cr_{35-0.5x}Fe_x$ (x = 0, 2, 5, 6 at.%).

Fe content (at.%)	Absorption capacity (wt%)	Useful capacity (wt%)	Capacity remaining (wt%)	Capacity remaining as % of absorption capacity	Plateau pressure (MPa)
0	1.89	1.56	0.33	17.46	0.41
2	0.89	0.44	0.45	50.56	1.30
5	1.21	0.75	0.46	38.02	1.92
6	0.90	0.68	0.22	24.44	1.34

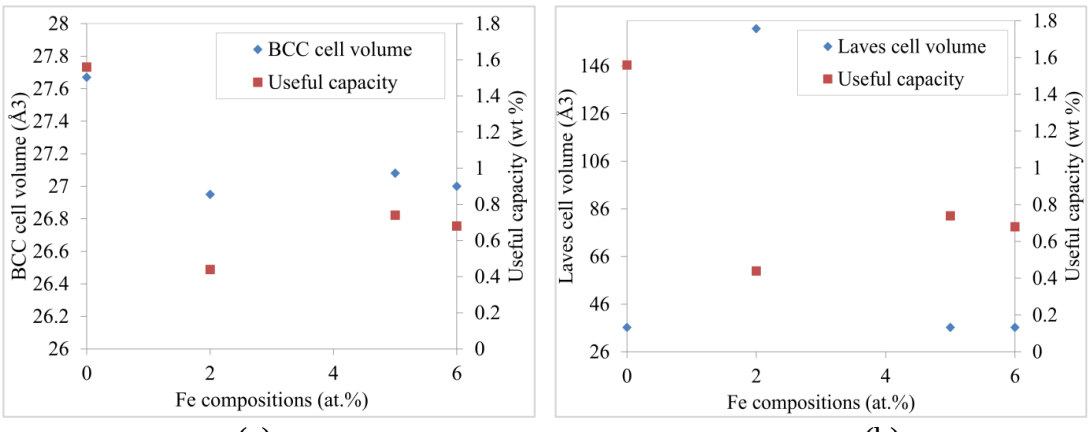

(a) (b)

Figure 5.8. Influence of (a) BCC cell volume and (b) Laves cell volume on useful capacity.

5.4.2. Effect of isotherm temperature on absorption capacity.

Figure 5.9 shows that the maximum absorption capacity decreased with increased isotherm temperature for all Fe compositions: this observation is similar to literature [63, 205, 215]. At lower temperatures the kinetic energy of the gas is low, thereby making it easier for the host metal to absorb the less energised gas. However, at higher temperature the gas has a higher kinetic energy and moves with higher velocity, thereby hindering absorption[19]. This explains the observed inverse relationship between the isotherm temperature and maximum absorption capacity.

The observed decrease in H desorption and increase in plateau pressure at higher testing (isotherm) temperatures is consistent with the findings of Mi *et al.*[170], Jeong-Hyun *et al.*[89] and Taizhong *et al.*[78]. Mi *et al.*[70] measured hydrogen desorption of $Ti_{27.25}Cr_{28.05}V_{37.25}Fe_{7.45}Ce_{1.0}$ at 25 - 180°C and found that desorption decreased as temperature increased, *i.e.* the highest desorption was achieved at 25°C. In the work of Jeong-Hyun *et al.*[89], desorption isotherms of a $Ti_{0.32}Cr_{0.43}V_{0.25}$ alloy measured at 30- 150°C showed that the highest usable hydrogen of 2.63 wt% was achieved at 30°C. Huang *et al.*[110] measured the desorption isotherms of $TiCr_{1.2}(VFe)_{0.8}$, *i.e.* $(Ti_{32}Cr_{38}(VFe)_{27})$ at 0°C, 30°C and 60°C and found that the hydrogen absorption/desorption increased with decreased temperature. The maximum usable hydrogen content of 3.2 wt% was achieved at 0°C.

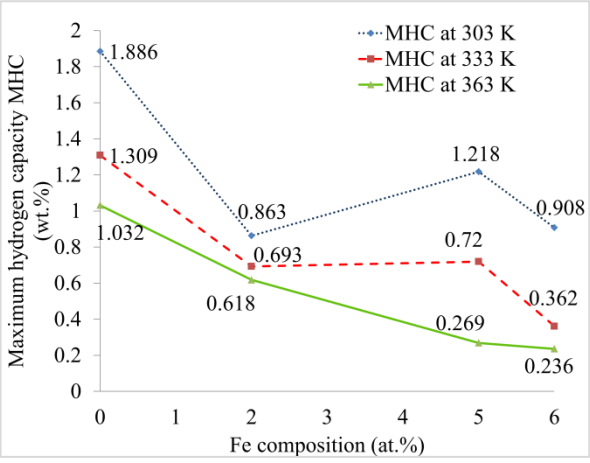

Figure 5.9. Effect of isotherm temperature on maximum H capacity of the Fe alloys.

5.4.3. Effect of heat treatment on hydrogen storage properties

The influence of heat treatment on RHSC of the alloys is shown in Figure 5.10. Both treatment processes increased the useful storage capacity in the 2 at.% Fe alloy and reduced it in the 0 and 6 at.% Fe alloys. The useful capacity of the 5 at.% Fe alloy increased after annealing but the capacity decreased after quenching.

In the Fe-free sample, the RHSC decreased after heat treatment. Annealing reduced the capacity from 1.56 to 1.42 wt%, while quenching reduced it to 0.96 wt%.The decrease in BCC cell volume (Table 4.2) explains the reduction in capacity for the annealed sample. The increase in Laves cell volume seems to have compensated for the small increase in BCC cell volume, thus could be responsible for the observed decrease in capacity of the quenched sample.

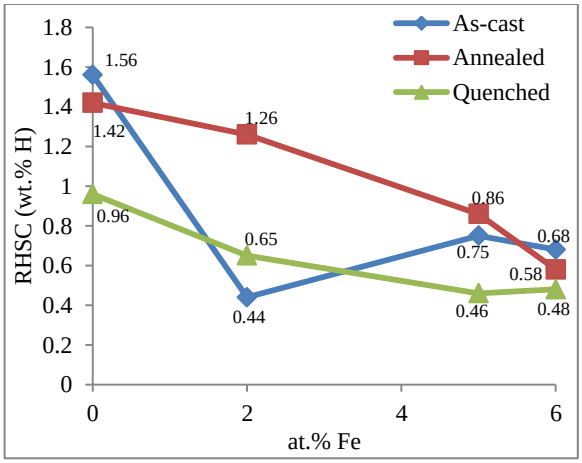

Figure 5.10. Effect of %Fe in heat treated sample on RHSC of $Ti_{25-0.5x}V_{40}Cr_{35-0.5x}Fe_x$ (x = 0,2,4,6).

Literature has shown that the BCC phase enhances H capacity[10, 52, 55], as an increase in BCC cell volume implies the availability of more space leading to increased storage capacity. Laves phases are detrimental to storage capacity[26, 73, 166, 210], *i.e.* alloys with larger Laves cell volumes or high Laves proportions are known for lower hydrogen capacity.

The plateau property is affected by both the homogeneity and oxygen content in Ti-V based hydrogen storage alloys[210]. Inhomogeneity of microstructure can be minimized by heat treatment at higher temperatures for a short time [69].

The Laves cell volume of the as-cast Fe free sample did not change after annealing (Table 4.2), therefore the decrease in capacity after annealing was due to the decrease in BCC cell volume. For the quenched sample, the increase in BCC cell volume was 1.3%, while the Laves cell value increased by 27.4%. The enlargement of the Laves cell volume therefore counteracts the increase in BCC cell volume, thereby giving a reason for the observed decrease in useful capacity after quenching.

Table 5.3 shows that the plateau pressure of as-cast Fe-free alloy decreased after annealing, but increased after quenching. The observed reduction in plateau pressure after annealing is explained by the homogenized microstructure. In addition, the sample was annealed in vacuum-sealed quartz tube, thereby preventing oxygen intake. The quenched sample was exposed to oxygen in the quenching medium, therefore the rise in plateau pressure could be due to the higher oxygen content.

The enthalpy and entropy of hydride formation increased after both treatment processes. The interstice volume in the alloy decreased when the lattice parameter contracted. This volume reduction lead to reduced metal-hydrogen distances, hence increased the binding energy. The contraction of the lattice parameter of the primary phase after heat treatment of the Fe-free alloy explains the increase in enthalpy and entropy.

Figure 5.10 shows that both treatment processes increased the reversible hydrogen storage capacity RHSC of the 2 at.% Fe alloy. The capacity increased from 0.44 to 1.26 wt% after annealing, and to 1.26 wt% in quenched sample. The observed increase in useful capacity after heat treatment was due to the increase in BCC cell volume as shown in Table 4.3. Annealing removed the larger cell volume Laves phase in as-cast sample, this suggests another reason for the higher hydrogen capacity observed in the annealed sample. The observed $P4_2/mnm$ *(136)* space group in the quenched alloy was not detrimental to hydrogen capacity, otherwise its large cell volume should have made the capacity decrease.

Table 5.3 also shows that the plateau pressure of the 2 at.% Fe alloy decreased after annealing from 1.32 to 0.68 MPa, and increased to 2.34 MPa after quenching. In order to plot a van't Hoff curve and calculate the enthalpy ΔH and entropy ΔS, there must be plateau in three P-C isotherms. Otherwise, if only two of the isotherms had a plateau (hence a known plateau pressure), the enthalpy and entropy can be obtained by solving the van't Hoff equation (Equation 2.1) simultaneously. However, if only one of the isotherms had a plateau, the enthalpy and entropy cannot be evaluated. For this reason, there is no information on ΔH and ΔS (in Table 5.3) for the heat treated samples of the Fe-containing alloys.

Table 5.3. Effect of heat treatment on H capacity and plateau pressure of $Ti_{25-0.5x}V_{40}Cr_{35-0.5x}Fe_x$ (x = 0, 2, 4, 6) at 303K.

x	Sample	Absorption capacity (wt%)	Capacity remaining (wt.%)	Useful capacity (wt%)	Capacity remaining as % of absorption capacity	Plateau pressure (MPa)	ΔH (kJ/mol H_2)	ΔS (J/mol.K)
0	As-cast	1.89	0.33	1.56	17	0.41	40.59	121.49
	Annealed	1.76	0.34	1.42	19	0.09	45.90	131.9
	Quenched	1.20	0.25	0.95	21	0.90	27.43	89.6
2	As-cast	0.86	0.42	0.44	49	1.32	110.4	36
	Annealed	1.54	0.28	1.26	18	0.68	-	-
	Quenched	1.04	0.39	0.65	38	2.34	-	-
5	As-cast	1.22	0.47	0.75	39	1.92	51.8	22.57
	Annealed	1.17	0.31	0.86	26	1.86	-	-
	Quenched	0.85	0.40	0.46	47	-	-	-
6	As-cast	0.91	0.23	0.68	25	1.34	31.5	106.2
	Annealed	0.97	0.39	0.58	40	-	-	-
	Quenched	0.87	0.39	0.48	45	-	-	-

The useful hydrogen capacity of the 5 at,% Fe alloy increased after annealing and decreased after quenching. Table 4.4 shows that cell volume of the primary phase increased slightly from 26.95 $Å^3$ in as-cast sample to 27.08 $Å^3$ after annealing: a small proportion of another BCC phase was also observed. The combined effects of increased cell volume of the primary phase and the small proportion of BCC after annealing agrees with the increase in the observed capacity. The additional Laves

phase formed after quenching could be responsible for the decline in H capacity of the quenched sample.

The plateau pressure of the 5 at.% Fe alloy reduced after annealing, due to the enlarged cell volume of primary phase. The mechanism of reduction in the plateau pressure due to enlargement of cell volume has been discussed in the earlier part of this section. A steep isotherm was obtained in the quenched sample (i.e. no plateau and plateau pressure).

Table 5.3 shows that the useful hydrogen capacity of the 6 at.%Fe alloy decreased after heat treatment. Table 4.5 shows that the BCC cell volume decreased and the Laves cell volume increased due to heat treatment. The combined effect of decreased BCC cell volume and increased Laves cell volume was responsible for the reduction in hydrogen capacity after heat treatment. The plateau pressure for the 303K isotherm was 1.34 MPa and there was no plateau in 333K and 363K isotherms.

Liu *et al.* [141] reported that annealing reduced hydrogen absorption pressure and that prolonging the annealing time of $Ti_{1.02}Cr_{1.1}M_{0.3}Fe_{0.6}$ flattened the desorption plateau and reduced the plateau pressure of the alloy. The hydrogen desorption capacity and activation properties of $V_{35}Ti_{20}Cr_{45}$ was enhanced by heat treating the alloy at 1223 K for 72 hours [214]. It was reported that as-cast $Ti_{10}V_{77}Cr_6Fe_6Zr_6$ was heat treated at 1373 K for 8 h and 1523 K for 5 min and quenched; the plateau was flattened, but hydrogen storage capacity decreased after heat treatment [54]. The findings are in agreement with 2 and 4 at.% Fe compositions in this work, where annealing enhanced hydrogen storage.

Short summary

The highest absorption and useful capacity was obtained in the as-cast Fe-free sample, while the lowest value was in the as-cast 2 at.% Fe alloy. The absorption and useful capacity reduced with addition of Fe. Both treatments increased the useful capacity of the 2 at.% Fe alloy, but decreased the capacity in the 0, 5 and 6 at.% Fe alloys.

Summary of the chapter

All the alloys contained BCC (V) and Laves phases. The corrosion rate initially decreased with the addition of 2 at.% Fe, and later increased with the addition of 5 and 6 at.% Fe. The lowest corrosion rate (0.0004 mm/y) and highest hardness (430 HV_2) was observed in the sample with 2 at.% Fe, which had the highest phase proportion of C14 Laves. An increase in isotherm testing temperature resulted in decreased hydrogen desorption capacity and increased plateau pressures of the alloys. Addition of Fe to the base alloy decreased the RHSC and increased the pressure of the plateau. Thus, the optimum RHSC was achieved at 303K and 0 at.% Fe, which had the smallest cell volume of Laves.

CHAPTER 6: Effect of rhodium substitution and heat treatment on properties of $Ti_{25}V_{40}Cr_{35}$

Overview

This chapter assesses the effect of substituting equal amounts of chromium and titanium with 0.05 and 0.10 at.% Rh on the microstructure and phases, hardness, corrosion resistance and hydrogen storage properties of the base alloy $Ti_{25}V_{40}Cr_{35}$ (A1). It also assesses the effect of heat treatment of the Rh-containing alloys on the microstructure and properties.

6.1. Effect of rhodium addition and the heat treatment on the microstructure and phases

To evaluate the effect of Rh additions on $Ti_{25}V_{40}Cr_3$, EDX and XRD crystallographic data of the phases identified in the as-cast 0, 0.05 and 0.10 at.% Rh samples were extracted from Tables 4.2, 4.6 and 4.7 respectively, and presented in Table 6.1 for ease of reference.

Similarly, the EDX analyses for heat treated 0, 0.05 and 0.10 at.% Rh samples were extracted from Tables 4.2, 4.6 and 4.7 respectively. The $Ti_{25-0.5x}V_{40}Cr_{35-0.5x}Rh_x$ (x = 0, 0.05, 0.10 at.%) alloys' respective XRD patterns (as-cast, annealed and quenched from Figures 4.2, 4.10 and 4.11) are presented in Figure 6.2 for ease of reference.

6.1.1. Effect of rhodium addition on the microstructure and phases

The as-cast microstructure and phases in $Ti_{25}V_{40}Cr_{35}$ alloy (Rh-free) were discussed in Section 5.1. When 0.05 at.% Rh was substituted for Cr and Ti in $Ti_{25}V_{40}Cr_{35}$, the resulting structure was primary bcc (V) with intergranular Laves phase and solid state precipitation surrounding the intergranular Laves regions, as shown in Figure 4.9 (b). A similar structure was observed with addition of 0.10 at.% Rh (Figure 4.12

b) but the precipitates was less prominent. Table 6.1 shows that with the addition of 0.05 at.% Rh, there was no significant increase in cell volume of Laves, while that of BCC was slightly reduced (Figure 6.3 a). In the as-cast 0.10 Rh alloy, the cell volume of BCC increased from 27.67 $Å^3$ in Rh-free to 27.75 $Å^3$ while that of Laves decreased from 36.24 $Å^3$ to 34.48 $Å^3$.

Table 6.1: EDS of as-cast $Ti_{25-0.5x}V_{40}Cr_{35-0.5x}Rh_x$ (x = 0, 0.05, 0.10)

Sample	Phases XRD	Compositions * (at.%)				Phase proportion (% area)	Phase description			
		Ti	V	Cr	Rh		Space group (No.)	a (*Å*)	c (*Å*)	Cell vol. ($Å^3$)
A1 (x=0)	BCC (V)	22.0 (0.7)	42.8 (0.46)	35.2 (0.82)	-	88.5	*Im*3*m* (229)	3.0246	-	27.67
	αTi	66.1 (1.6)	18.9 (1.2)	15.0 (0.8)	-	11.5	*P*6$_3$/*mmc* (194)	2.98	4.72	36.24
A5 (x=0.05)	BCC (V)	28.5 (3.8)	38.8 (2.2)	32.7 (1.7)	-	82.7	*Im*3*m* (229)	3.0257	-	27.70
	αTi	71.8 (5.8)	14.6 (3.0)	13.5 (2.8)	0.5 (0.4)	17.3	*P*6$_3$/*mmc* (194)	2.98	4.73	36.25
A6 (x=0.10)	BCC (V)	20.10 (2.8)	42.4 (3.2)	37.5 (6.1)	-	88.0	*Im*3*m* (229)	3.0275	-	27.75
	αTi	62.3 (6.3)	19.1 (3.4)	18.6 (3.2)	0.5 (0.4)	12.0	*P*6$_3$/*mmc* (194)	2.95	4.67	34.48

*Standard deviation in parentheses

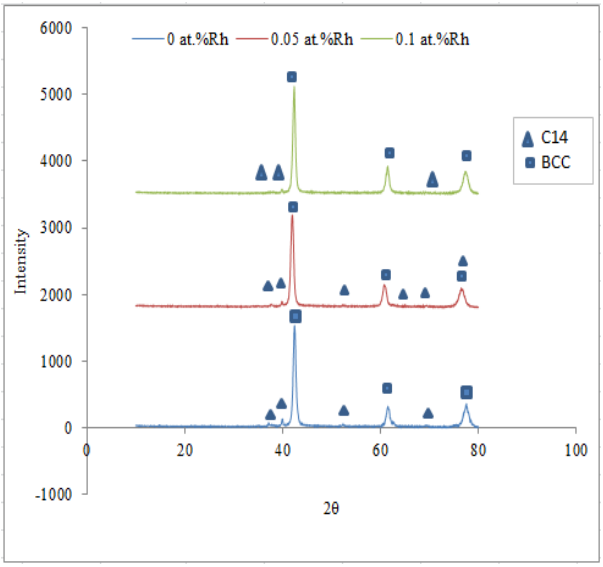

Figure 6.1. XRD patterns of as-cast $Ti_{25-0.5x}V_{40}Cr_{35-0.5x}Rh_x$ (x = 0, 0.05, 0.10) at.% alloy.

Table 4.6 shows that only the αTi phase of the as-cast 0.05% Rh sample had a detectable amount of Rh, and the highest phase proportion of 37.8 area % was observed. The αTi phase proportion declined to 32.2 and 31.4 area % in the annealed and quenched samples respectively. This implies that 0.05 at.% Rh was favourable for αTi phase formation, whereas heat treatment reduced the proportion of αTi.

The αTi phase in the as-cast 0.10 Rh sample had the smallest cell volume of 34.48 $Å^3$ compared to αTi in annealed (167.81 $Å^3$) and quenched (49.99 $Å^3$) samples, as shown in Figures 6.1 and 6.3.

The Thermo-Calc phase predictions in the Fe-, Rh- and Pd-containing alloys were very similar to that of the base alloy A1. SSOL4 predicted BCC (V) and αTi (HCP A3) phases for both 0.05 and 0.10 Rh alloys. The TTTI3 database gave only BCC (V) and C15_FCC Laves phases for the 0.10 Rh alloy.

Phases found experimentally in the 0.05 Rh alloy were BCC (V) and αTi, indicating that the SSOL4 prediction is closer to experimental result than TITI3 because an additional C15 Laves was predicted. For the 0.10 Rh alloy, the experimental phases were BCC, αTi and Laves.

6.1.2 Effect of heat treatment on the microstructure and phases

The effect of heat treatment on phases of the Rh-free alloy was discussed in Section 5.1. Figure 6.2 are the XRD patterns of as-cast and heat treated $Ti_{25-0.5x}V_{40}Cr_{35-0.5x}Rh_x$ (x = 0, 0.05, 0.10 at.%) alloy while Figure 6.3 shows the effect of heat treatment on the cell volume of the phases. Annealing increased the αTi cell volume to the same value in all Rh-containing alloys. In 0.05 at.% Rh, Figure 6.3a shows that the αTi cell volume of the as-cast sample increased after both treatments, from 34.48 to 49.99 $Å^3$ after quenching, but increased to 167.81 $Å^3$ after annealing. The cell volume of the V-rich BCC phase in the 0.05Rh alloy increased to 28.09 $Å^3$ after annealing, but quenching had no effect on the volume.

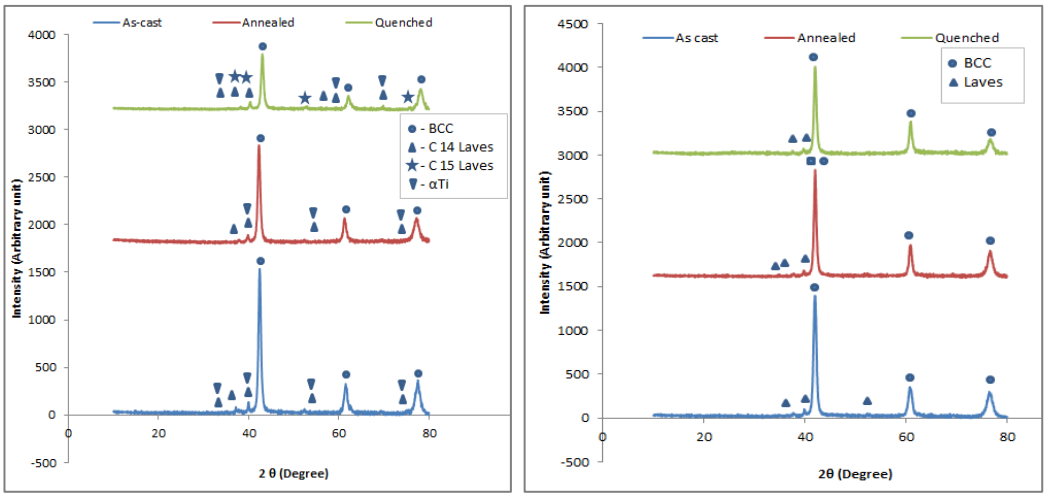

a) 0 at.% Rh alloy b) 0.05at.% Rh alloy

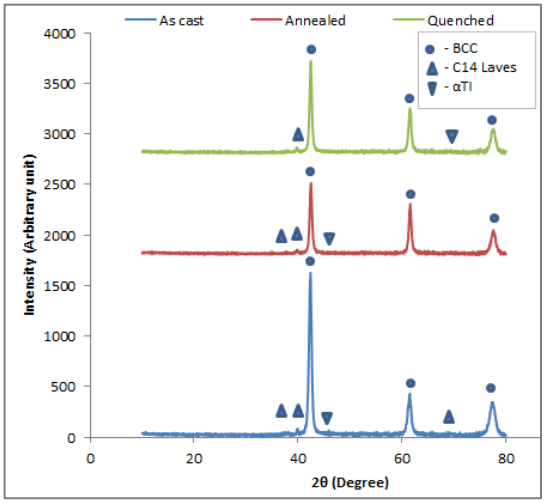

c) 0.10at.% Rh alloy

Figure 6.2. XRD patterns of as cast and heat treated $Ti_{25-0.5x}V_{40}Cr_{35-0.5x}Rh_x$ (x = 0, 0.05, 0.10 at.%) alloy.

For the 0.10 Rh alloy, a noticeable increase in Laves cell volume was observed after both treatments. The Laves cell volume increased from 35.3 to 167.81 $Å^3$ (C14 Laves) after annealing, while quenching increased the volume to 334.5 $Å^3$ (C36 Laves). However both treatments had no effect on the volume of BCC in the 0.10 Rh alloy.

The EDX analyses in Table 4.6 show a reduction in phase proportion of αTi from 75.7% in the as-cast alloy to 45.5% in the annealed and 36% in the quenched sample.

Figure 6.3a shows that with addition of Rh the cell volume of Laves in the annealed alloys did not change, but increased in the quenched alloys. The BCC cell volume of

the annealed alloys (Figure 6.3 b) increased with addition of 0.05 at.% Rh, but remained constant with the further addition to 0.10 at.% Rh. The BCC cell volume in the quenched alloys decreased from 36.15 $Å^3$ in the base alloy to 28.09 $Å^3$ in both the 0.05 and 0.10 at.% Rh alloys.

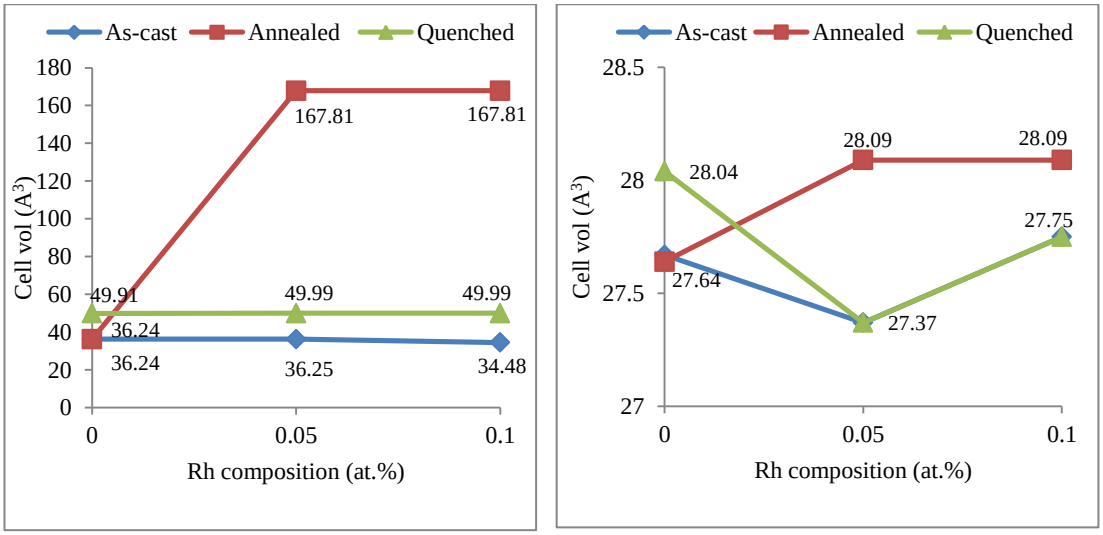

a) αTi phase b) BCC phase

Figure 6.3. Effect of Rh substitution and heat treatment on cell volume of BCC and Laves phases.

Addition of PGMs to the Ti-V-Cr system has not been reported, but Pd additive to other Ti-V metals for hydrogen storage has been reported. Jen and Wu[211] investigated the plastic deformation and hysteresis for hydrogen storage in Pd-Rh alloys but the phase structure was not reported. However, Ashworth *et al.*[164] mentioned that the main phase in a Pd-modified Ti alloys produced by powder metallurgy was BCC. It has been reported that XRD peaks of as-prepared Mg-La-Pd trilayer film included peaks of Mg(002) and Pd(111)[103]. Liu *et. al*[184]. reported C14 Laves and V-based solid solution phase in $Ti_{0.8}Zr_{0.2}V_{2.7}Mn_{0.5}Cr_{0.8}Ni_{1.0}Pd_x$ (x = 0 – 0.2).

Summary

The as-cast and heat treated alloys contained BCC (V) and αTi phases, but EDX undetectable amount of αTi was also found in as-cast sample of 0 and 0.10 at.% Rh alloys. Addition of Rh changed the αTi cell volume in both the 0.05 and 0.10 at.%

Rh alloys. The cell volume of BCC decreased with addition of 0.05 at.%Rh, but increased in the 0.10 at.% Rh alloy. Heat treatment had no effect on the BCC cell volume in the 0.10 at.% Rh alloys. The largest BCC cell volume was 28.09 $Å^3$. The quenched 0.10 at.% Rh sample had the highest Laves cell volume (334.5 $Å^3$). The presence of Rh in phases of the alloys had no effect on their cell volumes. The Thermo-Calc prediction of two phases in 0.05 and 0.10 at.% Rh alloys agreed with the experimental results.

6.2. Effect of rhodium addition and heat treatment on hardness

6.2.1. Effect of rhodium addition on hardness

The average of five Vickers hardness values of the as-cast, annealed and quenched 0, 0.05 and 0.10 at.% Rh samples are shown in Figure 6.4. The hardness of the as-cast $Ti_{25}V_{40}Cr_{35}$ alloy decreased slightly with Rh additions. The αTi phase has a higher hardness than BCC (V).[112] The higher proportion of αTi in the Rh-containing alloys should lead to higher hardness. Contrarily, the Rh-containing as-cast alloys were softer, therefore this finding is recommended for further investigations.

For the annealed samples, there was no significant change in hardness with addition of 0.05 at.% Rh, but a large reduction was observed with addition of 0.10 at.% Rh. There was a slight increase in hardness for the quenched samples with addition of 0.05 at.% Rh, but a 10 HV decrease with addition of 0.10 at.% Rh.

6.2.2. Effect of heat treatment on hardness

The effect of heat treatment on the Rh-free base alloy was discussed in Section 5.2. Figure 6.4 shows that both treatments only slightly increased the hardness of the alloys with 0.05 at.% Rh, but with addition of 0.10 at.% Rh, a noticeable decrease in hardness was observed after heat treatment.

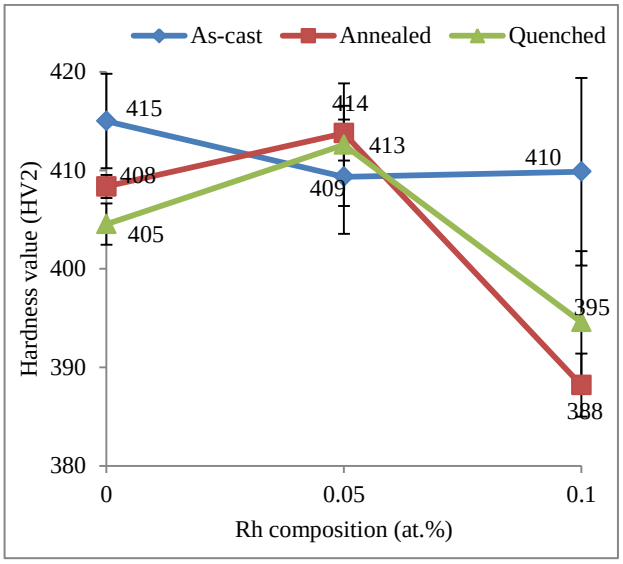

Figure 6.4. Effect of rhodium additions and heat treatment on hardness.

Summary

Addition of 0.05 at.% Rh had no significant effect on hardness value for any alloy condition. However at 0.10 at.% Rh, heat treatment reduced the hardness substantially. The quenched 0.1 at.% Rh sample has the lowest hardness of 388 HV, while the annealed 0.05 sample had the highest HV of 414 of the Rh-added alloys.

6.3. Effect of rhodium addition and heat treatment on corrosion properties

6.3.1. Effect of rhodium addition on corrosion

The Tafel curves for the as-cast $Ti_{25-0.5x}V_{40}Cr_{35-0.5x}Rh_x$ (x = 0, 0.05, 0.10 at.%) samples are shown in Figure 6.5 and the corresponding corrosion rates of the alloys are shown in Figure 6.6.

Addition of Rh decreased E_{corr} of the as-cast Rh-free alloy from -767 mV to -793 mV (0.05 Rh) and -825 mV (0.10 Rh) as shown in Figure 6.5. The corrosion current also decreased with increased Rh: from 1 μA/cm^2 in as-cast Rh-free alloy to 0.77 μA/cm^2 for the 0.05 at.% Rh alloy, and 0.37 μA/cm^2 for the 0.10 at.% Rh alloy.

Addition of 0.05 at.% Rh reduced the corrosion rate from 0.0110 to 0.0009 mm/y, but only to 0.001 mm/y with addition of 0.10 at.% Rh. Rhodium is one of the noble

metals known as good corrosion inhibitors[103], so the observed reduction in corrosion rate with addition of Rh is justified. This observed decrease in corrosion rate can be explained by substituting lower electronegativity elements Ti (1.54 on the Pauling scale) and Cr (1.66) with the higher electronegativity Rh (2.28), since high electronegativity favours a reduction in corrosion rate[105]. This was also substantiated by Schutz[144] who found that corrosion challenges of Ti-based alloys in aggressive environments can be practically and cost effectively overcome by minor additions of platinum group metals such as Pd and Ru at <0.25 at.%.

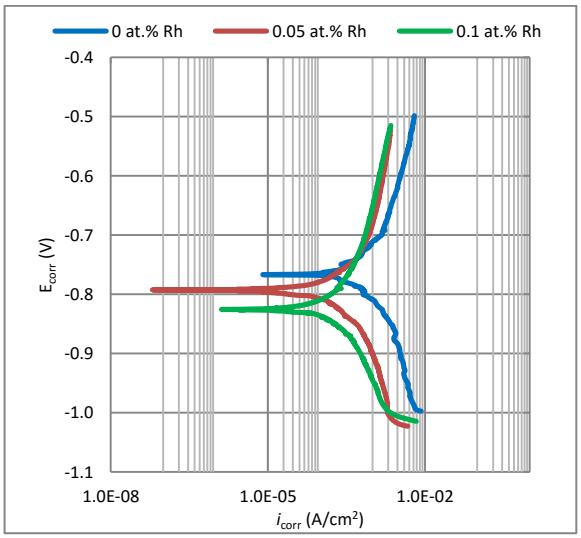

Figure 6.5. Potentiodynamic curves of as-cast $Ti_{25-0.5x}V_{40}Cr_{35-0.5x}Rh_x$ (x = 0, 0.05, 0.10 at.%) alloys.

For all the three alloy conditions, the lowest corrosion rate was found with addition of 0.05 at.% Rh, followed by a slight increase in the rate with addition of 0.10 at.% Rh.

Lal and Porcelli[189] also found that the corrosion rate of titanium metal surfaces exposed to strong acid media was highly inhibited by coating the surface with Rh. Addition of 0.04-0.08 wt% Pd to Ti-3Al-2.5V, Ti-6Al-4V, Ti-3Al-5V-6Cr-4Zr-4Mo alloys greatly improved the corrosion resistance in dilute sulphuric acid[146]. Ruthenium additions to Ti-3Al-2.5V, Ti-6Al-4V, Ti-3Al-5V-6Cr-4Zr-4Mo alloys effectively inhibited titanium crevice corrosion in hot halite and sulphate environments[143]. The corrosion rate of CP-Ti was considerably lowered in 6, 9 and

11.5 M HNO_3, and boiling 15.65 M HNO_3 when alloyed with Ni, Pd, Ru and Cr[124]. Binary alloys formed by addition of 10 wt% Ag, Au, Pd, or Pt to Ti had higher corrosion current density[66].

6.3.2. Effect of heat treatment on corrosion rate

Figure 6.6 shows that after annealing the 0.05 at.% Rh alloy, the corrosion rate decreased slightly from 0.0009 to 0.0007 mm/y and increased to 0.0014 mm/y after quenching. For 0.10 at.% Rh addition, both treatments increased the corrosion rate, but the quenched sample had the lowest corrosion resistance. The corrosion rate increased from 0.0010 mm/y in the as-cast sample to 0.0015 and 0.0023 mm/y for the annealed and quenched samples respectively.

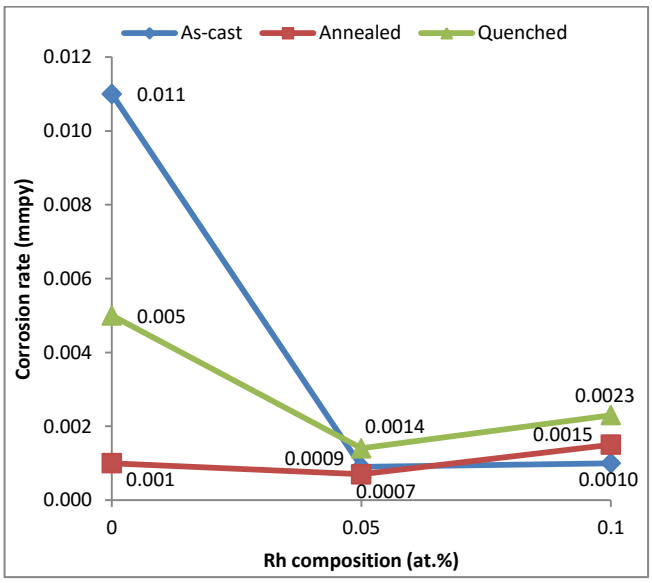

Figure 6.6. Effect of Rh composition and heat treatment on corrosion rate of $Ti_{25}V_{40}Cr_{35}$.

Phase structure and oxide layer are among the factors that determine the corrosion rate of an alloy. The Laves structure has been reported to have a thinner oxide layers than the BCC structure,[55] and the oxide layer is important for passivation[49, 150, 151]. It is therefore implied that for the alloy being investigated, the corrosion rate will increase when the proportion of the Laves phase increases. High Laves phase

proportion is therefore suggested as the reason for the observed increase in corrosion rate of as-cast sample at 0.05 at.% Rh composition, despite the high Cr content.

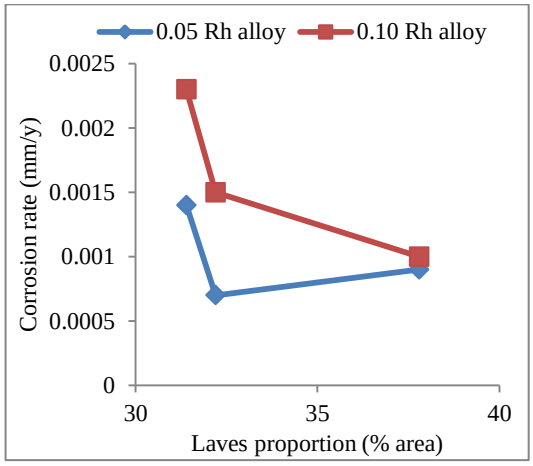

a) EDX composition b) Laves proportion.

Figure 6.7. Effect of Laves proportion in $Ti_{25-0.5x}V_{40}Cr_{35-0.5x}Rh_x$ (x = 0, 0.05, 0.10 at.%) alloys on corrosion rate.

Summary

Addition of Rh reduced the corrosion rate. In the 0.05 at.% Rh alloys, the corrosion rates of all three conditions were similar. Both treatments increased the rate of corrosion slightly of the Rh-containing alloys and the 0.05 at.% Rh in annealed condition had the lowest corrosion rate.

6.4. Effect of rhodium addition and heat treatment on hydrogen storage

6.4.1. Effect of rhodium addition on hydrogen storage properties

The absorption/desorption PCT curves of as-cast $Ti_{25-0.5x}V_{40}Cr_{35-0.5x}Rh_x$ (x = 0, 0.05, 0.10 at.%) are shown in Figure 6.8. No plateau was observed at 363 K in the 0.10 at.% Rh alloy. The hydrogen capacity increased with increase in pressure on the absorption isotherms and decreased with decrease in H pressure on the desorption isotherms, which is consistent with literature[97, 199, 202]. The trend is explained in Section 5.4.1

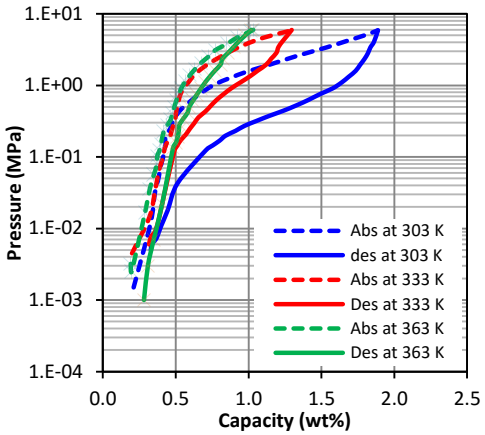

a) 0 at.% Rh

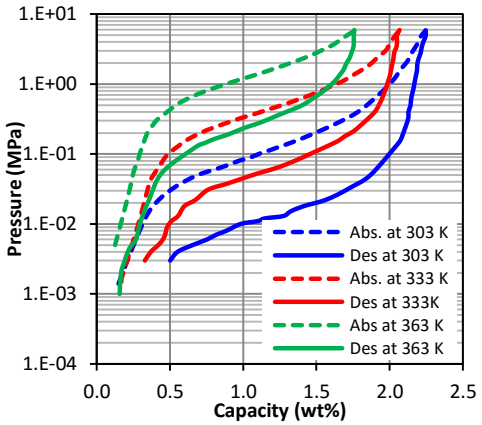

b) 0.05 at.% Rh

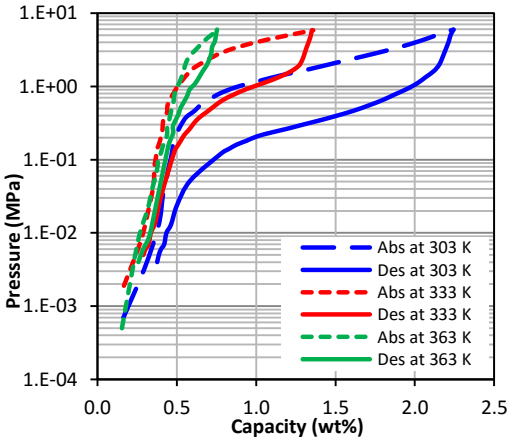

c) 0.10 at.% Rh

Figure 6.8. Absorption/desorption PCT curves of as-cast $Ti_{25-0.5x}V_{40}Cr_{35-0.5x}Rh_x$ (x = 0, 0.05, 0.10) alloys.

In the as-cast alloys, the RHSC increased with Rh content. Table 6.2 and Figure 6.9 show that the RHSC increased from 1.56 wt% in the Rh-free alloy to 1.74 wt% (0.05 at.% Rh) and further to 1.87 wt% (0.10 at.% Rh). Hydrogen desorption under ambient conditions is desirable for practical application in fuel cells [19, 210], hence the desorption PCT curves at 303 K for the as-cast 0, 0.05 and 0.10 at.% Rh compositions are shown in Figure 6.10. The useful capacity increased with increase in Rh content as shown in Table 6.2.

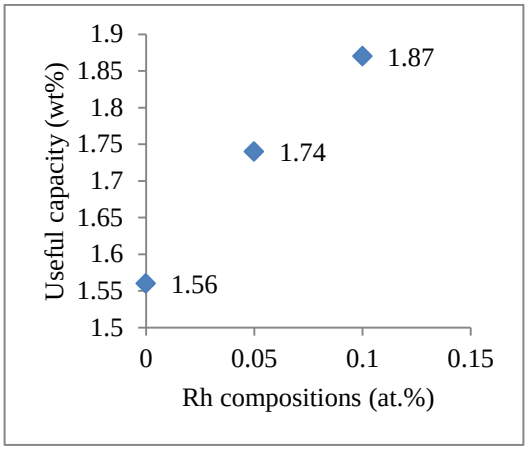

Figure 6.9. Influence of Rh composition on useful capacity of as-cast $Ti_{25}V_{40}Cr_{35}$.

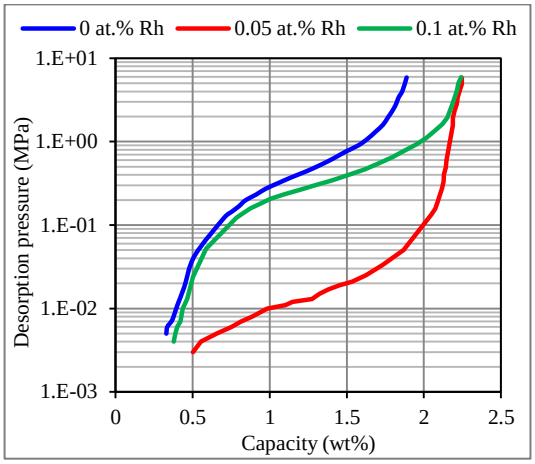

Figure 6.10. Desorption curves of as-cast $Ti_{25-0.5x}V_{40}Cr_{35-0.5x}Rh_x$ (x = 0, 0.05, 0.10) at 303 K.

Generally, the BCC phase is known to enhance H capacity[10, 52, 55], while the Laves phase is detrimental to storage capacity[26, 73, 166, 210]. An increase in the BCC cell volume implies an increased availability of H absorption space, hence an increase in storage capacity. A Laves phase with a large cell volume results in low hydrogen storage capacity[208]. The increase in BCC cell volume of the as-cast 0.10 at.% Rh alloy was responsible for the higher RHSC. Since the cell volume of BCC remained constant with addition of 0.05 at.% Rh, a slight decrease in the Laves cell volume could be responsible for the observed increase in RHSC.

Table 6.2. Thermodynamic properties of as-cast nominal $Ti_{25-0.5x}V_{40}Cr_{35-0.5x}Rh_x$ (x = 0, 0.05, 0.10 at.%) alloys.

X	Hydrogen capacity$^{\$}$ (wt%)		Capacity remaining$^{\$}$ (wt%)	Plateau pressure$^{\#}$ (MPa)	$-\Delta H^{\#}$ (kJ/mol H_2)	$-\Delta S^{\#}$ (J/mol.K)
	Absorption	RHSC				
0	1.89	1.56	0.33	0.41	40.59	121.49
0.05	2.25	1.74	0.50	0.02	41.79	104.11
0.10	2.24	1.87	0.37	0.35	41.99	128.19

$ Measured at 303 K; # Obtained from 303 and 333 K isotherms

In Table 6.2, the hydrogen absorption capacity increased wih addition of Rh over the base alloy and the RHSC increased with increasing Rh from 0.05 to 0.10 at.%. Table 6.2 shows that H-desorbed or useful hydrogen was higher in the Rh-containing as-cast alloys, implying that more γ-phase hydride was formed during the hydrogen absorption process. The highest remaining capacity was observed in the 0.05 at.% Rh alloy, implying that more mono-hydride was formed during the hydrogen absorption process than in the 0.10 at.% Rh as-cast sample. The highest RHSC, *i.e.* useful hydrogen, was observed in the 0.10 at.% Rh alloy, suggesting that more di-hydride was formed in the absorption process.

In Figure 6.11, the hydrogen capacity of as-cast 0.05 at.% Rh alloy increased from 1.74 wt% to 2.25 wt% after annealing, but decreased to 1.65 wt% after quenching. However, the hydrogen capacity in 0.10 at.% Rh sample increased slightly after both heat treatments: from 1.87 wt% in the as-cast sample to 2.05 wt% after annealing the sample and 2.01 wt% after quenching.

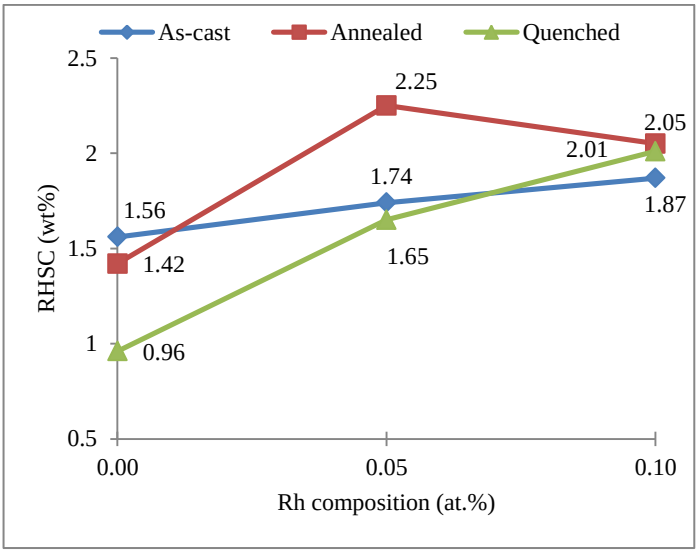

Figure 6.11. Effect of heat treatment on RHSC of $Ti_{25-0.5x}V_{40}Cr_{35-0.5x}Rh_x$ (x=0, 0.05, 0.10 at.%) alloy.

Table 6.2 and Figure 6.10 show that the plateau pressure decreased with addition of rhodium. The strain energy of the interstitial site determines the flatness of plateau and reduction in plateau pressure is an indication of lowered strain energy.[55] Addition of 0.05 at.% Rh reduced the plateau pressure substantially from 0.42 to 0.02 MPa, but with addition of 0.10 at.% Rh the plateau pressure only decreased to 0.35 MPa. This indicates that the strain in the interstitial site was significantly reduced by addition of 0.05 at.% Rh compared to 0.10 at.% Rh. An increase in BCC cell volume leads to an increase in interstitial space and consequently reduction of plateau pressure and interstitial strain. The reduction in plateau pressure at 0.10 at.% Rh is thus due to the increase in BCC cell volume. This is in agreement with work done by Hang *et al.*[144] and Lundin[158]. Contrarily, the plateau pressure was reduced in 0.05 at.% Rh alloy despite the reduction in cell volume of Laves. This phenomenon is similar to that of $(V_{30}Ti_{35}Cr_{25}Fe_{10})_{100-x}Al_x$ (x = 0 - 5) alloys[198] where the lattice parameter of BCC increased with Al content but the plateau pressure also increased. Lee and Perng [92] also found a similar phenomenon in $TiFe_{1-x}Al_x$ (x = 0, 0.025, 0.05, 0.10). The atomic radius of aluminium (0.1432 nm) is closer to that of titanium (0.1448 nm), but larger than that of iron (0.1241 nm), therefore when Al substituted Fe, the cell volume was expected to increase and the plateau pressure was expected

to decrease. Contrarily, despite the increase in BCC volume, the plateau pressure increased.

The dissociation enthalpy provides a measure of the strength of the interaction between the hydrogen and the adsorbent surface or pore structure [7]. The enthalpy increased with addition of Rh: from 40.59 to 41.79 kJ/mol (0.05 at.% Rh) and 41.99 kJ/mol (0.10 at.% Rh). This indicates that presence of Rh strengthened the H-metal bond which agrees with Lu *et al.*[109]. The strength of interaction was increased by 22.7% for the 0.05 at.% Rh alloy but only 3.4% for the 0.10 at.% Rh alloy. This implies that more energy was required to break the H-metal bond in the 0.05 at.% Rh alloy.

The degree of orderliness or randomness of a substance is measured by its entropy[7]. A low entropy indicates a highly ordered crystalline structure. A decrease in entropy from 121.49 (base alloy) to 104.11 (0.05 at.% Rh) and an increase to 128.19 J/mol.K (0.10 at.% Rh) is an indication of higher ordered hydrogen with 0.05 Rh addition and higher disorder of hydrogen on the host metal with 0.10 at.% Rh addition. The disorder decreased by 14.3% in the 0.05 Rh alloy and increased by 5.5% in the 0.10 at.% Rh alloy.

There is no evidence of previous work about the effect of Rh addition on hydrogen storage properties of Ti-V-Cr alloys. However, the effect of other platinum group metals on hydrogen storage characteristics has been reported. Yamashita *et al.*[193] reported that the plateau pressure and activation temperature was lowered in $TiFe_{1-x}Pd_x$ ($0.05 \leq x \leq 0.30$ at.%) alloys as x increased, although the hydrogenation capacity was not significantly improved.

Chemical surface modification of TiFe with Pd on has shown that Pd deposition improved hydrogenation properties at moderate hydrogen pressure[188]. Other investigations on the effect of Pd nanoparticles on hydrogen storage in Ti-Nb-Ru alloys[17], Ti-V-Cr alloys[104], and Ti-V based alloys[37] have also been reported. A study on plastic deformation and hysteresis for hydrogen storage in $Pd_{0.9}Rh_{0.10}$ showed that the alloy can absorb up to 0.72 H/M ratio[71]. Rh nanoparticles supported on graphene

as a catalyst for chemical hydrogen storage in amine boranes was also reported by Shen *et al.*[126]. All the investigations thus far showed that the addition of PGMs enhances the hydrogen storage characteristics.

This work showed that addition of 0.10 at.% Rh was superior to 0.05 at.% Rh in terms of RHSC and the thermodynamic properties. However, the plateau pressure was considerably higher (0.35 MPa) in 0.10 at.% Rh compared to 0.02 MPa in 0.05 at.% Rh.

Table 4.6 shows that only the αTi phase in the as-cast 0.05 at.% Rh alloy contained detectable levels of rhodium and the RHSC was 1.74 wt%. For samples without Rh, the capacity decreased after quenching and rose after annealing. For 0.10 at.% Rh (Table 4.7), the Laves phase in the as-cast 0.10 at.% Rh sample had 0.50 at.% Rh and the storage capacity was lower compared to the annealed and quenched sample which does not contain Rh.

6.4.2. Effect of measurement temperature on maximum hydrogen capacity

Figure 6.12 shows that the maximum hydrogen capacity increased with decreasing temperature. In the as-cast alloy, Figure 6.12 a) shows that at 303, 333, and 363 K, the Rh-free alloy absorbed up to 1.89, 1.31 and 1.03 wt% hydrogen, the 0.05 Rh alloy had the highest hydrogen absorption capacities of 2.25, 2.08 and 1.77 wt%, whereas an increase in Rh content to 0.10 at.% yielded lower H capacities of 2.24, 1.36 and 0.76 wt%. Similarly, the annealed samples (Figure 6.12 b) and the as-cast (Figure 6.12 a) showed the same trend.

The highest absorption capacities of 1.76, 2.57 and 2.41 wt% were found at 303 K isotherm for the annealed 0, 0.05 and 0.10 at.% Rh samples respectively, while the lowest hydrogen absorption capacities of 0.73, 2.45 and 0.92 wt% for annealed 0, 0.05 and 0.10 at.% Rh alloy were obtained at 363 K. A similar trend was observed in the quenched samples, as shown in Figure 6.9 c, but the highest H capacity for the 303 K isotherm was found at 0.10 at.% Rh (2.35 wt%).

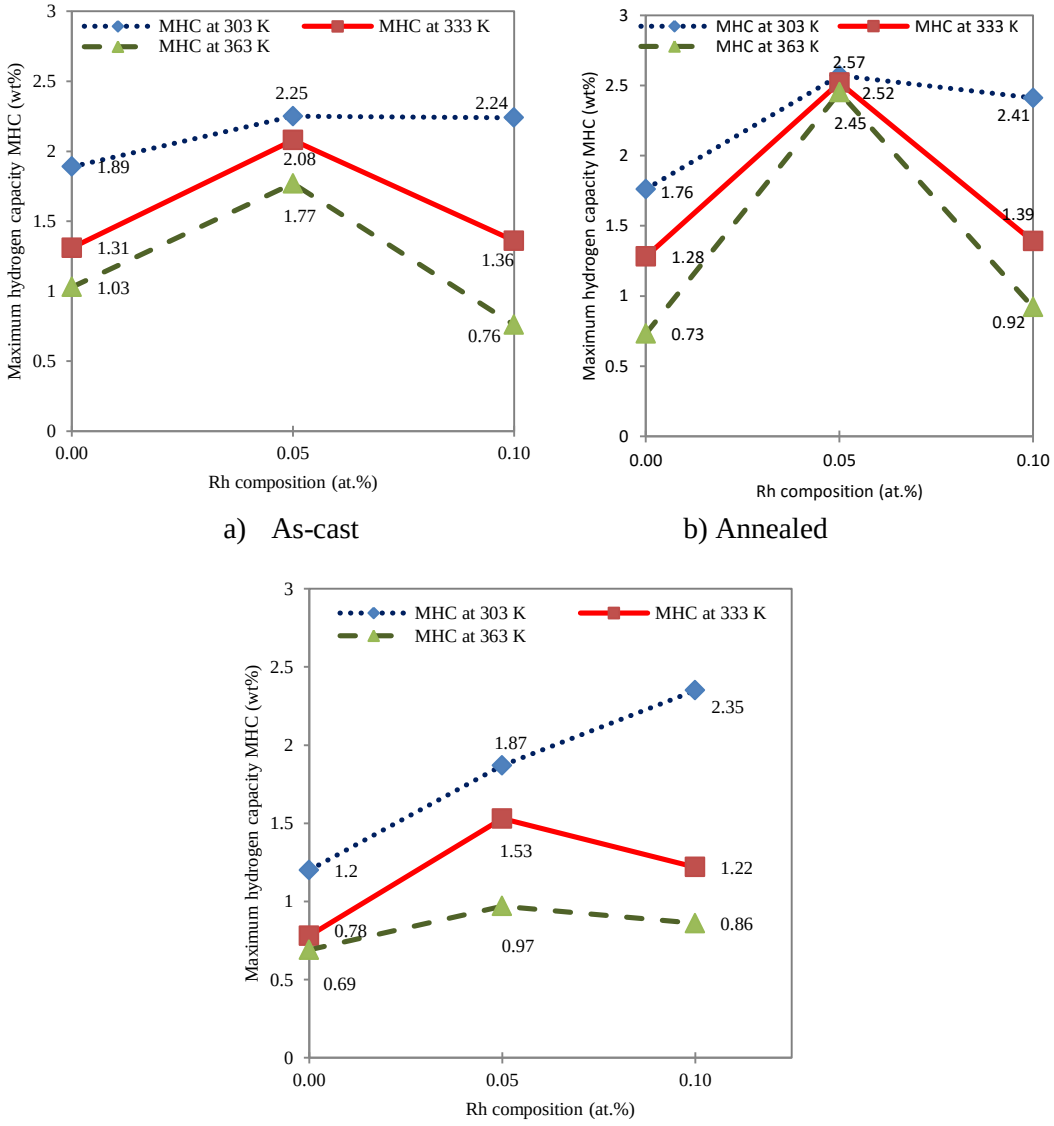

a) As-cast b) Annealed

c) Quenched

Figure 6.12. Effect of testing temperature and addition of Rh on maximum H capacity of: a) as-cast; b) annealed; c) quenched $Ti_{25-0.5x}V_{40}Cr_{35-0.5x}Rh_x$ (x = 0, 0.05, 0.10) alloys.

Similar to Huang *et al.*[171], Young *et al.* [187] and Zhou *et al.*[178] the absorption capacity decreased with increasing temperature, because of the increasing in kinetic energy of hydrogen molecules at elevated temperature.[25, 73] At lower temperatures, the kinetic energy is lower, and absorption by the host metal is facilitated.

6.4.3. Effect of heat treatment on hydrogen storage properties

The absorption/desorption capacities of as-cast and heat treated Rh-containing alloys are listed in Table 4.10. The effect of heat treatment on the useful or reversible storage capacity of $Ti_{25-x}V_{40}Cr_{35-x}Rh_x$ (x = 0, 0.05, 0.10 at.%) alloy was presented in Figure 6.11.

At 0.05 at.% Rh, annealing increased the reversible storage capacity of the alloy from 1.74 to 2.25 wt%, whereas the capacity decreased to 1.65 wt% after quenching. The BCC phase is known to favour, while Laves phases are detrimental to, hydrogen desorption[26, 74, 166, 210, 211]. An increase in proportion and/or cell volume of BCC implies availability of more space for accommodating H atoms; conversely, an increase in cell volume and/or proportion of the Laves phase means less hydrogen absorption space or sites. The observed increase in storage capacity after annealing was therefore a result of increase in the proportion and cell volume of BCC, while the observed decrease in the capacity after quenching was attributed to the increase in cell volume of Laves from 36.25 $Å^3$ in the as-cast to 49.99 $Å^3$ in the quenched sample.

The plateau pressure rose after heat treatment, from 0.017 to 0.22 MPa after annealing, and to 0.30 MPa after quenching. The strain energy of the interstitial site determines the flatness of plateau, so a decrease in plateau pressure is an indication of lowered strain energy[55]. When there are more available space/sites for absorption of hydrogen molecules, the H-metal-H distance increases, reducing in the interstitial strain, and consequently the plateau pressure[95]. When there is less space for hydrogen molecules on the host, as with an increase in Laves cell volume, the molecules are confined to less space on the host, which results in higher interstitial strain and plateau pressure. Both the cell volume of Laves and BCC rose after annealing. From the above explanation, an increase in cell volume of BCC by 1.2% was expected to give more space for hydrogen absorption and reduce the plateau pressure. However, the increase in cell volume of Laves which reduced the available space for hydrogen absorption, counteracted the effect of increased BCC cell volume, and this led to the observed increase in plateau pressure. After quenching,

the cell volume of BCC was unchanged, but that of αTi increased and a C36 Laves was formed. This led to the observed reduction in the hydrogen absorption sites, hence an increase in plateau pressure was observed.

The plot of *1/T* against the natural log of plateau pressure, *P* (Equation 2.1) yielded the van`t Hoff plot shown in Figure 6.13. The desorption enthalpy was obtained from the slope and the desorption entropy from the intercept on the *ln P* axis. There was no plateau for the quenched sample at the 363 K isotherm, hence only two points could be plotted. However, the values of P and T at the two points were inserted in Equation 2.1 and solved simultaneously to obtain ΔH and ΔS for the quenched sample.

Table 6.4 shows the calculation of desorption enthalpy and entropy of $Ti_{24.975}V_{40}Cr_{34.975}Rh_{0.05}$. Negative enthalpy signifies endothermic reaction, while positive value signifies exothermic. The enthalpy rose after heat treatment from -42±1 to -44±1 kJ/mol H_2 after annealing, and decreased to -37.0±1 kJ/mol H_2 after quenching. As enthalpy is a measure of interaction between the H and its host, the H-metal bond was strengthened by quenching and weakened by annealing. The calculated enthalpy was in the same range as Mazzolai *et al.*[206]: who found ΔH for $Ti_{35}Cr_{47}V_{18}$ and $Ti_{35}Cr_{43}V_{22}$ hydrogen storage alloys to be -35±6 kJ/mol and -39±2 kJ/mol respectively.

In the 0.05 at.% Rh alloy, the entropy increased from 104 J/mol.K to ~110 J/mol.K after both treatments (Table 6.3). An increase in entropy after heat treatment is an indication that the H atom became more disorganised on the host metal after heat treatment[104].

At 0.10 at.% Rh, both annealing and quenching increased the RHSC from 1.87 to 2.05 and 2.01 wt% respectively, as shown in Figure 6.11. The cell volumes of BCC after both heat treatments were the same, while those of αTi increased with increased Rh. However, as shown in Table 4.7, the V composition in the primary phase (BCC) increased after heat treatment. Reports have shown that V content plays an important role in achieving high hydrogen capacity[84, 139, 154], as V in the bulk of an alloy can introduce cracks which induce absorption of hydrogen[209]. Increase in V content in

the main phase could therefore be responsible for the observed increase in capacity after heat treatment.

Table 6.3. Calculation of desorption enthalpy and entropy for $Ti_{24.975}V_{40}Cr_{34.975}Rh_{0.05}$

	R = 8.3145	As-cast	Annealed	Quenched
Isotherm T (K)	1000/T (K^{-1})	Ln P (MPa)	Ln P (MPa)	Ln P (MPa)
303	3.30	-4.04	-4.27	-1.52
333	3.00	-2.63	-2.75	-0.19
363	2.75	-1.30	-1.37	-
	Slope, m	-5.03	-5.32	-
	Intercept, c	12.52	13.25	-
	ΔH = mR (kJ/mol)	-41.79	-44.20	-37.21
	ΔS = cR (J/mol.K)	104.11	110.18	110.13

The van`t Hoff plot for the effect of heat treatment in $Ti_{24.975}V_{40}Cr_{34.975}Rh_{0.05}$ and $Ti_{24.95}V_{40}Cr_{34.95}Rh_{0.10}$ are shown in Figures 6.13 and 6.14 respectively. No plateau was observed at 363 K for any of the 0.10 at.% Rh samples, therefore only two data points could be plotted. Due to the lack of reliability of van't Hoff plot method for only two data points, ΔH and ΔS were calculated from Equations 2.2 and 2.3 respectively, and are presented in Table 6.4.

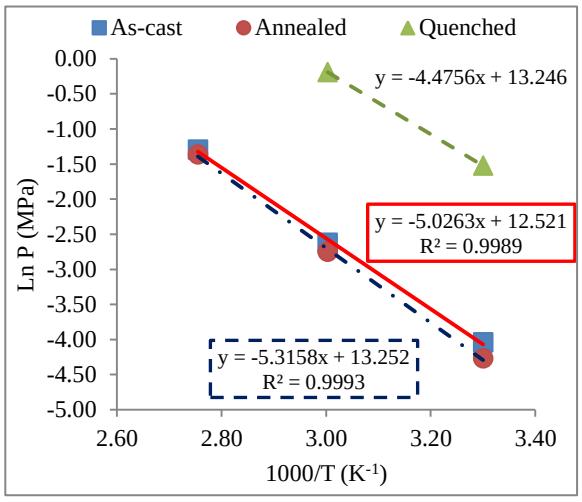

Figure 6.13. Van`t Hoff plot of effect of heat treatment on $Ti_{24.975}V_{40}Cr_{34.975}Rh_{0.05}$.

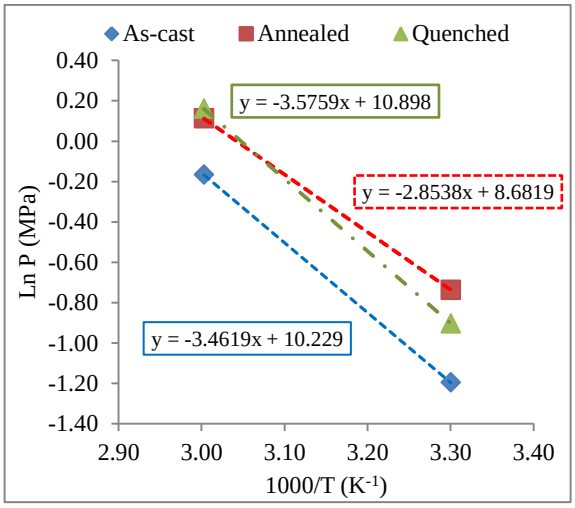

Figure 6.14. Van`t Hoff plot of effect of heat treatment on $Ti_{24.95}V_{40}Cr_{34.95}Rh_{0.10}$.

Table 6.4. Calculation of desorption enthalpy and entropy of as-cast and heat treated $Ti_{24.95}V_{40}Cr_{34.95}Rh_{0.10}$

R = 8.3145		As-cast	Annealed	Quenched
T	1000/T	Ln P	Ln P	Ln P
303	3.30	-1.20	-0.74	-0.90
333	3.00	-0.17	0.11	0.16
363	2.75	-	-	-
	Slope, m	-3.46	-2.85	-3.58
	Intercept, c	10.23	8.68	10.90
	ΔH = mR	-28.78	-23.70	-29.77
	ΔS = cR	85.05	72.17	90.61
	ΔH*	41.98	42.77	46.74
	ΔS*	128.19	142.32	155.58

*values obtained from Equations 2.2 and 2.3 using 303K and 333K isotherms

Properties of the alloy at 303 K are important for practical application in fuel cells[19], so the plateau pressure value at 303 K was considered. The pressure increased from 0.42 to 0.48 MPa after annealing, and decreased to 0.41 MPa after quenching. An increase in the αTi proportion led to an increase in the plateau pressure and a decrease in hydrogen capacity, which is consistent with literature[46]. The observed increase in the plateau pressure is therefore due to the slight increase in the proportion of Laves phase after heat treatment.

Annealing increased the enthalpy of hydride desorption (-ΔH) from 41.79 to 44.20 kJ/mol, and quenching decreased the -ΔH to 37.21 kJ/mol. The entropy (-ΔS) rose

from 104.11 to 110.13 J/mol.K after quenching, and to 110.18 J/mol.K after annealing. This implies that the strength of interaction between the H atom and the host metal increased after annealing, but decreased after quenching.

Summary

The annealed 0.05 at.% Rh alloy had the best RHSC. In the as-cast alloys, the 0.10 at.% Rh alloy had the highest useful capacity, although the best plateau characteristics were observed in the 0.05 at.% Rh alloy. The quenched Rh-free sample had the lowest RHSC (0.96), while the capacity increased to 2.01 in quenched 0.10 at.% Rh alloy.

Summary of the chapter

Both the rhodium-free and rhodium-containing alloys had primary BCC (V) and a secondary Laves phase. The addition of 0.05 at.% Rh did not change the cell volume of BCC, but reduced cell volume of Laves, thereby resulting in increased H capacity. Further increase in Rh composition to 0.10 at.% led to an increase in the cell volume of both BCC and Laves phases. Both annealing and quenching treatments increased the cell volume of Laves. The BCC cell volume was not altered by quenching, but increased after annealing.

Addition of 0.05 at.% Rh increased the hardness marginally for any alloy condition. However, both annealing and quenching reduced the hardness substantially in the 0.10 at.% Rh alloy.

The corrosion rate of $Ti_{25}V_{40}Cr_{35}$ reduced with additions of Rh. Annealing and quenching substantially decreased the corrosion rate in the Rh-free alloy, while the rate increased marginally in annealed 0.05 at.% Rh alloy, and increased in the quenched sample. Both annealing and quenching increased the corrosion rate in the 0.10 at.% Rh alloy.

Both absorption capacity and RHSC increased and the plateau pressure decreased with additions of Rh. The useful capacity and thermodynamic properties at 0.10 at.% Rh composition were superior to 0.05 at.% Rh composition, but the plateau pressure

was considerably higher for 0.10 at.% Rh. The RHSC in Rh-free sample decreased marginally after annealing, but decreased substantially after quenching. In the 0.05 at.% Rh sample, the RHSC increased after annealing, but decreased after quenching. However, in the 0.10 at.% Rh sample, the RHSC increased after both annealing and quenching. The enthalpy of hydrogen desorption increased after annealing the 0.05 at.% Rh sample, but decreased after quenching, while the enthalpy increased in both annealing and quenching for the 0.10 at.% Rh sample. Both the enthalpy and entropy increased after heat treatment in the 0.10 at.% Rh alloy.

CHAPTER 7: Effect of palladium substitution and heat treatment on properties of $Ti_{25}V_{40}Cr_{35}$

Overview

This chapter presents and discusses the effect of substituting equal amounts of chromium and titanium with 0.05 and 0.10 at.% palladium on the microstructure, phases, hardness, corrosion behaviour and hydrogen storage characteristics of $Ti_{25}V_{40}Cr_{35}$. It also presents and discusses the effect of heat treatment on the properties of $Ti_{25-0.5x}V_{40}Cr_{35-0.5x}Pd_x$ (x = 0.05, 0.10).

7.1. Effect of palladium addition and heat treatment on microstructure and phases of $Ti_{25}V_{40}Cr_{35}$

Figures 4.13 and 4.15 show the microstructures of alloys $Ti_{24.975}V_{40}Cr_{34.975}Pd_{0.05}$ (A7) and $Ti_{24.95}V_{40}Cr_{34.95}Pd_{0.10}$ (A8), respectively. The EDX analyses of the phases of as-cast 0, 0.05 and 0.10 at.% Pd alloys were extracted from Tables 4.2, 4.8 and 4.9 and are presented in Table 7.1 for ease of reference. Similarly, the XRD patterns of as-cast 0, 0.05 and 0.10 at.% Pd were extracted from Figures 4.2, 4.14 and 4.16 and are shown in Figures 7.1 and 7.2. XRD patterns showing the effect of heat treatment on $Ti_{25-0.5x}V_{40}Cr_{35-0.5x}Pd_x$ (x = 0, 0.05, 0.10) are shown in Figure 7.2.

7.1.1. Effect of palladium addition on the microstructure and phases

Table 7.1 shows that the Pd-containing alloys contained two phases; primary BCC and secondary (αTi) or βTi . Addition of Pd decreased the Ti content in the BCC phase and increased it in the secondary phase. Addition of 0.05 at.% Pd decreased the phase proportion of BCC from 89.7 % in the Pd-free sample to 81.5 %, while the proportion of Laves phase increased from 10.3 to 18.5 %. The BCC cell volume increased from 27.67 $Å^3$ in the Pd-free sample to 27.75 $Å^3$ in the 0.05 at.% Pd sample, while the volume of the secondary phase increased from 36.24 to 59.68 $Å^3$.

Increasing the Pd composition to 0.10 at.% did not significantly change the compositions of the BCC phase, but the proportion increased to 91.4%. The

secondary phase volume increased from 35.22 $Å^3$ in the Pd-free sample to 40.72 $Å^3$, while that of BCC marginally increased by 0.08 $Å^3$.

Table 7.1. EDS of as-cast $Ti_{25-0.5x}V_{40}Cr_{35-0.5x}Pd_x$ (x = 0, 0.05, 0.10).

X	**Phases XRD**	**Compositions (at.%) ***				**Phase proportion (% area)**	**Phase description**			
		Ti	**V**	**Cr**	**Pd**		**Space group (No.)**	**a (*Å*)**	**c (*Å*)**	**Cell volume ($Å^3$)**
0	BCC (V)	22.0 (0.7)	42.8 (0.5)	35.2 (0.8)		89.7	*Im*3*m* (229)	3.0246	-	27.67
	αTi	22.5 (3.0)	43.5 (3.3)	34.0 (4.8)		10.3	$P6_3/mmc$ (194)	2.95	4.67	35.22
0.05	BCC (V)	18.6 (1.4)	44.8 (2.2)	36.6 (1.3)		81.5	*Im*3*m* (229)	3.0275	-	27.75
	βTi	50.5 (4.8)	25.7 (2.4)	23.8 (2.5)	0.4 (0.1)	18.5	*Fd*3*m* (225)	3.91	-	59.68
0.10	BCC (V)	19.1 (0.8)	43.6 (3.6)	37.3 (4.6)		91.4	*Im*3*m* (229)	3.0275	-	27.75
	αTi	63.7 (1.4)	18.5 (1.1)	17.8 (0.6)		8.6	$P6_3/mmc$ (194)	2.95	4.69	40.72

*Standard deviation in parentheses

The atomic radius of Ti (2.00 Å) is close to that of V (1.92 Å), Cr (1.85 Å) and Pd (1.79 Å). The cell volume of the secondary phase in the Pd-containing samples increased noticeably due to large increase in Ti content from 22.5 at.% in Pd-free sample to 50.5 at.% in 0.05 Pd alloy and 63.7 at.% in 0.10 Pd sample. The BCC cell volumes in the three samples are similar because of similar elemental compositions.

The XRD pattern in Figure 7.1 shows major peaks as BCC (V), with an abundance of 81.5 area % for 0.05 at.% Pd, while the minor peaks corresponds to βTi phase. The BCC XRD peaks were shifted to the left with increasing addition of Pd.

In the quenched samples, Pd additions increased the volume of secondary phase and 0.10 at.% Pd decreased the BCC volume. In the annealed samples, the trend was similar to the as-cast: increase in secondary phase volume with 0.05at.% Pd and decrease with 0.10 at.% Pd, slight increase in BCC volume with 0.05 at.% Pd but no change with further increase to 0.10 at.% Pd.

The observation agrees with literature. Liu *et al.*[98] found that the $Ti_{0.8}Zr_{0.2}V_{2.7}Mn_{0.5}Cr_{0.8}Ni_{1.0}Pd_x$ (x = 0, 0.05, 0.10, 0.105, 0.2 at.%) alloys had C14 Laves phase and a V-based solid solution BCC phase. Jeng *et al.*[124] found BCC as the main phase and a minor Laves phase in Pd-containing $Ti_{33}V_{33}Cr_{34}$ alloys.

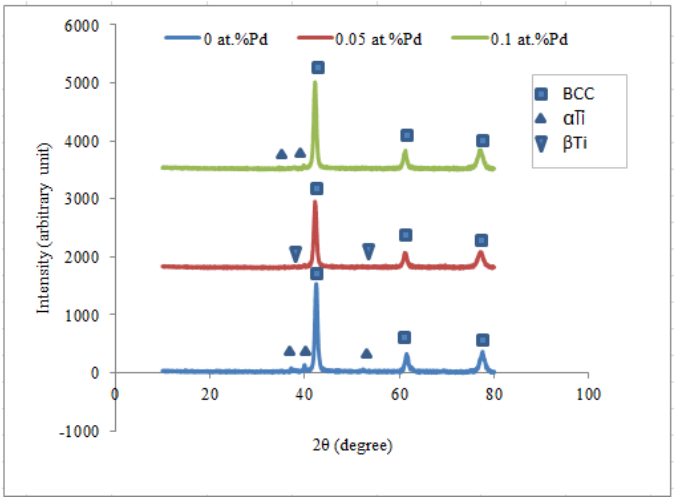

Figure 7.1. XRD patterns of as-cast $Ti_{25-0.5x}V_{40}Cr_{35-0.5x}Pd_x$ (x = 0, 0.05, 0.10 at.%) alloys.

Table 4.8 shows that Laves phase of as-cast and quenched 0.05 at.% Pd samples had similar, detectable amounts of Pd, but different cell volumes. Similarly, although both phases in the as-cast and heat treated 0.10 at.% Pd samples had no detectable Pd, the cell volumes differed. The Ti/Cr ratios in the αTi phase in heat treated samples were similar but different from the ratio in as-cast sample. However the Ti/Cr ratio in the BCC phase were similar for both the as-cast and treated samples.

Thermo-Calc modelling of phases in the Pd-free sample was discussed in Section 5.1. For the 0.05 Pd alloy, the SSOL4 database predicted BCC and (αTi) phases (HCP_A3), while the TTTI3 database gave $\alpha TiCr_2$ (C 15_FCC) in addition to the two phases from SSOL4The prediction of BCC agrees with the experimental findings, but C15 Laves was found contrary to the prediction of C14 Laves.

The TTTI3 database predicted BCC, (αTi) and C15_FCC phases. The prediction of BCC and C15 Laves phases were confirmed experimentally, although the C14 Laves was not found.

For the 0.10 at.% Pd alloy, SSOL4 predicted BCC and HCP_A3. BCC and (αTi) phases were found experimentally, in agreement with the SSOL4 prediction. Experimentally, only two phases, BCC and C14 Laves phases, were found, contrary to the predicted BCC, C14 and C15 Laves phases.

7.1.2. Effect of heat treatment on the microstructure and phases

The microstructures of the as-cast and heat treated samples for 0.05 and 0.10 at.% Pd alloys are shown in Figures 4.13 and 4.15 respectively. The observed XRD patterns for the as-cast and heat treated 0.05 at.% Pd alloys are in Figure 4.14, while similar patterns for 0.10 at.% Pd alloy are in Figure 4.16. The EDX analysis and crystallographic parameters for 0.05 and 0.10 Pd alloys are listed in Tables 4.8 and 4.9 respectively. For ease of reference, the XRD patterns of as-cast and heat treated $Ti_{25-0.5x}V_{40}Cr_{35-0.5x}Pd_x$ (x = 0, 0.05, 0.10 at %) alloys are shown in Figure 7.2.

Figure 7.3a shows that second phase cell volume of 0.05 and 0.10 at.% Pd alloys decreased after annealing, and increased after quenching. Table 4.8 shows that the increase in BCC cell volume of quenched 0.05 alloy was due to the higher Ti content in the phase. In the annealed 0.05 at.% Pd alloy, the titanium content in the αTi phase increased by 15.5 at.% Ti. The atomic radii of Ti, Cr and V are very similar[94], therefore the observed decrease in cell volume after annealing is an indication that the combined decrease in V and Cr content counteracts the effect of increase in Ti content.

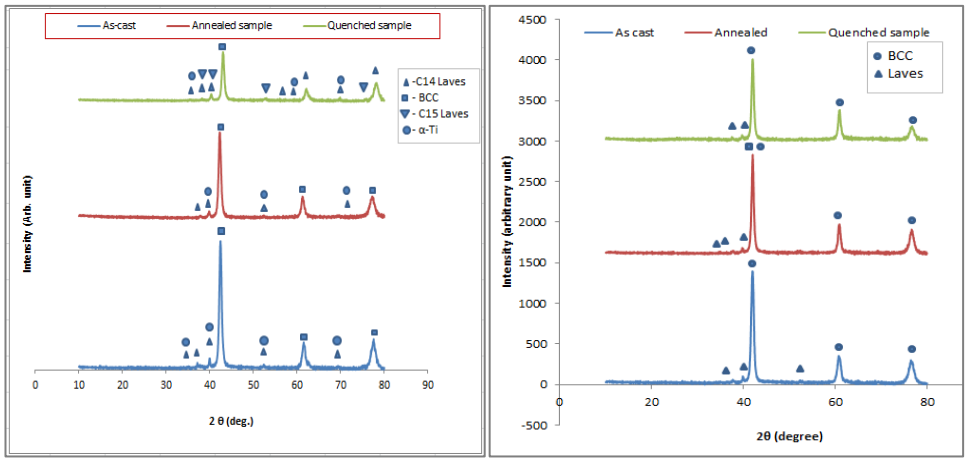

a) $x = 0$ b) $x = 0.05$

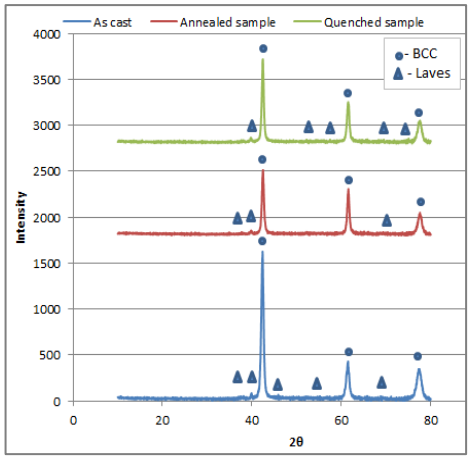

c) $x = 0.10$

Figure 7.2. XRD patterns of as-cast, annealed and quenched $Ti_{25-0.5x}V_{40}Cr_{35-0.5x}Pd_x$ (x = 0, 0.05, 0.10 at %) alloys

Figure 7.3b shows that annealing had no effect on the BCC phase cell volume in Pd containing alloys, similar to the Pd-free sample. Table 4.9 shows that the V content of BCC in the 0.10 at.% Pd sample decreased after heat treatment. Annealing reduced the phase proportion of BCC from 91.4 to 90.0 %, but quenching increased it to 94.9 area %. Tables 4.8 and 4.9 show that there was no change in the cell volume of BCC after annealing, because the composition of elements in the phase was similar. However, the BCC cell volume increased from 27.75 $Å^3$ in the as-cast condition to 28.09 $Å^3$ after quenching due to the increased Ti content.

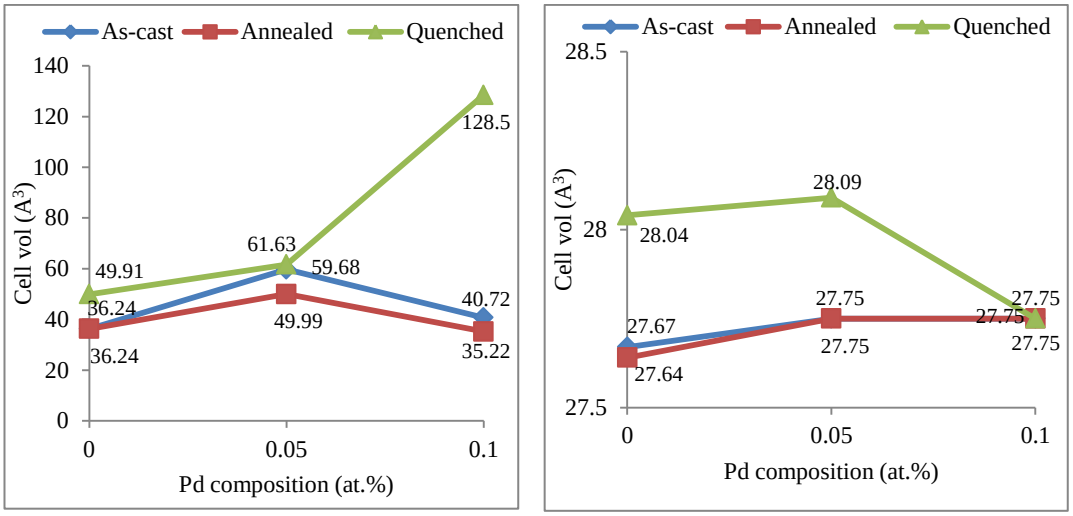

a) αTi phase b) BCC phase

Figure 7.3. Effect of Pd and heat treatment on cell volume of phases.

Summary

Addition of 0.05 at.% Pd increased the cell volumes of both αTi and BCC phases for all conditions, addition of 0.10 at.% Pd increased the secondary volume, but decreased the BCC volume in the quenched condition. The secondary volume decreased in both annealed and quenched sample, but the BCC volume was similar for the annealed and quenched alloys. Annealing decreased the cell volume of αTi but had no effect on cell volume of BCC at 0.05 and 0.10 Pd alloys. However, the cell volume of Laves and BCC phases increased after quenching. For Pd-containing alloys, the phase prediction using the SSOL4 database was more accurate than using the TTTI3 database.

7.2. Effect of palladium addition and heat treatment on hardness

7.2.1. Effect of palladium addition on hardness

Figure 7.4 shows that in the as-cast sample, the hardness decreased slightly from 415 to 410 HV_2 with addition of 0.05 at.% Pd. Increasing the Pd composition to 0.10 at.% then increased the hardness to 425 HV_2. The hardness values of Cr, Ti and Pd are 1060, 970 and 461 MPa[94]. In $Ti_{25-0.5x}V_{40}Cr_{35-0.5x}Pd_x$ (x = 0, 0.05, 0.10 at.%) alloys, Pd is substituting harder elements Ti and Cr, therefore agreeing with the

observed decrease in hardness in 0.05 Pd alloy. The higher hardness in the 0.10 at.% Pd alloy could be due to high Cr content (Table 7.1).

The as-cast curve shows that the hardness value decreased in 0.05 at.% Pd alloy and increased in 0.10 at.% Pd sample. On the annealed curve, the hardness decreased with addition of Pd, but there was no noticeable effect of increased in Pd on hardness value on the quenched curve. Lack of relevant literature on hardness of Ti-V-Cr-Pd quaternary alloy hinders comparison.

Table 4.8 shows that the BCC proportion in as-cast sample was less than the quenched sample by 1.5 area % but the hardness in as-cast sample was higher by 4 HV_2. However, both the hardness and the BCC proportion in the annealed sample was less than in the as-cast sample. The trend was similar to the 0.10 at.% Pd alloy, the BCC proportion in the as-cast sample was less than in quenched sample, but the hardness was higher in the as-cast sample. The BCC proportions in as-cast and annealed samples were similar, but the as-cast sample had higher hardness (Table 4.9).

7.2.1. Effect of heat treatment on hardness

Hardnesses of all the samples decreased after heat treatment (Figure 7.4). The Pd-free sample in the quenched condition had the lowest hardness, whereas the 0.05 at.% and 0.10 at.% Pd samples in the annealed condition had the lowest hardnesses . However, the decrease in hardness was more noticeable in the 0.10 at.% Pd sample. In all Pd compositions, the as-cast sample had highest hardness while annealing decreased the hardness in the 0.05 and 0.10 at.% Pd alloys.

For as-cast 0 at.% Pd alloy, the hardness decreased from 415 to 408 HV_2 after annealing and 405 HV_2 after quenching. Addition of 0.05 at.% Pd decreased the hardness from 410 to 402 HV_2 after annealing and 406 HV_2 after quenching. The hardness of Cr is higher that of V, Ti and Pd[94]. The decrease in hardness of 0.05 at.% Pd alloy after heat treatment could be attributed to decrease in Cr content in the primary phase (Table 4.8).

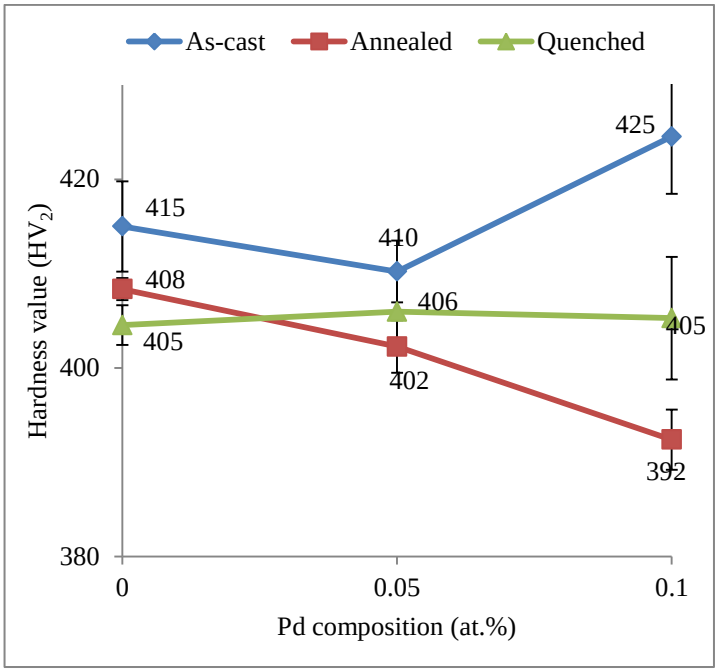

Figure 7.4. Effect of heat treatment on hardness of $Ti_{25-0.5x}V_{40}Cr_{35-0.5x}Pd_x$ (x = 0, 0.05, 0.10 at.%) alloys.

Summary

Hardness decreased from 415 to 410 HV_2 with addition of 0.05 at.% Pd but increased to 425 HV_2 in the 0.10 at.% Pd alloy. Heat treatment reduced hardness in all the three conditions. The lowest value was observed in the annealed 0.10 at.% Pd alloy, while the highest hardness was in the as-cast 0.10 at.% Pd alloy.

7.3. Effect of palladium addition and heat treatment on corrosion

7.3.1. Effect of palladium addition on corrosion

The Tafel curves for the as-cast $Ti_{25-0.5x}V_{40}Cr_{35-0.5x}Pd_x$ (x = 0, 0.05, 0.10 at.%) alloys are shown in Figure 7.5. The corrosion rates of the alloys with 0, 0.05 and 0.10 at.% Pd compositions are shown Figure 7.6. The shapes of the Tafel curves in Figure 7.56 are similar to those described in Section 5.3.1.

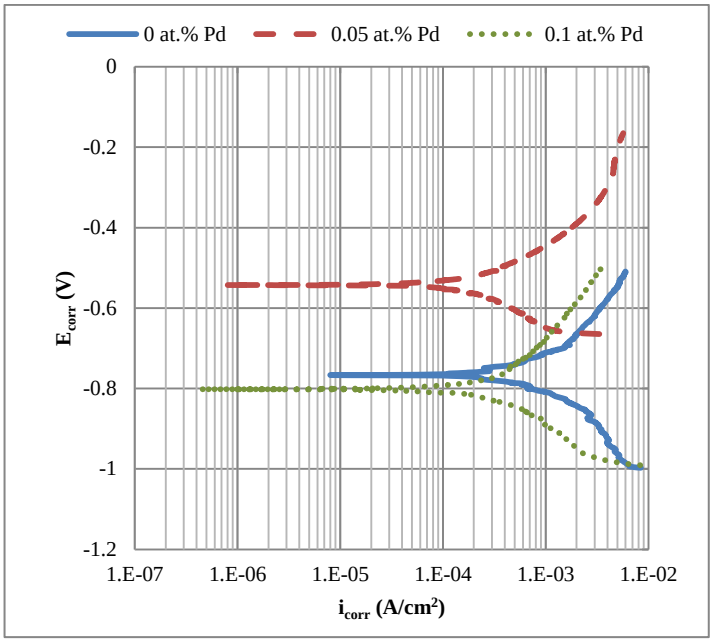

Figure 7.5. Potentiodynamic curves for $Ti_{25-0.5x}V_{40}Cr_{35-0.5x}Pd_x$ (x = 0, 0.05, 0.10 at.%) alloys in 6M KOH solution.

In Figure 7.5, E_{corr} increased from -767 mV in the Pd-free sample to -543 mV in the 0.05 at.% Pd alloy, but decreased to -802 mV in the 0.10 at.% Pd sample. However, Pd decreased the i_{corr} in both 0.05 and 0.10 at.% Pd alloys.

In Figure 7.6, the corrosion rate decreased from 0.011 to 0.0014 mm/y with addition of 0.05 at.% Pd, and increased slightly to 0.0025 mm/y with 0.10 at.% Pd addition. The electronegativity value (on the Pauling scale) for Cr, Ti and Pd is 1.66, 1.54 and 2.20 respectively[103]. The observed reduction in the corrosion rate could be attributed to substitution of elements with lower electronegativity (Cr and Ti) with Pd, which has a higher value[105]. In addition, Pd is one of the noble metals which inhibit corrosion[145].

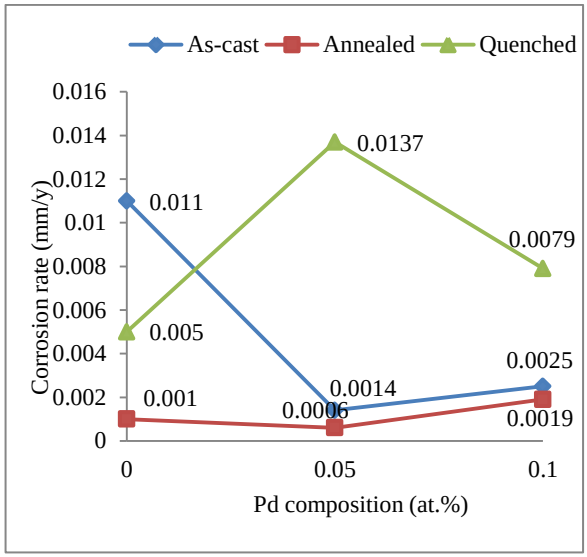

Figure 7.6. Effect of heat treatment on corrosion rate of $Ti_{25-0.5x}V_{40}Cr_{35-0.5x}Pd_x$ (x = 0, 0.05, 0.10 at.%) alloy in 6M KOH solution.

The result in this work is consistent with Handzilk and Fitzner[165] who reported that crevices of commercially pure CP-Ti can corrode at -38 °C in neutral brines, but with addition of Pd, crevice corrosion in similar environment will not occur until 127°C is exceeded.

An addition of 0.12 at.% Pd to titanium also greatly improved resistance to reducing environments such as hydrochloric and dilute sulphuric acid[10]. Tian *et al.*[196] found that corrosion rate decreased with increased Pd content in $Mg_{0.9}Ti_{0.10}Ni_{1-x}Pd_x$ (x = 0, 0.05, 0.10, 0.15 at.%) hydrogen storage electrode alloys.

Other platinum group metals exhibit similar corrosion behaviour. The presence of Ru has been shown to inhibit the corrosion rate of Ti–20Nb–xRu (x = 0.0, 0.5, 1.0, 1.5 at.%) alloys[17]. The corrosion rate of WC–Co cemented carbide alloys in sulphuric acid was reduced by addition of Ru[133], and the corrosion rate of carbon was substantially decreased with addition of Pt[103].

Table 4.8 shows that the secondary phases of as-cast and quenched 0.05 at.% Pd samples contained 0.4 at.% Pd, and the corrosion rate of quenched sample was higher than the as-cast sample. In the 0.10 at.% Pd samples, no detectable Pd was found in any of the phases of as-cast, annealed and quenched samples, and the corrosion rate differed in all the samples.

7.3.1. Effect of heat treatment on corrosion

Annealing reduced the corrosion rate in both Pd-free and Pd-containing alloys, but quenching reduced the rate in Pd-free alloy and increased it in Pd-containing alloys. In the 0.05 at.% Pd alloy, annealing reduced the rate of corrosion from 0.0014 to 0.00016 mm/y, while quenching increased the rate to 0.0137 mm/y. The corrosion rate of the as-cast 0.10 at.% Pd alloy reduced from 0.0025 to 0.0019 mm/y after annealing, and increased to 0.0079 mm/y after quenching. Therefore, quenching did not favour corrosion of 0.10 at.% Pd.

Laves phase strengthened alloys are characterized by their brittleness, wear and corrosion resistance[196]. Low corrosion rates of Tribaloy® 700 alloy (a cobalt-free nickel-based alloy) in sodium was attributed to its typical Laves structure[76]. Tribaloy® alloys are family of materials typically consisting of hard intermetallic Laves phase dispersed in a cobalt or nickel eutectic or solid solution matrix. Therefore, in Tables 4.8 and 4.9 the increase in Laves proportions in the annealed samples of 0.05 and 0.10 at.% Pd alloys could be responsible for the decrease in corrosion rates. Similarly, the reduction in the proportion of Laves in the quenched samples of 0.05 and 0.10 at.% Pd samples explains the higher corrosion rates.

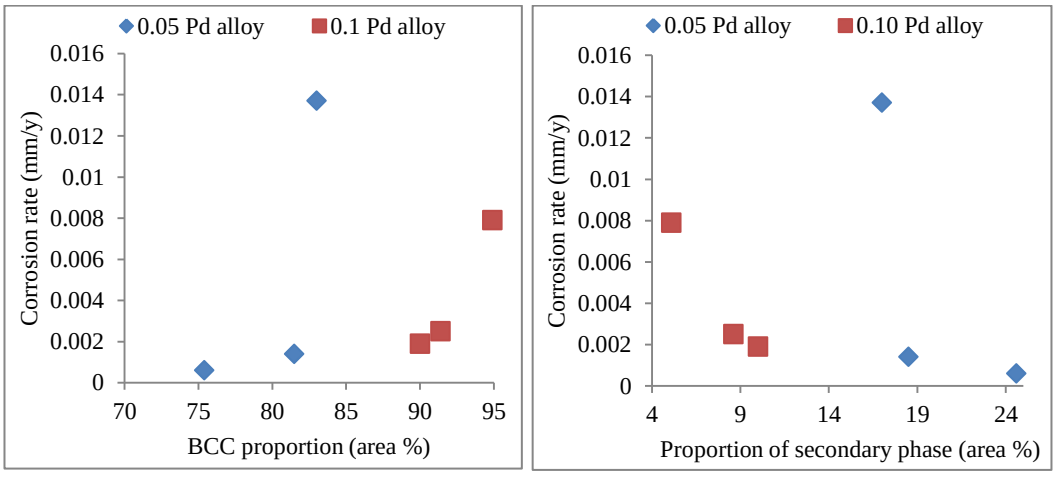

a) b)

Figure 7.7. Influence of a) BCC proportion and b) secondary phase proportion on corrosion rate of $Ti_{25-0.5x}V_{40}Cr_{35-0.5x}Pd_x$ (x = 0.05, 0.10 at.%) alloys.

Summary

Pd additions decreased the corrosion rates of the base alloy. In the Pd-containing samples, the corrosion rate was further decreased by annealing, but increased by quenching. The highest corrosion rate was observed in the quenched 0.05 at.% Pd alloy and the lowest was in the annealed 0.05 at.% Pd alloy.

7.4. Effect of palladium and heat treatment on hydrogen storage

7.4.1. Effect of palladium addition on hydrogen storage

Absorption/desorption isotherms for as-cast $Ti_{24.975}V_{40}Cr_{34.975}Pd_{0.05}$ and $Ti_{24.95}V_{40}Cr_{34.95}Pd_{0.10}$ are shown in Figure 7.8. The effect of Pd on desorption isotherms of as-cast $Ti_{25}V_{40}Cr_{35}$ is shown in Figure 7.9 and the influence of isotherm temperature and Pd on RHSC is shown in Figure 7.10. The change in thermodynamic properties with additions of Pd to $Ti_{25}V_{40}Cr_{35}$ is presented in Table 7.2.

In Figures 7.8, the upper dashed curves are for absorption where hydrogen capacity increased with hydrogen pressure, while the lower solid curves are for desorption where hydrogen capacity decreased with hydrogen pressure. Hydrogen pressure was lowest at the start of the absorption process. As the H pressure increased, so the host metal absorbed more hydrogen. During desorption, more hydrogen atoms were desorbed from the adsorbate with increase in H pressure, which explains the observed trend in hydrogen pressure and capacity.

Figure 7.9 shows that the desorption curves of the as-cast 0.05 and 0.10 at.% Pd alloys had a flattened and wider plateau compared to the Pd-free sample. A flattened plateau shows a decrease in plateau pressure and a wider plateau signifies an increase in hydrogen capacity. In Table 7.2, the absorption and useful capacity increased with additions of Pd. The absorption capacity increased from 1.89 to 2.50 wt% in the 0.05 at.% Pd alloy and 2.51 wt% in 0.10 at.% Pd, while the useful capacity increased from 1.56 to 2.164 and 2.158 wt% for 0.05 and 0.10 at.% Pd compositions respectively. The plateau pressure decreased from 0.226 to 0.110 MPa in the 0.05 at.% Pd sample and to 0.114 MPa in the 0.10 at.% Pd sample. The increase in Pd from 0.05 to 0.10 at.% had no significant effect on useful capacity.

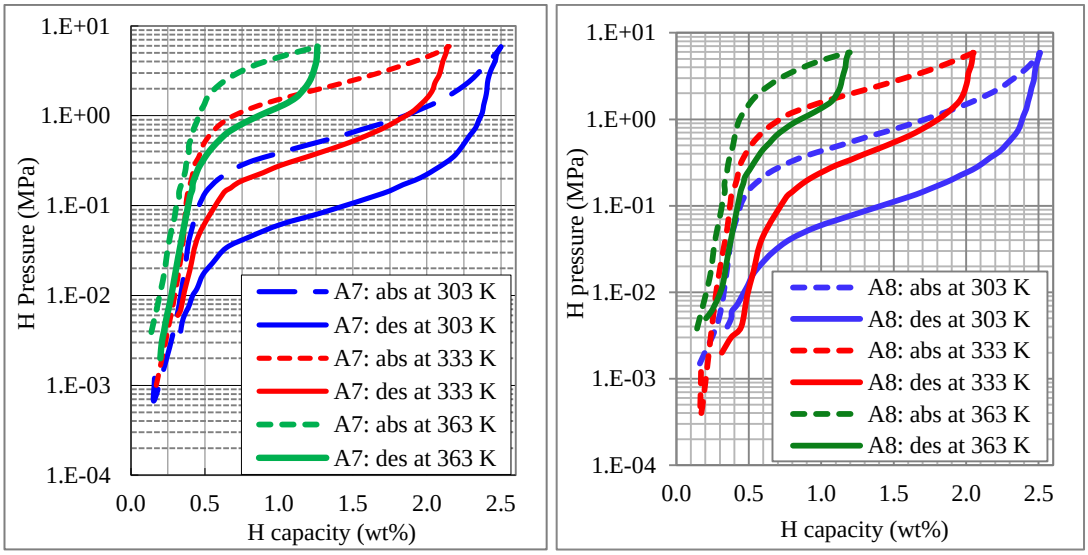

a) b)

Figure 7.8. Ab/desorption curves of as-cast a) 0.05 at.% Pd alloy and b) 0.10 at.% Pd alloy.

Figure 7.9 shows that addition of 0.05 at.% Pd significantly lowered the plateau pressure and that increasing the amount of Pd from 0.05 to 0.10 at.% had no significant effect on both the hydrogen ab/desorption capacity and thermodynamic properties, therefore 0.05 at.% Pd composition is economical.

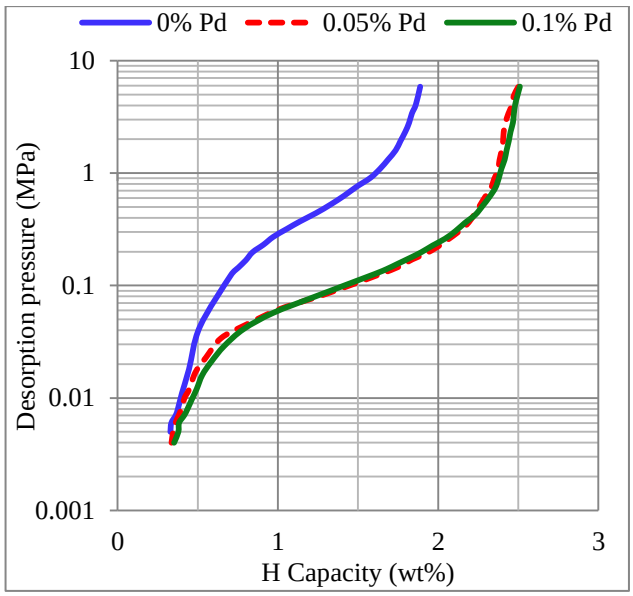

Figure 7.9. Effect of Pd on desorption curve of as-cast $Ti_{25}V_{40}Cr_{35}$ at 303 K.

Generally, the BCC phase is known to enhance hydrogen capacity, and Laves phase is detrimental to the capacity[10, 52, 55]; increases in cell volume and/or proportion of BCC implies availability of more hydrogen absorption sites and consequently increased storage capacity. The increase in cell volume of BCC (Figure 7.10) with addition of Pd could be responsible for the observed increase in RHSC.

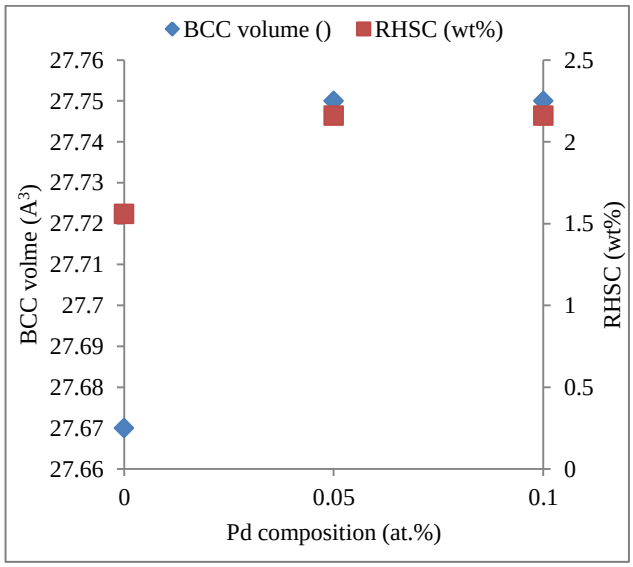

Figure 7.10. Effect of BCC volume on RHSC of $Ti_{25-0.5x}V_{40}Cr_{35-0.5x}Pd_x$ (x = 0.05, 0.10 at.%) alloys.

The van't Hoff plot of the Pd alloys in Figure 7.11 shows the effect of Pd composition. The slope and intercept was used to calculate the enthalpy and entropy of hydride desorption for 0.05 and 0.10 at.% Pd alloys. The values for 0 at.% Pd (the base alloy) was obtained from Equations 2.2 and 2.3, the results are shown in Table 7.2.

A flatter plateau or reduced plateau pressure is an indication of low strain energy[55]. Table 7.2 shows that addition of palladium to the as-cast alloy significantly reduced the plateau pressure from 0.23 to ~0.1 MPa, implying that the strain in the interstitial sites reduced with addition of palladium. Expansion in cell volume leads to increased interstice volume of the alloy and consequently increase the metal-hydrogen distance. As the metal-hydrogen distance is increased, the binding energy between metal and hydrogen atom is reduced, and consequently the interstitial strain energy is lowered[55]. This explains why there is reduction in plateau pressure to ~0.10 MPa

when the BCC cell volume increased from 27.67 to 27.75 Å^3 in both 0.05 and 0.10 at.% Pd alloys (Tables 4.8 and 4.9).

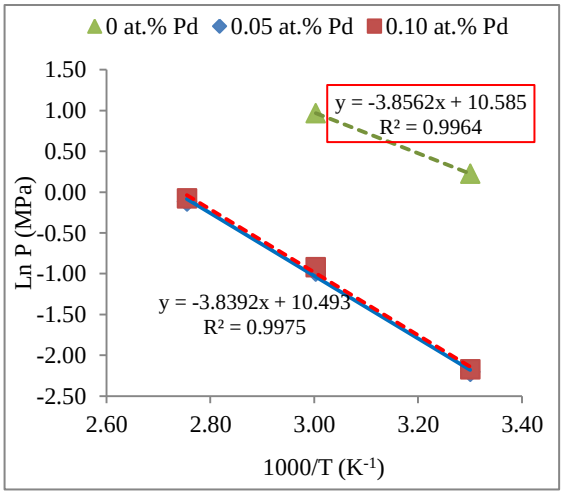

Figure 7.11. Van`t Hoff plot of $Ti_{25-0.5x}V_{40}Cr_{35-0.5x}Pd_x$ (x = 0, 0.05, 0.10 at.%) alloy.

The insignificant increase in H_2 capacity with increased Pd from 0.05 to 0.10 at.% is similar to the observation in Al addition to a (V) based BCC $(V_{30}Ti_{35}Cr_{25}Fe_{10})_{100-x}Al_x$ (x = 0 - 5 at.%) alloy, where the useful capacity was 1.6, 1.59 and 1.59 wt% for x = 0, 0.6 and 1.0 at.% respectively[198]. Although the maximum hydrogen capacity of ~1.9 wt% for $Ti_{25}V_{40}Cr_{35}$ in this work was less than ~2.2 wt% for $V_{0.68}Ti_{0.2}Cr_{0.12}$[147], the effective capacity of 1.56 wt% in this work is higher than 1.5 wt.% reported in $V_{0.68}Ti_{0.2}Cr_{0.12}$, whereas the $V_{0.68}Ti_{0.2}Cr_{0.12}$ alloy is more expensive due to higher V content.

Another observation from Table 7.2 is that the capacities remaining (14%) at the end of the desorption process in the Pd containing alloys were lower than 17 %, i.e. 86 % of the hydrogen absorbed was the RHSC. The high desorption capacity observed in Pd-containing alloys showed that the addition of Pd is likely to favour formation of the γ-phase (di-hydride). The hydrogen capacities that remained absorbed of the 0.34 wt% (0.05 at.% Pd) and 0.35 wt% (0.10 at.% Pd) samples are then likely to be those of monohydride, hence Pd is expected not to favour formation of the β-phase (mono-hydride).

Table 7.2. Thermodynamic properties of as-cast $Ti_{25-0.5x}V_{40}Cr_{35-0.5x}Pd_x$ (x = 0, 0.05, 0.10 at.%) alloy

x	Absorption capacity (wt%)	Capacity remaining (wt%)	Useful capacity (wt%)	Capacity remaining as % of absorbed capacity (%)	Plateau pressure (MPa)	$-\Delta H$ ($kJ.mol^{-1} H_2$)	$-\Delta S$ ($J\ mol^{-1}.K^{-1}$)
0	1.89	0.33	1.56	17	0.410	40.59	121.49
0.05	2.50	0.34	2.16	14	0.110	31.92	87.24
0.10	2.51	0.35	2.16	14	0.114	32.06	88.01

Table 7.2 also shows that process of hydride formation for the as-cast samples was exothermic. Addition of Pd reduced ΔH from 40.59 to 31.92 and 32.06 kJ mol^{-1} H_2 in the 0.05 and 0.10 at.% Pd alloys respectively. So with addition of Pd, less energy was required to break the bonds between H and its host and less heat was evolved.

Table 4.8 shows that both the C15 Laves phases of as-cast and the αTi quenched 0.05 at.% Pd samples contained 0.4 at.% Pd but different H_2 capacities. All the phases in as-cast and heat treated samples of 0.10 at.% Pd alloy had no Pd and had different capacities, therefore the different H capacities could be attributed to Pd composition in the phases.

7.4.2. Effect of testing temperature on hydrogen storage

For all alloy conditions in Figure 7.12, the maximum absorption capacity decreased with increased isotherm temperatures. For instance, the maximum hydrogen capacity of the as-cast Pd-free sample decreased from 1.89 wt% (303 K) to 1.30 wt% (333 K) and 1.00 wt% (363 K). However, in the as-cast 0.05 at.% Pd sample, the maximum capacity was 1.76 wt% when measured at 303 K, and the value decreased to 2.14 at 333 K and 1.26 wt% at 363 K. The maximum capacity in the 0.10 at.% Pd sample was 2.51, 2.05 and 1.19 at temperatures of 303, 333 and 363 K respectively. The trend was similar for the annealed and quenched samples and the suggested mechanism have been explained earlier in this section.

When the isotherm temperature is increased, the kinetic energy of the gas increases, making absorption of the energised gas more difficult, hence a decrease in absorption rate occurs. Decreased in temperature leads to lowering of kinetic energy, hence the

less energised gas is easily absorbed by the host, thereby resulting in an increase in the absorption capacity. The optimum values of useful capacity and the lowest plateau pressures were obtained at a temperature of 303 K for all samples.

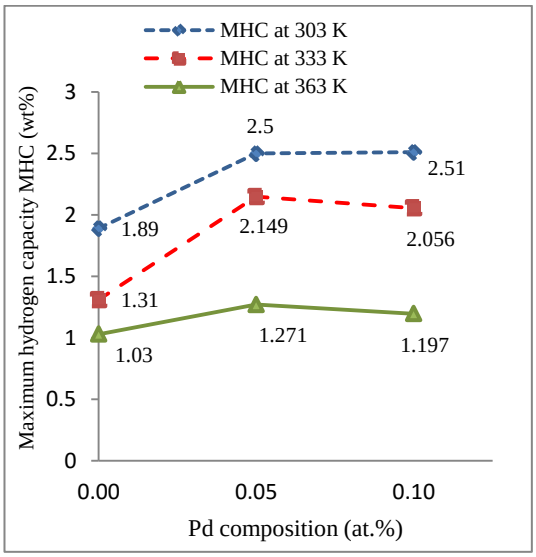

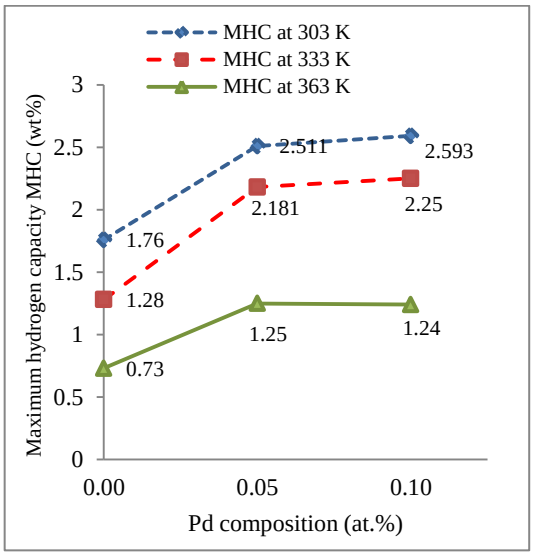

a) As-cast b) Annealed

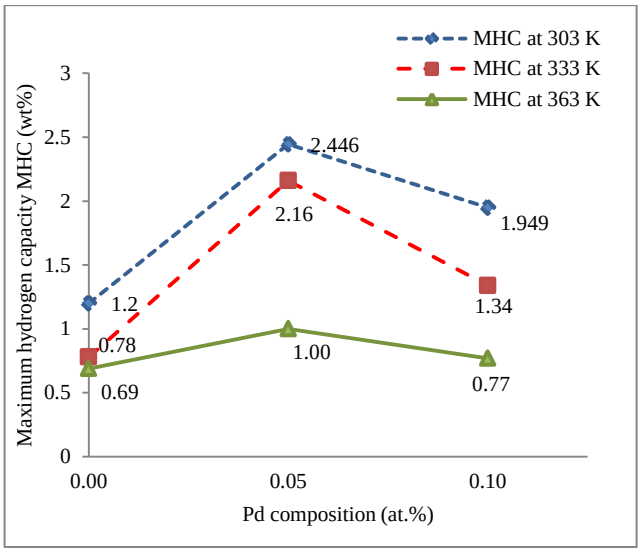

b) Quenched

Figure 7.12. Effect of isotherm temperature and Pd on maximum H capacity.

7.4.3. Effect of heat treatment on hydrogen storage properties

The RHSC of as-cast and heat treated samples of $Ti_{25-0.5x}V_{40}Cr_{35-0.5x}Pd_x$ (x = 0.05, 0.10 at.%) alloys are presented in Figure 7.13.

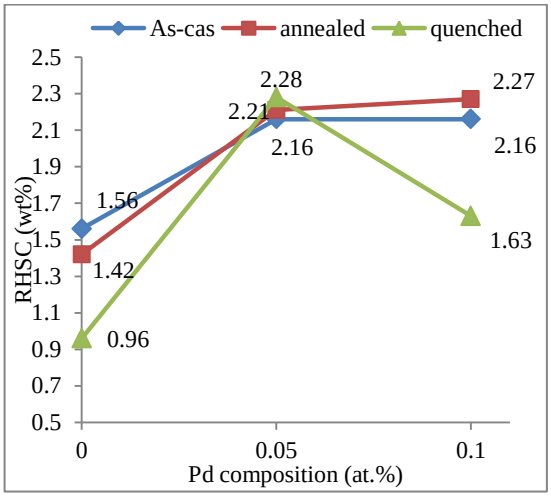

Figure 7.13. Effect of heat treatment on RHSC of $Ti_{25-0.5x}V_{40}Cr_{35-0.5x}Pd_x$ (x = 0, 0.05, 0.10 at.%) alloys.

The effect of heat treatment on RHSC of Pd-free sample was discussed in Section 5.4.3. In 0.05 at.% Pd, annealing increased the RHSC of the alloy from 2.16 to 2.21 wt%, while quenching increased it to 2.28 wt%. An increase in the cell volume of BCC (shown in Table 4.8) explains the reason for the rise in useful capacity of the quenched sample. Although the cell volume of BCC was unchanged after annealing, the Laves cell volume decreased, thus explaining the increase in RHSC.

It was observed that increasing Pd content to 0.10 at.% did not have significant improvement on the storage capacity of the as-cast alloy. However, annealing the 0.10 at.% Pd alloy increased the RHSC to a relatively higher value (2.27 wt%), while quenching reduced the capacity to 1.63 wt%. Although the cell volume of BCC did not change after both treatment processes, the reduction in Laves cell volume could be responsible for the increased capacity after annealing, while the observed decrease in the capacity after quenching could be a result of an enlarged Laves cell volume.

The van't Hoff plot for effect of heat treatment on Pd-containing alloys is shown in Figure 7.14. The shape of the curve is similar for the annealed and quenched samples, indicating similar thermodynamics properties, as shown in Table 7.3.

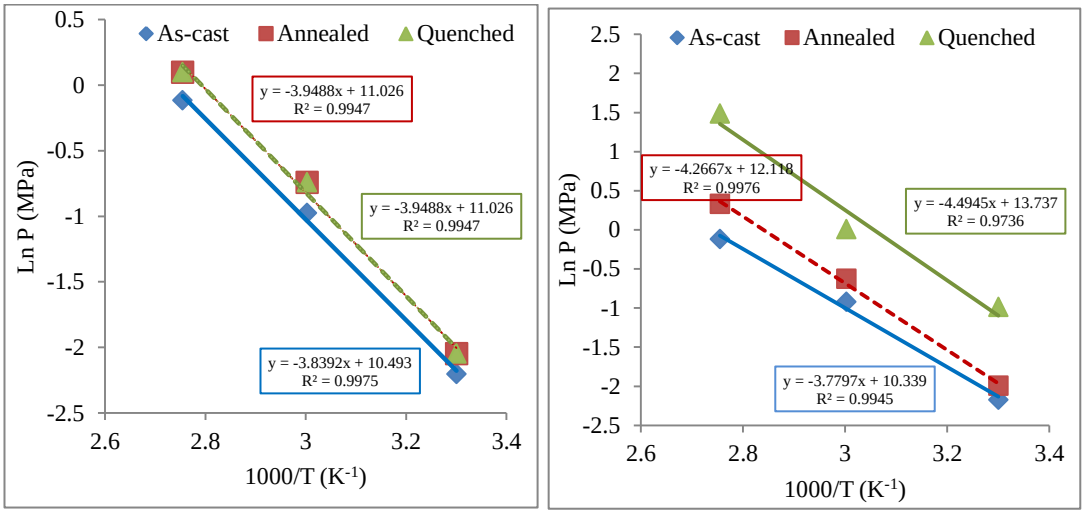

a) 0.05 at.% Pd alloy b) 0.10 at.% Pd alloy

Figure 7.14. Van't Hoff plots showing the effect of heat treatment on Pd alloys.

The slope and intercept values in Figures 7.14 a) and b) were used to obtain the thermodynamic properties in Table 7.3. In Figure 7.14a), the plot for annealed and quenched sample of the 0.05 at.% Pd alloy overlapped hence the equal values of ΔH and of ΔS in Table 7.3.

For the 0.05 at.% Pd alloy, the enthalpy of desorption increased from 31.92 to 32.83 kJ/mol H_2 after both annealing and quenching. This implies that heat treatment led to an increase in energy required to break metal-hydrogen bonds and more heat was liberated in the process.

The increase in entropy from 87.24 to 91.68 J/mol.K after heat treatment is an indication of higher disorder of the hydrogen atom on the host. Table 7.3 shows a similar trend for the 0.10 Pd alloy, *i.e.* heat treatment increased both the entropy and enthalpy of hydrogen desorption.

Table 7.3. Thermodynamics properties of as-cast and heat treated Pd containing alloys.

Pd compositions *x* (at.%)	Samples	Useful capacity (wt%)	$\Delta H = mR$ (kJ/mol H_2)	$\Delta S = Rc$ (J/mol.K)
0.05	As-cast	2.16	-31.92	87.24
	Annealed	2.21	-32.83	91.68
	Quenched	2.28	-32.83	91.68
0.10	As-cast	2.16	-31.43	88.01
	Annealed	2.27	-35.48	100.76
	Quenched	1.63	-37.37	114.22

Summary

Addition of Pd improved the absorption and RHSC and reduced entropy and enthalpy compared to the base alloy. Addition of 0.05 at.% Pd increased the RHSC from 1.86 to 2.16 wt%, but further increase in Pd from 0.05 to 0.10 at.% had no significant effect on the hydrogen capacity, therefore to save cost, 0.05 at.% Pd is sufficient. Heat treatment further increased the capacity of the as-cast sample in the 0.05 at.% Pd alloy, but annealing increased it, while quenching decreased the capacity of 0.10 at.% Pd alloy. The enthalpy and entropy of hydrogen desorption decreased after both treatments.

Summary of the chapter

The Pd-containing alloys contained both BCC and Laves phases, and Pd increased the cell volume of both phases. Addition of palladium reduced the corrosion rate, desorption plateau pressure, enthalpy and entropy of desorption. A marginal increase in RHSC was observed when the Pd composition was increased from 0.05 to 0.10 at.%. Both annealing and quenching further increased the RHSC in 0.05 Pd alloy but annealing increased and quenching decreased the H capacity of the 0.10 at.% Pd alloy.

For the 0.05 at.% Pd sample, annealing did not change the cell volume of BCC but reduced that of the Laves phase. Heat treatment had no effect on the BCC cell volume in the 0.10 at.% Pd sample. The cell volume of Laves decreased after annealing, but increased after quenching. Heat treatment reduced the hardness of both 0.05 and 0.10 at.% Pd alloys. Corrosion rates of as-cast 0.05 and 0.10 at.% Pd

alloys decreased after annealing but increased after quenching. The H capacity of the as-cast 0.05 and 0.10 at.% Pd alloys was enhanced after both heat treatments, except for quenched 0.10 at.% Pd.

CHAPTER 8: Summary

Overview

This chapter presents a summary of all the results in two sections based on specific objectives of the research:

- The effect of partial substitution of Fe or a PGM for Cr and Ti on the structure, mechanical properties and hydrogen storage characteristics of the $Ti_{35-0.5x}V_{40}Cr_{25-0.5x}M_x$ alloy (if M = Rh or Pd, x = 0.05, 0.10; if M = Fe, x = 0, 2, 5, 6 at.%).
- The effects of heat treatments on the structure, hardness, corrosion resistance and hydrogen storage characteristics.

8.1. Effect of substituting Fe or a PGM on the base alloy

The summary of all results is shown in Table 8.1. The effect of additives and heat treatments on hardness is shown in Figure 8.1, while similar figures for corrosion rate and RHSC of all alloys are Figures 8.2 and 8.3 respectively.

All of the alloys contained a primary bcc (V) phase and various intergranular minor phases. $Ti_{25-0.5x}V_{40}Cr_{35-0.5x}Fe_x$ (x = 0, 2, 5, 6 at.%) alloys contained (αTi) and C14 Laves secondary phases. Addition of Fe decreased the volume of the primary phase. Fe increased corrosion rates in all samples, except in 2 at.% Fe. Hardness increased with additions of Fe. Addition of Fe decreased the RHSC, while the plateau pressure in Fe-containing alloys was higher than in the Fe-free sample.

Addition of Rh increased the cell volume of both the BCC and (αTi) phases in the 0.05 at.% Rh alloy, but increased the BCC and decreased the (αTi) volume in the 0.10 at.% Rh sample. Rh decreased the corrosion rate and the hardness, but enhanced the RHSC of the base alloy.

The secondary phase in 0.10 at.% Pd was (αTi) while (βTi) was the secondary phase in 0.05 at.% Pd. As in the Rh-containing alloys, the presence of Pd decreased the

corrosion rate in 6M KOH. Addition of 0.05 Pd decreased the hardness, but the hardness increased in the 0.10 at.% Pd alloy. The Pd-containing samples had superior useful capacity (RHSC) and plateau properties to both the Fe and Rh containing alloys.

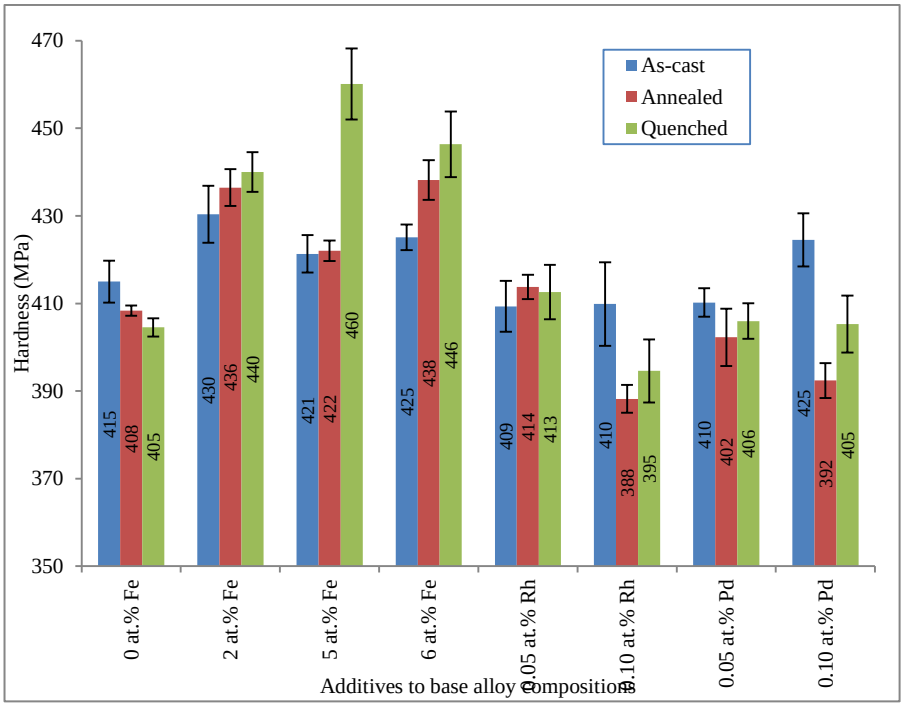

Figure 8.1. Effect of additives and heat treatment on hardness of all alloys.

8.1. Effect of heat treatment on the alloys

The primary bcc (V) phase volume in the 2 and 5 at.% Fe, and the Rh-containing alloys increased after annealing. The volume was unchanged after annealing Pd-containing alloys, but reduced the volume of bcc (V) in the base and 6 at.% Fe alloys. Quenching decreased the bcc (V) volume in 6 at.% Fe, had no effect on Rh-containing and 0.10 at.% Pd alloys, but increased the volume in 0, 2 and 5 at.% Fe samples.

Annealing and quenching decreased the hardness in the Fe-free sample, but increased the hardness in Fe-containing alloys. The hardness of the 0.05 at.% Rh alloy increased after both treatments, but that of 0.10 at.% Rh decreased. Both treatments

decreased the hardness in Pd-containing alloys. The quenched 5 at.% Fe sample had the highest hardness (460±6.22 MPa) and the quenched Fe-free sample had the lowest hardness (405±5.80 MPa).

Table 8.1. Summary of all results.

Alloys		RHSC	Plateau pressure	ΔH	ΔS	Hardness	Corrosion	Phases					
								Volume			Proportion		
								BCC	Secondary	Tertiary	BCC	Secondary	Tertiary
0% Fe	As-cast	1.56	0.41	**40.59**	54.5	415	0.011	27.67	36.24		89.7	10.3	
	Annealed	1.42	0.09	45.90	131.9	408	0.001	27.64	36.24	167.81	86.5	13.5	
	Quenched	0.96	0.9.	**27.43**	89.6	405	0.005	28.04	49.91		85.7	14.3	
2% Fe	As-cast	**0.44**	1.3	**110.40**	36	430	**0.0004**	27.08	36.24	161.7	78.5	20.2	**1.3**
	Annealed	1.26	0.68	-	-	436	0.0009	27.37	36.24	334.5	82	18	
	Quenched	0.65	**2.34**	-	-	440	0.0017	27.37	**354.4**	167.8	81.5	16.5	2
5% Fe	As-cast	0.75	1.92	51.80	**22.57**	421	0.034	26.95	36.24	167.8	**67.5**	**32.5**	
	Annealed	0.86	1.86	-	-	422	0.001	27.08	**28.26**	**36.24**	90	**2**	**8**
	Quenched	0.46	-	-	-	**460**	0.002	27.08	36.24	49.91	74.3	20	5.7
6% Fe	As-cast	0.68	1.34	31.50	106.2	425	0.016	27	36.24	167.81	85.5	14.5	
	Annealed	0.58	-	-	-	438	0.001	26.95	49.91		73.5	26.5	
	Quenched	0.48	-	-	-	446	**0.037**	**26.71**	51.68	**334.5**	76.4	23.6	
0.05% Rh	As-cast	1.74	**0.02**	41.79	104.11	409	0.0009	27.37	36.25		82.2	17.8	
	Annealed	2.25	0.02	44.20	110.18	414	0.0007	28.09	167.81		81.8	18.2	
	Quenched	1.65	0.21	37.21	110.13	413	0.0014	27.37	49.99		82.0	18	
0.10% Rh	As-cast	1.87	0.29	41.98	128.19	410	0.001	27.75	34.48		84.8	15.2	
	Annealed	2.05	0.21	42.77	142.32	**388**	0.0015	**28.09**	167.81		82.5	17.5	
	Quenched	2.01	0.25	46.74	**155.58**	395	0.0023	27.75	49.99	334.5	83	17	
0.05% Pd	As-cast	2.16	2.16	31.43	85.96	410	0.0014	27.75	59.68		88.5	11.5	
	Annealed	2.21	2.21	32.83	91.68	402	0.0006	27.75	49.99		89.5	10.5	
	Quenched	**2.28**	2.28	32.83	91.68	406	0.0137	28.09	52.09		86	14	
0.10% Pd	As-cast	2.16	2.16	31.43	85.96	425	0.0025	27.75	40.72		91.4	8.6	
	Annealed	2.27	2.27	35.48	100.76	392	0.0019	27.75	35.22		90	10	
	Quenched	1.63	1.63	37.37	114.42	405	0.0079	27.75	128.5		**92.6**	7.4	
	Maximum	**2.28**	**2.34**	**110.40**	**155.58**	**460**	**0.037**	**28.09**	**354.4**	**334.5**	**92.6**	**32.5**	**8.00**
	Minimum	**0.44**	**0.02**	**27.43**	**22.57**	**388**	**0.0004**	**26.71**	**28.26**	**36.24**	**67.50**	**2.00**	**1.30**

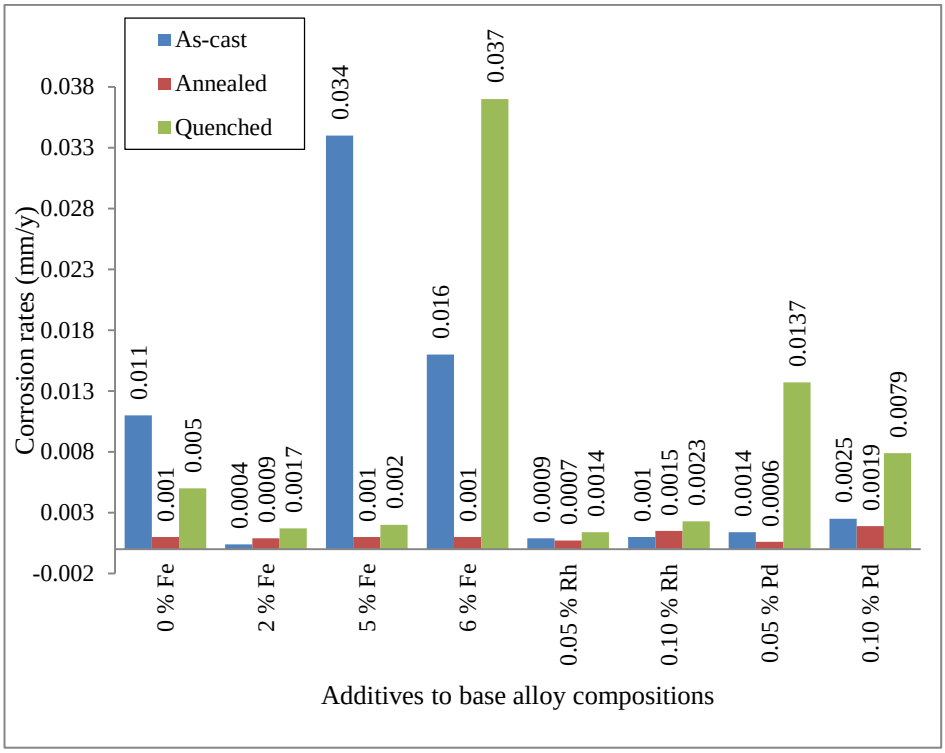

Figure 8.2. Effect of additives and heat treatment on corrosion rate of all the alloys.

The corrosion rate decreased after annealing 0, 5 and 6 at.% Fe; 0.05 at.% Rh and Pd-containing alloys, while the rate increased after annealing the 2 at.% Fe and 0.10 at.% Rh alloys. Quenching decreased the corrosion rate of the 0 and 5 at.% Fe alloys, but increased the rate in 2 and 6 at.% Fe, Rh-containing and Pd-containing samples. Table 8.1 and Figure 8.2 shows that the highest corrosion rate was in the quenched 6 at.% Fe sample (0.037 mm/y) and the lowest rate was in the as-cast 2 at.% Fe (0.0004 mm/y).

Annealing increased the useful capacity (RHSC) in 2 and 5 at.% Fe, Rh-containing and Pd-containing samples but decreased it in 0 and 6 at.% Fe samples. Quenching was favourable for useful hydrogen capacity (RHSC) in 2 at.% Fe, 0.10 at.% Rh and 0.05 at.% Pd samples but detrimental to the capacity in 0, 5 and 6 at.% Fe; 0.05 at.% Rh and 0.10 at.% Pd samples. The highest RHSC was in the quenched 0.05 at.% Pd sample.

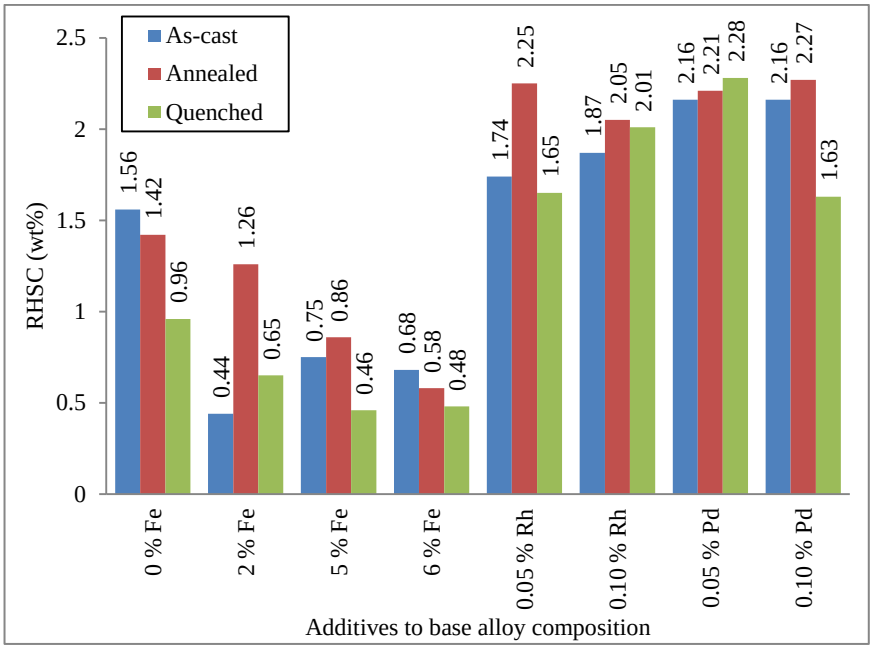

Figure 8.3. Effect of additives and heat treatment on RHSC of all alloys.

The hydrogen capacity of as-cast 0.05 and 0.10 at.% Pd were similar, although the 0.05 at.% Pd alloy in the quenched condition had a better hydrogen capacity than the 0.10 at.% Pd sample. The corrosion rate of as-cast 0.05 at.% Pd was lower making it a more suitable electrode material in 6 M KOH solution, so addition of 0.10 at.% Pd would not be cost effective in terms of hydrogen capacity and corrosion resistance. The annealed 0.05% Rh (2.25 wt%) had a similar RHSC to 0.05% Pd (2.28 wt%), so it could be a viable alternative, although the 2015 price of rhodium was a third higher than the palladium price per ounce.

As expected, the addition of iron was detrimental to hydrogen storage in $Ti_{25}V_{40}Cr_{35}$, although the annealed samples showed less reduction than the as-cast and quenched samples. If there is a cost-performance trade off, iron amounts of less than 2 at.% could be studied further as possible alternatives. The heat treatments should also be evaluated to improve performance.

In the PGM-containing alloys, annealing produced RHSC values higher than 2.2 wt% H. The lower PGM additions (0.05 at.%) show promise, and further work should be done to optimise heat treatments of these alloys.

CHAPTER 9: Conclusions

The microstructure, hardness, corrosion behaviour and hydrogen storage characteristics of $Ti_{35-0.5x}V40Cr_{25-0.5x}Fe_x$ (x = 0, 2, 5, 6 at.%) and $Ti_{35-0.5x}V_{40}Cr_{25-0.5x}M_x$ (M = Rh or Pd; x = 0.05, 0.10 at.%) were studied. The influence of heat treatment on the properties was also investigated. The main conclusions are:

1. The reversible hydrogen storage capacity (RHSC) of the base alloy was enhanced with addition of Pd and Rh, but decreased with Fe addition.
2. The quenched 0.05 at.% Pd sample had the highest RHSC of 2.28 wt%, and the annealed 0.10 at.% Pd sample had the second highest of 2.27 wt%, while the lowest RHSC of 0.44 wt% was observed in the as-cast 2 at.% Fe sample.
3. The addition of 0.10 at.% Pd showed no significant improvement on the RHSC of the 0.05 at.% Pd alloy, The respective RHSC for 0.05 and 0.10 at.% was 2.159 and 2.164 wt%, thus addition of 0.05 at.% Pd would be sufficient. The RHSC of the annealed 0.05 at.% Rh (2.25 wt% H) is close to the value obtained in 0.10 at.% Pd, so it could be an alternative to the quenched 0.05 at.% Pd.
4. Annealing improved the RHSC of all samples except the Fe-free and 6 at.% Fe sample, while quenching was detrimental to RHSC of all the samples except the 2 at.% Fe, 0.05 at.% Pd and 0.10 at.% Rh samples.
5. Although the 2 at.% Fe alloy had the lowest RHSC, it could find its application as an electrode in 6M KOH solution electrolyte because of its low corrosion rate.
6. Similar to other PGMs, additions of Rh or Pd decreased the corrosion rate in 6M KOH. The rate also decreased with addition of 2 at.% Fe, but increased with higher amounts of 5 and 6 at.% Fe.
7. The corrosion rate of the base alloy decreased after annealing the 0.05 at.% Rh, 5 and 6 at.% Fe alloys, while the rate increased after annealing the 2 at.% Fe and 0.10 at.% Rh samples. Annealing reduced the corrosion rate of Pd-containing alloys, but quenching increased the rate.

8. The as-cast 2 at.% Fe alloy had the lowest corrosion rate (0.0004 mm/y) and the quenched 6 at.% Fe was the least corrosion resistant sample with a corrosion rate of 0.037 mm/y.

9. The hardness of the base alloy increased with additions of Fe and 0.10 at.% Pd, but decreased with additions of Rh and 0.05 at.% Pd.

10. Both annealing and quenching increased the hardness in the 0.05 at.% Rh and Fe-containing samples.

11. The highest hardness (460 HV2) was observed in the quenched 5% Fe sample, while the lowest (388 HV2) was in the annealed 0.10 at.% Rh.

CHAPTER 10: Recommendations

These alloys have only been assessed over one absorption-desorption cycle. Further work should therefore be considered to determine the behaviour over multiple cycles, as would be experienced in reality.

Analysis (such as XRD, SEM and EDS) of the hydrogenated samples should be carried out in further studies. This will reveal the amount of di-hydride and mono-hydride formed during the hydrogenation process.

More detailed SEM of the secondary phases should be done to establish the exact nature of the secondary phases.

References

1. *US DoE Fuel cell technology program (safety codes and standard)*. (January, 2011). United States.
2. Hydrogen storage technology roadmap. (2005) *United States Department of Energy FreedomCAR and fuel partnership*. Washington.
3. *Fuel cell technology program (Hydrogen storage).* (January, 2011). United States, Department of Energy Retrieved from www.eere.energy.gov/informationcenter.
4. I. R. Harris. (1987). The potential of hydrogen in permanent magnet production. *Journal of the Less-Common Metals, 131*(1–2), 245-262. doi: 10.1016/0022-5088(87)90524-8.
5. M. Anissimov. (2012). What Are Some Uses of Hydrogen? *wiseGEEK clear answers for common questions*. Retrieved from *www.wisegeek.org/what-are-some-uses-of-hydrogen.htm*.
6. P.D Goodell, G.D. Sandrock, E.L. Huston (1980) Kinetic and dynamic aspects of rechargeable metal hydrides. *Journal of Less Common Metals* 73:135–142
7. Y. Zhang, X. Zhuang, Y. Zhu, L. Zhan, Z. Pu, N. Wan, L. Li (2016). Effects of additive Pd on the structures and electrochemical hydrogen storage properties of $Mg_{67}Co_{33}$-based composites or alloys with BCC phase. *Journal of Alloys and Compounds, 622, Pp 580-586.*
8. M. Pezat, B. Darriet and P. Hagenmuller. (1980). A comparative study of magnesium-rich rare-earth-based alloys for hydrogen storage. *Journal of the Less-Common Metals, 74*(2), 427-434. doi: http://dx.doi.org/10.1016/0022-5088(80)90181-2.
9. H. A. Klehne. (2003). *Battery Technology Handbook* Vol. 2nd Edition. Renningen-Masheim, Germany: Expert Verlag GmbH.
10. B. Darriet, M. Pezat, A. Hbika and P. Hagenmuller. (1980). Application of magnesium rich rare-earth alloys to hydrogen storage. *International Journal of Hydrogen Energy, 5*(2), 173-178. doi: http://dx.doi.org/10.1016/0360-3199(80)90094-4.
11. Z. Chen, X. Xiao, L. Chen, X. Fan, L. Liu, S. Li, H. Ge and Q. Wang. (2014). Influence of Ti super-stoichiometry on the hydrogen storage properties of $Ti_{1+x}Cr_{1.2}Mn_{0.2}Fe_{0.6}$ (x = 0–0.1) alloys for hybrid hydrogen storage 0application. *Journal of Alloys and Compounds, 585*, 307-311. doi: http://dx.doi.org/10.1016/j.jallcom.2013.09.141.
12. J. S. Harris and W. L. Snyder. (1969). Homogeneous solution grown epitaxial GaAs by tin doping. *Solid-State Electronics, 12*(5), 337-340. doi: 10.1016/0038-1101(69)90088-4.
13. L. Hao, C. Yungui, Y. Yigang, W. Chaoling and T. Mingda. (2007). Cyclic properties of hydrogen absorption and desorption in V–Ti–Cr–Fe(Al,Si) alloy. *Materials Science and Engineering: A, 448*(1–2), 128-134. doi: 10.1016/j.msea.2006.10.055.
14. F. Roux. (2005). 2005 Annual Report. In K. Rumble (Ed.). South Africa: implats.
15. M. S. Bawa and E. A. Ziem. (1982). Long-term testing and stability of $CaNi_5$ alloy for a hydrogen storage application. *International Journal of Hydrogen*

Energy, *7*(10), 775-781. doi: http://dx.doi.org/10.1016/0360-3199(82)90067-2.

16. P.D Goodell, G.D. Sandrock, E.L. Huston (1980) Kinetic and dynamic aspects of rechargeable metal hydrides. *Journal of Less Common Metals* 73:135–142.
17. M. D. Hampton, D. V. Shur, C. Zaginali and V. I. Trefilov. (2002). *Hydrogen Materials' Science and Chemistry of Metal Hydrides.* Vol. 71. Dodrechi, Boston, London: Kluver Academic Publisher.
18. B. Sakintuna, F. Lamari-Darkrim and M. Hirscher. (2007). Metal hydride materials for solid hydrogen storage: A review. *International Journal of Hydrogen Energy*, *32*(9), 1121-1140. doi: 10.1016/j.ijhydene.2006.11.022
19. Z. Hang, X. Xiao, D. Tan, Z. He, W. Li, S. Li, C. Chen and L. Chen. (2010). Microstructure and hydrogen storage properties of $Ti_{10}V_{84-x}Fe_6Zr_x$ (x = 0; 1–8) alloys. *International Journal of Hydrogen Energy*, *35*(7), 3080-3086. doi: 10.1016/j.ijhydene.2009.07.019.
20. Z. Cao, L. Ouyang, H. Wang, J. Liu, L. Sun, M. Felderhoff, M. Zhu (2016). Development of Zr-Fe-V alloys for hybrid hydrogen storage system. *International Journal of Hydrogen Energy*, ***In Press, Corrected proof****, Available online 8 May 2016.*
21. D. P. Broom. (2008). Hydrogen sorption measurements on potential storage materials: Experimental methods and measurement accuracy *Office for Official Publications of the European Communities, Luxembourg* (Vol. EUR 23242 EN).
22. E. Akiba and H. Iba. (1998). Hydrogen absorption by Laves phase related BCC solid solution. *Intermetallics*, *6*(6), 461-470. doi: http://dx.doi.org/10.1016/S0966-9795(97)00088-5
23. S-J Qiua,H-L Chu, Y Zhang, L-X Sun, F Xua, Z CaO (2008) , The electrochemical performances of Ti–V-based hydrogen storage composite electrodes prepared by ball milling method *International Journal of Hydrogen Energy, 3 3, Pp. 7 4 7 1 – 7 4 7 8.*
24. S.-W. Cho, C.-S. Han, C.-N. Park and E. Akiba. (1999). Hydrogen storage characteristics of Ti–Zr–Cr–V alloys. *Journal of Alloys and Compounds*, *289*(1–2), 244-250. doi: 10.1016/s0925-8388(99)00162-0.
25. V. Y. Labaton, S. G. Donn, R. H. Watson and E. Whitehead. (1963). Kinetics of the reaction of hydrogen with zirconium-titanium alloy. *Journal of Inorganic and Nuclear Chemistry*, *25*(6), 641-656. doi: http://dx.doi.org/10.1016/0022-1902(63)80153-0.
26. R. C. Weast, M. J. Astle and W. H. Beyer. (1983). *CRC Handbook of Chemistry and Physics.* 64th Edition. London: CRC Press.
27. J. M. Ogden. (1999). Developing an infrastructure for hydrogen vehicles: a Southern California case study. *International Journal of Hydrogen Energy*, *24*(8), 709-730. doi: 10.1016/s0360-3199(98)00131-1.
28. M. L. Trudeau. (1999). Advanced materials for energy storage. Berlin-Heidelberg: Springer-Verlag. p200.
29. B. Strategy. (June 2011). *A Beneficiation strategy for the mineral industry of South Africa* Republic of South Africa: South African Government Retrieved from www.info.gov.za/view/DownloadFileAction?id=147564 accessed 12/7/13.

30. D. B. Willey, I. R. Harris and A. S. Pratt. (1999). The improvement of the hydrogenation properties of nickel-metal hydride battery alloy by surface modification with platinum group metals (PGMs). *Journal of Alloys and Compounds, 293–295*, 613-620. doi: 10.1016/s0925-8388(99)00353-9.
31. Diesel fumes causes lung cancer, W.H.O. says. (June 13 2012). *The New York Times*.
32. A. P. Mills. (1992). *Materials of construction: The manufacture and properties.* Vol. 2. University of Wisconsin, Madison: John Wiley and Sons Inc.
33. J. L. Murray. (1987). The Ti-V system, Phase Diagrams of Binary Titanium Alloys. In J. L. Murray (Ed.), (pp. 319-327). Metals Park, OH USA: ASM International.
34. F. Wei and H. M. Flower. (1989). *Phase separation reactions in Ti-50V alloys* Vol. 5.
35. J. L. Murray. (1987). The Ti-Cr system, Phase Diagrams of Binary Titanium Alloys. In J. L. Murray (Ed.), (pp. 68-78). Metals Park, OH USA: ASM International.
36. J. F. Smith. (1989). The Cr-V system, Phase Diagrams of Binary Vanadium Alloys. (pp. 58-62). Metals Park, OH: ASM International.
37. N. N. Samsonova and P. B. Budberg. (1966). Effect of V and Mo on the properties and phase transformation of the intermetallic compound $TiCr_2$. *Poroshk Metallurgical, 8*(49), 1882-1888.
38. N. N. Samsonova, P. B. Budberg, I. I. Kornilov and U. A. Asanov. (1966). Interaction of the $TiCr_2$ intermetallic with V. *Izv Akad Nauk SSSR, Neorg. mater, 2*(1), 882-885.
39. M. Enomoto. (1992). The Cr-Ti-V system (Chromium-Titanium-Vanadium). *Journal of Phase Equilibria, 13*(2), 195-199.
40. J. L. Murray. (1981). The Ti-V system. *Bull Alloy Phase Diagram, 2*(1), 48-55.
41. K. S. Kumar and P. M. Hazzledine. (2004). Polytypic transformations in Laves phases. *Intermetallics, 12*(7–9), 763-770. doi: http://dx.doi.org/10.1016/j.intermet.2004.02.017.
42. A. J. Maeland, G. G. Libowitz and J. P. Lynch. (1984). Hydride formation rates of titanium-based b.c.c. solid solution alloys. *Journal of the Less-Common Metals, 104*(2), 361-364. doi: http://dx.doi.org/10.1016/0022-5088(84)90420-X.
43. G. Litjering; and C. W. James. (2003). *Engineering Materials and Processes*. Germany: Springer-Verlag. Pp.379-382.
44. J. J. McEwan. (2004). *Corrosion control in South Africa*. CorrISA, Republic of South Africa: Kelvin. Pg.136.
45. US DoE, Hydrogen storage technology roadmap. (United States Department of Energy FreedomCAR and fuel partnership, 2005). Washington Downloaded from www.nrel.gov/docs/fy08osti/39146.pdf. Accessed 5/8/12
46. R. H. Crabtree. (2008). Hydrogen storage in liquid organic heterocycles *Energy Environmental Science 1*, 134-138. doi: 10.1039/B805644G.
47. US DoE, Hydrogen storage technology roadmap. (United States Department of Energy FreedomCAR and fuel partnership). Washington Downloaded from www.nrel.gov/docs/fy08osti/39146.pdf. Accessed 09/05/16.

48. J. Graetz and J. J. Reilly. (2007). Kinetically stabilized hydrogen storage materials. *Scripta Materialia, 56*(10), 835-839. doi: 10.1016/j.scriptamat.2007.01.007.
49. A. P. Woodhead and D. P. Broom. (2007). The activation of $LaNi_5$-H. *Hiden Iso chema Applications Article, 125, 200-205*.
50. G. Sandrock. (1999). A panoramic overview of hydrogen storage alloys from a gas reaction point of view. *Journal of Alloys and Compounds, 293–295*, 877-888. doi: 10.1016/s0925-8388(99)00384-9.
51. M. He and W. G. Wang. (2010). Mechanisms of improving the cyclic stability of V–Ti-based hydrogen storage electrode alloys. *Journal of Alloys and Compounds, 508* 592-598. doi: 10.1016/j.jallcom.2010.08.132.
52. Y. Nakamura, K. Oguro, I. Uehara and E. Akiba. (2000). X-ray diffraction peak broadening and degradation in LaNi5-based alloys. *International Journal of Hydrogen Energy, 25*(6), 531-537. doi: 10.1016/s0360-3199(99)00066-x.
53. D. P. Broom. (2011). *Hydrogen Storage Materials; The Characterisation of thier storage properties.* London: Springer-Verlag London Limited.
54. K. A. G. Amankwah and J. A. Schwarz. (1991). Assessment of the effect of impurity gases on the storage capacity of hydrogen on activated carbon using the concept of effective adsorbed phase molar volume. *International Journal of Hydrogen Energy, 16*(5), 339-344. doi: 10.1016/0360-3199(91)90170-n.
55. K. Feucht, W. Hurich, N. Komoschinski and R. Povei. (1988). Hydrogen drive for road vehicles-results from the fleet test run in Berlin. *International Journal of Hydrogen Energy,13*(4), 243-250. doi: 10.1016/0360-3199(88)90092-4.
56. S. Suwarno, J. K. Solberg, J. P. Maehlen, B. Krogh, B. T. Børresen, E. Ochoa-Fernandez, E. Rytter, M. Williams, R. Denys and V. A. Yartys. (2012). Microstructure and hydrogen storage properties of as-cast and rapidly solidified Ti-rich Ti–V alloys. *Transactions of Nonferrous Metals Society of China, 22*(8), 1831-1838. doi: 10.1016/s1003-6326(11)61394-0
57. C. Ghosh, J. Basu, D. Ramachandran and E. Mohandas. (2015). Alloy design and microstructural evolution in V–Ti–Cr alloys. *Materials Characterization, 106*, 292-301. doi: http://dx.doi.org/10.1016/j.matchar.2015.06.032.
58. S. Chalk and L. Inouye. (2004). *The President's U.S hydrogen initiative. In Sperling, D, Cannon JS (eds) the hydrogen energy transition: moving towards the post petroleum age in transportaion.* Oxford: Elsevier Academic Press.
59. Q. Wang, D. Zhu, W. Zhou, C. Zhong, C. Wu, Y. Chen (2016). High-temperature electrochemical performance of low-cost La–Ni–Fe based hydrogen storage alloys with different preparation methods. *Materials Research Bulletin, 76, Pp 28-36.*
60. S. W. Lambert, D. Chandra, W. N. Cathey, F. E. Lynch and R. C. Bowman Jr. (1992). Investigation of hydriding properties of LaNi4.8Sn0.2, LaNi4.27Sn0.24 and La0.9Gd0.1Ni5 after thermal cycling and aging. *Journal of Alloys and Compounds, 187*(1), 113-135. doi: http://dx.doi.org/10.1016/0925-8388(92)90527-G.
61. F. Rouquerol, J. Rouquerol and K. Sing. (1999). *Adsorption by powders and porous solids: principles, methodology and applications.* London: Academic Press.

62. S. Suwarno, J. K. Solberg, J. P. Maehlen, B. Krogh, B. T. Børresen, E. Ochoa-Fernandez, E. Rytter, M. Williams, R. Denys and V. A. Yartys. (2012). Microstructure and hydrogen storage properties of as-cast and rapidly solidified Ti-rich Ti–V alloys. *Transactions of Nonferrous Metals Society of China*, *22*(8), 1831-1838. doi: 10.1016/s1003-6326(11)61394-0.
63. M. Yang, X. Zhao, Y. Ding, L. Ma, X. Qu and Y. Gao. (2010). Electrochemical properties of titanium-based hydrogen storage alloy prepared by solid phase sintering. *International Journal of Hydrogen Energy 35(4)* 2717-2721. doi: 10.1016/j.ijhydene.2009.04.045.
64. W. Young, Z. Yongqing, Z. Weidong, H. Hongliang and W. Yaoqi. (2010). Behavior of Hydrogen Absorption/Desorption of Ti600, TC21 and Ti40 Alloys. *Rare Metal Materials and Engineering*, *39*(9), 1509-1512. doi: http://dx.doi.org/10.1016/S1875-5372(10)60120-8..
65. S. F. Santos and J. Huot. (2009). Hydrogen storage in $TiCr_{1.2}(FeV)_x$ BCC solid solutions. *Journal of Alloys and Compounds*, *472*(1–2), 247-251. doi: 10.1016/j.jallcom.2008.04.062.
66. L. E. A. Berlouis, N. Comisso and G. Mengoli. (2006). Changes in hydrogen storage properties of binary mixtures of intermetallic compounds submitted to mechanical milling. *Journal of Electroanalytical Chemistry*, *586*(1), 105-111. doi: 10.1016/j.jelechem.2005.09.023.
67. J.-Y. Wang, R.-R. Jeng, J.-K. Nieh, S. Lee, S.-L. Lee and H.-Y. Bor. (2007). Comparing the hydrogen storage alloys—TiCrV and vanadium-rich TiCrMnV. *International Journal of Hydrogen Energy*, *32*(16), 3959-3964. doi: 10.1016/j.ijhydene.2007.05.025.
68. K. I. Yokoyama, T. Ogawa, K. Asaoka and J. I. Sakai. (2005). Evaluation of hydrogen absorption properties of Ti–0.2mass% Pd alloy in fluoride solutions. *Journal of Alloys and Compounds*, *400*(1–2), 227-233. doi: 10.1016/j.jallcom.2005.03.048.
69. P. Pei, S. Xiping, Z. Ming, Z. Peilong and C. Guoliang. (2008). influence of V content on hydrogen storage properties in low vanadium Ti-V-Cr alloy.pdf. *Rare Metal Materials and Engineering*, *37*(8), 1419-1423.
70. H. S. Chung and J. Y. Lee. (1986). Effect of partial substitution of Mn and Ni for Fe in FeTi on hydriding kinetics. *International Journal of Hydrogen Energy*, *11*(5), 335-339. doi: http://dx.doi.org/10.1016/0360-3199(86)90153-9.
71. E. L. Huston and G. D. Sandrock. (1980). Engineering properties of metal hydrides. *Journal of the Less-Common Metals*, *74*(2), 435-443. doi: http://dx.doi.org/10.1016/0022-5088(80)90182-4.
72. D. Planté, J. Andrieux, L. Laversenne and S. Miraglia. (2015). In situ X-Ray diffraction study of hydrogen sorption in V-rich Ti–V–Cr bcc solid solutions. *Journal of Alloys and Compounds*, *648*, 79-85. doi: http://dx.doi.org/10.1016/j.jallcom.2015.05.254.
73. H. C. Lin, K. M. Lin, K. C. Wu, H. H. Hsiung and H. K. Tsai. (2007). Cyclic hydrogen absorption–desorption characteristics of TiCrV and $Ti_{0.8}Cr_{1.2}V$ alloys. *International Journal of Hydrogen Energy 32* 4966 4972. doi: 10.1016/j.ijhydene.2007.07.057.

74. Y. Tominaga, S. Nishimura, T. Amemiya, T. Fuda, T. Tamura, T. Kuriwa, A. Kamegawa and M. Okada. (1999). Structures and electrochemical performances of Laves phase alloy *Materia Trans. JIM., 40*, 871-880.
75. M. Okada, T. Kuriiwa, T. Tamura, H. Takamura and A. Kamegawa. (2001). *Met. Mater. Inter., 7*, 67-74.
76. D. Tou, W. Zhu, M. Jianfeng and N. Xua. (2008). Application of commercial ferrovanadium to reduce cost of Ti–V-based BCC phase hydrogen storage alloys. *Materials Science and Engineering, A 476*, 34-38. doi: 10.1016/j.msea.2007.04.080.
77. T. Huang, Z. Wu, G. Sun and N. Xu. (2007). Microstructure and hydrogen storage characteristics of $TiMn_{2-x}V_x$ alloys. *Intermetallics*, *15*(4), 593-598. doi: 10.1016/j.intermet.2006.10.035.
78. H. Taizhong, W. Zhu, S. Guoxin and X. Naixin. (2008). Influences of Partial Substitution of VFe Alloys for Cr on Structure and Hydrogen Storage Performances of $TiCr_{1.8}$ Alloy. *Rare Metal Materials and Engineering, 37*(3), 386-390. doi: 10.1016/s1875-5372(09)60010-2.
79. Y. Qiao, M. Zhao, M Li, X. Zhuc and G. Caoc (2006). Microstructure and electrochemical performance of $Ti_{0.17}Zr_{0.08}V_{0.34}Pd_{0.01}Cr_{0.1}Ni_{0.3}$ electrode alloy. *Scripta Materialia 55, Pp. 279–282.*
80. K. Shirasaki, T. Tamura, T. Kuriiwa, T. Goto, A. Kamegawa, H. Takamura and M. Okada (2002). Cyclic properties of protium absorption-desorption in Ti-V-Cr alloys. *Material Transactions, 43(5) pp1115-1119.*
81. A. Martínez and D. S. dos Santos (2012). Hydrogen absorption/Desorption Properties in the TiCrV Based Alloys. *Materials Research, 15(5), Pp. 809-812.*
82. Y. Yigang, C. Yungui, L. Hao, Z. Xiaoxiao, W. Chaoling, T. Mingda and L. Pang. (2008). Hydrogen storage properties of V–Ti–Cr–Fe alloys. *Journal of Alloys and Compounds 454*(5), 427-431. doi: 10.1016/j.jallcom.2006.12.093.
83. S. Suwarno, J. K. Solberg, J. P. Maehlen, B. Krogh and V. A. Yartys. (2012). Influence of Cr on the hydrogen storage properties of Ti-rich Ti–V–Cr alloys. *International Journal of Hydrogen Energy*, *37*(9), 7624-7628. doi: 10.1016/j.ijhydene.2012.01.149.
84. Y. Yan, Y. Chen, X. Zhou, H. Liang, C. Wu and M. Tao. (2008). Some factors influencing the hydrogen storage properties of 30V–Ti–Cr–Fe alloys. *Journal of Alloys and Compounds*, *453*(1–2), 428-432. doi: 10.1016/j.jallcom.2006.11.122.
85. C. Wu, A. Borgschulte, U. Frischknecht, Y. Yan, F. Yang, L. Luo, Y. Chen and A. Züttel (2013). Surface Properties of $V_{40}(TiCr)_{51}Fe_8Mn$ Alloy during Hydrogenation/dehydrogenation Cycles. *Journal of Alloys and Compounds 150, 256-261*. doi: http://dx.doi.org/10.1016/j.jallcom.2013.01.119.
86. X. B. Yu, Z. Wu, B. J. Xia and N. X. Xu. (2004). Enhancement of hydrogen storage capacity of Ti–V–Cr–Mn BCC phase alloys. *Journal of Alloys and Compounds*, *372*(1–2), 272-277. doi: 10.1016/j.jallcom.2003.09.153.
87. K. Young, T. Ouchi, B. Huang, B. Reichman and M. A. Fetcenko. (2011). The structure, hydrogen storage, and electrochemical properties of Fe-doped C14-predominating AB_2 metal hydride alloys. *International Journal of Hydrogen Energy*, *36*(19), 12296-12304. doi: 10.1016/j.ijhydene.2011.06.117.

88. H. Pan, R. Li, Y. Liu, M. Gao, H. Miao, Y. Lei and Q. Wang. (2008). Structure and electrochemical properties of the Fe substituted Ti–V-based hydrogen storage alloys. *Journal of Alloys and Compounds, 463*(1–2), 189-195. doi: 10.1016/j.jallcom.2007.09.042.
89. Y. Jeong-Hyun, G. Shim, S.-W. Cho and C.-N. Park. (2007). Effects of desorption temperature and substitution of Fe for Cr on the hydrogen storage properties of $Ti_{0.32}$ $Cr_{0.43}$ $V_{0.25}$ alloy. *International Journal of Hydrogen Energy 32*, 2977-2981.
90. S.-W. Cho, H. Enokib and E. Akibab. (2000). Effect of Fe addition on hydrogen storage characteristics of $Ti_{0.16}Zr_{0.05}Cr_{0.22}V_{0.57}$. alloy *Journal of Alloys and Compounds 307(3-4)*, 304–310.
91. S. M. Lee and T. P. Perng. (1994). Effect of the second phase on the initiation of hydrogenation of TiFe1−xMx (M = Cr,Mn) alloys. *International Journal of Hydrogen Energy, 19*(3), 259-263. doi: 10.1016/0360-3199(94)90095-7.
92. S. M. Lee and T. P. Perng. (1999). Correlation of substitutional solid solution with hydrogenation properties of $TiFe_{1-x}M_x$ (M=Ni, Co, Al) alloys. *Journal of Alloys and Compounds, 291*(1–2), 254-261. doi: http://dx.doi.org/10.1016/S0925-8388(99)00262-5.
93. H. Miao, M. Gao, Y. Liu, Y. Lin, J. Wang and H. Pan. (2007). Microstructure and electrochemical properties of Ti–V-based multiphase hydrogen storage electrode alloys. *International Journal of Hydrogen Energy, 32*(16), 3947-3953. doi: 10.1016/j.ijhydene.2007.05.006.
94. M. Williams, M. V. Lototsky, M. W. Davids, V. Linkov, V. A. Yartys and J. K. Solberg. (2011). Chemical surface modification for the improvement of the hydrogenation kinetics and poisoning resistance of TiFe. *Journal of Alloys and Compounds, 509, Supplement 2*(0), S770-S774. doi: 10.1016/j.jallcom.2010.11.063.
95. M. W. Davids, M. Lototskyy, A. Nechaev, Q. Naidoo, M. Williams and Y. Klochko. (2011). Surface modification of TiFe hydrogen storage alloy by metal-organic chemical vapour deposition of palladium. *International Journal of Hydrogen Energy, 36*(16), 9743-9750. doi: 10.1016/j.ijhydene.2011.05.036.
96. W. Grochala and P. P. Edwards. (2004). Thermal decomposition of the non-interstitial hydrides for the storage and production of hydrogen. *Chemistry. Review., 104*, 1283-1315.
97. N. Lopez, Z. Łodziana, F. Illas and M. Salmeron. (2004). When Langmuir is too simple: H_2 dissociation on Pd(111) at high coverage. *Phys Rev Lett 93*, 146103.
98. T. Mitsui, M. K. Rose, E. Fomin, D. F. Ogletree and M. Salmeron. (2003). Dissociative hydrogen adsorption on palladium requires aggregates of three or more vacancies. *Nature, 422*, 705-707.
99. I. Yamashita, H. Tanaka, H. Takeshita, N. Kuriyama, T. Sakai and I. Uehara. (1997). Hydrogenation characteristics of $TiFe_{1-x}Pd_x$ ($0.05 \leq {}_x \leq 0.30$) alloys. *Journal of Alloys and Compounds, 253–254*, 238-240. doi: 10.1016/s0925-8388(96)02925-8.
100. S. Takenaka, T. Kaburagi, C. Yamada, K. Nomura and K. Otsuka. (2004). Storage and supply of hydrogen by means of the redox of the iron oxides

modified with Mo and Rh species. *Journal of Catalysis, 228*(1), 66-74. doi: http://dx.doi.org/10.1016/j.jcat.2004.08.027.

101. J. A. Murshidi, M. Paskevicius, D. A. Sheppard and C. E. Buckley. (2011). Structure, morphology and hydrogen storage properties of a $Ti_{0.97}Zr_{0.019}V_{0.439}Fe_{0.097}Cr_{0.045}Al_{0.026}Mn_{1.5}$ alloy. *International Journal of Hydrogen Energy, 36*(13), 7587-7593. doi: 10.1016/j.ijhydene.2011.03.137.
102. L. A. Pickering. (2013). *Ti-V-Mn Based Metal hydrides for hydrogen storage and compression applications.* Ph.D., University of Birmingham, Birmingham. UK.
103. A. Lopez-Suarez, J. Rickards and R. Trejo-Luna. (2003). Analysis of hydrogen absorption by Ti and Ti–6Al–4V using the ERDA technique. *International Journal of Hydrogen Energy 28* 1107-1113. doi: 10.1016/S0360-3199(02)00202-1.
104. M. Uno, K. Takahashi, T. Maruyama, H. Muta and S. Yamanaka. (2004). Hydrogen solubility of BCC titanium alloys. *Journal of Alloys and Compounds, 366*(1–2), 213-216. doi: 10.1016/s0925-8388(03)00749-7.
105. S. K. Kulshreshtha, R. Sasikala, P. Suryanarayana, A. J. Singh and R. M. Iyer. (1988). Studies on hydrogen storage material FeTi: Effect of Sn substitution. *Materials Research Bulletin, 23*(3), 333-340. doi: http://dx.doi.org/10.1016/0025-5408(88)90006-2.
106. B. Abrashev, T. Spassov, S. Bliznakov and A. Popov. (2010). Microstructure and electrochemical hydriding/dehydriding properties of ball-milled TiFe-based alloys. *International Journal of Hydrogen Energy, 35*(12), 6332-6337. doi: 10.1016/j.ijhydene.2010.03.129.
107. L. Chen, L. Liu, X. Xiao, C. Xu, J. Sun, S. Li, H. Ge and L. Jiang. (2015). Influence of annealing treatment on the microstructure and hydrogen storage performance of $Ti_{1.02}Cr_{1.1}Mn_{0.3}Fe_{0.6}$ alloy for hybrid hydrogen storage application. *Journal of Alloys and Compounds, 636*, 117-123. doi: http://dx.doi.org/10.1016/j.jallcom.2015.02.138.
108. K. Young, T. Ouchi, B. Huang, B. Reichman and M. A. Fetcenko. (2012). Studies of copper as a modifier in C14-predominant AB2 metal hydride alloys. *Journal of Power Sources, 204*(0), 205-212. doi: 10.1016/j.jpowsour.2012.01.030.
109. Y. Yigang, C. Yungui, L. Hao, W. Chaoling, T. Mingda and M. Tu. (2006). Effect of Al on hydrogen storage properties of $V_{30}Ti_{35}Cr_{25}Fe_{10}$ alloy. *Journal of Alloys and Compounds 426* 253-255. doi: 10.1016/j.jallcom.2005.12.122.
110. T. Huang, Z. Wu, G. Sun and N. Xu. (2008). Hydrogen storage characteristics of composite $TiCr_{1.8}$ + *x* wt% $LaNi_5$ alloys. *Journal of Alloys and Compounds, 450*(1–2), 505-507. doi: 10.1016/j.jallcom.2006.11.115.
111. K. Young, T. Ouchi, J. Nei, and L. Wang. Annealing effects on Laves phase-related body-centered-cubic solid solution metal hydride alloys. *Journal of Alloys and Compounds 654 (2016) Pp216-225.*
112. S. Basak, K. Shashikala and S. K. Kulshreshtha. (2008). Hydrogen absorption characteristics of Zr substituted alloy. *International Journal of Hydrogen Energy, 33*(1), 350-355. doi: 10.1016/j.ijhydene.2007.07.023.
113. H. Miao, M. Gao, Y. Liu, D. Zhu and H. Pan. (2008). An improvement on cycling stability of Ti–V–Fe-based hydrogen storage alloys with Co

substitution for Ni. *Journal of Power Sources, 184*, 627-632. doi: 10.1016/j.jpowsour.2008.02.065.

114. A. Guéguen and M. Latroche. (2011). Influence of the addition of vanadium on the hydrogenation properties of the compounds $TiFe_{0.9}$ V_x and $TiFe_{0.8}$ $Mn_{0.1}$ V_x (x = 0, 0.05 and 0.1). *Journal of Alloys and Compounds, 509*(18), 5562-5566. doi: 10.1016/j.jallcom.2011.02.036.
115. C.-C. Shih, C.-M. Shih, Y.-Y. Su, L. H. J. Su, M.-S. Chang and S.-J. Lin. (2004). Effect of surface oxide properties on corrosion resistance of 316L stainless steel for biomedical applications. *Corrosion Science, 46*(2), 427-441. doi: http://dx.doi.org/10.1016/S0010-938X(03)00148-3.
116. C. Sung-Wook, H. Chang-Suck, P. Choong-Nyeon and E. Akibab. (1999). Hydrogen storage characteristics of Ti–Zr–Cr–V alloys. *Journal of Alloys and Compounds, 289*, 244-250.
117. A. Takasaki and K. F. Kelton. (2006). Hydrogen storage in Ti-based quasicrystal powders produced by mechanical alloying. *International Journal of Hydrogen Energy, 31*(2), 183-190. doi: 10.1016/j.ijhydene.2005.04.025.
118. N. Rajalakshmi and K. S. Dhathathreyan. (1999). Hydrogen solubility properties of $Ti_{0.42}Zr_{0.08}Fe_{0.50}$ alloy. *International Journal of Hydrogen Energy, 24*(7), 625-629. doi: 10.1016/s0360-3199(98)00121-9.
119. X. Zhao, J. Zhou, X. Shen, M. Yang and L. Ma. (2012). Structure and electrochemical hydrogen storage properties of AB_2-type Ti–Zr–Ni alloys. *International Journal of Hydrogen Energy, 37*(6), 5050-5055. doi: 10.1016/j.ijhydene.2011.12.010.
120. G. Yuan, H. Kato, K. Amiya and A. Inoue. (2005). Excellent creep properties of Mg–Zn–Cu–Gd-based alloy strengthened by quasicrystals and Laves phases. *Journal of Materials Research, 20*(05), 1278-1286. doi: doi:10.1557/JMR.2005.0156.
121. K. Shirasaki, T. Tamura, T. Kuriiwa, T. Goto, A. Kamegawa, H. Takamura and M. Okada (2002). Cyclic properties of protium absorption-desorption in Ti-V-Cr alloys. *Material Transactions, 43(5) pp1115-1119.*
122. L. Shouping, Q. Guibao, L. Xiaojun, L. Jin and B. Chenguang. (2010). Structures and Properties of $TiMn_{2-5x}(V_4Fe)_x$ (x = 0.30, 0.35) Hydrogen Storage Alloys. *Rare Metal Materials and Engineering, 39*(2), 214-218. doi: 10.1016/s1875-5372(10)60082-3.
123. S. M. Lee and T. P. Perng. (2000). Effects of boron and carbon on the hydrogenation properties of TiFe and $Ti_{1.1}Fe$. *International Journal of Hydrogen Energy, 25*(9), 831-836. doi: 10.1016/s0360-3199(99)00107-x.
124. R.-R. Jeng, S.-L. Lee, C.-W. Hsu, Y.-P. Wu and J.-C. Lin. (2008). Effects of the addition of Pd on the hydrogen absorption–desorption characteristics of $Ti_{33}V_{33}Cr_{34}$ alloys. *Journal of Alloys and Compounds, 464*(1–2), 467-471. doi: 10.1016/j.jallcom.2007.10.010.
125. F. Maillard, A. Bonnefont and F. Micoud. (2011). An EC-FTIR study on the catalytic role of Pt in carbon corrosion. *Electrochemistry Communications, 13*(10), 1109-1111. doi: http://dx.doi.org/10.1016/j.elecom.2011.07.011.
126. J. Shen, L. Yang, K. Hu, W. Luo and G. Cheng. (2015). Rh nanoparticles supported on graphene as efficient catalyst for hydrolytic dehydrogenation of amine boranes for chemical hydrogen storage. *International Journal of*

Hydrogen Energy, *40*(2), 1062-1070. doi: http://dx.doi.org/10.1016/j.ijhydene.2014.11.031.

127. S.I. Towata, T. Noritake, A. Itoh, M. Aoki and K. Miwa. (2013). Effect of partial niobium and iron substitution on short-term cycle durability of hydrogen storage Ti–Cr–V alloys. *International Journal of Hydrogen Energy*, *38*(7), 3024-3029. doi: http://dx.doi.org/10.1016/j.ijhydene.2012.12.100.
128. O. S. Ryosuke and M. Yoshinori. (2004). *Preparation of Ti-V-Cr hydrogen absorbtion alloy powder*. Paper presented at the The Joint International Conference on "Sustainable Energy and Environment (SEE)", Hua Hin, Thailand.
129. K. Young, J. Koch, T. Ouchi, A. Banik and M. A. Fetcenko. (2010). Study of AB_2 alloy electrodes for Ni/MH battery prepared by centrifugal casting and gas atomization. *Journal of Alloys and Compounds*, *496*(1–2), 669-677. doi: 10.1016/j.jallcom.2010.02.161.
130. M. Abe and T. Kuji. (2007). Hydrogen absorption of TiFe alloy synthesized by ball milling and post-annealing. *Journal of Alloys and Compounds*, *446–447*, 200-203. doi: 10.1016/j.jallcom.2006.12.063.
131. Y. Q. Hu, H. F. Zhang, C. Yan, L. Ye, B. Z. Ding and Z. Q. Hu. (2004). Preparation and hydrogenation of body-centered-cubic $TiCr_2$ alloy. *Materials Letters*, *58*(5), 783-786. doi: 10.1016/j.matlet.2003.07.011.
132. J.-Y. Wang. (2009). Comparison of hydrogen storage properties of $Ti_{0.37}V_{0.38}Mn_{0.25}$ alloys prepared by mechanical alloying and vacuum arc melting. *International Journal of Hydrogen Energy 3(4)* 3771-3777.
133. H. Itoh, H. Arashima, K. Kubo and T. Kabutomori. (2002). The influence of microstructure on hydrogen absorption properties of Ti–Cr–V alloys. *Journal of Alloys and Compounds*, *330–332*(0), 287-291. doi: 10.1016/s0925-8388(01)01530-4.
134. H. Nagel and R. S. Perkins. (June 1975). crystallographic investigation of ternary vanadium hydrides. *Zeitschriflt luer Metallkunde*, *66*, 362-366.
135. K. Christmann. (1988). Interaction of hydrogen with solid surfaces. *Surface Science Reports*, *9*(1–3), 1-163. doi: 10.1016/0167-5729(88)90009-x.
136. Y. Ibaraki, A. Yamamoto and T. Sasaki. (1978). Method oh heat treating titanium alloy US patent 19.
137. J. Evans, I. R. Harris and L. S. Guzei. (1979). An investigation of some palladium-titanium and some palladium-titanium-hydrogen alloys. *Journal of the Less-Common Metals*, *64*(2), P39-P57. doi: 10.1016/0022-5088(79)90186-3.
138. S. M. Lee, T. P. Perng, H. K. Juang, S. Y. Chen, W. Y. Chen and S. E. Hsu. (1992). Microstructures and hydrogenation properties of $TiFe_{1-x}M_x$ alloys. *Journal of Alloys and Compounds*, *187*(1), 49-57. doi: 10.1016/0925-8388(92)90519-f.
139. M. Tsukahara, K. Takahashi, T. Mishima, A. Isomura and T. Sakai. (1996). Heat-treatment effects of V-based solid solution alloy with TiNi-based network structure on hydrogen storage and electrode properties. *Journal of Alloys and Compounds*, *243*(1–2), 133-138. doi: 10.1016/s0925-8388(96)02372-9.

140. H. J. Chuang, S. S. Huang, C. Y. Ma and S. L. I. Chan. (1999). Effect of annealing heat treatment on an atomized AB_2 hydrogen storage alloy. *Journal of Alloys and Compounds, 285*(1–2), 284-291. doi: 10.1016/s0925-8388(98)01050-0.
141. X. Liu, L. Jiang, Z. Li, Z. Huang and S. Wang. (2009). Improve plateau property of $Ti_{32}Cr_{46}V_{22}$ BCC alloy with heat treatment and Ce additive. *Journal of Alloys and Compounds, 471*(1–2), L36-L38. doi: http://dx.doi.org/10.1016/j.jallcom.2008.04.004.
142. M. Williams, M. Lotosky, A. Nechaev, V. Yartys, J. K. Solberg, R. V. Denys and V. M. Linkov. (2010). Palladium mixed-metal surface-modified AB_5 -type intermetallides enhance hydrogen sorption kinetics. *South African Journal of Science, 106*(9/10), 6-13.
143. S.-W. Cho, J.-H. Yoo, H.-K. Chang, W.-B. Kim, D.-S. Kil and J.-G. Ahn. (2011). Changes in the microstructure and hydrogen storage properties of Ti–Cr–V alloys by ball milling and heat treatment. *Journal of Alloys and Compounds, 509*(18), 5545-5550. doi: 10.1016/j.jallcom.2011.02.005.
144. Z. Hang, X. Xiao, S. Li, H. Ge, C. Chen and L. Chen. (2012). Influence of heat treatment on the microstructure and hydrogen storage properties of Ti10V77Cr6Fe6Zr alloy. *Journal of Alloys and Compounds, 529*, 128-133. doi: http://dx.doi.org/10.1016/j.jallcom.2012.03.044.
145. M. Yamamoto and M. Kanda. (1997). Investigation of AB_5 type hydrogen storage alloy corrosion behavior in alkaline electrolyte solutions. *Journal of Alloys and Compounds, 253–254*(0), 660-664. doi: 10.1016/s0925-8388(96)02914-3.
146. ASTM. (1999). Standard Practice for Calculation of Corrosion Rates and Related Information from Electrochemical Measurements (Vol. G 102 - 89). West Conshohocken, United States.: ASTM.
147. S.-W. Cho, C.-S. Han, C.-N. Park and E. Akiba. (1999). The hydrogen storage characteristics of Ti–Cr–V alloys. *Journal of Alloys and Compounds, 288*(1–2), 294-298. doi: 10.1016/s0925-8388(99)00096-1.
148. U. S. G. Survey (Producer). (2015, 1/12/15). Mineral Commodity Summary.
149. U.S. Geological Survey (Producer). (2015). Mineral Commodity Summaries.
150. B. Huge, O. Hiroaki, S.D.Hampton., G.M. Davidson, M. A. Flemin, L. Kacprzak and H. Lampman. (2004). *ASM Handbook; Alloy Phase Diagram* Vol. 3: ASM International Matrial park, Ohio.
151. N. H. Vet. (2005). Analyze particles using ImageJ doi:http://rsbweb.nih.gov/ij/download.html. 11/03/14.
152. M. Jafari, M. Nobakthi, H. Jammezhad and K. Bayati. (2013). Density functional theory study of the α → ω martensitic transformation in titanium induced by hydrostatic pressure. *Condensed Matter Physics, 16*(3), 1-6. doi: 10.5488/CMP.16337.3.
153. T. Ferreira and W. Rasband. (2011). The ImageJ User Guide 1.44 (pp. 200). Retrieved from http://imagej.nih.gov/ij/docs/user-guide.pdf. doi:http://imagej.nih.gov/ij/docs/user-guide.pdf.
154. X. B. Yu, J. Z. Chen, Z. Wu, B. J. Xia and N. X. Xu. (2004). Effect of Cr content on hydrogen storage properties for Ti-V-based BCC-phase alloys. *International Journal of Hydrogen Energy 29* (4), 1377-1381. doi: 10.1016/j.ijhydene.2004.01.015.

155. U. Ulrich, K. Asano, T. Bergfeldt, V. S. K. Chakravadhanula, R. Dittmeyer, H. Enoki, C. Kübel, Y. Nakamura, A. Pohl and M. Fichtner. (2014). Effect of oxygen on the microstructure and hydrogen storage properties of V–Ti–Cr–Fe quaternary solid solutions. *International Journal of Hydrogen Energy, 39*(35), 20000-20008. doi: http://dx.doi.org/10.1016/j.ijhydene.2014.08.152.
156. Y. Yan, Y. Chen, H. Liang, X. Zhou, C. Wu, M. Tao and L. Pang. (2008). Hydrogen storage properties of V–Ti–Cr–Fe alloys. *Journal of Alloys and Compounds*, *454*(1–2), 427-431. doi: 10.1016/j.jallcom.2006.12.093.
157. J.-H. Yoo, G. Shim, S.-W. Cho and C.-N. Park. (2007). Effects of desorption temperature and substitution of Fe for Cr on the hydrogen storage properties of alloy. *International Journal of Hydrogen Energy, 32*(14), 2977-2981. doi: http://dx.doi.org/10.1016/j.ijhydene.2007.01.012.
158. H. Güleryüz and H. Çimenoğlu. (2004). Effect of thermal oxidation on corrosion and corrosion–wear behaviour of a Ti–6Al–4V alloy. *Biomaterials, 25*(16), 3325-3333. doi: http://dx.doi.org/10.1016/j.biomaterials.2003.10.009.
159. P. Shi, W. F. Ng, M. H. Wong and F. T. Cheng. (2009). Improvement of corrosion resistance of pure magnesium in Hanks' solution by microarc oxidation with Sol–Gel TiO_2 sealing. *Journal of Alloys and Compounds, 469*(1–2), 286-292. doi: http://dx.doi.org/10.1016/j.jallcom.2008.01.102.
160. R. L. Hungerford and A. W. Tracy. (1945). *Effect of iron on corrosion of Cu-Ni alloy.* Paper presented at the Proc. Amer. Soc. Test. Mat.
161. L. J. Swartzendruber and L. H. Bennett. (1968). The effect of Fe on the corrosion rate of copper rich Cu-Ni alloys. *Scripta metallurgica, 2*, 6-12.
162. X. P. Liu, F. Cuevas, L. J. Jiang, M. Latroche, Z. N. Li and S. M. Wang. (2009). Improvement of the hydrogen storage properties of Ti–Cr–V–Fe BCC alloy by Ce addition. *Journal of Alloys and Compounds, 476*(1–2), 403-407. doi: http://dx.doi.org/10.1016/j.jallcom.2008.09.042.
163. J.-H. Yoo, G. Shim, C.-N. Park, W.-B. Kim and S.-W. Cho. (2009). Influence of Mn or Mn plus Fe on the hydrogen storage properties of the Ti-Cr-V alloy. *International Journal of Hydrogen Energy, 34*(22), 9116-9121. doi: http://dx.doi.org/10.1016/j.ijhydene.2009.08.064.
164. M. A. Ashworth, A. J. Davenport, R. M. Ward and H. G. C. Hamilton. (2010). Microstructure and corrosion of Pd-modified Ti alloys produced by powder metallurgy. *Corrosion Science, 52*(7), 2413-2421. doi: http://dx.doi.org/10.1016/j.corsci.2010.03.006.
165. P. Handzlik and K. Fitzner. (2013). Corrosion resistance of Ti and Ti–Pd alloy in phosphate buffered saline solutions with and without H_2O_2 addition. *Transactions of Nonferrous Metals Society of China, 23*(3), 866-875. doi: http://dx.doi.org/10.1016/S1003-6326(13)62541-8.
166. G. Alefeld and J. Volki. (1978). *Hydrogen in metal II. Application oriented properties*. Berlin-Heidelberg: Springer-Verlag. P.387.
167. R. C. Bowman and B. Fultz. (2002). Metallic Hydrides I: Hydrogen Storage and Other Gas-Phase Applications. *MRS Bulletin, 27*(09), 688-693. doi:10.1557/mrs2002.223.
168. M.-J. Huang, E.-J. Park, W.-J. Moon, H.-J. Song and Y.-J. Park. (2015). Characterization of passive layers formed on Ti–10 wt% (Ag, Au, Pd, or Pt)

binary alloys and their effects on galvanic corrosion. *Corrosion Science, 96*, 152-159. doi: http://dx.doi.org/10.1016/j.corsci.2015.04.007.

169. A. Martínez and D. S. dos Santos (2012). Hydrogen absorption/Desorption Properties in the TiCrV Based Alloys. *Materials Research, 15(5), Pp. 809-812.*

170. J. Mi, F. Lü, X. Liu, L. Jiang, Z. Li and S. Wang. (2010). Enhancement of cerium and hydrogen storage property of a low-cost Ti-V based BCC alloy prepared by commercial ferrovanadium. *Journal of Rare Earths*, *28*(5), 781-784. doi: http://dx.doi.org/10.1016/S1002-0721(09)60200-3.

171. T. Huang, Z. Wu, B. Xia, J. Chen, X. Yu, N. Xu, C. Lu and H. Yu. (2003). $TiCr_{1.2}(V–Fe)_{0.6}$—a novel hydrogen storage alloy with high capacity. *Science and Technology of Advanced Materials, 4*(6), 491-494. doi: http://dx.doi.org/10.1016/j.stam.2003.12.001.

172. C.-Y. Seo, J.-H. Kim, P. S. Lee and J.-Y. Lee. (2003). Hydrogen storage properties of vanadium-based b.c.c. solid solution metal hydrides. *Journal of Alloys and Compounds, 348*(1–2), 252-257. doi: http://dx.doi.org/10.1016/S0925-8388(02)00831-9.

173. K. Young, T. Ouchi and M. A. Fetcenko. (2009). Pressure–composition–temperature hysteresis in C14 Laves phase alloys: Part 1. Simple ternary alloys. *Journal of Alloys and Compounds, 480*(2), 428-433. doi: http://dx.doi.org/10.1016/j.jallcom.2008.12.113.

174. M. Tsukahara, K. Takahashi, T. Mishima, T. Sakai, H. Miyamura, N. Kuriyama and I. Uehara. (1995). Metal hydride electrodes based on solid solution type alloy TiV_3Ni_x ($0 \leq x \leq 0.75$). *Journal of Alloys and Compounds*, *226*(1–2), 203-207. doi: http://dx.doi.org/10.1016/0925-8388(95)01570-1.

175. V. A. Yartys, S. V. Mitroknin, V. N. Verbetski and K. N. Semenko. (1992). A panoramic overview of hydrogen storage alloys from a gas reaction point of view *Russian Materials Journal., 37*, 16-22.

176. Q. Wang, D. Zhu, W. Zhou, C. Zhong, C. Wu, Y. Chen (2016). High-temperature electrochemical performance of low-cost La–Ni–Fe based hydrogen storage alloys with different preparation methods. *Materials Research Bulletin, 76, Pp 28-36.*

177. H. Y. Zhou, F. Wang, J. Wang, Z. M. Wang, Q. R. Yao, J. Q. Deng, C. Y. Tang and G. H. Rao. (2014). Hydrogen storage properties and thermal stability of $V_{35}Ti_{20}Cr_{45}$ alloy by heat treatment. *International Journal of Hydrogen Energy, 39*(27), 14887-14895. doi: http://dx.doi.org/10.1016/j.ijhydene.2014.07.054.

178. Y. Zhou, J. Chen, Y. Xu and Z. Liu. (2013). Effects of Cr, Ni and Cu on the Corrosion Behavior of Low Carbon Microalloying Steel in a Cl− Containing Environment. *Journal of Materials Science & Technology*, *29*(2), 168-174. doi: http://dx.doi.org/10.1016/j.jmst.2012.12.013.

179. L. Mi-Jing, L. Fang, I. Xiaopeng, L. Z. Lijun and W. Shumao. (2010). Enhancement of cerium and hydrogen storage property of a low-cost Ti-V based BCC alloy prepared by commercial ferrovanadium. *Journal of Rare Earths, 28*(5), 781784. doi: 10.1016/S1002-0721(09)60200-3.

180. W. Baumann and A. Leineweber. (2010). Solid solubility by anti-site atoms in the C36-TiCr2 Laves phase revealed by single-crystal X-ray diffractometry.

Journal of Alloys and Compounds, *505*(2), 492-496. doi: http://dx.doi.org/10.1016/j.jallcom.2010.06.117.

181. A. Guéguen and M. Latroche. (2011). Influence of the addition of vanadium on the hydrogenation properties of the compounds TiFe0.9Vx and TiFe0.8Mn0.1Vx (x = 0, 0.05 and 0.1). *Journal of Alloys and Compounds*, *509*(18), 5562-5566. doi: http://dx.doi.org/10.1016/j.jallcom.2011.02.036.
182. Y. Qiao, M. Zhao, M Li, X. Zhuc and G. Caoc (2006). Microstructure and electrochemical performance of $Ti_{0.17}Zr_{0.08}V_{0.34}Pd_{0.01}Cr_{0.1}Ni_{0.3}$ electrode alloy. *Scripta Materialia 55, Pp. 279–282.*
183. X. B. Yu, Z. X. Yang, S. L. Feng, Z. Wu and N. X. Xu. (2006). Influence of Fe addition on hydrogen storage characteristics of Ti–V-based alloy. *International Journal of Hydrogen Energy*, *31*(9), 1176-1181. doi: http://dx.doi.org/10.1016/j.ijhydene.2005.09.008.
184. Y. Liu, S. Zhang, R. Li, M. Gao, k. Zhong, H. Miao and H. Pan. (2008). Electrochemical performances of the Pd-added Ti-V-based hydrogen storage alloys. *International Journal of Hydrogen Energy*, *33*(2), 728-734. doi: http://dx.doi.org/10.1016/j.ijhydene.2007.10.032.
185. Y. Zhang, X. Zhuang, Y. Zhu, L. Zhan, Z. Pu, N. Wan, L. Li (2016). Effects of additive Pd on the structures and electrochemical hydrogen storage properties of $Mg_{67}Co_{33}$-based composites or alloys with BCC phase. *Journal of Alloys and Compounds, 622, Pp 580-586.*
186. A. C. Michael and C. Daniela. (1996). Microstructure and high-temperature phases transition in Kalsilite. *Americal Mineralogist*, *81*, 561-584.
187. K. Young, T. Ouchi, J. Nei, and L. Wang. Annealing effects on Laves phase-related body-centered-cubic solid solution metal hydride alloys. *Journal of Alloys and Compounds 654 (2016) Pp216-225.*
188. R. W. Schutz and D. E. Thomas. (1987). *Corrosion of Titanium and Titanium alloys* 9th Edition. Vol. 13. Pg.670-706.
189. S. Lal and T. P. Porcelli. (1982). Process for inhibiting Titanium Corrosion Google Patents 1982.
190. R. W. Schutz. (1996). Ruthenium Enhanced Titanium Alloys. *Platinum Metals Review*, *40*(2), 54-61.
191. S. Ningshen, M. Sakairi, K. Suzuki and T. Okuno. (2015). Corrosion performance and surface analysis of Ti–Ni–Pd–Ru–Cr alloy in nitric acid solution. *Corrosion Science*, *91*, 120-128. doi: http://dx.doi.org/10.1016/j.corsci.2014.11.010.
192. F. Maillard, A. Bonnefont and F. Micoud. (2011). An EC-FTIR study on the catalytic role of Pt in carbon corrosion. *Electrochemistry Communications*, *13*(10), 1109-1111. doi: http://dx.doi.org/10.1016/j.elecom.2011.07.011.
193. A. Guéguen, J. M. Joubert and M. Latroche. (2011). Influence of the C14 $Ti_{35.4}$ $V_{32.3}$ $Fe_{32.3}$ Laves phase on the hydrogenation properties of the body-centered cubic compound $Ti_{24.5}$ $V_{59.3}$ $Fe_{16.2}$. *Journal of Alloys and Compounds*, *509*(6), 3013-3018. doi: http://dx.doi.org/10.1016/j.jallcom.2010.10.213.
194. T. Dou, Z. Wu, J. Mao and N. Xu. (2008). Application of commercial ferrovanadium to reduce cost of Ti–V-based BCC phase hydrogen storage

alloys. *Materials Science and Engineering: A, 476*(1–2), 34-38. doi: 10.1016/j.msea.2007.04.080.

195. X. Song, P. Pei, P. Zhang and G. Chen. (2006). Effect of vanadium content on hydrogen storage property in Ti-V-Cr alloys. *Rare Metals, 25*(6, Supplement 1), 374-377. doi: http://dx.doi.org/10.1016/S1001-0521(07)60109-0.
196. Q.F. Tian, Y. Zhang, Z.C. Tan, F. Xu, L.X. Sun, T. Zhang and H.T. Yuan. (2006). Effects of Pd substitution for Ni on corrosion performances of $Mg_{0.9}Ti_{0.1}Ni_{1-x}Pd_x$ hydrogen storage alloys. *Transactions of Nonferrous Metals Society of China, 16*(3), 497-501. doi: http://dx.doi.org/10.1016/S1003-6326(06)60086-1.
197. A. Biesiekierski, D. H. Ping, Y. Yamabe-Mitarai and C. Wen. (2014). Impact of ruthenium on microstructure and corrosion behavior of β-type Ti–Nb–Ru alloys for biomedical applications. *Materials & Design, 59*, 303-309. doi: http://dx.doi.org/10.1016/j.matdes.2014.02.058.
198. T. Kuriiwa, T. Maruyama, A. Kamegawa and M. Okada. (2010). Effects of V content on hydrogen storage properties of V–Ti–Cr alloys with high desorption pressure. *International Journal of Hydrogen Energy, 35*(17), 9082-9087. doi: http://dx.doi.org/10.1016/j.ijhydene.2010.06.024.
199. R. N. Johnson and D. G. Farwick. (1978). Friction, wear and corrosion of laves-hardened nickel alloy hardsurfacing in sodium. *Thin Solid Films, 53*(3), 365-373. doi: http://dx.doi.org/10.1016/0040-6090(78)90229-8.
200. J. Hanawalt, M. Avrami, J Lacher, S. Brunaauer. (1938). Phases and affinity for protium absorption. *Anal. Chem., 10*, 475-479.
201. X.-Q. Wang and J.-T. Wang. (2010). Structural stability and hydrogen diffusion in alloys. *Solid State Communications, 150*(35–36), 1715-1718. doi: http://dx.doi.org/10.1016/j.ssc.2010.06.004
202. D. N. Williams, B. G. Koehl and E. S. Bartlett. (1969). The reaction of titanium with hydrogen gas at ambient temperatures. *Journal of the Less-Common Metals, 19*(4), 385-398. doi: http://dx.doi.org/10.1016/0022-5088(69)90183-0.
203. I. I. Kornilov and S. G. Boriskina. (1964). Hydrogen storage characteristics of Laves phase Part I. *Russ. J. Inorg. Chem. (Engl. Transl.), 9*, 388-395.
204. I. I. Kornilov, P. B. Budberg, K. I. Shakova and S. P. Alisova. (1965). Hydrogen storage characteristics of Laves phase Part II *Doki. Akad. Nauk SSSR, 161*, 1378-1383.
205. A. Kamegawa, T. Kuriiwa, H. Takamura, T. Tamura and M. Okada. (2002). Hydrogen storage characteristics of a V-rich alloy. *Materials Trans., JIM, 40*, 470-478.
206. G. Mazzolai, B. Coluzzi, A. Biscarini, F. M. Mazzolai, A. Tuissi, F. Agresti, S. Lo Russo, A. Maddalena, P. Palade and G. Principi. (2008). Hydrogen-storage capacities and H diffusion in bcc TiVCr alloys. *Journal of Alloys and Compounds 466*, 7.
207. L. C. Ming, M. H. Manghnani and K. W. Katahara. (1981). Phase transformations in the Ti-V system under high pressure up to 25 GPa. *Acta Metallurgica, 29*(3), 479-485. doi: http://dx.doi.org/10.1016/0001-6160(81)90071-7.

208. C.-C. Shen, J. C. P. Chou, H.-C. Li, Y.-P. Wu and T.-P. Perng. (2010). Effect of interstitial boron and carbon on the hydrogenation properties of Ti25V35Cr40 alloy. *International Journal of Hydrogen Energy, 35*(21), 11975-11980. doi: 10.1016/j.ijhydene.2010.07.166.
209. K. Young, J. Nei, D. Wong, F and L. Wang. (2014). Structural, hydrogen storage, and electrochemical properties of Laves phase-related body-centered cubic solid solution metal hydride alloys. *International Journal of Hydrogen Energy, 36(10) 789-790.*
210. R. Burch and N. B. Mason. (1979). Absorption of hydrogen by titanium-cobalt and titanium-nickel intermetallic alloys. Part 1- Experimental results. *Journal of Chemical Society. Faraday Trans. 1., 75*, 17-22.
211. S. U. Jen and T. C. Wu. (2005). Young's modulus and hardness of Pd thin films. *Thin Solid Films, 492*(1–2), 166-172. doi: http://dx.doi.org/10.1016/j.tsf.2005.06.048.
212. R. J. Van Thyne, H. D. Kessler and M. Hansen. (1953). . Addition of Titanium: A Highly Effective Strategy for Enhancing Corrosion Resistance *Tran. Am. Inst. Min. Metall. Pet. Eng., 197*, 1209-1212.
213. R. W. Schutz. (2003). F.N. Speller Award Lecture: Platinum Group Metal Additions to Titanium: A Highly Effective Strategy for Enhancing Corrosion Resistance. *Corrosion, 59*(12), 1043-1057.
214. J. H. Potgieter, N. Thanjekwayo, P. Olubambi, N. Maledi and S. S. Potgieter-Vermaak. (2011). Influence of Ru additions on the corrosion behaviour of WC–Co cemented carbide alloys in sulphuric acid. *International Journal of Refractory Metals and Hard Materials, 29*(4), 478-487. doi: http://dx.doi.org/10.1016/j.ijrmhm.2011.02.007.
215. M. X. Yao, J. B. C. Wu, S. Yick, Y. Xie and R. Liu. (2006). High temperature wear and corrosion resistance of a Laves phase strengthened Co–Mo–Cr–Si alloy. *Materials Science and Engineering, A, 435–436*, 78-83. doi: http://dx.doi.org/10.1016/j.msea.2006.07.054.
216. X. B. Yu, Z. Wu, Q. R. Chen, T. Dou, J. Z. Chen, B. J. Xia and N. X. Xu. (2007). Effect of V addition on activation performances of $TiMn_{1.25}Cr_{0.25}$ hydrogen storage alloy. *Journal of Materials Processing Technology, 182*(1–3), 549-554. doi: http://dx.doi.org/10.1016/j.jmatprotec.2006.09.016.
217. H. Miyamura, T. Sakai, N. Kuriyama, H. Tanaka, I. Uehara and H. Ishikawa (1997). Hydrogenation and phase structure of Ti–Fe–V alloys. *Journal of Alloys and Compounds, 253–254*, 232-234. doi: http://dx.doi.org/10.1016/S0925-8388(96)03028-9.
218. E. Akiba and M. Okada. ((2002). Metallic hydride III: Body-Centered-Cubic Solid-Solution alloys. (pp. 699-703): Materials Research Society.

Appendixes 1

Titles and Abstracts of the local Conference presentations and posters.

2. Conference presentation (The 8th International conference of the African Materials Research Society, Accra, Ghana).

Corrosion and hydrogen storage characteristics of a vanadium-rich Ti-V-Cr hydrogen storage alloy

J.M. Abdul [1,2,3] and L.H. Chown [1,2,3,4]

[1] School of Chemical and Metallurgical Engineering, [2] African Materials Science and Engineering Network (AMSEN), [3] Materials for Energy Research Group (MERG), [4] DST-NRF Centre of Excellence in Strong Materials, *all University of the Witwatersrand, Private Bag 3, WITS 2050, Johannesburg, South Africa*

Abstract

The microstructure, hardness, corrosion behaviour and hydrogen storage properties of a $Ti_{35}V_{40}Cr_{25}$ at.% alloy were investigated. The V-rich alloy was produce under argon in an open hearth crucible furnace. The microstructure of the arc-melted alloy was examined by scanning electron microscopy, and the phases were identified by X-ray diffraction. The as-cast alloy contained a primary (V) body centered cubic phase and an intergranular α-Ti phase. The average Vickers hardness of the alloy was measured as 415±5 HV_2. The potentiodynamic corrosion rate under ambient conditions in 6M KOH was determined as 0.011 mm/y. The hydrogen absorption/desorption characteristics were examined by performing pressure-composition-temperature measurements at temperatures of 30, 60 and 90°C. The maximum hydrogen absorption capacity of 1.9 wt% H was measured at 30°C, the H capacity remaining in the metal after desorption was 0.33 wt%, while the useful, reversible desorption capacity was 1.56 wt% H. This alloy is a potential candidate for use as hydrogen tank as it has a relatively high reversible capacity.

Keywords: Hydrogen storage properties, corrosion rate, hardness, BCC (V) alloy

3. Poster presentations (2014 Inter-Faculty Poster Presentation)

Microstructure and corrosion behaviour of $Ti_{25}V_{40}Cr_{35}$ hydrogen storage alloy

J.M. Abdul [1,2,3] and L.H. Chown [1,2,3,4]

[1] School of Chemical and Metallurgical Engineering, [2] African Materials Science and Engineering Network (AMSEN), [3] Materials for Energy Research Group (MERG), [4] DST-NRF Centre of Excellence in Strong Materials, *all University of the Witwatersrand, Private Bag 3, WITS 2050, Johannesburg, South Africa*

Abstract

Production and characterisation of as-cast $Ti_{25}V_{40}Ti_{35}$ alloy for hydrogen storage was performed and the microstructure, corrosion behaviour in 6 M KOH and hydrogen storage characteristics of the alloy were investigated.

Elemental powder constituents of the alloy were melted in a button-arc furnace under argon atmosphere. The ingot was re-melted 4 times to ensure homogeneity. The as-cast alloys were cut and metallographically prepared to a final polish of 0.02μm and examined by XRD and scanning electron microscopy. Pottentiostatic corrosion test on the alloys was performed using AutoLab corrosion test apparatus. PCT measurement on the Sievert's apparatus was carried out between pressure of $0<P(Mpa)<6$ and a temperature of $303.15 \leq T(K) \leq 333.15$. Van't Hoff relation was used to calculate the thermodynamic properties of the alloy.

The microstructure of the alloy is dominated by v-rich BCC (78.5% area fraction). If the alloy is used as an electrode in 6Mole/lt. KOH solution at ambient temperature and the current density of the solution is kept at -22mA/Cm^2 (i_{corr}), the alloy will not corrode. Otherwise the corrosion rate of the alloy in the above stated condition will be 427.4 mmpy. The optimum operating condition of the hydrogen store is 30°C in a pressure range of 0.005 and 3.387 Ma and the RHSC in this condition is 1.559wt%. Increasing the operating temperature of the store will lead to decrease in RHSC and increase in plateau pressure.

Key words: Microstructure, corrosion behaviour, hydrogen storage characteristics, van't Hoff relationship

Appendix 2 Full paper of the accepted Journal article including the acceptance letter

Influence of Fe on hydrogen storage properties of V-rich ternary alloys

J.M. Abdul [1,2,3] and L.H. Chown [1,2,3,4]

[1] School of Chemical and Metallurgical Engineering, [2] African Materials Science and Engineering Network (AMSEN), [3] Materials for Energy Research Group (MERG), [4] DST-NRF Centre of Excellence in Strong Materials, *all University of the Witwatersrand, Private Bag 3, WITS 2050, Johannesburg, South Africa*

[*]Corresponding author. Tel: +234 805 562 9924, +27 074 069 6713. Email addresses: jmabdul@gmail.com; jmabdul66@yahoo.com

Influence of Fe on the hydrogen storage properties of V-rich ternary alloys

Abstract

To investigate the influence of Fe on Ti-V-Cr hydrogen storage alloy, $Ti_{35-0.5x}V_{40}Cr_{25-0.5x}Fe_x$ (x = 0, 2, 5, 6 at.%) alloys were prepared by arc melting under argon in open hearth crucible furnace. The microstructures were examined by scanning electron microscopy (SEM) with energy dispersive x-ray spectroscopy (EDX), and the phases were identified by X-ray diffraction (XRD) using Cu-K_α radiation. Hydrogen storage characteristics were systematically investigated by pressure-composition-temperature PCT measurement at 303, 333 and 363 K. XRD result showed that the alloys contained primary BCC (V) and secondary αTi and Laves phases. Fe reduced the cell volume and proportion of BCC phase. The proportion of BCC phase ranges from 67 to 90 area%, while secondary phase proportion was found to be 10 to 33 area%. Iron reduced the absorption/desorption capacity, increased the plateau pressure and promotes formation of β-phase hydride. The best hydrogen storage properties were obtained in Fe-free sample.

Keywords: Ti-V based alloys; microstructure; Laves phase; phase analysis; hydrogen storage characteristics

1. Introduction

Fossil fuel is a vital ingredient for running modern industry, but the resultant worsening environmental pollution is a major disadvantage [21], hence the need for cleaner energy source. Hydrogen fuel is a promising alternative to fossil fuel, but storage and transportation is a major challenge to its wide range of applications [3]. Many types of hydrogen storage alloys ranging from AB, AB_2 and AB_5 has been studied in details [1; 5; 6; 7; 17]. Absorption capacity of Ti-V-Cr alloys was found to be high, but reversible capacity was low [17]. Cho *et al.* [7] observed a region of high absorption capacity in the ternary Ti-V-Cr alloy. In the past, efforts have been made on reducing the cost of the alloy by substituting the most expensive element, V with cheaper elements such as Zr [11], VFe [19], Fe [16], Mn [29]. Effect of Fe on hydrogen storage characteristics of hydrogen storage alloys has been investigated [9; 16; 25; 28], but not in the region identified by Cho *et al.*. This work therefore investigated the effect of substituting Fe (at Cr and Ti site) on hydrogen storage characteristic of $Ti_{35}V_{40}Cr_{25}$ at.% alloy, which falls within the region identified by Cho *et al.*.

2. Experimental procedure

The starting materials for the alloys were: iron (325-290 mesh, 99% purity, 0.01% C and 0.015 wt% phosphorus and sulphur); chromium (<0.3 mm, 99.8% purity); vanadium (-325 mesh, 99.5% purity); titanium (-325 mesh, 99.5% purity). Small ingots of $Ti_{25-0.5x}V_{40}Cr_{35-0.5x}Fe_x$ (x = 0, 2, 5, 6 at.%) were produced by arc melting in a water-cooled copper hearth furnace under argon atmosphere. The ingots were re-melted three times for homogeneity.

The crystal structures and lattice parameters of the alloys were determined by XRD using Cu K_α radiation with 2θ from 10 to 80°. Elemental compositions of the phases were

found by SEM analyses using a FEI Nova NanoSEM 200® fitted with EDAX® Advanced Microanalysis Solution. The proportions of the phases (in area %) was calculated using ImageJ 1.44 software.

A Sieverts-type apparatus was used for the measurement of the pressure composition isotherm (PCI) curves. After crushing the samples into particles < 75 µm in size, 1 g of each alloy was sealed into a stainless steel reactor. The samples were heated up to 573 K, hydrogen at 3 MPa was introduced into the apparatus for 30 minutes. This was followed by slow cooling to room temperature in hydrogen. The alloys absorbed most of the hydrogen and pulverize in this step. After the absorption process, the samples were heated up to 573 K and chamber was evacuated with a mechanical pump for 1 hour to dehydrogenate completely for PCT measurements at 303, 333 and 363 K successively.

3. Results and discussion

3.1 Microstructures and phases

Figure 1 shows the SEM backscattered (BSE) micrographs of the as-cast $Ti_{25-0.5x}V_{40}Cr_{35-0.5x}Fe_x$ (x = 0, 2, 5, 6 at.%) alloys. All the samples contained primary, light grey BCC and secondary, dark intergranular Laves phases.

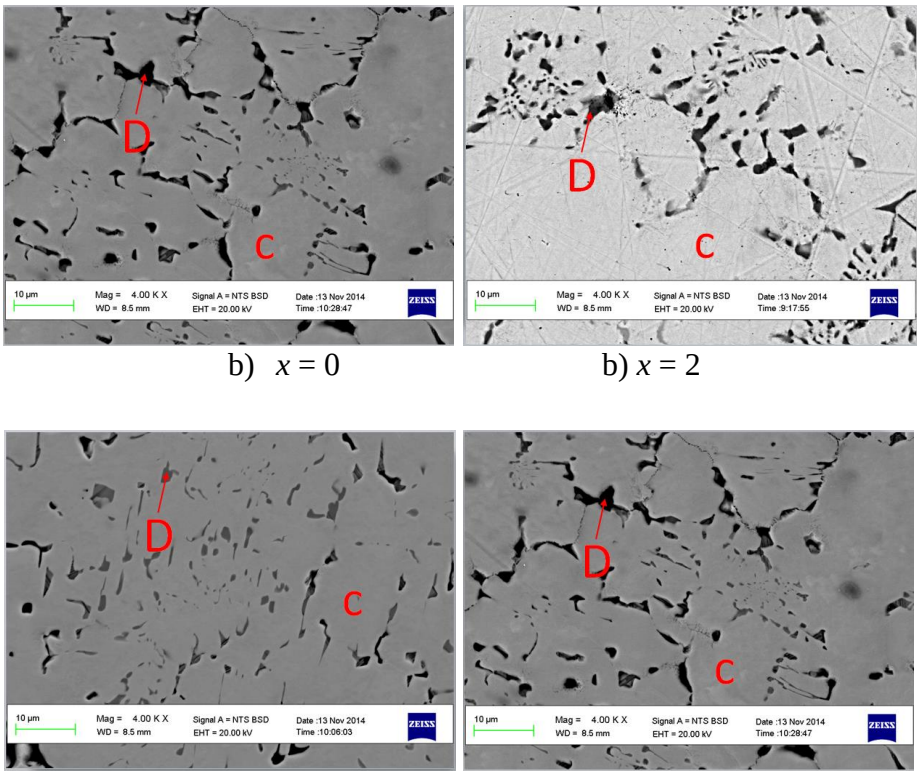

b) x = 0 b) x = 2

c) x = 5 d) x = 6

Figure 1. Microstructures of as-cast $Ti_{25-0.5x}V_{40}Cr_{35-0.5x}Fe_x$ (x = 0, 2, 5, 6 at.%) alloys.

Table 1. EDX analysis and crystallographic parameters of $Ti_{35-0.5x}V_{40}Cr_{25-0.5x}Fe_x$ (x = 0, 2, 5, 6 at.%).

Fe content (at.%)	Phase	Composition (at.%)					Lattice parameters (Å)		Cell volume (Å^3)	Phase proportion (%)
		Ti	V	Cr	Fe	Ti/Cr ratio	a	c		
0	BCC	22.0 (0.7)*	42.8 (0.4)	35.2 (0.8)	-	0.6	3.0246		27.67	89.7
	αTi	66.1 (1.6)	18.9 (1.2)	15.0 (0.8)	-	4.4	2.98	4.72	36.24	10.3
2	BCC	17.7 (1.1)	43.5 (1.6)	36.5 (2.2)	2.3 (0.7)	0.5	3.003		27.08	78.5
	αTi	23.0 (3.7)	41.4 (2.4)	35.5 (1.4)	2.0 (0.2)	0.6	2.98	4.73	36.24	20.2
	C 14 Laves	24.7 (0.8)	37.8 (0.7)	34.0 (0.4)	3.5 (0.3)	0.7	4.85	7.94	161.7	1.3
5	BCC	24.4 (2.8)	37.4 (2.5)	33.0 (1.0)	5.2 (3.1)	0.7	2.9981		26.98	67.5
	αTi	78.3 (5.4)	11.2 (2.9)	8.9 (2.0)	1.5 (0.6)	8.8	2.98	4.73	36.24	32.5
6	BCC	15.5 (2.2)	44.0 (2.5)	35.5 (0.4)	5.0 (4.9)	0.4	2.9981		26.98	75
	αTi	79.5 (5.4)	11.0 (2.7)	8.5 (2.5)	1.0 (0.2)	9.4	2.98	4.73	36.24	25

* Standard error in parentheses

XRD patterns (Figure 2) showed the main peaks of vanadium BCC and minor peaks of αTi and C14-Laves phases. Image analysis showed that BCC proportion was higher than Laves. For instance, in Fe-free sample ($Ti_{25}V_{40}Cr_{35}$ i.e. x = 0) Table 1 showed that the BCC phase was ~90 area % and Laves phase was ~10 area %. This is in agreement with XRD result confirming that the main peak was V-based BCC solid solution and the dark phase was Laves. Jeong-Hyun [14] observed Laves and BCC phases in $Ti_{0.32}Cr_{0.43-x}V_{0.25}Fe_x$ ($0 \leq x \leq 0.10$) but the later phase dominates the structure of the alloys. Huang *et. al.* [18] also found BCC and Lave in $TiCr_{1.8-x}(VFe)_x$.

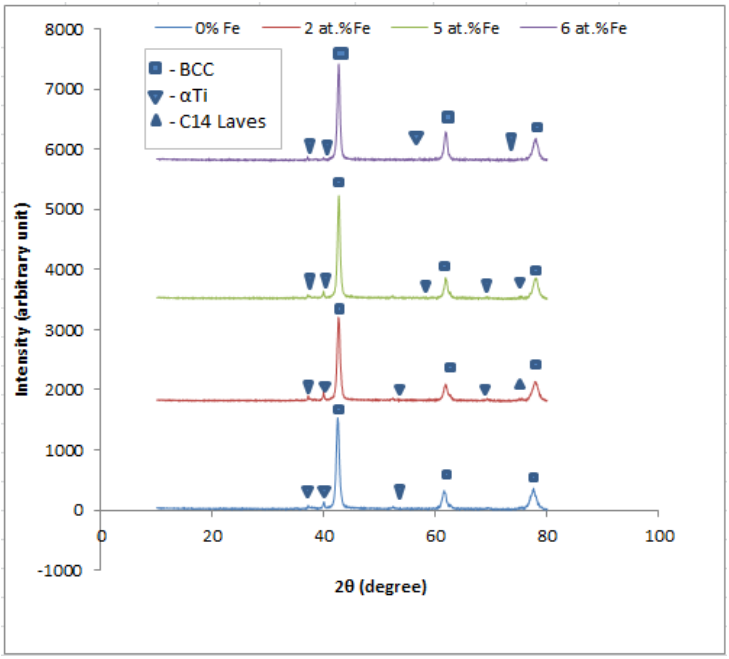

Figure 2. XRD pattern of $Ti_{25-0.5x}V_{40}Cr_{35-0.5x}Fe_x$ (x = 0, 2, 5, 6) alloys.

Figure 3 showed that the cell parameters of the primary phase decreased with increase in Fe content, which agrees with the findings of Yoo *et al.* [14]. This is because in $Ti_{25-0.5x}V_{40}Cr_{35-0.5x}Fe_x$ (x = 0, 2, 5, 6 at.%) alloys, Fe an element with smaller atomic radius (1.72 Å) is replacing larger atomic radius elements Cr (1.85 Å) and Ti (2 Å).

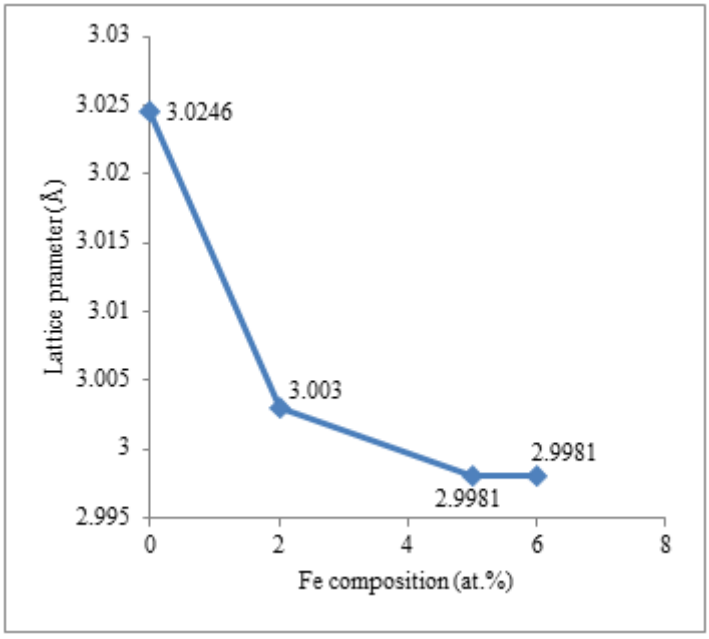

Figure 3. Relationship of lattice parameters and Fe compositions in $Ti_{25-0.5x}V_{40}Cr_{35-0.5x}Fe_x$ (x = 0, 2, 5, 6 at.%) alloys.

EDS analysis in Table 1 showed that the range of elemental compositions of primary BCC (V) phase were 15-25 at.% Ti; 37-44 at.% V; 33-36 at.% Cr and 0-5 at.% Fe while that

of the Laves phase contained 23-80 at.% Ti; 11-42 at.% V; 8.5-36 at.% Cr and 1-4 at.% Fe. The Ti content in the Laves phase increased with Fe content except in 2% Fe alloy. The table also showed that addition of Fe reduced the proportion of primary phase but increased that of Laves phase. The change in phase proportion was also indicated in the micrographs in Figures 1(a) – (d).

3.2 Absorption/desorption curves

Figures 4(a) – (d) are the PCT ab/desorption isotherms measured at 303, 333 and 363 K for $Ti_{25-0.5x}V_{40}Cr_{35-0.5x}Fe_x$ (x = 0, 2, 5, 6 at.%) alloys. The upper curves in broken lines are the absorption isotherms while the lower unbroken lines are the desorption isotherms. The pressure increased with hydrogen capacity on the absorption isotherms and decreased with hydrogen capacity on the desorption isotherms, this is in line with literature [15; 24; 26]. The trend is justified because at inception of absorption, hydrogen atom resides on the surface of the adsorbate, hence imposed some amount of pressure on it. As the absorption progresses, more hydrogen atoms are attached to the surface of the host metal, thereby increasing the hydrogen pressure. However, during desorption hydrogen atom are released from the surface of the host hence reducing the gas pressure on it, the pressure is further reduced as desorption progresses till a situation when only stable metal hydride remains on the host metal. For an alloy with dual-phase structure, the phase with higher affinity attracts H atom first [4; 10; 11] i.e. BCC phase is occupied before Laves.

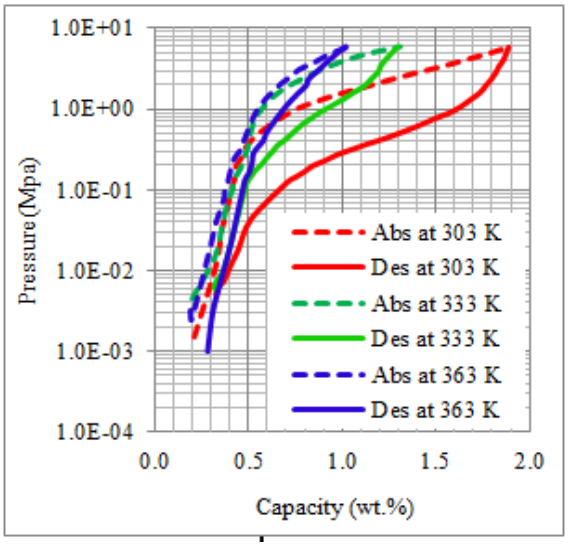

b) x = 0

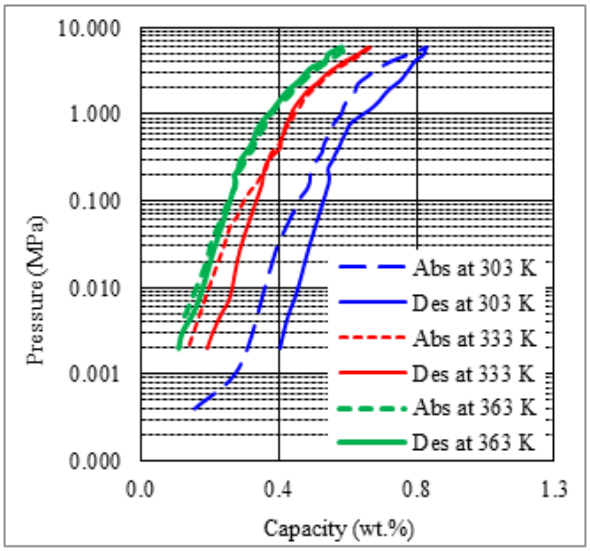

b) x = 2

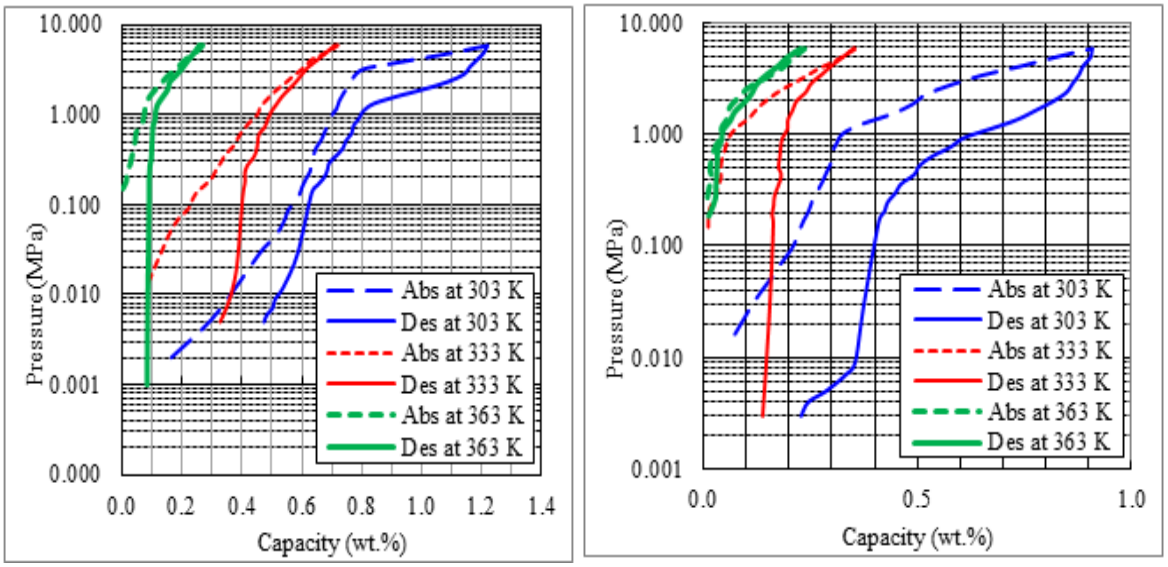

d) $x = 5$ d) $x = 6$

Figure 4. Absorption/desorption isotherms of $Ti_{25-0.5x}V_{40}Cr_{35-0.5x}Fe_x$ (x = 0, 2, 5, 6 at.%) alloys.

Figure 5 showed that the maximum absorption capacity decreased with increase in isotherm temperature for all at.% Fe compositions, this observation is similar to literature [12; 27; 30]. At lower temperature the kinetic energy of the gas is low thereby making it easier for the host metal to absorb the less energised gas. However at higher temperature the gas possesses higher kinetic energy and moves with higher velocity thereby hindering absorption. This explains the observed inverse relationship between the isotherm temperature and maximum absorption capacity.

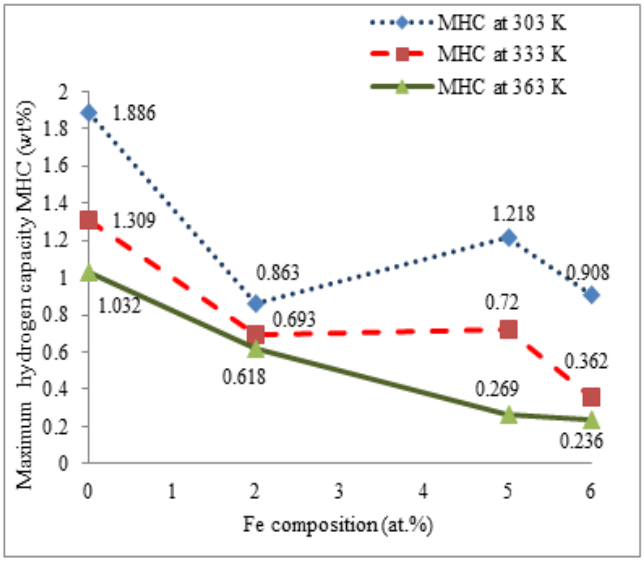

Figure 5. Effect of isotherm temperature on maximum H capacity.

For practical application in fuel cell, hydrogen desorption under ambient condition is desirable [2; 8; 13], therefore desorption curves of $Ti_{25-0.5x}V_{40}Cr_{35-0.5x}Fe_x$ (x = 0, 2, 5, 6 at. %) alloys at 30 °C are presented in Figure 6. The figure revealed that plateau pressure rose with addition of Fe. It was shown in Figure 3 that BCC cell volume decreased with increase in Fe content in the alloy, thus the observed decrease in cell volume of BCC led to reduction in H absorption sites, decrease in the distance between neighbouring hydrogen atoms, and consequently the observed increase in plateau pressure.

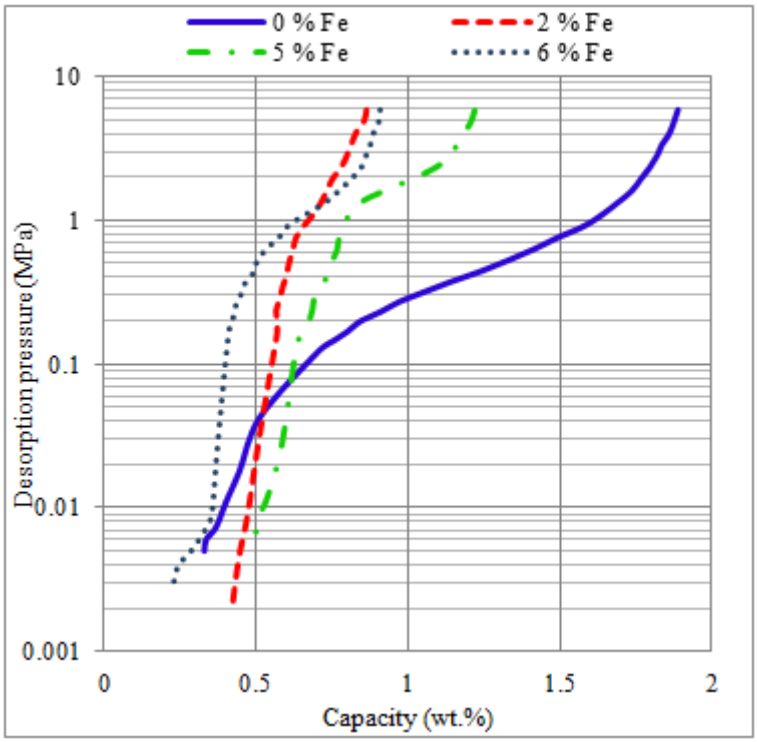

Figure 6. Effect of Fe on H desorption in $Ti_{25-0.5x}V_{40}Cr_{35-0.5x}Fe_x$ (x = 0, 2, 5, 6 at.%) alloys.

Table 2 showed that addition of Fe resulted to reduction in useful storage capacity. Fe-free sample had the highest absorption capacity (1.89 wt%) and useful storage capacity (1.56 wt.%). The 2 at.% Fe sample had the least absorption and useful capacity of 0.89 and 0.44 wt% respectively; Yoo *et al.* [25] also found that substituting Fe for Cr was not favourable to hydrogen desorption. Laves phase is known to be detrimental to H capacity, while BCC phase is favorable to it [12; 16; 23]. When cell volume of BCC increased, the interstitial holes increased thereby creating additional site for H atom to reside, consequently leading to high H capacity. Increase in cell volume of Laves is a consequential decrease in H capacity. The high absorption and reversible capacity observed in Fe-free sample is therefore attributed to high BCC cell volume while the least storage capacity of 0.44 wt% at 2 at.% Fe was due to the additional large cell volume Laves in the sample (see Table 1). This also explains the trend in Figure 7a showing that sample with large BCC cell volume had high useful capacity and vice versa while Figure 7b showed that sample with large Laves cell volume had low useful capacity and vice versa.

Table 2. Hydrogen storage properties of $Ti_{25-0.5x}V_{40}Cr_{35-0.5x}Fe_x$ (x = 0, 2, 5, 6 at.%).

Fe content (at.%)	Absorption capacity (wt.%)	Useful capacity (wt.%)	Capacity remaining (wt.%)	Capacity remaining as % of absorption capacity	Plateau pressure (MPa)
0	1.89	1.56	0.33	17.46	0.41
2	0.89	0.44	0.45	50.56	1.30
5	1.21	0.75	0.46	38.02	1.92
6	0.90	0.68	0.22	24.44	1.34

Another phenomenon in Table 2 is that the % hydrogen capacity remaining after desorption process increased with Fe addition. During absorption process in V-based alloys, two kinds of hydrides are formed i.e. mono-hydride (β-phase) and di-hydride (γ-phase) [20; 22]. The former are not easily decomposed but the latter decompose easily under moderate conditions of temperature and pressure. Table 2 showed that H-desorbed was higher in the Fe-free alloy, ~ 17% of the absorbed hydrogen was not desorbed, implying that more γ-phase hydride was formed during the hydrogen absorption process. The high % capacity remaining in 2 at.% Fe alloy implied that more mono-hydride was formed during the hydrogen absorption process.

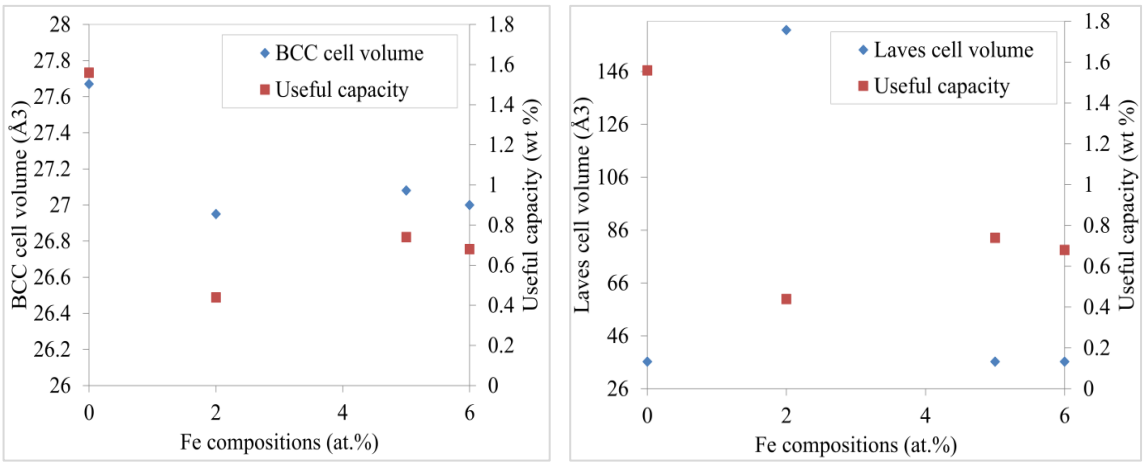

(a) (b)

Figure 7. Influence of (a) BCC cell volume and (b)Laves cell volume on useful capacity.

4. Conclusions

The effect of 2, 5 and 6 at.% Fe (substituted at Ti and Cr site) on microstructure and hydrogen storage characteristics of $Ti_{35}V_{40}Cr_{25}$ have been investigated and the main conclusions were:

1. Both the Fe-free and Fe-containing alloys have two phases with BCC and Laves structure. Fe did not change the crystal structure of the base alloy but reduced lattice parameter of BCC
2. The plateau pressure of the base alloy increased with Fe addition.
3. The hydrogen absorption and useful capacities of $Ti_{35}V_{40}Cr_{25}$ decreased with Fe addition, the highest H capacity and best plateau characteristics was observed in Fe-free alloy; while the least absorption and useful capacities were observed in 2 at.% Fe composition and
4. With addition of Fe, the capacity remaining as a percentage of maximum absorption capacity increased, indicating that Fe promotes formation of β-phase hydride.

Acknowledgement

The work is supported by African Material Science and Engineering Network, AMSEN and the National Research Found NRF Thuthuka programme.

References

1. M. Abe and T. Kuji. (2007). Hydrogen absorption of TiFe alloy synthesized by ball milling and post-annealing. *Journal of Alloys and Compounds, 446–447*, 200-203. doi: 10.1016/j.jallcom.2006.12.063
2. G. Alefeld and J. Volki. (1978). *Hydrogen in metal II. Application oriented properties*. Berlin-Heidelberg: Springer-Verlag. Pg.387.
3. G. Alefeld and J. Völkl. (1978). *Hydrogen in Metals II*. Berlin-Heidelberg: Springer-Verlag.
4. M. A. Ashworth, A. J. Davenport, R. M. Ward and H. G. C. Hamilton. (2010). Microstructure and corrosion of Pd-modified Ti alloys produced by powder metallurgy. *Corrosion Science, 52*(7), 2413-2421. doi: http://dx.doi.org/10.1016/j.corsci.2010.03.006
5. S. Basak, K. Shashikala and S. K. Kulshreshtha. (2008). Hydrogen absorption characteristics of Zr substituted alloy. *International Journal of Hydrogen Energy, 33*(1), 350-355. doi: 10.1016/j.ijhydene.2007.07.023
6. L. E. A. Berlouis, N. Comisso and G. Mengoli. (2006). Changes in hydrogen storage properties of binary mixtures of intermetallic compounds submitted to mechanical milling. *Journal of Electroanalytical Chemistry 586* 7.
7. H. Bjurström, S. Suda and D. Lewis. (1987). A numerical expression for the P-C-T properties of metal hydrides. *Journal of the Less-Common Metals, 130*(365-370), 365. doi: 10.1016/0022-5088(87)90130-5
8. D. P. Broom. (2008). Hydrogen sorption measurements on potential storage materials: Experimental methods and measurement accuracy *Office for Official Publications of the European Communities, Luxembourg* (Vol. EUR 23242 EN).
9. S.-W. Cho, H. Enokib and E. Akibab. (2000). Effect of Fe addition on hydrogen storage characteristics of $Ti_{0.16}Zr_{0.05}Cr_{0.22}V_{0.57}$ alloy *Journal of Alloys and Compounds 307*, 304–310.
10. P. Handzlik and K. Fitzner. (2013). Corrosion resistance of Ti and Ti–Pd alloy in phosphate buffered saline solutions with and without H_2O_2 addition. *Transactions of Nonferrous Metals Society of China, 23*(3), 866-875. doi: http://dx.doi.org/10.1016/S1003-6326(13)62541-8
11. Z. Hang, X. Xiao, D. Tan, Z. He, W. Li, S. Li, C. Chen and L. Chen. (2010). Microstructure and hydrogen storage properties of $Ti_{10}V_{84-x}Fe_6Zr_x$ (x = 0; 1–8) alloys. *International Journal of Hydrogen Energy, 35*(7), 3080-3086. doi: 10.1016/j.ijhydene.2009.07.019
12. T. Huang, Z. Wu, B. Xia, J. Chen, X. Yu, N. Xu, C. Lu and H. Yu. (2003). $TiCr_{1.2}(V–Fe)_{0.6}$—a novel hydrogen storage alloy with high capacity. *Science and Technology of Advanced Materials, 4*(6), 491-494. doi: http://dx.doi.org/10.1016/j.stam.2003.12.001
13. Hydrogen storage technology roadmap. (2005) *United States Department of Energy FreedomCAR and fuel partnership*. Washington.
14. Y. Jeong-Hyun, G. Shim, S.-W. Cho and C.-N. Park. (2007). Effects of desorption temperature and substitution of Fe for Cr on the hydrogen storage properties of $Ti_{0.32}Cr_{0.43}V_{0.25}$ alloy. *International Journal of Hydrogen Energy 32*, 2977-2981.
15. X. P. Liu, F. Cuevas, L. J. Jiang, M. Latroche, Z. N. Li and S. M. Wang. (2009). Improvement of the hydrogen storage properties of Ti–Cr–V–Fe BCC alloy by Ce addition. *Journal of Alloys and Compounds, 476*(1–2), 403-407. doi: http://dx.doi.org/10.1016/j.jallcom.2008.09.042
16. H. Pan, R. Li, Y. Liu, M. Gao, H. Miao, Y. Lei and Q. Wang. (2008). Structure and electrochemical properties of the Fe substituted Ti–V-based hydrogen storage alloys. *Journal of Alloys and Compounds, 463*(1–2), 189-195. doi: 10.1016/j.jallcom.2007.09.042
17. C. Sung-Wook, H. Chang-Suck, P. Choong-Nyeon and E. Akibab. (1999). Hydrogen storage characteristics of Ti–Zr–Cr–V alloys. [Journal]. *Journal of Alloys and Compounds, 289*, 244-250.
18. H. Taizhong, W. Zhu, S. Guoxin and X. Naixin. (2008). Influences of Partial Substitution of VFe Alloys for Cr on Structure and Hydrogen Storage Performances of $TiCr_{1.8}$ Alloy. *Rare Metal Materials and Engineering, 37*(3), 386-390. doi: 10.1016/s1875-5372(09)60010-2

19. D. Tou, W. Zhu, M. Jianfeng and N. Xua. (2008). Application of commercial ferrovanadium to reduce cost of Ti–V-based BCC phase hydrogen storage alloys. *Materials Science and Engineering, A 476*, 34-38. doi: 10.1016/j.msea.2007.04.080
20. M. Tsukahara, K. Takahashi, T. Mishima, T. Sakai, H. Miyamura, N. Kuriyama and I. Uehara. (1995). Metal hydride electrodes based on solid solution type alloy TiV_3Ni_x ($0 \le x \le 0.75$). *Journal of Alloys and Compounds, 226*(1–2), 203-207. doi: http://dx.doi.org/10.1016/0925-8388(95)01570-1
21. US DoE, Hydrogen storage technology roadmap. (United States Department of Energy FreedomCAR and fuel partnership, 2005). Washington Downloaded from www.nrel.gov/docs/fy08osti/39146.pdf.
22. Y. Yan, Y. Chen, X. Zhou, H. Liang, C. Wu and M. Tao. (2008). Some factors influencing the hydrogen storage properties of 30V–Ti–Cr–Fe alloys. *Journal of Alloys and Compounds, 453*(1–2), 428-432. doi: 10.1016/j.jallcom.2006.11.122
23. Y. Yigang, C. Yungui, L. Hao, W. Chaoling, T. Mingda and M. Tu. (2006). Effect of Al on hydrogen storage properties of $V_{30}Ti_{35}Cr_{25}Fe_{10}$ alloy. *Journal of Alloys and Compounds 426* 253-255. doi: 10.1016/j.jallcom.2005.12.122
24. Y. Yigang, C. Yungui, L. Hao, Z. Xiaoxiao, W. Chaoling, T. Mingda and L. Pang. (2008). Hydrogen storage properties of V–Ti–Cr–Fe alloys. *Journal of Alloys and Compounds 454*(5), 427-431. doi: 10.1016/j.jallcom.2006.12.093
25. J.-H. Yoo, G. Shim, S.-W. Cho and C.-N. Park. (2007). Effects of desorption temperature and substitution of Fe for Cr on the hydrogen storage properties of alloy. *International Journal of Hydrogen Energy, 32*(14), 2977-2981. doi: http://dx.doi.org/10.1016/j.ijhydene.2007.01.012
26. J.-H. Yoo, G. Shim, C.-N. Park, W.-B. Kim and S.-W. Cho. (2009). Influence of Mn or Mn plus Fe on the hydrogen storage properties of the Ti-Cr-V alloy. *International Journal of Hydrogen Energy, 34*(22), 9116-9121. doi: http://dx.doi.org/10.1016/j.ijhydene.2009.08.064
27. K. Young, T. Ouchi and M. A. Fetcenko. (2009). Pressure–composition–temperature hysteresis in C14 Laves phase alloys: Part 1. Simple ternary alloys. *Journal of Alloys and Compounds, 480*(2), 428-433. doi: http://dx.doi.org/10.1016/j.jallcom.2008.12.113
28. K. Young, T. Ouchi, B. Huang, B. Reichman and M. A. Fetcenko. (2011). The structure, hydrogen storage, and electrochemical properties of Fe-doped C14-predominating AB_2 metal hydride alloys. *International Journal of Hydrogen Energy, 36*(19), 12296-12304. doi: 10.1016/j.ijhydene.2011.06.117
29. X. B. Yu, Z. Wu, B. J. Xia and N. X. Xu. (2004). Enhancement of hydrogen storage capacity of Ti–V–Cr–Mn BCC phase alloys. *Journal of Alloys and Compounds, 372*(1–2), 272-277. doi: 10.1016/j.jallcom.2003.09.153
30. Y. Zhou, J. Chen, Y. Xu and Z. Liu. (2013). Effects of Cr, Ni and Cu on the Corrosion Behavior of Low Carbon Microalloying Steel in a Cl− Containing Environment. *Journal of Materials Science & Technology, 29*(2), 168-174. doi: http://dx.doi.org/10.1016/j.jmst.2012.12.013

4. Full paper under review with Cogent Engineering (A Taylor and Francis Journal)

Hydrogen storage characteristics and corrosion behaviour of V-rich Ti-V-Cr-Fe alloy

J.M. Abdul [1,2,3] and L.H. Chown [1,2,3,4]

[1] School of Chemical and Metallurgical Engineering, [2] African Materials Science and Engineering Network (AMSEN), [3] Materials for Energy Research Group (MERG), [4] DST-NRF Centre of Excellence in Strong Materials, *all University of the Witwatersrand, Private Bag 3, WITS 2050, Johannesburg, South Africa*

[*]Corresponding author. Tel: +234 805 562 9924, +27 074 069 6713. Email addresses: jmabdul@gmail.com; jmabdul66@yahoo.com

Hydrogen storage characteristics and corrosion behaviour of V-rich Ti-V-Cr-Fe alloy

Abstract

In this work, we investigated the effect of heat treatment on microstructure, hydrogen storage characteristics and corrosion rate of a Ti-V-Cr-Fe alloy. The arc-melted alloy was cut into three samples, two of which were separately quartz-sealed under vacuum and heated to 1000 °C for 1 hour; a sample was quenched and the other furnace cooled to ambient temperature. The crystal structure of the samples were studied by XRD and SEM BSE, and the absorption/desorption characteristics were investigated using Sievert apparatus. Pottentiostatic corrosion test on the alloys was performed using an AutoLab® corrosion test apparatus and electrochemical cell. All the samples had BCC and Laves phase structures. The corrosion rate and maximum absorption and useful capacities increased after both heat treatments. Annealed sample had the highest absorption and useful capacity. The plateau pressure of the as-cast alloy increased after quenching. The corrosion rate increased from 0.0004 in as-cast sample to 0.0009 mm/y after annealing and 0.0017 mm/y after quenching.

***Keyword**:* Ti-V-Cr-Fe alloy, hydrogen storage characteristics, corrosion rate, heat treatment, crystal structure

1. Introduction

Ti-V-Cr BCC solid solution alloys are very promising because of their high absorption capacity at room temperature [32; 39]. Some of the identified shortcomings of the alloy is the poor P-C-T plateau characteristics, low hydrogen desorption capacity and long activation time [2; 11; 26; 36]. In an attempt to improve on the shortcomings, additives such as Fe, Zr and Mn in controlled quantities has been found to be effective in lowering cost and enhancing overall performance of the alloy [18; 19; 40; 53]. Further studies include effect of heat treatment on the hydrogen absorption properties. Okada *et al*. [32] found that moderate heat treatment enhances the storage capacity and flattens desorption plateau of $Ti_{25}Cr_{40}V_{35}$ alloy when annealed at 1573 K for 1 minute. Liu *et al*. [29] reported that heat treatment effectively improved the flatness of plateau and improved hydrogenation capacity of $Ti_{32}Cr_{46}V_{22}$ alloy by lowering the oxygen concentration and homogenizing the composition and microstructure. Hydrogen desorption capacity of 2.3 wt.% was achieved when $Ti_{32}Cr_{40}V_{25}$ was annealed at 1653 K for 1 minute [12]. Chuang *et al*. [13] found that annealing of atomized powder of Ti-Zr based alloy at 850 °C for 4 hours greatly enhanced the discharge capacity. Hang *et al*. [17] heat treated $Ti_{10}V_{77}Cr_6Fe_6Zr$ alloy at relatively lower temperature but elongated soaking time by annealing at 1523 K for 5 minutes and 1373 K for 8 hours, and found that sample annealed at 1523 K for 5 minutes has the best overall hydrogen storage properties with desorption capacity of 1.82 wt.% and dehydriding plateau pressure of

0.75MPa. This work is to investigate the influence of heat treatment on hydrogen storage capacity and corrosion rate of $Ti_{34}V_{40}Cr_{24}Fe_2$. Hydrogen storage alloys are sometimes used as anode in NiMH batteries, hence the need to investigate the corrosion behaviour of the alloy in such condition.

2. Experimental

A 10g weight sample of $Ti_{34}V_{40}Cr_{24}Fe_2$ at.% alloy was prepared in a water-cooled, copper-crucible arc melting furnace under argon atmosphere. The ingot was turned over and remelted three times to ensure homogeneity. After melting, the ingot was cut to three pieces. Two cut samples were vacuum-sealed in separate silica glass tubes in readiness for heat treatment.

The two quartz-sealed specimens were loaded into a heat treatment furnace where it was heated to 1000 °C for 1 hour. One tube was immediately removed and broken in cold water to quench the alloy, hence locking the microstructure while the second sample was slowly furnace-cooled to room temperature.

Crystal structure and lattice parameters in the as-cast and heat-treated samples were determined by XRD analysis, using a Bruker D2_Phaser X-ray® diffraction machine with Cu-K_α radiation from $2\theta = 10^o$ to 80^o. Elemental compositions of the phases were determined using a FEI Nova NanoSEM 200® scanning electron microscope (SEM) fitted with EDAX® advanced microanalysis solution. The amount of the phases was determined by image analysis using ImageJ freeware.

Pottentiostatic corrosion test on the alloys was performed using an AutoLab® corrosion test apparatus and electrochemical cell consisting of tri-electrode; platinum reference electrode, Ag/AgCl counter electrode, and test alloy as the working electrode; aqueous solution of 6 mol/L KOH was used as the electrolyte. The alloys were cut into rectangular shape; a copper wire of suitable length was attached to one side of the specimen with aluminium tape and covered in cold-resin for 24-hours to enable curing while leaving only the test surface exposed. After the curing, the test surface was ground to 120 grit size. The corrosion experiments were performed at 25 °C, Tafel curves were recorded from -1.4V to -0.2 V with a scanning rate of 1 mV/sec.

Measurement of the pressure composition temperature (PCT curves) was performed using Sieverts-type apparatus. Samples were crushed into particle sizes of < 75 μm and 1g of each alloy was sealed into a stainless steel reactor and heated up to 573 K. Hydrogen at 3 MPa pressure was introduced into the apparatus for 30 minutes, followed by slow cooling to room temperature in hydrogen. The alloys absorb most of the hydrogen and pulverize in this step. After the absorption process, the samples were heated up to 573 K and chamber was evacuated for 1 hour with a mechanical pump to dehydrogenate completely for PCT measurements at 303, 333 and 363 K successively.

3. Results and discussion

3.1. Microstructure

Figure 1 shows the back scattering electron images of as-cast and heat treated $Ti_{34}V_{40}Cr_{24}Fe_2$. The microstructure of the alloy was a primary, light grey phase (C) with a black intergranular phase (D) in all three samples. In addition, a dark grey intergranular phase (E) was observed in the as-cast sample, the dark grey phase have different compositions from D. EDX analyses on the dark portions (E) on micrograph of annealed sample have the same elemental compositions as the Laves. XRD pattern in Figure 2 showed that the primary, light grey phase corresponds to main peak of BCC (V) while the black intergranular and the dark phases were the minor peaks of C14 Laves. Annealing removed the dark grey Laves phase while quenching increased the proportion of the phase from 1.3 to 32.5 %. Quenching introduced twinning in the secondary Laves phase shown inside the circle (F).

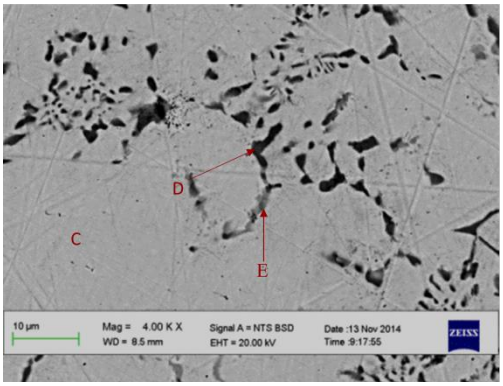

a) As-cast sample

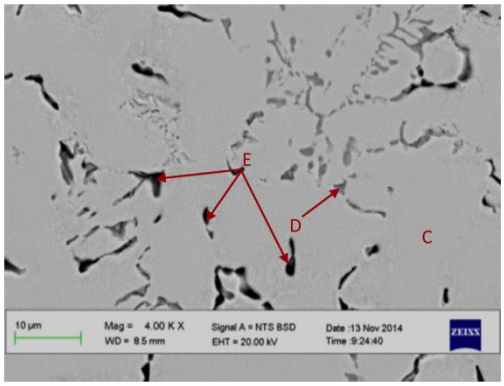

b) annealed sample

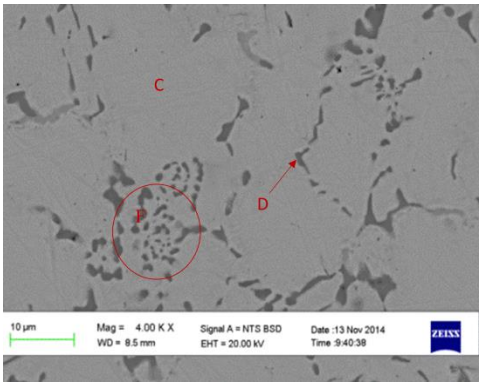

c) Quenched sample

Figure 1. SEM BSE micrograph of as-cast and heat treated $Ti_{34}V_{40}Cr_{24}Fe_2$.

Table 1 showed that the bcc (V) in all the three samples contained 17-22 at.% Ti, 40-44 at.% V and ~36 at.% Cr. The black intergranular C14 Laves phase contained 23-66 at.% Ti, 18-41 at.% V and 14-36 at.% Cr. The annealing treatment removed the dark grey C14 Laves (cell volume 161.7 $Å^3$) while quenching dissolved Laves phase with smaller cell volume. Ti/Cr ratio in the BCC phase was ~ 0.6 for all three samples, however, the ratio in Laves phase increased from 0.6 to 4.4 after annealing and ~2 after quenching.

The proportion of BCC (V) phase in as-cast sample was ~79%. The proportion of dark phase and light grey C14 Laves phases was 20% and 1.3% respectively. Annealing had no effect on the composition of the BCC phase but increased the proportion to 82%. Quenching reduced the proportion of BCC by 11% and increased Ti content by ~4 at.%. Proportion of the Laves phase was slightly reduced from 20% in as-cast sample to 18% in annealed sample, but it increased to 32.5% after quenching.

Table 1. EDX and crystallographic parameters of as-cast and heat treated $Ti_{34}V_{40}Cr_{24}Fe_2$.

Sample	Phases XRD	Composition (at.%)* Ti	V	Cr	Fe	Ti/Cr ratio	Phase proportion (% area)	Crystallographic description Space group (no.)	a	c	Cell vol. ($Å^3$)
As-cast	BCC (V)	17.7 (1.1)	43.5 (1.6)	36.5 (2.2)	2.3 (0.7)	0.5	78.5	$Im\bar{3}m$ (229)	3.00		27.08
	C14 (Laves)	23.0 (3.7)	41.4 (2.4)	35.5 (1.4)	2.0 (0.2)	0.6	20.2	$P6_3/mmc$ (194)	2.98	4.73	36.24
	C14 (Laves)	24.7 (0.8)	37.8 (0.7)	34.0 (0.4)	3.5 (0.3)	0.7	1.3	$P6_3/mmc$ (194)	4.85	7.94	161.7
Annealed	BCC (V)	17.7 (1.9)	43.5 (1.3)	36.5 (2.9)	2.3 (0.2)	0.5	82.0	$Im\bar{3}m$ (229)	3.01		27.37
	C14 (Laves)	65.9 (5.2)	18.6 (2.8)	14.9 (2.2)	0.6 (0.2)	4.4	18.0	$P6_3/mmc$ (194)	2.98	4.73	36.24
Quenched	BCC (V)	21.8 (1.5)	40.0 (1.3)	35.6 (1.2)	2.6 (1.7)	0.6	67.5	$Im\bar{3}m$ (229)	3.01		27.37
	C14 (Laves)	47.3 (3.7)	21.6 (2.5)	24.7 (1.4)	6.4 (0.5)	1.9	32.5	$P6_3/mmc$ (194)	4.85	7.94	161.7

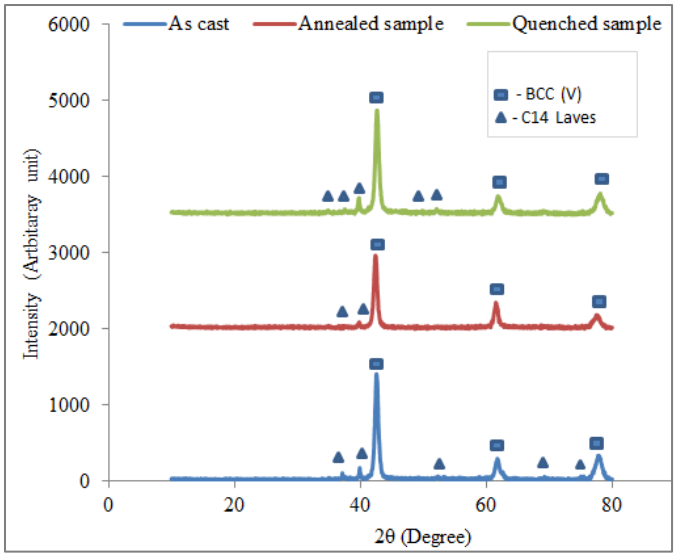

Figure 2. XRD pattern of as-cast and heat treated $Ti_{34}V_{40}Cr_{24}Fe_2$ alloy.

3.2. Hydrogen storage characteristics

Table 2 shows that both heat treatment processes increased the reversible hydrogen storage capacity RHSC, the capacity increased from 0.44 to 1.26 wt% after annealing and to 1.26 wt% in quenched sample literature have shown that annealing increased hydrogen capacity [12; 13]. BCC phase enhances H capacity [5; 16; 18] and increase in its cell volume implies availability of more H absorption sites or space leading to increase in storage capacity. Laves phase is detrimental to storage capacity [10; 42; 50; 53], alloys with larger Laves cell volume or high Laves proportion are known for lower hydrogen capacity. Therefore the observed increase in useful capacity after heat treatment was due to increase in BCC cell volume. The larger cell volume Laves phase in as-cast sample was dissolved after annealing; this suggests another reason for the higher hydrogen capacity observed in the annealed sample.

Table 2 also showed that the plateau pressure reduced after annealing and rose after quenching. The pressure of plateau decreased from 1.32 to 0.68 MPa after annealing and increased to 2.34 MPa after quenching. Plateau property is affected by both the homogeneity and oxygen content in Ti-V based hydrogen storage alloy [53]. Inhomogeneity of microstructure can be minimized by heat treatment at higher temperature for a short time[22]. The observed reduction in plateau pressure after annealing is suggested by the homogenized microstructure. In addition, the sample was annealed in vacuum-sealed quartz tube thereby preventing oxygen intake. The quenched sample was exposed to oxygen in the quenching medium; therefore the rise in plateau pressure is attributed to the higher oxygen content.

Table 2. Effect of heat treatment on H storage properties of $Ti_{34}V_{40}Cr_{24}Fe_2$ alloy

Sample	Absorption capacity (wt%)	Capacity remaining (wt.%)	Useful capacity (wt%)	Plateau pressure (MPa)
As-cast	0.86	0.42	0.44	1.32
Annealed	1.54	0.28	1.26	0.68
Quenched	1.04	0.39	0.65	2.34

In Figure 3a the p-c isotherms for both as-cast and heat treated alloys were steep, an indication of high plateau pressure. However, the isotherm for the annealed sample showed a flatter and wider plateau. Flattened plateau is an indication of a reduction in plateau pressure and the wider plateau indicates higher hydrogen capacity.

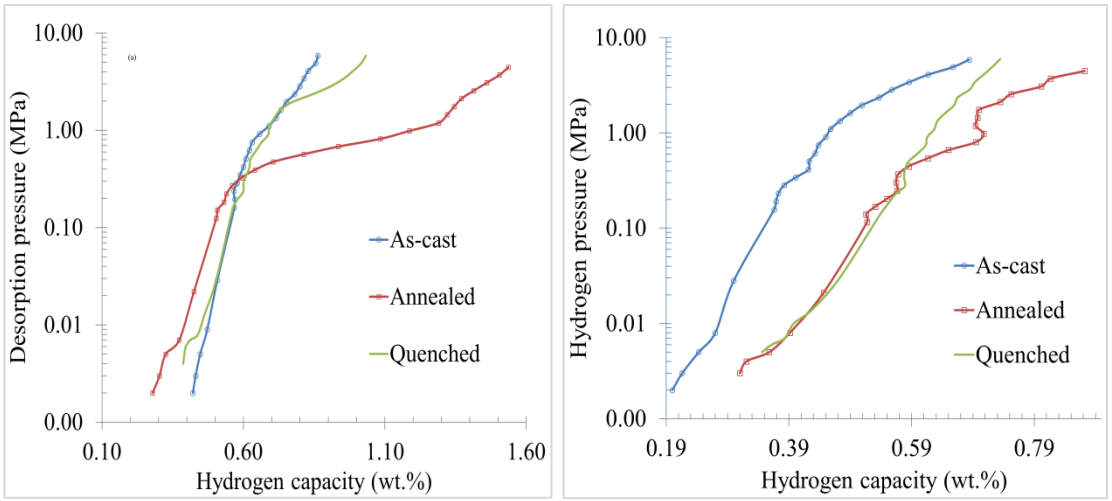

a) 30 isotherm b) 60 isotherm

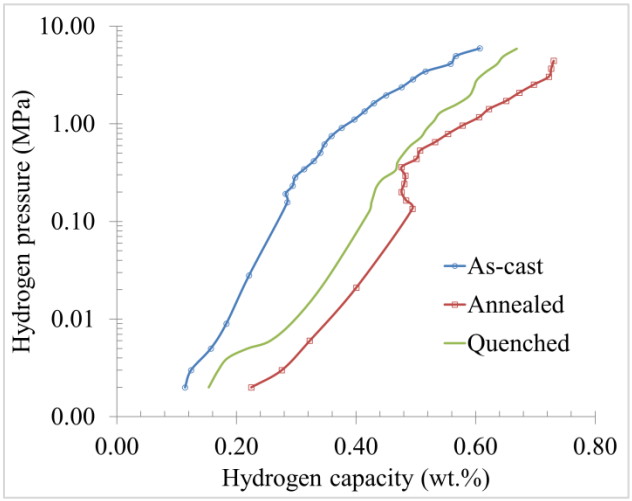

c) 90 isotherm

Figure 3. Desorption curves of as-cast and heat treated $Ti_{34}V_{40}Cr_{24}Fe_2$ alloy

In Figure 4, the maximum absorption capacity reduced with an increase in isotherm temperature, similar to literature [43]. For the as-cast sample, maximum absorption capacity was 0.86 wt.% at 30 °C, the capacity declined to 0.69 and 0.62 wt.% as the temperature rose to 60 and 90 °C respectively. Similar trend was observed for the annealed and quenched samples. Kinetic energy of gas increased with an increase in temperature; low kinetic energy is associated with lower temperature while increased temperature leads to high kinetic energy and more agitated gas. Hydrogen gas with low kinetic energy is easily absorbed than those with high kinetic energy because gas having higher kinetic energy moves faster thus requiring additional force to attract to the surface of the adsorbate. This explains the observed higher capacity at low temperature and lower capacity at high temperature.

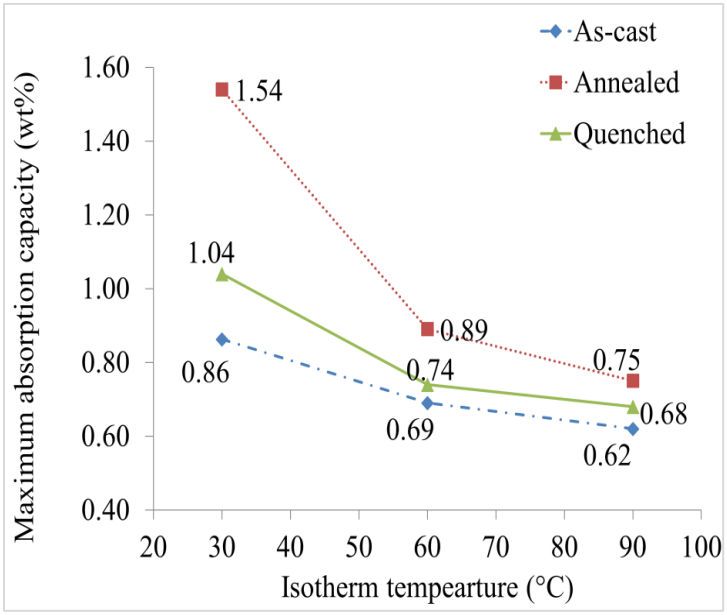

Figure 4. Influence of isotherm temperature on maximum hydrogen capacity.

3.3 Corrosion behaviour

Figure 5 is the Tafel curve and corrosion rate of $Ti_{34}V_{40}Cr_{24}Fe_2$ alloy. No significant change was observed in E_{corr} of the as-cast after annealing; however a decrease from -0.80 to -0.867 mV was observed after quenching. Both heat treatment processes increased the corrosion rate of the alloy. The rate increased from 0.0004 in as-cast alloy to 0.0009 mm/y after annealing and 0.0017mm/y after quenching.

Cr is known for improving corrosion resistance of alloy [24; 54]; samples containing high at.% Cr is expected to have low corrosion rate and vice versa. Therefore the increase in corrosion rate of heat treated samples could be a result of reduction in total Cr content. Phase structure and oxide layer are among the factors that determines corrosion rate of an alloy and Laves structure have been reported to have thinner oxide layer than BCC structure [18]. Oxide layer is known for

passivation of corrosion [15; 37; 38]. It could therefore be concluded that for a dual phase alloy like the alloys being investigated, corrosion rate will increase when the proportion of Laves with thinner oxide layer increases. High Laves phase proportion in the quenched sample therefore suggests the reason for the observed increase in corrosion rate.

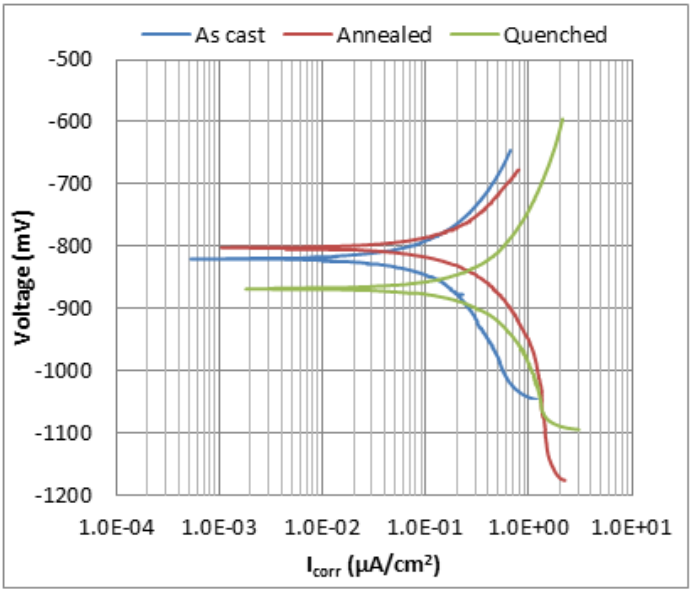

a) Terfel curve

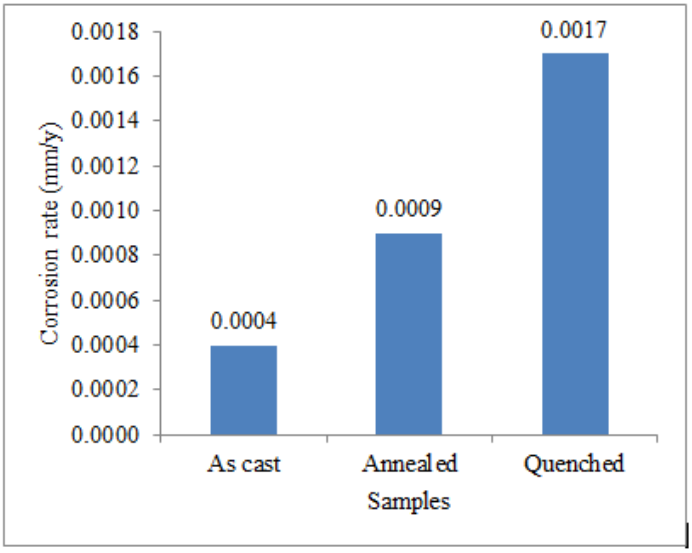

b) Corrosion rates

Figure 5. Tafel curve and corrosion rate of as-cast and heat treated $Ti_{34}V_{40}Cr_{24}Fe_2$.

4. Conclusion

The influence of heat treatment on the microstructure and hydrogen storage capacity of $Ti_{34}V_{40}Cr_{24}Fe_2$ at.% alloy has been investigated. Both the as-cast and heat treated samples contained BCC and Laves phases. Heat treatment was beneficial to hydrogen capacity but

detrimental to corrosion behavior. Though both heat treatment processes enhanced useful hydrogen capacity but annealed sample had a superior storage characteristics. Although both annealing and quenching increased the corrosion rate of the alloy, the rate of corrosion was found to be higher in quenched sample.

Acknowledgment

The work is supported by African Material Science and Engineering Network, AMSEN and the National Research Found NRF Thuthuka programme.

References

1. Akiba, E., & Iba, H. (1998). *Intermetallic, 6*, 461-470.
2. Ashworth, M. A., Davenport, A. J., Ward, R. M., & Hamilton, H. G. C. (2010). Microstructure and corrosion of Pd-modified Ti alloys produced by powder metallurgy. *Corrosion Science, 52*(7), 2413-2421. doi: http://dx.doi.org/10.1016/j.corsci.2010.03.006
3. Cho, S.-W., Enokib, H., & Akibab, E. (2000). Effect of Fe addition on hydrogen storage characteristics of $Ti_{0.16}$ $Zr_{0.05}$ $Cr_{0.22}$ $V_{0.57}$ alloy *Journal of Alloys and Compounds 307*, 304–310.
4. Cho, S.-W., Han, C.-S., Park, C.-N., & Akiba, E. (1999). The hydrogen storage characteristics of Ti–Cr–V alloys. *Journal of Alloys and Compounds, 288*(1–2), 294-298. doi: 10.1016/s0925-8388(99)00096-1
5. Cho, S.-W., Shim, G., Choi, G.-S., Park, C.-N., Yoo, J.-H., & Choi, J. (2007). Hydrogen absorption–desorption properties of Ti0.32Cr0.43V0.25 alloy. *Journal of Alloys and Compounds, 430*(1–2), 136-141. doi: http://dx.doi.org/10.1016/j.jallcom.2006.04.068
6. Chuang, H. J., Huang, S. S., Ma, C. Y., & Chan, S. L. I. (1999). Effect of annealing heat treatment on an atomized AB_2 hydrogen storage alloy. *Journal of Alloys and Compounds, 285*(1–2), 284-291. doi: 10.1016/s0925-8388(98)01050-0
7. Güleryüz, H., & Çimenoğlu, H. (2004). Effect of thermal oxidation on corrosion and corrosion–wear behaviour of a Ti–6Al–4V alloy. *Biomaterials, 25*(16), 3325-3333. doi: http://dx.doi.org/10.1016/j.biomaterials.2003.10.009
8. Handzlik, P., & Fitzner, K. (2013). Corrosion resistance of Ti and Ti–Pd alloy in phosphate buffered saline solutions with and without H_2O_2 addition. *Transactions of Nonferrous Metals Society of China, 23*(3), 866-875. doi: http://dx.doi.org/10.1016/S1003-6326(13)62541-8
9. Hang, Z., Xiao, X., Li, S., Ge, H., Chen, C., & Chen, L. (2012). Influence of heat treatment on the microstructure and hydrogen storage properties of $Ti_{10}V_{77}Cr_6Fe_6Zr$ alloy. *Journal of Alloys and Compounds 529*, 128–133.
10. Hang, Z., Xiao, X., Tan, D., He, Z., Li, W., Li, S., Chen, C., & Chen, L. (2010). Microstructure and hydrogen storage properties of $Ti_{10}V_{84-x}Fe_6Zr_x$ (x = 0;1–8) alloys. *International Journal of Hydrogen Energy, 35*(7), 3080-3086. doi: 10.1016/j.ijhydene.2009.07.019
11. Huang, T., Wu, J. Z., Chen, X. B., Yu, S. B., Xia, B., & Xu, N. (2004). *Material Sciece and Engineering, A 385*, 17.
12. Itoh, H., Arashima, H., Kubo, K., & Kabutomori, T. (2002). The influence of microstructure on hydrogen absorption properties of Ti–Cr–V alloys. *Journal of Alloys and Compounds, 330–332*(0), 287-291. doi: 10.1016/s0925-8388(01)01530-4
13. Kamimura, T., & Stratmann, M. (2001). The influence of chromium on the atmospheric corrosion of steel. *Corrosion Science, 43*(3), 429-447. doi: http://dx.doi.org/10.1016/S0010-938X(00)00098-6
14. Kuriwa, T., Tamura, T., Amemiya, T., Fuda, T., Kamegawa, A., Takamura, H., & Okada, M. (1999). *Journal of Alloys and Compounds, 293-295*, 433.
15. Liu, X., Jiang, L., Li, Z., Huang, Z., & Wang, S. (2009). Improve plateau property of $Ti_{32}Cr_{46}V_{22}$ BCC alloy with heat treatment and Ce additive. *Journal of Alloys and Compounds, 471*(1–2), L36-L38. doi: 10.1016/j.jallcom.2008.04.004
16. Okada, M., Kuriiwa, T., Tamura, T., Takamura, H., & Kamegawa, A. (2002). *Journal of Alloys and Compounds*(330-332), 511-516.
17. Seo, C., Kim, J., Lee, P., & Lee, J. (2003). *Journal of Alloys and Compounds, 348*, 252.
18. Shi, P., Ng, W. F., Wong, M. H., & Cheng, F. T. (2009). Improvement of corrosion resistance of pure magnesium in Hanks' solution by microarc oxidation with sol–gel TiO2 sealing. *Journal of Alloys and Compounds, 469*(1–2), 286-292. doi: http://dx.doi.org/10.1016/j.jallcom.2008.01.102

19. Shih, C.-C., Shih, C.-M., Su, Y.-Y., Su, L. H. J., Chang, M.-S., & Lin, S.-J. (2004). Effect of surface oxide properties on corrosion resistance of 316L stainless steel for biomedical applications. *Corrosion Science, 46*(2), 427-441. doi: http://dx.doi.org/10.1016/S0010-938X(03)00148-3
20. Tamura, T., Kazumi, T., Kamegwa, A., Takamura, H., & Okada, M. (2003). *Journal of Alloys and Compounds*(356-357), 505-509.
21. Tamura, T., Tominaga, Y., Matsumoto, K., Takamura, H., Fuda, T., Kuriiwa, T., Kamigawa, H., & Okada, M. (2002). *Journal of Alloys and Compounds, 330-332*, 522.
22. Tou, D., Zhu, W., Jianfeng, M., & Xua, N. (2008). Application of commercial ferrovanadium to reduce cost of Ti–V-based BCC phase hydrogen storage alloys. *Materials Science and Engineering, A 476*, 34-38. doi: 10.1016/j.msea.2007.04.080
23. Towata, S.-i., Noritake, T., Itoh, A., Aoki, M., & Miwa, K. (2013). Effect of partial niobium and iron substitution on short-term cycle durability of hydrogen storage Ti–Cr–V alloys. *International Journal of Hydrogen Energy, 38*(7), 3024-3029. doi: http://dx.doi.org/10.1016/j.ijhydene.2012.12.100
24. Yoo, J.-H., Shim, G., Cho, S.-W., & Park, C.-N. (2007). Effects of desorption temperature and substitution of Fe for Cr on the hydrogen storage properties of alloy. *International Journal of Hydrogen Energy, 32*(14), 2977-2981. doi: 10.1016/j.ijhydene.2007.01.012
25. Yu, X. B., Wu, Z., Xia, B. J., & Xu, N. X. (2004). Enhancement of hydrogen storage capacity of Ti–V–Cr–Mn BCC phase alloys. *Journal of Alloys and Compounds, 372*(1–2), 272-277. doi: 10.1016/j.jallcom.2003.09.153
26. Zhou, Y., Chen, J., Xu, Y., & Liu, Z. (2013). Effects of Cr, Ni and Cu on the Corrosion Behavior of Low Carbon Microalloying Steel in a Cl− Containing Environment. *Journal of Materials Science & Technology, 29*(2), 168-174. doi: http://dx.doi.org/10.1016/j.jmst.2012.12.013

5. Full paper ready for submission to Journal of Alloys and compounds (An Elsivier Journal).

Microstructure and hydrogen storage characteristics of rhodium substituted Ti-V-Cr alloys

Abstract

The effects of 0.05 and 0.10 at.% Rh addition on the microstructure and hydrogen storage properties of $Ti_{35}V_{40}Cr_{25}$ were investigated by X-ray diffraction and pressure-composition-temperature measurement. All three alloys contained a primary body centered cubic phase and a secondary Laves phases. Addition of rhodium enhanced both the hydrogen absorption and the useful hydrogen storage capacity. The absorption capacity was similar for both 0.05 and 0.10 at.% Rh alloys but desorption was highest with 0.10 at.% Rh addition. The plateau pressure was significantly reduced with addition of 0.05 at.% Rh, but only marginal reduction was observed with 0.10 at.% Rh. Both the enthalpy and entropy of hydride formation increased with the addition of rhodium.

Keywords: hydrogen storage, Laves phase-related BCC alloy, rhodium.

1. Introduction

Hydrogen is a promising energy source for modern industry because of its environmental friendliness. However, developing safe, reliable, compact, and cost-effective hydrogen storage technologies is one of the most technically challenging barriers to its widespread use as a form of energy [14; 45]. Hydrogen storage in gaseous or cryogenic forms are unattractive because of high safety challenges, as the storage is usually in high-pressure tanks of up to 700 bars, while storage in advanced materials is more promising [14; 21].

A number of studies have been conducted on hydrogen storage capacity of metallic alloys such as ternary Ti-V-Cr alloys [28; 33; 34]. Pei *et al.* [33] investigated the influence of V on hydrogen storage properties of $(TiCr)_{65}V_{35}$ and found a maximum hydrogen capacity of 2.86 wt% and desorption capacity of 1.75 wt%. A comparison of cyclic behaviour of $Ti_{0.8}Cr_{1.2}V$ and TiVCr alloys revealed that the alloys maintained maximum capacities of 2.5 and 2.0 wt% respectively

after 15 cycles [28]. In other work, a vanadium-based $V_{0.68}Ti_{0.2}Cr_{0.12}$ alloy had up to 1.5 wt% effective capacity [35], and a $Ti_{25}Cr_{30}V_{40}$ BCC alloy had a hydrogen capacity of ~2.2 wt% [3].

Investigations on the influence of alloying additions to Ti-V based alloys on desorption properties found maximum hydrogen desorption capacity of 1.44 wt% for $Ti_{10}V_{77}Cr_6Fe_6Zr$ [17] and the maximum absorption and desorption capacities of 2.0 wt% and 1.6 wt% respectively for V-7.4Zr-7.4Ti-7.4Ni [25] . The use of ferrovanadium as a substitute for vanadium to reduce the cost of the alloy $Ti_{34}Mn_{18}Cr_{16}V_{32-5x}(V_4Fe)_x$ (x = 0, 2, 3, 4, 5) was investigated by Tou *et al.* [42]. The best alloy with an effective hydrogen desorption capacity of 1.93 wt% and low cost was found at x = 3.

The effect of platinum group metals on hydrogen storage characteristics was studied by Yamashita *et al.* [47]. They found that the plateau pressure and activation temperature was lowered in $TiFe_{1-x}Pd_x$ ($0.05 \leq x \leq 0.30$ at.%) alloys as x increased, although the hydrogenation capacity was not significantly affected. Chemical surface modification of TiFe with Pd showed that Pd deposition improved hydrogenation properties at moderate hydrogen pressure [46]. Other investigations on the effect of Pd nanoparticles on hydrogen storage have also been done [6; 30; 41]. A study on plastic deformation and hysteresis for hydrogen storage in $Pd_{0.9}Rh_{0.1}$ showed absorption of up to 0.72 hydrogen-metal H/M ratio [23], but these alloys are expensive. Rh nanoparticles supported on graphene as a catalyst for chemical hydrogen storage in amine boranes was also reported by Shen *et al.* [7].

Cho *et al.* [11] identified a region of high absorption capacity in Ti-V-Cr ternary alloys. They observed that the effective hydrogen storage capacities in the range of hydrogen pressure, 0.003-5 MPa, was strongly dependent on the Ti/Cr ratio, and the maximum values were obtained at Ti/Cr ratios of ~0.75. The effects of various alloying additions on hydrogen storage characteristics of the ternary alloys in the identified region have been studied, but alloying of a Ti-V-Cr alloy with rhodium for hydrogen storage has never been reported. This work investigates the effect of small additions of Rh on the microstructure and hydrogen storage properties of a $Ti_{25-0.5x}V_{40}Cr_{35-0.5x}Rh_x$ (x = 0, 0.05, 0.10 at.%) alloy.

.

2. Experimental Procedure

Small ingots of $Ti_{25-0.5x}V_{40}Cr_{35-0.5x}Rh_x$ (x = 0, 0.05, 0.10 at.%) were produced by arc melting in a water-cooled copper hearth furnace under argon atmosphere. The ingots were re-melted three times for homogeneity of composition.

The crystal structures and lattice parameters of the as-cast alloys were determined by XRD using Cu K_α radiation with 2θ from 10 to 80°. Elemental compositions of the phases were found by SEM analyses using a FEI Nova NanoSEM 200® fitted with EDAX® Advanced Microanalysis Solution software. Some SEM imaging was also done on a Zeiss Sigma® field emission SEM.

A Sieverts-type apparatus was used for the measurement of the pressure composition isotherm (PCT curves). After crushing the samples into particles < 75 μm in size, 1g of each alloy was sealed into a stainless steel reactor. The samples were heated to 573 K, hydrogen at 3 MPa pressure was introduced into the apparatus for 30 minutes, followed by slow cooling to room temperature in hydrogen. This step enables hydrogen absorption and pulverisation of the alloy. After the absorption process, the samples were heated up to 573 K, the chamber was evacuated for 1 hour with a mechanical pump to fully dehydrogenate the alloy in preparation for PCT measurements at 303, 333 and 363 K.

3. Results and discussion

3.1 Phases and crystal structure

Figure 1 shows the SEM backscattered (BSE) micrographs of the as-cast $Ti_{25-0.5x}V_{40}Cr_{35-0.5x}Rh_x$ (x = 0, 0.05, 0.10) at.% alloys. All the samples contained a primary, light grey BCC and a secondary, dark intergranular Laves phases. The addition of 0.05 at.% Rh increased the proportion of the Laves phase and led to the formation of a needle-like Laves structure.

The main XRD peaks were identified as the (V) BCC phase and the minor peaks as the C14 Laves phase (Figure 2). With addition of 0.05at.% Rh, the BCC cell volume remained unchanged but that of the Laves phase decreased from 35.22 to 34.48 $Å^3$. As the rhodium content increased to 0.10 at.% Rh, the BCC cell volume increased from 27.75 to 28.09 $Å^3$ while that of Laves increased from 35.22 to 35.30 $Å^3$. The cell volume of a phase usually increases when an element

of larger atomic radius substitutes that of a smaller radius [49]. Rh has a solubility of up to 14 at.% in the (V) BCC phase [31]. In $Ti_{35-x0.5x}V_{40}Cr_{25-0.5x}Rh_x$, where Rh is substituting Ti and Cr, the atomic radius of Rh (173 pm) is larger than that of Cr (166 pm) but smaller than that of Ti (176 pm) [1]. Despite the small addition of rhodium, an increase in cell volume of the alloy implied that Rh substituted more Cr than Ti atoms in the BCC structure, otherwise a reduction in cell volume would have been observed. The proportion of the Laves phase increased from 11.5 to 17.3% in the 0.05 at.% Rh and 12 % in the 0.10 at.% Rh alloy. This indicated that formation of Laves was favoured by 0.05 at.% Rh addition.

3.2 Hydrogen storage properties

The absorption/desorption PCT curves of $Ti_{25-0.5x}V_{40}Cr_{35-0.5x}Rh_x$ (x = 0, 0.05, 0.10 at.%) are shown in Figure 3. No absorption or desorption plateaux were observed in the 0.10 at.% Rh alloy at a testing temperature of 363 K. Absorption began at a lower pressure in 303 K isotherms for all samples except for 0.10 Rh sample where it began at 0.0005MPa at 363 K isotherm.

Hydrogen desorption under ambient conditions is desirable for practical application in fuel cells [8; 53], and the desorption PCT curves at 303 K for 0, 0.05 and 0.10 at.% Rh compositions are shown in Figure 4. The useful capacity increased with increase in Rh content as shown in Table 2. Generally, the BCC phase is known to enhance H capacity [5; 16; 18], increase in its cell volume implies availability of more H absorption sites or space, hence an increase in storage capacity, while the Laves phase is detrimental to storage capacity[10; 42; 50; 53]. Laves phase with large cell volume result in low storage capacity[52]. The increase in BCC cell volume was responsible for the higher useful H capacity at 0.10 at.% Rh. Since the cell volume of BCC remained constant with addition of 0.05 at.% Rh, a slight decrease in the Laves cell volume could be responsible for the observed increase in useful capacity.

The maximum absorption content increased with decrease in temperature and the useful capacity increased with increase in Rh content (Figure 5). At the respective temperatures of 303, 333, and 363 K: the Rh-free alloy absorbed 1.89, 1.31 and 1.03 wt% hydrogen, the 0.05 Rh alloy had the highest hydrogen absorption capacities of 2.25, 2.08 and 1.77 wt%, whereas an increase in Rh content to 0.10 at.% yielded the maximum capacities of 2.24, 1.36 and 0.76 wt%. Similar to literature [20; 51; 54], the absorption capacity decreased with increase in temperature due to the

increase in kinetic energy of hydrogen at elevated temperature [9; 50]. At lower temperatures, the kinetic energy is lower and absorption by the host metal is facilitated.

. As shown in Figure 5, the useful capacity increased with Rh content: from 1.56 wt% in the Rh-free alloy to 1.74 wt% for the 0.05 Rh alloy, and further to 1.87 wt% for the 0.10 Rh alloy.

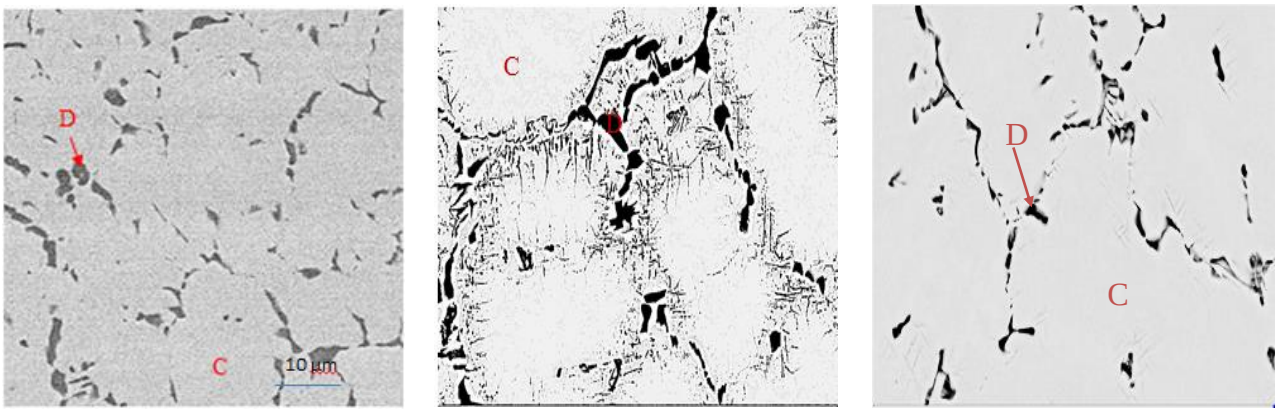

(a) x = 0 at.% (b) x = 0.05 at.% (c) x = 0.10 at.%

Figure 1. SEM BSE micrographs of $Ti_{25-0.5x}V_{40}Cr_{35-0.5x}Rh_x$ (x = 0, 0.05, 0.10) at.% alloy.

During the hydrogen absorption process in V-based alloys, two kinds of hydrides are formed: mono-hydride (β-phase) and di-hydride (γ-phase) [44; 48]. The mono-hydrides are not easily decomposed but the di-hydrides decompose easily under moderate conditions of temperature and pressure such as 298 K and above 0.01MPa [49]. Table 2 showed that the H desorbed, or useful hydrogen, was higher in the Rh-containing alloys, implying that more γ-phase hydride was formed during the hydrogen absorption process. The highest remaining capacity was observed in the 0.05 Rh alloy indicating that more mono-hydride was formed during the hydrogen absorption process. The maximum hydrogen desorption, or useful hydrogen, was observed in the 0.10 Rh alloy, suggesting that more di-hydride was formed in the absorption process.

More β-phase hydride than γ-phase was formed during the absorption process in the 0.05 Rh alloy because higher capacity remained in the alloy after desorption. For the 0.10 Rh alloy, much of the hydride formed during the absorption process was desorbed evidenced by the higher desorption capacity; indicating formation of more γ-phase hydride during the absorption process. Therefore, addition of 0.05 at.% Rh promoted formation of the β-phase (mono-hydride) while 0.10 Rh alloy favours formation of γ-phase (di-hydride).

Table 2 shows that the plateau pressure decreased with addition of rhodium. The strain energy of the interstitial site determines the flatness of plateau, and reduction in plateau pressure indicates lowered strain energy [18]. Addition of 0.05 at.% Rh reduced the plateau pressure from 0.42 to 0.02 MPa, but with addition of 0.10 at.% Rh the plateau pressure increased to 0.35 MPa. This indicates that the strain in the interstitial site was significantly reduced by 0.05 at.% Rh compared to 0.10 at.% Rh addition. An increase in BCC cell volume leads to an increase in interstitial space and consequently reduction of plateau pressure and interstitial strain. This justifies the reduction in plateau pressure with 0.10 at.% Rh addition, as the cell volume of the BCC phase increased. This is in agreement with work done by Hang et al. [5] and Lundin [3]. Contrarily, the plateau pressure was reduced in the 0.05 at.% Rh alloy despite the reduction in the Laves cell volume. This phenomenon is similar to that found in (V30Ti35Cr25Fe10)100-xAlx (x=0-5) alloys [49], where the lattice parameter of BCC increased with increase in Al content but the plateau pressure also increased. Lee and Perng [27] also found a similar phenomenon in TiFe1-xAlx (x = 0, 0.025, 0.05, 0.10). The atomic radius of aluminium (0.1432 nm) is closer to that of titanium (0.1448 nm), but larger than that of iron (0.1241 nm), so when Al substituted Fe, the cell volume was expected to increase and plateau pressure was expected to decrease. Contrarily, despite the increase in cell volume, the plateau pressure increased [27].

Table 2 shows the thermodynamic properties and the hydrogen storage characteristics of $Ti_{25-0.5x}V_{40}Cr_{35-0.5x}Rh_x$ (x = 0, 0.05, 0.10 at.%) alloys. Dissociation enthalpy provides a measure of the strength of the interaction between the hydrogen and the adsorbent surface or pore structure [4]. The enthalpy increased with addition of Rh, indicating that presence of Rh strengthens the H-metal bond. The strength of interaction was increased by 22.7% for the 0.05 Rh alloy and only 3.4% for the 0.10 Rh alloy. This implied that more energy was required to break the H-metal bond in the 0.05 Rh alloy.

The degree of orderliness or randomness of a substance is measured by its entropy [4], where a low entropy indicates a highly ordered crystalline structure. An increase in entropy is an indication of higher disorder. The observed increase in entropy with addition of Rh indicates higher disorder of hydrogen on the host metal. The disorder increased by 8.3% with 0.05 at.% Rh and 5.5% with 0.10 at.% Rh addition.

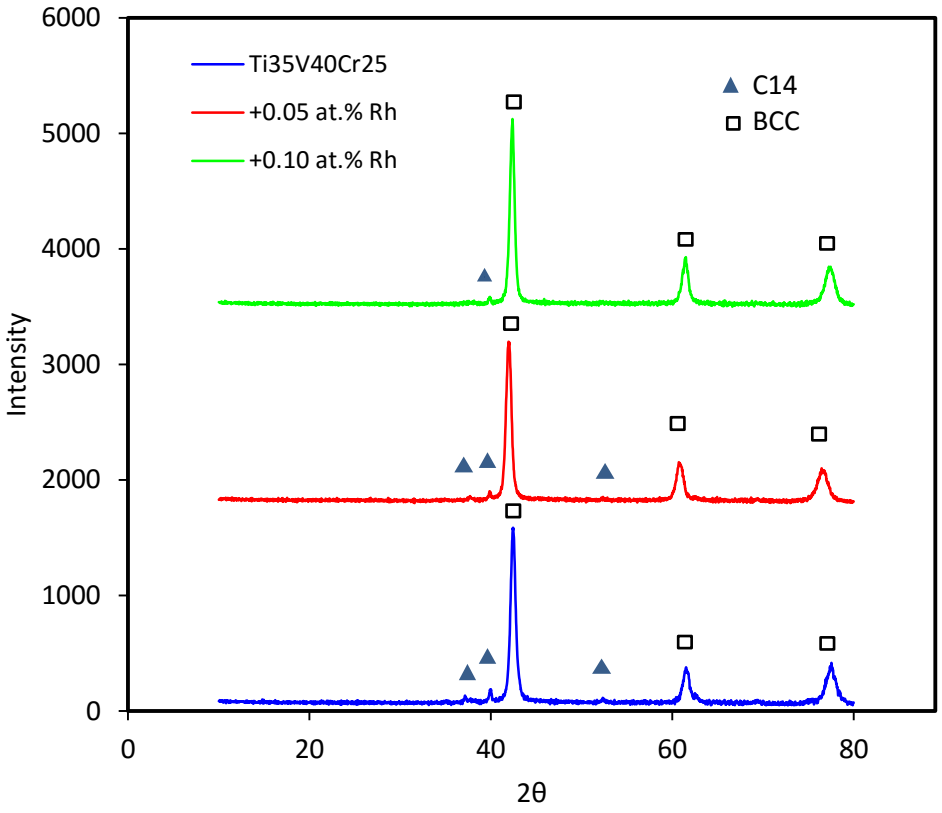

Figure 2. XRD pattern of the as-cast $Ti_{25-0.5x}V_{40}Cr_{35-0.5x}Rh_x$ (x = 0, 0.05, 0.10 at.%) alloy.

Table 1. Crystallographic parameters of as-cast $Ti_{25-0.5x}V_{40}Cr_{35-0.5x}Rh_x$ (x = 0, 0.05, 0.10 at.%) alloys

Sample	Phases XRD	Phase proportion (area %)	Phase description			
			Space group (No.)	a (*Å*)	c (*Å*)	Cell volume ($Å^3$)
0 at.% Rh	BCC (V)	88.5	*Im*3*m* (229)	3.03		27.75
	Laves (C14)	11.5	*P*63/*mmc* (194)	2.95	4.67	35.22
0.05 at.% Rh	BCC (V)	82.7	*Im*3*m* (229)	3.03		27.75
	Laves (C14)	17.3	*P*63/*mmc* (194)	2.92	4.67	34.48
0.10 at.% Rh	BCC (V)	88.0	*Im*3*m* (229)	3.04		28.09
	Laves (C14)	12.0	*P*63*mmc* (194)	2.95	4.68	35.30

Table 2. Thermodynamic properties of nominal $Ti_{25-0.5x}V_{40}Cr_{35-0.5x}Rh_x$ (x = 0, 0.05, 0.10 at.%) alloys.

Alloy composition (at.%)	Hydrogen capacity[$] (wt%)		Capacity remaining[$] (wt%)	Plateau pressure[#] (MPa)	$-\Delta H^{\#}$ (kJ/mol H_2)	$-\Delta S^{\#}$ (J/mol.K)
	Absorption	Desorption/ useful				
$Ti_{25}V_{40}Cr_{35}$	1.89	1.56	0.33	0.42	40.59	121.49
$Ti_{24.975}V_{40}Cr_{34.975}Rh_{0.05}$	2.25	1.74	0.50	0.02	49.82	131.59
$Ti_{24.95}V_{40}Cr_{34.95}Rh_{0.10}$	2.24	1.87	0.37	0.35	41.99	128.19

[$] Measured at 303 K

[#] Obtained from the 303 and 333 K PCT isotherms

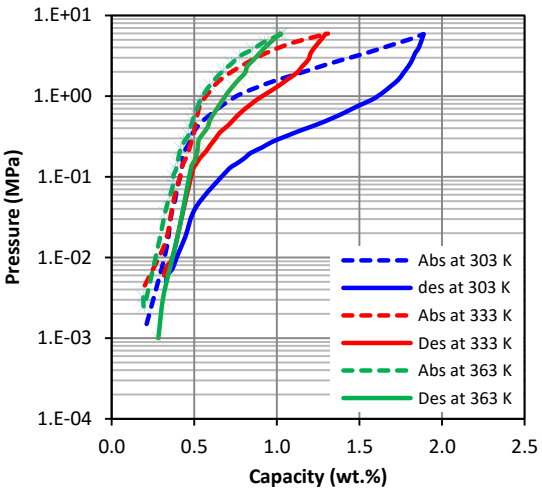

a) 0 at.% Rh

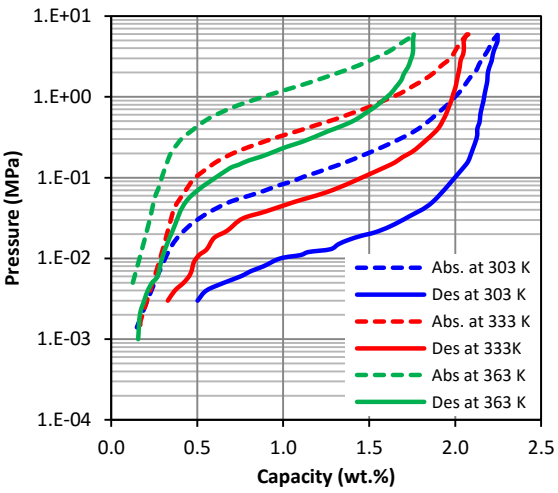

b) 0.05 at.% Rh

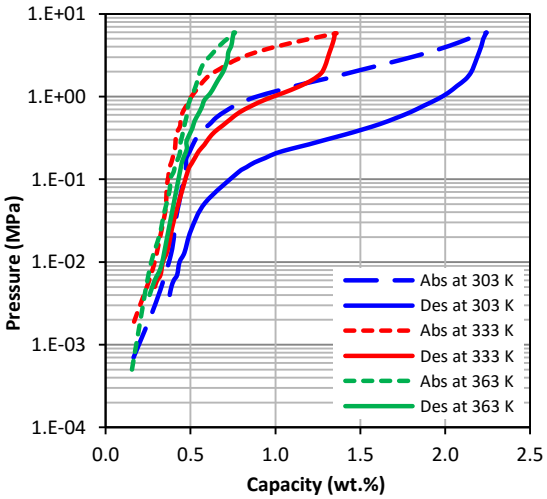

c) 0.10 at.% Rh

Figure 3. Absorption/desorption PCT curves of as-cast $Ti_{25-0.5x}V_{40}Cr_{35-0.5x}Rh_x$ (x = 0, 0.05, 0.10) alloys.

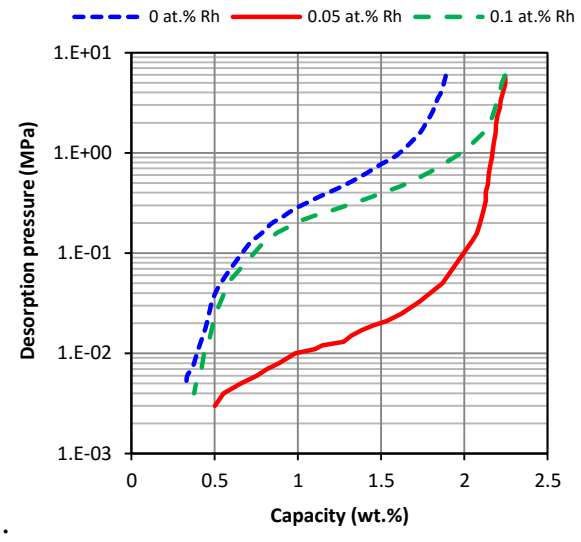

Figure 4. Desorption curves of as-cast $Ti_{25-0.5x}V_{40}Cr_{35-0.5x}Rh_x$ (x = 0, 0.05, 0.10) at 303 K.

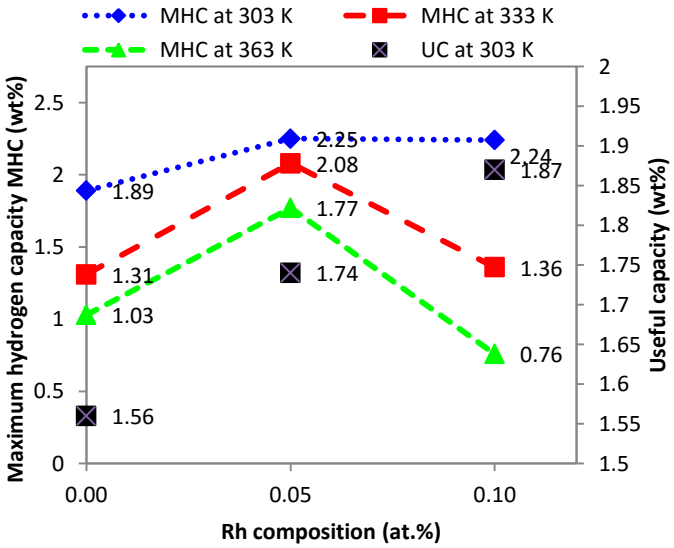

Figure 5. Variation of maximum H capacity and useful capacity (RHSC) with isotherm testing temperature and Rh composition.

4. Conclusions

The influence of 0.05 and 0.10 at.% Rh on the structure and hydrogen storage characteristics of a $Ti_{25}V_{40}Cr_{35}$ alloy has been investigated. The main conclusions are:

5. The three alloys contain a primary BCC (V) phase and a secondary Laves phase.
6. Addition of rhodium did not change the crystal structure of the base alloy, but increased the cell volume of the Laves phase in both the 0.05 and 0.10 at% Rh alloys. The BCC cell volume increased only with 0.10 at.% Rh addition.
7. The hydrogen absorption and useful capacities increased with Rh addition. The maximum hydrogen absorption of 2.25 wt% was observed in 0.05 Rh alloy but its useful capacity was lower than the value of 1.87 wt% observed in 0.10 Rh alloy. The best plateau characteristic was observed in 0.05 Rh alloy, its plateau pressure was considerably lower from 0.42 to 0.02 MPa, while a marginal reduction to 0.35 in 0.10 Rh alloy was observed.
8. Much of the hydride formed during absorption process in 0.05 Rh alloy was β-base phase hydride hence the observed lower hydrogen desorption. In 0.10 Rh alloy more γ-phase hydride was formed thereby signified with the high desorption capacity.
9. The H-metal bond was strengthened with Rh addition; the bond was stronger by ~23% in 0.05 Rh alloy and ~3% in 0.10 Rh alloy. Rh addition led to higher disorder or hydron on the host.

Acknowledgments

The work is supported by African Materials Science and Engineering Network (AMSEN) and the National Research Foundation (NRF) Thuthuka programme.

References

. Retrieved 3 Sep 2015 17:41:56 GMT, 2015 from http://www.ptable.com/

[2] Akiba, E., & Iba, H. (1998). *Intermetallic, 6*, 461-470.

[3] Akiba, E., & Iba, H. (1998). Hydrogen absorption by Laves phase related BCC solid solution. *Intermetallics, 6*(6), 461-470. doi: http://dx.doi.org/10.1016/S0966-9795(97)00088-5

Alefeld, G., & Völkl., J. (1978). *Hydrogen in Metals II*. Berlin-Heidelberg: Springer-Verlag.

[5] Ashworth, M. A., Davenport, A. J., Ward, R. M., & Hamilton, H. G. C. (2010). Microstructure and corrosion of Pd-modified Ti alloys produced by powder metallurgy. *Corrosion Science, 52*(7), 2413-2421. doi: http://dx.doi.org/10.1016/j.corsci.2010.03.006

[6] Biesiekierski, A., Ping, D. H., Yamabe-Mitarai, Y., & Wen, C. (2014). Impact of ruthenium on microstructure and corrosion behavior of β-type Ti–Nb–Ru alloys for biomedical applications. *Materials & Design, 59*, 303-309. doi: http://dx.doi.org/10.1016/j.matdes.2014.02.058

[7] Bowman, R. C., & Fultz, B. (2002). Metallic Hydrides I: Hydrogen Storage and Other Gas-Phase Applications. *MRS Bulletin, 27*(09), 688-693. doi: doi:10.1557/mrs2002.223

[8] Broom, D. (2008). Hydrogen sorption measurements on potential storage materials:experimental methods and measurement accuracy. *Office for Official Publications of the European Communities, Luxembourg, EUR 23242 EN*.

[9] Chen, Z., Xiao, X., Chen, L., Fan, X., Liu, L., Li, S., . . . Wang, Q. (2014). Influence of Ti super-stoichiometry on the hydrogen storage properties of $Ti_{1+x}Cr_{1.2}Mn_{0.2}Fe_{0.6}$ (x = 0–0.1) alloys for hybrid hydrogen storage application. *Journal of Alloys and Compounds, 585*, 307-311. doi: http://dx.doi.org/10.1016/j.jallcom.2013.09.141

[10] Cho, S.-W., Enokib, H., & Akibab, E. (2000). Effect of Fe addition on hydrogen storage characteristics of $Ti_{0.16}$ $Zr_{0.05}$ $Cr_{0.22}$ $V_{0.57}$ alloy *Journal of Alloys and Compounds 307*, 304–310.

[11] Cho, S.-W., Han, C.-S., Park, C.-N., & Akiba, E. (1999). The hydrogen storage characteristics of Ti–Cr–V alloys. *Journal of Alloys and Compounds, 288*(1–2), 294-298. doi: 10.1016/s0925-8388(99)00096-1

[12] Cho, S.-W., Shim, G., Choi, G.-S., Park, C.-N., Yoo, J.-H., & Choi, J. (2007). Hydrogen absorption–desorption properties of Ti0.32Cr0.43V0.25 alloy. *Journal of Alloys and Compounds, 430*(1–2), 136-141. doi: http://dx.doi.org/10.1016/j.jallcom.2006.04.068

[13] Chuang, H. J., Huang, S. S., Ma, C. Y., & Chan, S. L. I. (1999). Effect of annealing heat treatment on an atomized AB_2 hydrogen storage alloy. *Journal of Alloys and Compounds, 285*(1–2), 284-291. doi: 10.1016/s0925-8388(98)01050-0

. *Fuel cell technology program (Hydrogen storage).pdf*. (January, 2011). United States, Department of Energy Retrieved from www.eere.energy.gov/informationcenter.

[15] Güleryüz, H., & Çimenoğlu, H. (2004). Effect of thermal oxidation on corrosion and corrosion–wear behaviour of a Ti–6Al–4V alloy. *Biomaterials, 25*(16), 3325-3333. doi: http://dx.doi.org/10.1016/j.biomaterials.2003.10.009

[16] Handzlik, P., & Fitzner, K. (2013). Corrosion resistance of Ti and Ti–Pd alloy in phosphate buffered saline solutions with and without H_2O_2 addition. *Transactions of Nonferrous Metals Society of China, 23*(3), 866-875. doi: http://dx.doi.org/10.1016/S1003-6326(13)62541-8

[17] Hang, Z., Xiao, X., Li, S., Ge, H., Chen, C., & Chen, L. (2012). Influence of heat treatment on the microstructure and hydrogen storage properties of $Ti_{10}V_{77}Cr_6Fe_6Zr$ alloy. *Journal of Alloys and Compounds 529*, 128–133.

[18] Hang, Z., Xiao, X., Tan, D., He, Z., Li, W., Li, S., . . . Chen, L. (2010). Microstructure and hydrogen storage properties of $Ti_{10}V_{84-x}Fe_6Zr_x$ (x = 0;1–8) alloys. *International Journal of Hydrogen Energy, 35*(7), 3080-3086. doi: 10.1016/j.ijhydene.2009.07.019

[19] Huang, T., Wu, J. Z., Chen, X. B., Yu, S. B., Xia, B., & Xu, N. (2004). *Material Sciece and Engineering, A 385*, 17.

[20] Huang, T., Wu, Z., Xia, B., Chen, J., Yu, X., Xu, N., . . . Yu, H. (2003). TiCr1.2(V–Fe)0.6—a novel hydrogen storage alloy with high capacity. *Science and Technology of Advanced Materials, 4*(6), 491-494. doi: http://dx.doi.org/10.1016/j.stam.2003.12.001

. Hydrogen storage technology roadmap. (2005) *United States Department of Energy FreedomCAR and fuel partnership*. Washington.

[22] Itoh, H., Arashima, H., Kubo, K., & Kabutomori, T. (2002). The influence of microstructure on hydrogen absorption properties of Ti–Cr–V alloys. *Journal of Alloys and Compounds, 330–332*(0), 287-291. doi: 10.1016/s0925-8388(01)01530-4

[23] Jen, S. U., & Wu, T. C. (2005). Young's modulus and hardness of Pd thin films. *Thin Solid Films, 492*(1–2), 166-172. doi: http://dx.doi.org/10.1016/j.tsf.2005.06.048

[24] Kamimura, T., & Stratmann, M. (2001). The influence of chromium on the atmospheric corrosion of steel. *Corrosion Science, 43*(3), 429-447. doi: http://dx.doi.org/10.1016/S0010-938X(00)00098-6

[25] Kuriiwa, T., Tamura, T., Amemiya, T., Fuda, T., Kamegawa, A., Takamura, H., & Okada, M. (1999). New V-based alloys with high protium absorption and desorption capacity. *Journal of Alloys and Compounds, 293–295*, 433-436. doi: http://dx.doi.org/10.1016/S0925-8388(99)00325-4

[26] Kuriwa, T., Tamura, T., Amemiya, T., Fuda, T., Kamegawa, A., Takamura, H., & Okada, M. (1999). *Journal of Alloys and Compounds, 293-295*, 433.

[27] Lee, S. M., & Perng, T. P. (1999). Correlation of substitutional solid solution with hydrogenation properties of $TiFe_{1-x}M_x$ (M=Ni, Co, Al) alloys. *Journal of Alloys and Compounds, 291*(1–2), 254-261. doi: http://dx.doi.org/10.1016/S0925-8388(99)00262-5

[28] Lin, H. C., Lin, K. M., Wu, K. C., Hsiung, H. H., & Tsai, H. K. (2007). Cyclic hydrogen absorption–desorption characteristics of TiCrV and $Ti_{0.8}Cr_{1.2}V$ alloys. *International Journal of Hydrogen Energy 32* 4966 4972. doi: 10.1016/j.ijhydene.2007.07.057

[29] Liu, X., Jiang, L., Li, Z., Huang, Z., & Wang, S. (2009). Improve plateau property of $Ti_{32}Cr_{46}V_{22}$ BCC alloy with heat treatment and Ce additive. *Journal of Alloys and Compounds, 471*(1–2), L36-L38. doi: 10.1016/j.jallcom.2008.04.004

[30] Maillard, F., Bonnefont, A., & Micoud, F. (2011). An EC-FTIR study on the catalytic role of Pt in carbon corrosion. *Electrochemistry Communications, 13*(10), 1109-1111. doi: http://dx.doi.org/10.1016/j.elecom.2011.07.011

Massalski, T. B. (1990). *Binary Alloy Phase Diagrams.* (2nd ed. Vol. 1): ASM International, Materials Park, OH.

[32] Okada, M., Kuriiwa, T., Tamura, T., Takamura, H., & Kamegawa, A. (2002). *Journal of Alloys and Compounds*(330-332), 511-516.

[33] Pei, P., Xiping, S., Ming, Z., Peilong, Z., & Guoliang, C. (2008). influence of V content on hydrogen storage properties in low vanadium Ti-V-Cr alloy.pdf. *Rare Metal materials and engineering, 37*(8), 1419-1423.

[34] Pierard, N., Fonseca, A., Colomer, J. F., Bossuot, C., Benoit, J. M., Van Tendeloo, G., . . . Nagy, J. B. (2004). Ball milling effect on the structure of single-wall carbon nanotubes. *Carbon, 42*(8–9), 1691-1697. doi: http://dx.doi.org/10.1016/j.carbon.2004.02.031

[35] Seo, C.-Y., Kim, J.-H., Lee, P. S., & Lee, J.-Y. (2003). Hydrogen storage properties of vanadium-based b.c.c. solid solution metal hydrides. *Journal of Alloys and Compounds*, *348*(1–2), 252-257. doi: http://dx.doi.org/10.1016/S0925-8388(02)00831-9

[36] Seo, C., Kim, J., Lee, P., & Lee, J. (2003). *Journal of Alloys and Compounds*, *348*, 252.

[37] Shi, P., Ng, W. F., Wong, M. H., & Cheng, F. T. (2009). Improvement of corrosion resistance of pure magnesium in Hanks' solution by microarc oxidation with sol–gel TiO2 sealing. *Journal of Alloys and Compounds*, *469*(1–2), 286-292. doi: http://dx.doi.org/10.1016/j.jallcom.2008.01.102

[38] Shih, C.-C., Shih, C.-M., Su, Y.-Y., Su, L. H. J., Chang, M.-S., & Lin, S.-J. (2004). Effect of surface oxide properties on corrosion resistance of 316L stainless steel for biomedical applications. *Corrosion Science*, *46*(2), 427-441. doi: http://dx.doi.org/10.1016/S0010-938X(03)00148-3

[39] Tamura, T., Kazumi, T., Kamegwa, A., Takamura, H., & Okada, M. (2003). *Journal of Alloys and Compounds*(356-357), 505-509.

[40] Tamura, T., Tominaga, Y., Matsumoto, K., Takamura, H., Fuda, T., Kuriiwa, T., . . . Okada, M. (2002). *Journal of Alloys and Compounds*, *330-332*, 522.

[41] Tian, Q.-f., Zhang, Y., Tan, Z.-c., Xu, F., Sun, L.-x., Zhang, T., & Yuan, H.-t. (2006). Effects of Pd substitution for Ni on corrosion performances of Mg0.9 Ti0.1Ni1-xPdx hydrogen storage alloys. *Transactions of Nonferrous Metals Society of China*, *16*(3), 497-501. doi: http://dx.doi.org/10.1016/S1003-6326(06)60086-1

[42] Tou, D., Zhu, W., Jianfeng, M., & Xua, N. (2008). Application of commercial ferrovanadium to reduce cost of Ti–V-based BCC phase hydrogen storage alloys. *Materials Science and Engineering, A 476*, 34-38. doi: 10.1016/j.msea.2007.04.080

[43] Towata, S.-i., Noritake, T., Itoh, A., Aoki, M., & Miwa, K. (2013). Effect of partial niobium and iron substitution on short-term cycle durability of hydrogen storage Ti–Cr–V alloys. *International Journal of Hydrogen Energy*, *38*(7), 3024-3029. doi: http://dx.doi.org/10.1016/j.ijhydene.2012.12.100

[44] Tsukahara, M., Takahashi, K., Mishima, T., Sakai, T., Miyamura, H., Kuriyama, N., & Uehara, I. (1995). Metal hydride electrodes based on solid solution type alloy TiV_3Ni_x ($0 \leq x \leq 0.75$). *Journal of Alloys and Compounds*, *226*(1–2), 203-207. doi: http://dx.doi.org/10.1016/0925-8388(95)01570-1

. *US DoE Fuel cell technology program (safety codes and standard)*. (January, 2011). United States.

[46] Williams, M., Lototsky, M. V., Davids, M. W., Linkov, V., Yartys, V. A., & Solberg, J. K. (2011). Chemical surface modification for the improvement of the hydrogenation kinetics and poisoning resistance of TiFe. *Journal of Alloys and Compounds, 509, Supplement 2*(0), S770-S774. doi: 10.1016/j.jallcom.2010.11.063

[47] Yamashita, I., Tanaka, H., Takeshita, H., Kuriyama, N., Sakai, T., & Uehara, I. (1997). Hydrogenation characteristics of $TiFe_{1-x}Pd_x$ ($0.05 \leq {}_x \leq 0.30$) alloys. *Journal of Alloys and Compounds, 253–254*(0), 238-240. doi: 10.1016/s0925-8388(96)02925-8

[48] Yan, Y., Chen, Y., Zhou, X., Liang, H., Wu, C., & Tao, M. (2008). Some factors influencing the hydrogen storage properties of 30V–Ti–Cr–Fe alloys. *Journal of Alloys and Compounds, 453*(1–2), 428-432. doi: 10.1016/j.jallcom.2006.11.122

[49] Yigang, Y., Yungui, C., Hao, L., Chaoling, W., Mingda, T., & Tu, M. (2006). Effect of Al on hydrogen storage properties of $V_{30}Ti_{35}Cr_{25}Fe_{10}$ alloy. *Journal of Alloys and Compounds 426* 253-255. doi: 10.1016/j.jallcom.2005.12.122

[50] Yoo, J.-H., Shim, G., Cho, S.-W., & Park, C.-N. (2007). Effects of desorption temperature and substitution of Fe for Cr on the hydrogen storage properties of alloy.

International Journal of Hydrogen Energy, *32*(14), 2977-2981. doi: 10.1016/j.ijhydene.2007.01.012

[51] Young, K., Ouchi, T., & Fetcenko, M. A. (2009). Pressure–composition–temperature hysteresis in C14 Laves phase alloys: Part 1. Simple ternary alloys. *Journal of Alloys and Compounds*, *480*(2), 428-433. doi: http://dx.doi.org/10.1016/j.jallcom.2008.12.113

[52] Yu, X. B., Chen, J. Z., Wu, Z., Xia, B. J., & Xu, N. X. (2004). Effect of Cr content on hydrogen storage properties for Ti-V-based BCC-phase alloys. *International Journal of Hydrogen Energy 29* (4), 1377-1381. doi: 10.1016/j.ijhydene.2004.01.015

[53] Yu, X. B., Wu, Z., Xia, B. J., & Xu, N. X. (2004). Enhancement of hydrogen storage capacity of Ti–V–Cr–Mn BCC phase alloys. *Journal of Alloys and Compounds, 372*(1–2), 272-277. doi: 10.1016/j.jallcom.2003.09.153

[54] Zhou, Y., Chen, J., Xu, Y., & Liu, Z. (2013). Effects of Cr, Ni and Cu on the Corrosion Behavior of Low Carbon Microalloying Steel in a Cl− Containing Environment. *Journal of Materials Science & Technology*, *29*(2), 168-174. doi: http://dx.doi.org/10.1016/j.jmst.2012.12.013